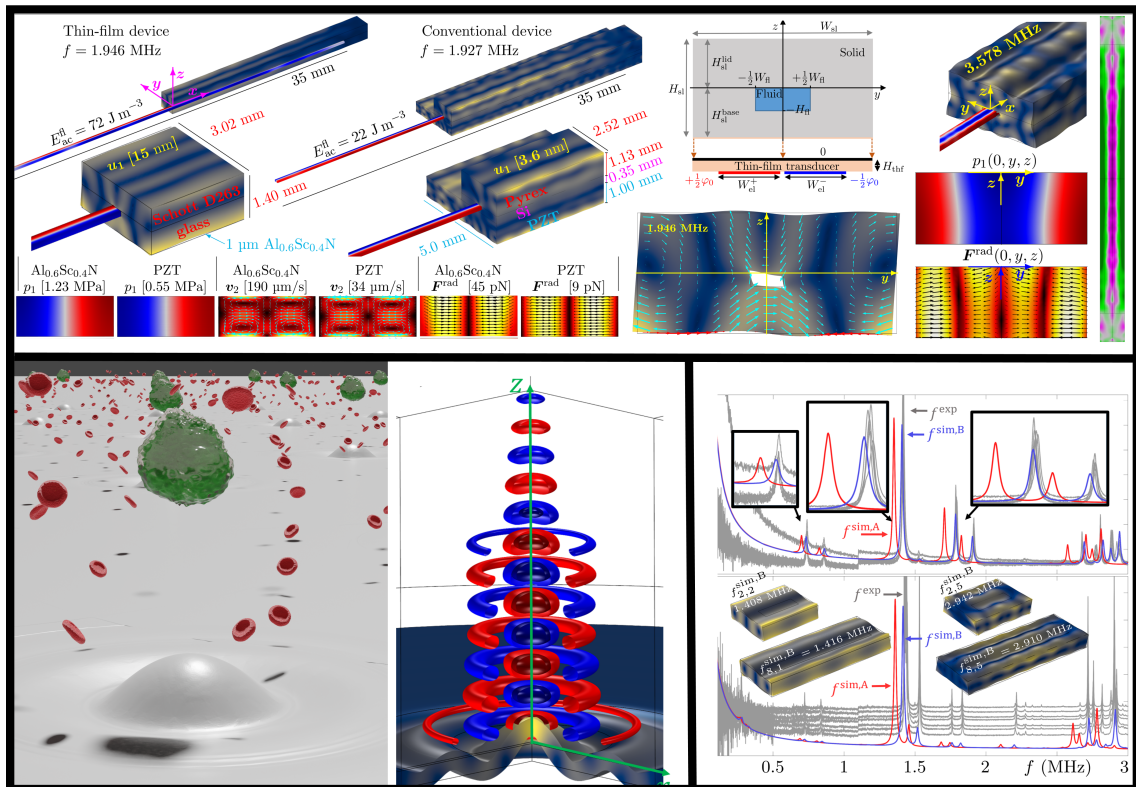


André Gugele Steckel

# Theory and modeling of thin-film actuation in microscale acoustofluidics



PhD Thesis

Advised by Professor Henrik Bruus

Department of Physics  
Technical University of Denmark

31 August 2021

**Cover illustration:** A collage of the work done in this thesis. Top pane show simulations of thin-film transducers used for acoustic particle handling, adapted from Ref. 1. Bottom right show thin-film transducers used for *in situ* determination of parameters, adapted from Ref. 2. Bottom left show an illustration of cancer cells be levitated and trapped in a fluid above a membrane, adapted from Ref. 3.

*Theory and modeling of thin-film actuation in microscale acoustofluidics*

Copyright © 2021 André Gugele Steckel. All Rights Reserved.  
Typeset using L<sup>A</sup>T<sub>E</sub>X.

Department of Physics  
Technical University of Denmark  
DTU Physics Building 309,  
DK-2800 Kongens Lyngby,  
Denmark

<http://www.fysik.dtu.dk/microfluidics>

Supervisor: Professor Henrik Bruus from Technical University of Denmark.  
Co-Supervisor: Professor Thomas Laurell from Lund University.

# Abstract

Acoustofluidics is the study of sound in fluids, which has been a steadily progressing research field. The field dates back more than 200 years to the study of the motion of small particles driven by air currents above metal Chladni plates, which were vibrated by dragging a violin bow on their edge. Today, acoustofluidics is used in systems manufactured in microelectromechanical systems (MEMS)-compatible clean rooms, where devices are designed and used with micrometer precision in liquid-filled channels several times the width of a human hair. In particular, the interplay between acoustofluidics and microfluidics has recently shown many interesting applications, utilizing both the acoustic radiation force and acoustic streaming to move particles submersed in fluids, in what is called acoustophoresis.

In the literature, these acoustofluidic devices have seen uses including, but not limited to, inkjet printers, cancer cell sorting, continuous flow separation of blood cells from blood plasma, label-free trapping and sorting, microfluidic mixers, acoustic tweezers, and many more. The field is rapidly expanding and evolving and there is still room for innovations and improvements. This thesis focuses on two specific problems in the field. First, one of the most common means of producing acoustofluidic devices is to fabricate them in ways that make it difficult to reproduce results from device to device, as well as making them difficult to mass produce. One such method is gluing lead zirconate titanate (PZT) piezoelectric transducers to the devices. This is done in such a fashion as to make each device different from the next, since small changes in the glue result in large differences in the end results. The use of piezoelectric transducers also means that these systems contains lead, which the European Union, for example, has passed legislation order to phase out, since lead is an environmentally hazardous material. However, lead is a difficult material to avoid in piezoelectric transducers, since it works much better than most other lead-free alternatives.

This thesis investigates implementing thin-film piezoelectric (PZE) transducers into acoustofluidic devices. One thin-film PZE that is commonly used in clean-room fabrication, and which is MEMS compatible, is aluminum nitride (AlN), and its newer and more exotic variant, aluminum scandium nitride (AlScN), which is a stronger PZE material but more difficult to manufacture. The main goal of this thesis is to determine how these thin-films can be used to actuate acoustofluidic devices and understand the underlying mechanism, as well as comparing our model to experiments and using that model to make predictions for thin-film acoustofluidic devices. The results are given in this thesis and are also presented in two published papers, and one in which is still in preparation.

In the first article, an ensemble of millimeter-sized glass blocks with AlN thin film on top and different top electrode patterns was investigated. In this paper, we described how they were fabricated, characterized, and simulated, and how the Young's modulus and Poisson's ratio of the glass were fitted by minimizing the difference between measured impedance spectra and the impedance spectra calculated from simulations. These devices showed high reproducibility, as well as demonstrating that glass bulk devices can be actuated by a thin-film, and that good agreement between simulations and measurements could be achieved. It was found that after having fitted the Young's modulus and Poisson's ratio of the glass, the relative deviation between the simulated and measured resonance peaks fell to  $(-0.5 \pm 0.1)\%$ , which was an order of magnitude lower than with the parameter values from the manufacturer, and therefore showed that this could be a method for *in situ* characterization of parameters. These parameter values are important, as they play a central role in the accuracy of our predictive simulations.

The second paper deals with the acoustofluidic applications of using PZE thin films to drive bulk acoustofluidic devices. Building upon the understanding of solid mechanical part of the model from the first paper, we have simulated glass devices with microfluidic channels of a few hundreds of micrometers in width and height and actuated by AlN, AlScN, and PZT thin-film transducers, all of which show acoustofluidic behavior. To compare how the acoustofluidic properties, such as acoustic streaming and radiation force, compare to a traditional device, we simulate a conventional device driven by a bulk PZT that constitutes 57% of the total volume of the device whereas the thin-film transducer only constitutes less than 0.1% of the volume. The pressure, acoustic streaming, and acoustic radiation force fields were then compared qualitatively between the two types of devices, and it was found that the devices performed comparably. This was again seen when comparing them in more quantitative terms, such as the average acoustical energy in the fluid, and the average time it took in each device to focus particles in the center of the channel. Various aspects of the mechanism were investigated, such as the underlying physical mechanism that governs the principle of thin-film actuation, as well as how the mechanical quality factor and thickness of the film do not significantly affect the system. Also shown was how electrode patterning can enhance the acoustic modes and that the system also works for the standing full-wave solution in the channel. The modes are clean and easy to identify, and the system is robust to a channel offset.

The last significant result in the thesis is the use of 1- $\mu\text{m}$ -thick AlScN thin-film actuator on a circular 10- $\mu\text{m}$ -thick membrane of silicon. The membrane investigated then has the top electrode on the thin film patterned to increase the mechanical actuation of the membrane, which allows for the effective actuation of higher-order membrane modes. These higher-order membrane modes then allow the pressure nodes to have a focus above the center of the membrane. The patterning increases the pressure hot spot for the fourth order mode several times over and the radiation force that follows, as a second-order field, scales with the square of this increase. We investigate the mechanism and show that the system is a combination of standing and traveling waves, which stems from waves traveling out from the antinodes in the membrane. This amplification of the membrane mode from effective electrode patterns is even more pronounced when going to higher-order modes, and for such a device it is shown that the acoustic hot spot above the center of

the membrane gives rise to acoustic trapping of cancer cells of the type MCF-7, when tuning the medium such that the acoustic contrast factor for the cells are negative, by adding Iodixanol which is a biologically inert fluid that is more compressible than water. We demonstrate that even with acoustic streaming there is a trap, and that the barrier that must be overcome when entering the trap can be minimized by tuning the parameter values of the liquid that the cells are submerged in.

The conclusion and outlook section summarizes the results of this thesis, as well as providing future research directions and indicating what would have been investigated had the PhD project continued.



# Resumé

This is the obligatory abstract in Danish. It is equivalent to the abstract except for the language.

Akustofluidik er et forsknings felt om studiet af lyd i væsker, hvilket er et forsknings område der går tilbage over 200 år. Fra studiet af små partikler der driver rundt i lufthvirvler over en Chladni plade fra tilbage i Ørsteds tid, som sættes i vibrationer af en violin bue trukket over kanten på af en metal plade, til den dag i dag hvor man fabrikere systemer i mikroelektromekaniske systemer (MEMS) og ren rum, hvor de designer systemer med mikrometer præcision og væske kanaler på brede og højde af nogle få menneske hår. Specielt sammenspillet mellem akustofluidik og mikrofluidik har på det seneste kastet mange interessante anvendelser af sig, specielt ved hjælp af den akustiske strålings kraft og den akustiske drevet strømning som bruges til at flytte partikler i væsker, generelt kaldet akustoforese.

Disse akustofluid systemer er i litteraturen blevet brugt til alt fra inkjet printere til sortering af kræft celler, kontinuert flow separation af blodceller fra blodplasma, mærkat-fri indfangelse og sortering af celler, mikrofluid mikserer, akustiske pincetter og meget mere. Forsknings feltet er i konstant udvidelse og udvikling, alligevel er der stadig plads til forbedringer. I sær er der to typiske problemer i forsknings feltet som relatere til denne afhandling. En af de typiske måder at fabrikere akustofluid systemer på er ved f.eks. at lime en blok af bly zirconate titanat (PZT) til systemerne, hvilket giver ikke særlig reproducerbare resultater, og gør der det svært at masse fabrikere disse system. Den måde det typisk gøres på gør hvert system unik, eftersom at små ændringer i limlaget gør store forskelle i slut resultatet. Et andet problem med det system er at det indeholder bly, som ved europæisk lovgivning er ved at blive faset ud af Europa, siden bly er et miljøfarligt materiale, og derfor skal der ledes efter alternativer.

Denne afhandling har undersøgt hvordan man kan implementere tynd-films piezoelektriske (PZE) transducer i akustofluid systemer. En traditionel PZE tynd-films transducer er aluminiumnitrid (AlN) som er MEMS og ren rums compatible, og den nye mere eksotiske variant aluminiumscandiumnitrid (AlScN) som er et stærkere PZE materiale dog med den hage at den er sværere at producere. Hvordan disse tynd-film kan bruges til at aktuere akustofluid systemer, forståelsen af den underliggende mekanisme, såvel som at sammenligne vores model med eksperimenter har været det overordet formål i denne afhandling. Det har i afhandlingen været opnået igennem to publiceret artikler og en der stadig er under udvikling.

I den første artikel bruges et ensemble af millimeter store glas blokke med AlN tynd-film på toppen, med forskellige topelektrode design, til at undersøge glassets egenskaber. I artikellen er det beskrevet hvordan de er lavet, karakteriseret, simuleret, og hvordan Youngs modulus og Poissons forholdet i glasset var fittet ved at minimere forskellen mellem impedans spektret fra målingerne og simuleringerne. Disse enheder viste at systemet er ganske reproducerbart, at glas blokke der er over 500 gange større end tynd-filmen kan aktueres af tynd-films transducere, og at der er god overensstemmelse mellem simuleringer og eksperimenter. Efter fittet af Youngs modulus og Poissons forholdet i glasset var der en relativ afvigelse mellem resonans toppene i simuleringen og eksperimenterne på  $(-0.5 \pm 0.1)\%$ , hvilket var en størrelses orden lavere end for de originale parameterværdier. Disse parameterværdier spiller en afgørende rolle for hvor god vores modeller passer med eksperimenter og hvor gode de er til at forudsige nye fænomener.

Den anden artikel handler om de appikationer der ligger i at bruge PZE tynd-film til at drive store akustofluid systemer, hvor tykke PZT transducere sammenlignes med en tynd-films transducere der er tusind gange mindre. Der bygges videre på den gode overensstemmelse der blev fundet i glas blok systemet i den første artikel, hvor der nu også er en fluid kanal indbygget på et par hundred mikrometer i højde og brede. Systemet undersøges med AlN, AlScN, og PZT tynd-films transducere, og for alle tre typer ses der akustofluid effekter i fluid kanalen, i form af akustisk strømning og akustisk strålings kraft. Disse sammenlignes med en traditionel enhed der drives af en mere traditionel tyk PZT, hvor PZE transducere udgør 57% af det totale volumen i den traditionelle enhed, og kun udgør 0.1% volumen i tynd-films enheden. Det akustiske tryk, strømning og strålings kraft sammenlignes på tværs af enhederne, i en mere kvalitativ sammenligning, hvor det sås at de to typer af aktivering gav nogenlunde de samme akustiske felter. Derefter blev der lavet en mere kvantitativ sammenligning hvor den gennemsnitlige akustiske energidensitet i væsken og den gennemsnitlige tid det tog at fokusere mikropartikler in kanalens center blev sammenlignet. Forskellige aspekter af den underliggende mekanisme blev undersøgt, så som det grundlæggende fysiske princip bag aktiveringen og hvordan den mekaniske kvalitets faktor, eller dæmpningen i filmen, ikke spillede en rolle for systemet samt at tykkelsen af filmen heller ikke ændrede systemet synderligt. Hvordan elektrode mønstreret spillede en rolle for at øge det akustiske system i det stående hel bølge tilfælde blev også undersøgt. Det sås at enhedens resonanser var meget symmetriske og nemme at genkende, og at systemet var robust overfor at kanalen kunne placeres en smule væk fra symmetrilinjen uden at det gjorde den store forskel.

Det sidste betydelige resultat i denne afhandling kom af at undersøge en 1  $\mu\text{m}$  tyk AlScN tynd-films transducer på en 10  $\mu\text{m}$  tyk silicium membran. Der blev undersøgt hvordan elektrode mønstrene på tynd-film transducere påvirkede membranen resonanserne, sådan at membranen effektivt kunne aktueres på dens højere ordens mekaniske membran modes. Disse højere ordens membran modes gav trykfelter der havde et tryk maksimum placeret over membranen, for den fjerde ordens membran mode. Den effektive aktivering af den højere ordens membran mode gav et meget kraftigere trykfelt, når elektrode mønsteret var optimeret, hvilket gjorde at de højere ordens akustiske effekter som f.eks. den akustiske strålings kraft er endnu kraftigere, siden de skalere med første ordens felter i anden potens. Forøgelse var kraftigere for endnu højere orden membran modes, hvor det

for sådan et system blev vist at trykfeltet kunne bruges til at fange og fastholde kræft celler af typen MCF-7, hvis vel og mærke at væsken blev valgt sådan at cellerne havde en negativ akustisk kontrast faktor. Dette blev opnået ved at bruge Iodixanol, som er en væske der ikke reagerer med de biologiske celler, men som er en mere komprimerbar væske end vand. Det var vist at selv med den akustiske strømning så var der et minimum hvor celler kunne fanges over membranen. Det var også vist at ved at ændre parameterverdierne i væsken så kunne den kraft barrierer som cellerne skulle overkomme for at komme ind i fælden blive minsket så meget at den næsten var væk.

De sidste tanker for afhandlingen blev samlet i en konklusion og et udsyn, hvor resultaterne sammenfattes og der diskuteres hvordan de potentielt kunne bruges i fremtiden. Der gives også et kort overblik på hvad der gerne ville have været undersøgt hvis der havde været mere tid i projektet.



# Preface

This thesis is submitted as partial fulfillment of the requirements for the degree of *Doctor of Philosophy* (PhD) from Technical University of Denmark (DTU). The work presented in this thesis was conducted from September 1, 2018, to August 31, 2021, in the Department of Physics, Section of Biophysics and Fluids, in the Theoretical Microfluidic Group, with Professor Henrik Bruus, from DTU, as main supervisor and Professor Thomas Laurell, from Lund University, as co-supervisor. This PhD project was funded by the *BioWings* project which in turn was funded by the European Union's Horizon 2020 *Future and emerging technologies* (FET open) program with grant number 801267. The project included a three-month external research stay at École polytechnique fédérale de Lausanne (EPFL), from October 20, 2019, to December 20, 2019, which was supported by the Otto Mønstedts, Reinholdt W. Jorck og Hustrus Fond, and Augustinus foundations. Of the 36 months of PhD study, six were spent taking obligatory courses, and eighteen of the remainder took place during the COVID-19 pandemic, with large portions spent under strict lockdown.



André Gugele Steckel  
Department of Physics  
Technical University of Denmark  
31 August 2021



# Acknowledgments

This PhD thesis is the result of 3 years work, and without the many people surrounding me this thesis would not have been the same. A special thanks goes out to my supervisor Prof. Henrik Bruus, whose dedication to, and understanding of, the field of acoustofluidics has been an invaluable support. A thanks goes out to the Theoretical Micro Fluidics (TMF) group: The alumni who helped define the field, and upon whom shoulders I stood so I could do the research that I did, in particular Dr. Nils R. Skov, Dr. Jacob S. Bach, and Dr. Wei Qiu, whom I had the pleasure of working with, and the current members of TMF, Assoc. Prof. Massimiliano Rossi, PhD stud. Jonas H. Jørgensen, William N. Bodé, Fabian Lickert, and Bjørn G. Winckelmann, for making a enjoyable work environment. I would like to thank the BioWings team for a nice collaboration and the EPFL team where I did my external research stay. Lastly, but not least, I would also like to thank my family and friends for their support and understanding when my attention was focused on my studies.



# Contents

<b>Abstract</b>	<b>iii</b>
<b>Resumé</b>	<b>vii</b>
<b>Preface</b>	<b>xi</b>
<b>Acknowledgments</b>	<b>xiii</b>
<b>List of publications</b>	<b>xvii</b>
<b>List of figures</b>	<b>xix</b>
<b>List of tables</b>	<b>xxi</b>
<b>List of symbols</b>	<b>xxiii</b>
<b>List of symbols</b>	<b>xxiii</b>
<b>1 Introduction to acoustofluidics</b>	<b>1</b>
1.1 Acoustofluidics: a top-down approach to sound . . . . .	2
1.2 Real-world applications of microfluidics for acoustofluidics . . . . .	3
1.3 Acoustofluidics in this thesis . . . . .	4
1.4 Thesis structure . . . . .	5
<b>2 Theory</b>	<b>7</b>
2.1 Fundamental equations and definitions . . . . .	8
2.1.1 Solid-mechanical equations and Voigt notation . . . . .	9
2.2 Perturbation expansions in fluids . . . . .	12
2.2.1 First-order fields . . . . .	13
2.2.2 Second-order field . . . . .	14
2.2.3 Effective boundary conditions and acoustic streaming . . . . .	15
2.2.4 Radiation force . . . . .	18
2.2.5 Particle velocity . . . . .	18
2.2.6 Acoustical energy density . . . . .	20
2.3 Axisymmetric models . . . . .	20

<b>3</b>	<b>Numerical modeling and validation of FEM in COMSOL</b>	<b>23</b>
3.1	Finite element method . . . . .	23
3.1.1	Weak form formulation . . . . .	24
3.1.2	Boundary conditions . . . . .	24
3.2	COMSOL implementation . . . . .	25
3.2.1	Material parameters . . . . .	26
3.2.2	Adaptive frequency stepping . . . . .	29
3.3	Numerical validation . . . . .	30
3.3.1	Axisymmetric compared to full 3D . . . . .	30
3.3.2	Mesh convergence analysis . . . . .	33
3.3.3	Comparison with experiments . . . . .	33
3.3.4	Mesh of thin films and electrodes . . . . .	34
<b>4</b>	<b>Summary of Results</b>	<b>37</b>
4.1	Paper I . . . . .	37
4.2	Paper II . . . . .	42
4.3	Paper III . . . . .	49
4.4	Conference Paper I . . . . .	50
4.5	Minor results I - Optimization of device width . . . . .	53
4.6	Minor results II - GHz acoustofluidic dampening . . . . .	54
<b>5</b>	<b>Publications</b>	<b>57</b>
5.1	Paper I: Phys. Rev. Appl. <b>16</b> , (2021) . . . . .	58
5.2	Paper II: J. Acoust. Soc. Amer. <b>150</b> , 634-645 (2021) . . . . .	70
5.3	Paper III: Manuscript in preparation . . . . .	88
5.4	Conference Paper I: Acoustofluidics 2020 . . . . .	103
<b>6</b>	<b>Conclusion and outlook</b>	<b>107</b>
6.1	Conclusion . . . . .	107
6.2	Outlook . . . . .	108
	<b>Bibliography</b>	<b>111</b>

# List of publications

## Peer-reviewed journal papers

- I André G. Steckel, Henrik Bruus, Paul Muralt, and Ramin Matloub, *Fabrication, Characterization, and Simulation of Glass Devices with AlN Thin-Film Transducers for Excitation of Ultrasound Resonances*, Phys. Rev. Appl. **16**, (2021). [2]
- II André G. Steckel and H. Bruus, *Numerical study of bulk acoustofluidic devices driven by thin-film transducers and whole-system resonance modes*, J. Acoust. Soc. Amer. **150**, 634-645 (2021). [1]

## Papers pending review

- III André G. Steckel and Henrik Bruus, *Numerical study of acoustic cell trapping above elastic membrane disks driven in higher-harmonic modes by thin-film transducers with patterned electrodes*, Manuscript submitted (*Under peer-review*) [3]

## Patent

- I André G. Steckel, Henrik Bruus, and Thomas Laurell, [*Title under Non-disclosure agreement until August 2022*], Patent application 21154133.9, submitted 28 January 2021.

## Peer-reviewed conference contributions

- I André G. Steckel and Henrik Bruus, *Numerical studies of acoustic actuation in glass capillaries by thin-film piezoelectric transducers*, The Swedish Center for Acoustofluidics and Cell Separation (SWECACS), 17 December 2018, **Oral presentation**.
- II André G. Steckel and Henrik Bruus, *Mode anti-crossing in thin-film-membrane-driven acoustofluidics*, Complex Motion in Fluids 18-24 August 2019, **Poster presentation**.

- 
- III André G. Steckel and Henrik Bruus, *Simulation of  $\text{Al}_{0.6}\text{Sc}_{0.4}\text{N}$  thin-film-membrane-driven acoustophoresis*, Acoustofluidics conference, 26-28 August 2019, **Poster presentation**.
- IV André G. Steckel and Henrik Bruus, *Numerical simulation of acoustic streaming generated by GHz AlN-thin-film transducers on AlN-SiO<sub>2</sub>-Bragg-reflector substrates*, Acoustofluidics conference, 26-27 August 2020, **Oral presentation**. Remark: Contributed talk at virtual conference
- V André G. Steckel and Henrik Bruus, *Numerical investigation of thin-film transducers for exciting whole-system resonances in bulk acoustofluidics devices*, Acoustofluidics conference, 26-27 August 2021, **Oral presentation**. Remark: Contributed talk at virtual conference

# List of Figures

1.1	Artistic illustration of an acoustofluidic application discussed in this thesis.	1
2.1	Polystyrene particles being focused in acoustofluidic microchannel. . . . .	19
3.1	Sketch of adaptive frequency stepping method. . . . .	29
3.2	Shows the the fields in both full 3D and 2D axisymmetric simulations for a 1- $\mu$ m-thick Pyrex membrane. . . . .	31
4.1	Paper I - Shows the design of glass devices and electrode patterns . . . . .	38
4.2	Paper I - Impedance measurements on devices A8-G8 and C2-G2 . . . . .	40
4.3	Paper I - Simulations of glass devices and comparison of calculated to measured impedance spectra. . . . .	41
4.4	Paper II - Sketch of thin-film actuated acoustofluidic bulk device. . . . .	43
4.5	Paper II - Cross section of a simulation of the device showing the core concept of the thin-film actuated bulk devices. . . . .	43
4.6	Paper II - Comparison of a thin-film actuated device with a bulk actuated device in terms of first- and second-order fields. . . . .	44
4.7	Paper II - Shows a thin-film driven systems dependence on thin-film Q-factor and thickness . . . . .	46
4.8	Paper II - Simulations of full-wave standing pressure mode in the channel and the effect of electrode patterning. . . . .	47
4.9	Simulations and optimization of the width of the device in Paper II . . . . .	52
4.10	Simulations of GHz acoustics, pressure, displacement, steaming and dampening. . . . .	54
4.11	Simulation of GHz acoustics, pressure, and displacement in an axisymmetric system. . . . .	55



# List of Tables

3.1	Parameter values of water . . . . .	26
3.2	Parameter values of Iodixanol . . . . .	26
3.3	Parameter values of piezoelectric materials AlN, AlScN, and PZT . . . . .	27
3.4	Parameters values of solids, Schott D263, Pyrex, and Silicon. . . . .	28
3.5	Parameters for 5- $\mu\text{m}$ -diameter polystyrene particles . . . . .	28



# List of symbols

Symbol	Description	Unit
$c$	Speed of sound	$\text{m s}^{-1}$
$c_{\text{fl}}$	Speed of sound in fluid	$\text{m s}^{-1}$
$c_{\text{lo}}$	Longitudinal speed of sound	$\text{m s}^{-1}$
$c_{\text{tr}}$	Transverse speed of sound in fluid	$\text{m s}^{-1}$
$f$	Frequency	Hz
$\lambda$	Wavelength	m
$\mathbf{r}$	Spacial coordinate	m
$t$	Time	s
$\rho$	Density	$\text{kg m}^{-3}$
$\rho_{\text{sl}}$	Density in the solid	$\text{kg m}^{-3}$
$\rho_0$	Zero order density in fluid	$\text{kg m}^{-3}$
$\rho_1$	First order density in fluid	$\text{kg m}^{-3}$
$\rho_2$	Second order density in fluid	$\text{kg m}^{-3}$
$\rho_{\text{pa}}$	Particle density	$\text{kg m}^{-3}$
$\mathbf{v}$	Velocity	$\text{m s}^{-1}$
$\boldsymbol{\sigma}$	Stress tensor	$\text{N m}^{-2}$
$p$	Pressure	Pa
$p_0$	Zero order pressure in fluid	Pa
$p_1$	First order pressure in fluid	Pa
$p_2$	Second order pressure in fluid	Pa
$\eta_0$	Dynamic viscosity	$\text{mPa s}$
$\eta_0^{\text{b}}$	Bulk viscosity	$\text{mPa s}$
$\mathbf{u}_1$	Displacement	m
$\mathbf{S}$	Strain tensor	1
$\mathbf{C}$	Coupling tensor	Pa
$\mathbf{E}$	Electric field	$\text{V m}^{-1}$
$\varphi$	Electric potential	V
$\mathbf{e}$	Piezoelectric coupling tensor	$\text{C m}^{-2}$
$\mathbf{D}$	Dielectric field	$\text{C m}^2$
$\boldsymbol{\varepsilon}$	Permittivity matrix	$\text{F m}^{-1}$
$\omega$	Angular frequency	$\text{rad s}^{-1}$
$i$	Imaginary number	1

Symbol	Description	Unit
$\kappa_0$	Compressibility in the fluid	TPa <sup>-1</sup>
$\kappa_{pa}$	Compressibility in the particle	TPa <sup>-1</sup>
$\mathbf{v}_1$	First order velocity field in the fluid	m s <sup>-1</sup>
$\mathbf{v}_2$	Second order velocity field in the fluid	m s <sup>-1</sup>
$\mathbf{v}_1^\delta$	Divergence free velocity field	m s <sup>-1</sup>
$\mathbf{v}_1^d$	Rotation free velocity field	m s <sup>-1</sup>
$k_s$	Boundary layer dampening length scale	m <sup>-1</sup>
$\delta$	Viscous boundary layer length scale	m
$\zeta$	Transverse coordinate	m
$\epsilon$	Small factor	1
$d$	Compressional length scale	m
$\mathbf{V}$	Velocity in the solid	m
$\eta$	Parallel coordinate	m
$\xi$	Parallel coordinate	m
$k_c$	Compressional wave number	m <sup>-1</sup>
$\Gamma_{fl}$	Damping coefficient in fluid	1
$T_0$	Time of a full period	s
$\nu_0$	Kinematic viscosity	m <sup>2</sup> s <sup>-1</sup>
$\mathcal{L}_{ac}^d$	Acoustic Lagrangian density	J m <sup>-3</sup>
$\mathcal{S}_{ac}^d$	Acoustic energy flux density	J m <sup>-2</sup> s <sup>-1</sup>
$\mathbf{F}_{rad}$	Acoustic radiation force	N
$\mathbf{F}_{drag}$	Drag force	N
$\mathbf{F}_{garv}$	Buoyancy corrected gravitational force	N
$a$	Particle radius	m
$f_0$	Monopole scattering coefficient	1
$f_1$	Dipole scattering coefficient	1
$U^{rad}$	Gorkov potential	J
$E_{ac}^{fl}$	Average acoustic energy density	J m <sup>-3</sup>
$V_{fl}$	Fluid volume	m <sup>3</sup>
$x$	Cartesian coordinate	m
$y$	Cartesian coordinate	m
$z$	Cartesian coordinate	m
$r$	Radial coordinate	m
$\phi$	Angular coordinate	1

Symbol	Description	Unit
$\hat{\mathbf{I}}$	Unit tensor	
$\partial_t$	Partial time derivative	
$\nabla \cdot$	Divergence operator	
$\nabla$	Gradient operator	
$\tilde{\cdot}$	Full time dependence	
$\langle \cdot \rangle$	Time average	
$\nabla_{\parallel} \cdot$	Parallel divergence operator	
$\mathbf{J}$	Generalized flux tensor	
$\mathbf{F}$	Generalized force vector field	
$h$	FEM solution function	
$\Theta_n$	FEM test function	
$\mathbf{N}$	Flux condition on the boundary	
$\mathbf{n}$	Normal vector	
$C$	Convergence parameter	
$g_n$	$n$ 'th solution to field $g$	
$g_{\text{ref}}$	Reference solution to field $g$	
$\Omega$	Computational domain	
$\partial\Omega$	Domain boundary	



# Chapter 1

## Introduction to acoustofluidics

This section contains a brief introduction to the field of acoustofluidics. It adopts a top-down approach, starting from a more wide-reaching and general description of sound and music and eventually considering acoustofluidics in microfluidic channels several times the width of a human hair. This is followed by a technical description of the rapidly expanding field of acoustofluidics and references to state-of-the-art literature. The acoustofluidics that relates more specifically to this thesis is then explained in more depth. Finally, we explain the thesis structure.

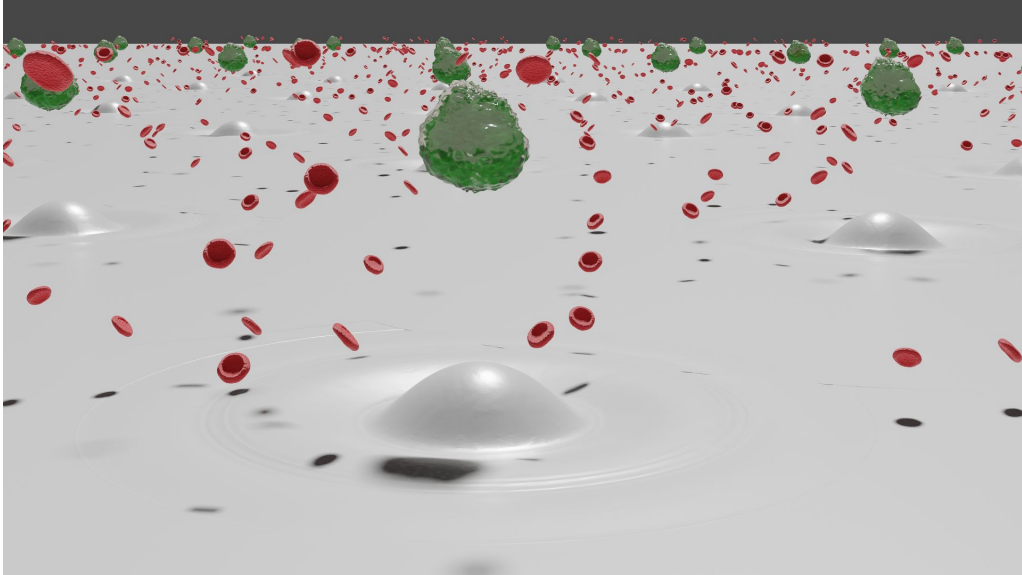


Figure 1.1: Artistic illustration of an acoustofluidic application discussed in this thesis. In the illustration cancer cells (green) are levitated and trapped above an array of membranes (grey surface), in a fluid with red blood cells (red) which are not trapped. The cancer cells can then be studied without sedimentation. Further discussed in Paper III, Section 5.3. Adapted from Ref. 3

## 1.1 Acoustofluidics: a top-down approach to sound

Acoustics is the study of sound; therefore, acoustofluidics, the primary focus of this thesis, is naturally the study of sound in fluids. Most people are familiar with sound, since they grow up with the ability to hear their surroundings before they can walk or talk. Since hearing is one of the senses that is simply there as we develop, many people accept it without further explanation. Sound fundamentally consists of mechanical vibrations, whether in solids, such as a wineglass struck with a spoon, or fluids, such as the air around the wineglass which allows the sound to travel to our ears. In this context, a solid is something that can withstand tangential forces, whereas fluids cannot; the term “fluid” encompasses both liquids and gases. Sound requires a medium through which to travel since it propagates through traveling compression and decompression in the mechanical stresses of the material. Just as when springs are compressed and released, they oscillate around their equilibrium position, so do the materials that can transmit sound. These materials could be considered to be a series of minute springs, such that sound travels through them, it is as if there were a reaction of small springs pulling and pushing on each other in turn. For instance, if air experiences a sudden force, for example, from a loudspeaker, then the nearby air will also experience the push, and the effect would travel outward through the medium at the speed of sound through traveling mechanical stresses.

The vibrational stresses exerted in a bulk fluid are compressional in nature, consisting in fluctuations in the pressure of the fluid, which gives rise to longitudinal waves. On the other hand, solids can maintain not only longitudinal or compressional stresses but also transverse or shear stresses, and therefore both longitudinal and transverse waves exist in solids. Waves will travel through a medium at the speed of sound in the medium,  $c$ , and therefore if the waves are produced at a specific frequency,  $f$ , then the wavelength is  $\lambda = \frac{c}{f}$ . The human ear is typically capable of discerning frequencies in the range from 20 hertz (Hz) to 20 kilohertz (kHz). With a speed of sound in dry air at 20 °C, that is, around 343 meters per second[4], the wavelength of the audible range is around 17 m to 1.7 cm. Musical instruments that rely on acoustical resonance typically follow a similar scheme where larger instruments produce deeper notes, lower frequency and larger wavelengths, and smaller versions of the same instrument produce higher notes, higher frequencies and smaller wavelengths. A typical example is the violin family, with the large contrabass producing deep notes and the smaller violin producing higher notes.

Sound waves come in both traveling and standing waves. Standing waves can be produced by interference of traveling waves; one typical example is a wave interfering with its reflections in an acoustical cavity, such as a guitar. The waves in an acoustical cavity match the round trip of the waves in the system, such that when they reflect on the surfaces, they interfere constructively with themselves, and therefore, over many oscillations, the sound is amplified. This is used in diverse types of instruments, such as violins or guitars, to selectively amplify some frequencies and not others through the design of the shape and the cavity of the instrument.

Sound waves at interfaces between different media experience reflections and refractions. One of the applications of this that most people are familiar with is ultrasound

scanning, used to noninvasively scan internal organs or fetuses. This is based on producing ultrasound—sound with a frequency above the limits of the human hearing—and picking up the reflected and scattered waves to reproduce an image of the scanned medium.

All these properties thus far serve to introduce acoustofluidics in terms that are familiar to a general audience. Many of the same ideas and concepts are still valid when going to a less familiar regime, that of acoustofluidics in microfluidics, and therefore this introduction can hopefully help the novice to better understand and visualize these fields.

## 1.2 Real-world applications of microfluidics for acoustofluidics

Microfluidics is the regime of fluidics where the critical length scale is in the micrometer range, from 1  $\mu\text{m}$  to 1000  $\mu\text{m}$ , where a micrometer is a thousandth of a millimeter. In this regime, fluids such as water exhibit behaviors notably distinct from those that they demonstrate under everyday conditions, and yet such fluids exist in every person, in that capillaries can be less than 10 micrometers in diameter[5]. Microfluidics allows for handling small amounts of fluids, and has given rise to a field of research called lab-on-a-chip technology, which as the name suggests simulates the operations that a lab might perform in some specific diagnosis, identification, or classification, but which can be handled on a chip[6–9]. Among the many lab-on-a-chip applications, one could highlight the use of many arrays-on-a-chip for genome sequencing, by for example nanopore DNA detection, which over the last few decades has brought whole-genome DNA sequencing down by orders of magnitude in cost, to a point where it is possible to do on a diagnostic basis [10, 11].

In microfluidics, the momentum of the fluid usually plays a much smaller role compared to the viscosity[12]. This causes laminar flows to be typical and turbulent flows to be uncommon[13]. This comes with its own advantages and disadvantages, one being that fluid flows in a channel will in general not mix, such that fluid inserted from the right in the channel will stay on the right while the fluid moves through the channel. This opens various possibilities: for instance, by placing cells in the right side of a channel, they will usually stay in the right side, which can be used as a feature in the design. However, this phenomenon can also be a problem, as many lab operations require that certain fluids be mixed for various reasons; phenomena that in larger fluid channels are a given, for example, that diffusion will cause some mixing, are no longer the case without specifically designed mixers.

Blood is a good example of a microfluidic flow in the body, and also a very interesting fluid because it can be used to diagnose various conditions, such as sepsis[14, 15], the presence of circulating tumor cells[16–18] therefore, the handling, sorting, upconcentrating, and manipulation of cells in microfluidics are important. There are many techniques available for this purpose, of which a promising candidate is acoustofluidics, since it is a label-free[19] and gentle method, which is partly why it has risen to prominence in recent years.

Acoustofluidics has applications in microfluidics that range from upconcentrating cells

in small volumes or droplets[20–24], cleaning cells by moving them one fluid to another[25, 26], label-free separation of cells based on size [19, 27] or acoustical impedance by changing the suspension fluid [28, 29], trapping of cells [26], and selective sorting of individual cells[30] to mixing of fluids[31–34] and various forms of manipulation such as acoustic tweezers[35–38] and acoustic levitation[39–50].

Acoustofluidics in microfluidics is a field that spans many orders of magnitude in frequency, from the kHz regime[51, 52], which uses sharp edge structures to generate streaming, to the GHz[53–55] regime, where it is used to generate streaming but also enables other types of particle manipulation and trapping by actuating close to the bulk acoustic resonance of thin films.

The list of applications are long, but in general fall into the categories of bulk acoustic wave (BAW) devices[56–60], surface acoustic wave (SAW) devices[61], and membrane devices[60, 62, 63]. Some use acoustic radiation force methods[64–72], which works by the mechanism that scattering of acoustic waves off cells or particles changes the momentum of the outgoing wave, which then exerts a force on the cells or particles. Some use acoustic streaming[73–76], which is the time-averaged effect of the nonlinear term in the Navier-Stokes equations, to generate flow rolls, either by bulk attenuation[77] or by boundary-driven streaming[78]. These are used for acoustophoresis, meaning motion driven by sound, and have been utilized in the manipulation and trapping of cells and particles in fluids by ultrasound[79–83] and particle separation in flow[81, 84, 85]. Many of the previously named applications also rely on these phenomena.

The field of acoustofluidics is driven by a creative community that produces a variety of methods and applications. The field is still flourishing and developing rapidly with avenues for further exploration. In Section 1.3, we will discuss some of the specific topics of this thesis.

### 1.3 Acoustofluidics in this thesis

While acoustofluidics is a well-developed and mature field, there are still challenges, some which will be investigated in this thesis. Each subfield within acoustofluidics has its own advantages, disadvantages, possibilities, and limitations. This thesis primarily considers bulk acoustic wave (BAW) systems and how thin-film technology could find applications in such systems. BAW systems can be tricky, and getting reproducible results from two devices, designed to be numerically equal, can sometimes be difficult, as small details can have large effects in a high-quality-factor (Q-factor) system. Devices produced today can have many elements that critical for device performance, such as gluing of piezoelectric actuators to devices by hand, where changes in the glue layer thickness and uniformity of only a few tens of micrometers can have large impacts on the device[86]. Sometimes even production tolerances between devices can be sufficiently large such that the acoustic resonances are not predictable enough for mass fabrication, which presents a problem from an industrial point of view. Not all acoustofluidic device systems have these problems; an excellent example of how reliable the systems can be is the droplet dispensers in an ink-jet printer, which shows that microscale acoustofluidics do work in an industrial

environment.

Another problem is that many devices use lead zirconate titanate (PZT) as the actuator, since PZT has such large piezoelectric coupling coefficients compared to most other piezoelectric materials, and therefore it is one of the most common piezoelectric materials[87]. However, since lead is a heavy metal and an environmentally hazardous material, it is being phased out by legislation in the European Union (EU)[88], and therefore is not a very enticing material to use in a mass production setting. This is particularly true of devices intended for the biomedical industry since most of the time they are intended as single-use devices due to the unacceptability of biological cross contamination. Therefore, a change of material away from lead is almost a requirement for mass production devices that require permanently glueing of a piezo unto the device. The search for new piezoelectric materials to replace PZT is ongoing[89–91], and developments within very strong electrostrictive gadolinium-doped ceria show great promise[92].

In this thesis, we look to thin films to solve two problems: reproducibility and lead-free actuators. Using an aluminum nitride (AlN) thin film on top of glass block devices showed that the devices are indeed reproducible, and that the simulations give good agreement with experiments. The AlN film is of course lead-free, and therefore a good alternative to PZT. The second paper shows that by simulation of acoustofluidic devices with AlN and AlScN, thin films can perform on par with conventional devices, when taking into account their acoustofluidic action on fluids. The thin-film driven devices, presented in that paper, almost represent a drop in displacement for PZT actuators in the devices designed for bulk PZT transducers. The disadvantages of thin-film devices include that they are more technically demanding to manufacture, compared to a PZT transducer, which can be bought and glued onto the device. The films also needs to be deposited in a clean room which is not a trivial matter. The last results in the thesis show how thin films with optimized electrodes patterns on a membrane can be used for trapping cells above the membrane. These are some of the subjects that will be discussed in this thesis. The structure of the thesis is explained in the following section.

## 1.4 Thesis structure

The thesis is divided into chapters, each covering a part of the thesis, with articles at the end that are self-contained.

**Chapter 1 Introduction** — This chapter represents an introduction to a general understanding of acoustics and acoustofluidics, as well as a short introduction to the advantages of acoustofluidics and the problems that this thesis has tried to solve.

**Chapter 2 Theory** — This chapter present a general introduction to the theory that is used in this thesis. It contains the solid-mechanical equations, acoustofluidic equations that is derived by using to first- and second-order perturbation theory, and a short description of boundary conditions, radiation force and particle velocity, and axisymmetric equations.

**Chapter 3 Numerical modeling in COMSOL** — This chapter is dedicated to the numerical calculations done in this thesis. It starts with a description of the finite element method, with weak form formulation, and the boundary conditions in such a method. The COMSOL implementation is described, as well as the material parameters used in the thesis, with a discussion of them, and the adaptive frequency stepping method. A section is dedicated to numerical validation.

**Chapter 4 Summary of results** — This chapter is a summary of some of the results produced in this thesis. It includes papers I-III, as well as a conference contribution to Acoustofluidics 2020, and minor results that have not been published.

**Chapter 5 Papers** — This includes the papers, (I) *Fabrication, Characterization, and Simulation of Glass Devices with AlN Thin-Film Transducers for Excitation of Ultrasound Resonances*, (II) *Numerical study of bulk acoustofluidic devices driven by thin-film transducers and whole-system resonance modes*, (III) *Numerical study of acoustic cell trapping above elastic membrane disks driven in higher-harmonic modes by thin-film transducers with patterned electrodes*, and a peer-reviewed conference contribution (IV) *Numerical simulation of acoustic streaming generated by GHz AlN-thin-film transducers on AlN-SiO<sub>2</sub>-Bragg-reflector substrates*.

**Chapter 6 Conclusion and outlook** — This chapter concludes the thesis with a collective discussion of the results, how they might be used in the future, as well as subjects that would have been interesting to explore further.

## Chapter 2

# Theory

Acoustofluidics has a rich history, stretching back over 200 years[80], with important developments along the way by historically important figures. Much of the fundamental theory is well-established in the literature[93, 94], particularly in a tutorial series [95–114] wherein almost all of the necessary background in acoustofluidics is mentioned. The specific model used in this thesis has been experimentally validated[2, 93], whereas much of the theory used here dates back decades, although recent developments have enabled effective numerical simulations in three dimensions (3D) leading to the investigations and precision that were not possible before. In particular, recent research by Bach and Bruus Ref. 78, with their effective boundary layer theory of pressure acoustics, has allowed the development of larger models, especially 3D. In conjunction with the development of including solids[115] and piezoelectric (PZE) materials[93] in simulations, this has allowed researchers to simulate devices that are closer to real experiments. This change from predefined displacements[66, 116–119] to models that better approximate how the actual devices work has enabled the investigation of devices that were not previously possible[1, 93].

The theory presented in this section should be seen as a short summary of that which is necessary for reproducing the numerical simulations in this thesis. The presentation of the theory follows the standard formulation of the theory available in for example Ref. 93 and Ref. 78, and is almost the same model as in those references, albeit occasionally with a slightly different implementation or a slightly different interpretation. The structure of this chapter is as follows: Section 2.1 is a short introduction to the fundamental equations of acoustofluidics and to definitions used throughout the thesis. Section 2.2.1 is a short introduction to first-order perturbation theory and Section 2.2.2 is an introduction to second-order steady-state streaming. The radiation force is described in Section 2.2.4 and the effective boundary conditions (BC) on the acoustic streaming are laid out in Section 2.2.3. With these tools, particle motion can be explained, which is done in Section 2.2.5. Lastly in Section 2.3, the axisymmetric equations are touched upon for simulations where they were used.

## 2.1 Fundamental equations and definitions

To describe acoustofluidic systems, we assume that the physics we are working with can be described by continuous fields. Fundamentally, the systems consist of atoms, which in nature are discrete, however at sufficiently large scales, the individual atoms behave as continuous fields in space and time that we describe as  $\tilde{F}(\mathbf{r}, t)$  for scalar fields and  $\tilde{\mathbf{F}}(\mathbf{r}, t)$  for vector fields, where  $\mathbf{r}$  is the special coordinate,  $t$  is the time, and the tilde over the fields indicate dependence on both space and time. The notation convention in this thesis is that vector and tensor fields are written in boldface, whereas scalar fields are not. Each field is a local average over a small, but still of finite, volume and a discussion on the lower limit of validity of the continuous field approximation can be found in Ref. 94. For all simulations, we assume we are far above this lower limit.

The fundamental physics we want to describe adheres to the principles of conservation of mass and momentum and from these relations, in a continuous medium, the following can be written,

$$\partial_t \tilde{\rho} = \nabla \cdot (-\tilde{\rho} \tilde{\mathbf{v}}), \quad (2.1a)$$

$$\partial_t (\tilde{\rho} \tilde{\mathbf{v}}) = \nabla \cdot [\tilde{\boldsymbol{\sigma}} - (\tilde{\rho} \tilde{\mathbf{v}}) \tilde{\mathbf{v}}], \quad (2.1b)$$

where  $\tilde{\rho}$  is the mass density,  $\tilde{\mathbf{v}}$  is the velocity,  $\partial_t$  is the partial time derivative,  $\nabla \cdot$  is the divergence operator, and  $\tilde{\boldsymbol{\sigma}}$  is the stress tensor. Eq. (2.1a) is the continuity equation, which states that the changes in mass in a small volume will require a net flow of mass through the surface surrounding that volume, and Eq. (2.1b) is conservation of momentum, stating that changes in the collective momentum of a small volume must require either a force acting on the volume or a net inflow of momentum.

The physics of the system can be made more concrete by requiring limitations on the definition of the stress tensor. For Newtonian fluids, we have that[120],

$$\tilde{\boldsymbol{\sigma}} = -\tilde{p} \hat{\mathbf{I}} + \eta_0 \left[ \nabla \tilde{\mathbf{v}} + (\nabla \tilde{\mathbf{v}})^T - 2/3 (\nabla \cdot \tilde{\mathbf{v}}) \hat{\mathbf{I}} \right] + \eta_0^b (\nabla \cdot \tilde{\mathbf{v}}) \hat{\mathbf{I}}, \quad (2.2)$$

where  $\hat{\mathbf{I}}$  is the unit tensor,  $\tilde{p}$  is the pressure,  $\eta_0$  is the dynamic viscosity,  $\eta_0^b$  is the bulk viscosity, and  $\nabla$  is the gradient operator. Inserting Eq. (2.2) into Eq. (2.1b) gives the Navier–Stokes equation,

$$\partial_t (\tilde{\rho} \tilde{\mathbf{v}}) = -\nabla \tilde{p} + \eta_0 \nabla^2 \tilde{\mathbf{v}} + \left( \eta_0/3 + \eta_0^b \right) \nabla (\nabla \cdot \tilde{\mathbf{v}}) - \nabla \cdot [(\tilde{\rho} \tilde{\mathbf{v}}) \tilde{\mathbf{v}}], \quad (2.3)$$

where it was assumed that  $\eta_0$  and  $\eta_0^b$  do not vary in space for the systems investigated in this thesis. The Navier–Stokes equation will prove useful later for the explanation of pressure acoustics in Section 2.2.

Momentum conservation also applies to solids, so Eq. (2.1b) must also define the movement of solids, where instead of a velocity, we are working with the displacement vector,  $\tilde{\mathbf{u}}_1$ , such that  $\partial_t \tilde{\mathbf{u}}_1 = \tilde{\mathbf{v}}_1$ . We assume that momentum does not flow in solids and that the strain,  $\tilde{\mathbf{S}} = \frac{1}{2} (\nabla \tilde{\mathbf{u}}_1 + (\nabla \tilde{\mathbf{u}}_1)^T)$ , is very small and therefore the nonlinear term in Eq. (2.1b) is not present in the solids we are calculating, which then gives,

$$\rho_{\text{sl}} \partial_t^2 \tilde{\mathbf{u}}_1 = \nabla \cdot \tilde{\boldsymbol{\sigma}}, \quad (2.4)$$

which is also called Cauchy's momentum equation[121], where we assumed that the mass density in the solid,  $\rho_{\text{sl}}$ , is time independent. If we assume we are working within the linear regime of the solid, then there is a relation between the stress and the strain such that,

$$\tilde{\boldsymbol{\sigma}} = \mathbf{C} : \tilde{\mathbf{S}}, \quad (2.5)$$

where  $\mathbf{C}$  is the coupling four-tensor with parameters that depend on the material. If we are working with piezoelectric materials, then the stress tensor depends not only on the strain matrix but also the electric field,  $\tilde{\mathbf{E}}$ , defined from the electric potential,  $\tilde{\varphi}$ , as  $\tilde{\mathbf{E}} = -\nabla \tilde{\varphi}$ , so that for piezoelectric materials,

$$\tilde{\boldsymbol{\sigma}} = \mathbf{C} : \tilde{\mathbf{S}} - \mathbf{e}^T \cdot \tilde{\mathbf{E}}, \quad (2.6)$$

where  $\mathbf{e}$  is the piezoelectric coupling three-tensor. We can supplement the system with the quasi-electrostatic Maxwell equation for the dielectric field,

$$\nabla \cdot \tilde{\mathbf{D}} = 0, \quad (2.7)$$

where for piezoelectric materials,

$$\tilde{\mathbf{D}} = \mathbf{e} : \tilde{\mathbf{S}} + \boldsymbol{\varepsilon} \cdot \tilde{\mathbf{E}}. \quad (2.8)$$

Notice that so far we have not used Voigt notation, but from Section 2.1.1 and forward we will do so.

### 2.1.1 Solid-mechanical equations and Voigt notation

The equations can be cumbersome because of the many high-rank tensors used; however, because of the symmetry requirements on the stress and strain tensors, the equations can be more conveniently expressed in Voigt notation. This reduces the  $3 \times 3$  stress and strain tensors into  $1 \times 6$  vectors, where only the 6 unique components are kept. The mechanical  $\mathbf{C}$  tensor is then reduced from  $3 \times 3 \times 3 \times 3 \times 3$  to  $6 \times 6$ , thereby reducing the number of elements without loss of generality. Due to the symmetries that exist in certain materials, such as in crystals or isotropic materials such as glass, the system will be invariant under some types of rotations, though exactly which operations depend on the specific symmetry of the material. The rotations under which the system is invariant under put limitations on the number of possible coupling coefficients in  $\mathbf{C}$ . In practice, this means that many of the maximal possible free coefficients in  $\mathbf{C}$  are often zero or identical. For example, for isotropic glass there are only two free variables out of the nine nonzero elements, which relate to transverse and longitudinal waves in glass. For isotropic materials, such as glass, and for cubic symmetric crystals, such as silicon, the  $\mathbf{C}$  matrix in Voigt notation is[93]

$$\mathbf{C} = \left( \begin{array}{ccc|ccc} C_{11} & C_{12} & C_{12} & 0 & 0 & 0 \\ C_{12} & C_{11} & C_{12} & 0 & 0 & 0 \\ C_{12} & C_{12} & C_{11} & 0 & 0 & 0 \\ \hline 0 & 0 & 0 & C_{44} & 0 & 0 \\ 0 & 0 & 0 & 0 & C_{44} & 0 \\ 0 & 0 & 0 & 0 & 0 & C_{44} \end{array} \right), \quad \text{for cubic symmetry,} \quad (2.9)$$

where for isotropic materials there is the additional constraint that  $C_{12} = C_{11} - 2C_{44}$ , and all the parameter values used in this thesis for a specific material can be found in Table 3.4. The only two free coefficients in isotropic materials are often given in other forms, such as with either Young's modulus,  $E$ , and Poisson's ratio,  $s$ , or with the longitudinal and transverse speeds of sound, with symbols  $c_{\text{lo}}$  and  $c_{\text{tr}}$  respectively. The translations among the different notations are unambiguous, and can be calculated as:[122]

$$C_{11} = \rho c_{\text{lo}}^2 = \frac{1-s}{(1-2s)(1+s)} E, \quad (2.10a)$$

$$C_{44} = \rho c_{\text{tr}}^2 = \frac{1}{2(1+s)} E. \quad (2.10b)$$

For hexagonal crystal structures, such as lead zirconate titanate (PZT) and aluminium nitride (AlN), the mechanical couplings matrix in Voigt notation is[93],

$$\mathbf{C} = \left( \begin{array}{ccc|ccc} C_{11} & C_{12} & C_{13} & 0 & 0 & 0 \\ C_{12} & C_{11} & C_{13} & 0 & 0 & 0 \\ C_{13} & C_{13} & C_{33} & 0 & 0 & 0 \\ \hline 0 & 0 & 0 & C_{44} & 0 & 0 \\ 0 & 0 & 0 & 0 & C_{44} & 0 \\ 0 & 0 & 0 & 0 & 0 & C_{66} \end{array} \right), \quad \text{for hexagonal symmetry,} \quad (2.11)$$

and the additional restriction that  $C_{66} = \frac{1}{2}(C_{11} - C_{12})$ , again with the material parameters in Table 3.3. The piezoelectric coupling matrix  $\mathbf{e}$  also is simplified from a tensor of rank three,  $3 \times 3 \times 3$  to a tensor of rank two,  $3 \times 6$ , in Voigt notation, such that for a hexagonal piezoelectric materials, such as PZT and AlN, in Voigt notation the matrix is:[93]

$$\mathbf{e} = \begin{pmatrix} 0 & 0 & 0 & 0 & e_{15} & 0 \\ 0 & 0 & 0 & e_{15} & 0 & 0 \\ e_{31} & e_{31} & e_{33} & 0 & 0 & 0 \end{pmatrix}, \quad (2.12)$$

with parameter values in Table 3.3. For thin films where the film is free to expand in the direction perpendicular to the surface, there is a correction to the piezoelectric coefficient  $e_{31}$ , such that:[60, 123–125]

$$e_{31,f} = e_{31} - \frac{C_{13}}{C_{33}} e_{33}. \quad (2.13)$$

The permittivity matrix,  $\boldsymbol{\varepsilon}$ , is unchanged under Voigt notation and for hexagonal materials is defined as,

$$\boldsymbol{\varepsilon} = \begin{pmatrix} \varepsilon_{11} & 0 & 0 \\ 0 & \varepsilon_{11} & 0 \\ 0 & 0 & \varepsilon_{33} \end{pmatrix}. \quad (2.14)$$

The coefficients for the coupling tensors  $\mathbf{C}$ ,  $\mathbf{e}$ , and  $\boldsymbol{\varepsilon}$  are complex-valued, where the imaginary parts are responsible for losses and the attenuation of the waves. The imaginary part is difficult to measure, and as we do not know these parts, we assume that the system can be described by an overall dampening factor for each material given in Table 3.3 and Table 3.4.

These equations together with the appropriate boundary conditions are enough to simulate the solid-mechanical part of the models. The boundary conditions for the solid-mechanical part are continuity of stress and velocity, and zero free changes on the surface for the electric portion. Furthermore, the electric field is driven by the electric potential, which is defined by electrodes attached to the piezoelectric materials. The potential oscillates with a specific frequency which drives the acoustics in the system. The boundary conditions can therefore be written as:

$$\tilde{\boldsymbol{\sigma}} \cdot \mathbf{n} = \mathbf{0} \quad \text{and} \quad \tilde{\mathbf{D}} \cdot \mathbf{n} = 0, \quad \text{at solid and PZE air interface,} \quad (2.15a)$$

$$\tilde{\varphi} = 0, \quad \text{at ground electrode,} \quad (2.15b)$$

$$\tilde{\varphi} = \frac{1}{2}\varphi_0 e^{-i\omega t}, \quad \text{at positive electrode,} \quad (2.15c)$$

$$\tilde{\varphi} = -\frac{1}{2}\varphi_0 e^{-i\omega t}, \quad \text{at negative electrode,} \quad (2.15d)$$

where  $\varphi_0$  is half the potential amplitude,  $f$  is the frequency,  $\omega$  is the angular frequency, and  $i = \sqrt{-1}$  is the imaginary number corresponding to the square root of negative one. When the solid and PZE are in contact with a fluid, then the boundary condition is also continuous stress and velocity; however, since we use the effective boundary conditions described later, there are slight changes to these and therefore they will be defined there. The boundary condition Eq. (2.15a) means that we are neglecting the effects of air on the system. As anyone who has tapped a wine glass at a party to get attention knows, that mechanical oscillations in the glass generate pressure waves which we hear as sound; hence, the boundary condition cannot be completely true, as there must be losses into the air. However, for the systems we simulate, the displacement is very small. The effect of air has been experimentally observed by Reichert *et al.* Ref. [60], in a membrane system where the displacements comparatively larger, compared to a bulk system, and therefore more sensitive to air. They showed that running the system in air instead of vacuum did not change the resonance frequency significantly but did change the Q factor of the system by 60%. Since we do not fully know the dampening in the system, and since we are working with much smaller displacements in our bulk systems, we elect to neglect the effects of the air.

Since in Eq. (2.15c) we actuate with a time harmonic electric potential, the displacement fields are also time-harmonic in nature, because of the linearity of the equations. However because of the nonlinearity of the Navier–Stokes equation, there is a possibility that these time-harmonic motions can result in time steady behavior, which will be discussed in the following section, which deals with perturbation expansions in fluids.

## 2.2 Perturbation expansions in fluids

In the acoustofluidic systems that we want to describe in this thesis, the fields are time-harmonic with a fundamental frequency defined by the applied electric potential boundary condition. Explicit references to time dependent fields are denoted with a tilde. Fields that are purely time-harmonic have had their time dependence split off from their spatial dependence, and are denoted without a tilde. This means that for scalar fields and vector fields,

$$\tilde{F}(\mathbf{r}, t) = F(\mathbf{r})e^{-i\omega t}, \quad \omega = 2\pi f, \quad (2.16a)$$

$$\tilde{\mathbf{F}}(\mathbf{r}, t) = \mathbf{F}(\mathbf{r})e^{-i\omega t}, \quad \text{with } i = \sqrt{-1}. \quad (2.16b)$$

To proceed further with the governing fluid equations, we will need to introduce perturbation theory for the pressure,  $p$ , the mass density of the fluid,  $\rho$ , and the velocity,  $v$ , such that,

$$\tilde{p} = p_0 + p_1e^{-i\omega t} + \tilde{p}_2, \quad (2.17a)$$

$$\tilde{\rho} = \rho_0 + \rho_1e^{-i\omega t} + \tilde{\rho}_2, \quad (2.17b)$$

$$\tilde{\mathbf{v}} = \mathbf{0} + \mathbf{v}_1e^{-i\omega t} + \tilde{\mathbf{v}}_2, \quad (2.17c)$$

where each term in the series is smaller than the previous one, such that  $\mathbf{v}_1/c_{\text{fl}} \ll 1$ , where  $c_{\text{fl}}$  is the speed of sound in the fluid,  $\rho_1/\rho_0 \ll 1$  and  $p_1/p_0 \ll 1$ , and likewise for the second order compared to the first order. We split up the time dependence such that the zeroth-order fields are time-independent and the first-order fields are time-harmonic, to match the time-harmonic boundary conditions from the displacement field that actuate the fluid. In Section 2.2.2 it is shown that the second-order fields have a time-steady and double harmonic component, however for now the second-order fields simply have some general time and space dependence. We are working with a quiescent fluid; hence, the zeroth-order velocity is zero.

Lastly, with the systems that we treat in this thesis, the adiabatic assumption must be valid, such that the isentropic compressibility,  $\kappa_0$  can be calculated as,

$$\kappa_0 = \frac{1}{\rho_0} \left( \frac{\partial \rho}{\partial p} \right)_S = \frac{1}{\rho_0 c_{\text{fl}}^2}, \quad (2.18)$$

where it follows from Eq. (2.18) that  $\frac{1}{\rho_0} \left( \frac{\rho_1}{p_1} \right) = \frac{1}{\rho_0 c_{\text{fl}}^2} \Rightarrow \rho_1 = \frac{1}{c_{\text{fl}}^2} p_1$ . Using this in combination with the Navier–Stokes equation Eq. (2.3) makes it possible to explain the

pressure acoustics, and subsequently, the effective boundary conditions developed by Bach and Bruus[78] that have been used in this thesis.

### 2.2.1 First-order fields

The perturbation fields Eq. (2.17a), Eq. (2.17b), and Eq. (2.17c) can be inserted into the Navier–Stokes equation Eq. (2.3) and the continuity equation Eq. (2.1a). Collecting the terms to first order gives,

$$-i\omega\rho_1 = -\rho_0\nabla\cdot\mathbf{v}_1, \quad (2.19a)$$

$$-i\omega(\rho_0\mathbf{v}_1) = -\nabla p_1 + \eta_0\nabla^2\mathbf{v}_1 + \left(\eta_0/3 + \eta_0^b\right) [\nabla(\nabla\cdot\mathbf{v}_1)], \quad (2.19b)$$

where the explicit time dependence on the first-order fields has been used and subsequently divided out. Taking the divergence of Eq. (2.19b), and inserting Eq. (2.19a), together with the relation from Eq. (2.18),  $\rho_1 = \frac{1}{c_0^2}p_1$ , gives the equation for pressure acoustics:

$$\frac{i\omega}{\rho_0 c_{\text{fl}}^2} p_1 = \nabla\cdot\mathbf{v}_1, \quad (2.20a)$$

$$\frac{\omega^2}{c_{\text{fl}}^2} p_1 = -\nabla^2 p_1 - \frac{-i\omega(4\eta_0/3 + \eta_0^b)}{\rho_0 c_{\text{fl}}^2} (\nabla^2 p_1). \quad (2.20b)$$

Here we see that the equation has solutions in the form of a damped wave equation in the pressure field, and by introducing some constants, we obtain the Helmholtz equation,

$$k_c^2 p_1 + \nabla^2 p_1 = 0, \quad k_c^2 = k_0^2 \frac{1}{1 - i\Gamma_{\text{fl}}}, \quad k_0 = \frac{\omega}{c_{\text{fl}}}, \quad \Gamma_{\text{fl}} = \frac{\omega(4\eta_0/3 + \eta_0^b)}{\rho_0 c_{\text{fl}}^2}. \quad (2.21)$$

However, returning to the divergence of the continuity equation, Eq. (2.19a), it is apparent that this would lead to Helmholtz decomposition into a divergence free velocity field,  $\mathbf{v}_1^\delta$  and a rotation free velocity field,  $\mathbf{v}_1^d$ , which has been done before by Ref. 78, 126, 127 and others,

$$\mathbf{v}_1 = \mathbf{v}_1^\delta + \mathbf{v}_1^d, \quad \nabla \times \mathbf{v}_1^d = \mathbf{0}, \quad \nabla \cdot \mathbf{v}_1^\delta = 0. \quad (2.22)$$

This also makes sense, since transverse waves cannot propagate in liquids, but can propagate in the solids that surround the fluid; therefore, there must be a transition phase at the boundary, where such waves are damped to comply with the no-slip boundary condition in liquids. Inserting Eq. (2.22) into Eq. (2.19a) and Eq. (2.19b) gives:

$$\partial_t \rho_1 = -\rho_0 \nabla \cdot \mathbf{v}_1^d, \quad (2.23a)$$

$$\rho_0 \partial_t (\mathbf{v}_1^\delta + \mathbf{v}_1^d) = -\nabla p_1 - \eta_0 \nabla \times (\nabla \times \mathbf{v}_1^\delta) + \left(4\eta_0/3 + \eta_0^b\right) [\nabla(\nabla\cdot\mathbf{v}_1^d)]. \quad (2.23b)$$

where we have used the vector identity  $\nabla^2 \mathbf{B} = \nabla(\nabla \cdot \mathbf{B}) - \nabla \times \nabla \times \mathbf{B}$  [128]. We can solve for the individual fields  $\mathbf{v}_1^\delta$  and  $\mathbf{v}_1^d$  separately since they work on different length scales. Another way to see that they must separate is to realize that since one velocity represents transverse waves and the other represents longitudinal waves, we can take either the rotation or divergence of Eq. (2.23b) respectively, and noting that after doing so, each operation only leaves one of the fields. By separating the solutions and combining Eq. (2.23a) and Eq. (2.23b), as well as the relation from Eq. (2.18),  $\rho_1 = \frac{1}{c_0^2} p_1$ , we are left with the following equations for the short- and long-range first-order velocities,

$$\nabla^2 \mathbf{v}_1^\delta + k_s^2 \mathbf{v}_1^\delta = \mathbf{0}, \quad k_s = \frac{1+i}{\delta}, \quad (2.24a)$$

$$\nabla^2 \mathbf{v}_1^d + k_c^2 \mathbf{v}_1^d = \mathbf{0}, \quad \delta = \sqrt{\frac{2\nu_0}{\omega}}, \quad (2.24b)$$

as was found in Ref. [78], where we see that  $\mathbf{v}_1^\delta$  is damped within the boundary-layer dampening length scale,  $k_s$ , where  $\delta$  is the length scale of the viscous boundary layer. Through this separation into bulk and boundary layer fields, Bach and Bruus Ref. [78] developed effective boundary conditions on a curved elastic cavity, see Section 2.2.3.

### 2.2.2 Second-order field

With the equations for the first-order fluid fields, one can then expand Navier–Stokes and the continuity equation to second order and take the time average. Because the second-order fields are driven by products of first-order fields we expect the second-order fields to have either a steady-state or a double harmonic solution. By taking the time average, the double harmonic solutions do not contribute to the equation, and only the time-steady second order contributions are left. The time average of a second-order field is here defined as  $\mathbf{F}_2 = \langle \tilde{\mathbf{F}}_2 \rangle = \frac{1}{T_0} \int_0^{T_0} \tilde{\mathbf{F}}_2(\mathbf{r}, t) dt$ , where  $T_0$  is the time of a full period, and the definition here is that any second-order field that is without tilde,  $\tilde{\cdot}$ , and brackets,  $\langle \cdot \rangle$ , is time-averaged. For a product of two first-order fields, the time average is defined as  $\langle \text{Re} [\tilde{\mathbf{A}}_1(\mathbf{r}, t)] \text{Re} [\tilde{\mathbf{B}}_1(\mathbf{r}, t)] \rangle = \frac{1}{T_0} \int_0^{T_0} \frac{1}{2} (\mathbf{A}_1 e^{-i\omega t} + \mathbf{A}_1^* e^{i\omega t}) \frac{1}{2} (\mathbf{B}_1 e^{-i\omega t} + \mathbf{B}_1^* e^{i\omega t}) dt = \frac{1}{2} \text{Re} [\mathbf{A}_1(\mathbf{r}) \mathbf{B}_1^*(\mathbf{r})]$ , where  $\mathbf{B}_1^*$  is the complex conjugate of  $\mathbf{B}_1$ . The second-order time-averaged equations of the continuity equation and Navier–Stokes are therefore:

$$0 = -\nabla \cdot \left( \frac{1}{2} \text{Re} [\rho_1 \mathbf{v}_1^*] + \rho_0 \mathbf{v}_2 \right), \quad (2.25a)$$

$$\mathbf{0} = -\nabla p_2 + \eta_0 \nabla^2 \mathbf{v}_2 + \left( \eta_0/3 + \eta_0^b \right) \nabla(\nabla \cdot \mathbf{v}_2) - \rho_0 \nabla \cdot \left( \frac{1}{2} \text{Re} [\mathbf{v}_1 \mathbf{v}_1^*] \right). \quad (2.25b)$$

These equations can then be used to calculate the acoustic streaming; however, the boundary conditions are still missing. They will be discussed in Section 2.2.3.

### 2.2.3 Effective boundary conditions and acoustic streaming

The effective boundary-layer theory used in this thesis is that developed by Bach and Bruus in Ref. 78, where it analytically accounts for the boundary layer in curved elastic cavities. Since the boundary layer no longer needs to be resolved to the same degree, this enables the effective simulation of large systems such as the many-wavelength systems in 2D, or in particular in 3D, where without this effective theory it would not have been possible to simulate these systems. Because of the importance of such simulations in this thesis, the effective boundary conditions derived by Bach and Bruus in Ref. 78 should be mentioned and their validity for the systems simulated in this thesis should be discussed. However, since the boundary conditions are not trivial to explain, it might be confusing to the reader to simply state them without at least indicating how Bach and Bruus Ref. 78 derived them and which assumptions were made. Therefore, a short summary of the two boundary conditions used in this thesis will be given in this section; however, all credit goes to the authors for the results, and for a thorough explanation see the article by Bach and Bruus Ref. 78. For a slightly different take on the same, see the PhD thesis by Bach 129.

#### First-order effective boundary theory

The effective boundary conditions were developed for a generalized coordinate system, where  $\zeta$  is the transverse coordinate at any point on the surface. This allows them to make some general approximations about how the fields look close to the surface. These approximations require that  $\epsilon = \frac{\delta}{d} \ll 1$ , where  $\delta = \sqrt{\frac{2\nu_0}{\omega}}$  is the boundary layer length scale, and that  $d = \min\{k_0^{-1}, R\}$  which is the lower bound on the wavelength or surface variations. This allows Bach and Bruus to throw away terms on the order of  $\mathcal{O}(\epsilon)$ , as such terms are supposed to be small, and the theory is only expected to be correct to the order of  $\epsilon$ . On the boundary,  $\zeta \lesssim \delta \ll d$ , they do separation of variables of the fields by denoting them with a superscript of zero  $\mathbf{A}(\xi, \eta, \zeta) = \mathbf{A}^0(\xi, \eta, 0)a(\zeta)$ . Therefore the surface fields  $\mathbf{A}^0(\xi, \eta, 0)$  have vector components orthogonal to the surface, but no derivatives in that direction. The first-order boundary condition on the surface is the no-slip velocity, which for the solid surface velocity,  $\mathbf{V}_1^0$ , and the short- and long-range fields is defined as

$$\mathbf{V}_1^0 = \mathbf{v}_1^0 = \mathbf{v}_1^{d0} + \mathbf{v}_1^{\delta 0}. \quad (2.26)$$

The idea is to implement the boundary condition without explicit reference to the short range velocity. This can be done by looking at the orthogonal component of Eq. (2.26),

$$v_{1\zeta}^{d0} = V_{1\zeta}^0 - v_{1\zeta}^{\delta 0}. \quad (2.27)$$

The last term can be replaced by using the fact that the transverse waves are incompressible,  $\nabla \cdot \mathbf{v}_1^{\delta 0} = 0$ , and that on the surface the field is  $\mathbf{v}_1^{\delta 0}(\xi, \eta, \zeta) = \mathbf{v}_1^{\delta 0}(\xi, \eta, 0)e^{ik_s\zeta} + \mathcal{O}(\epsilon)$ . Then:

$$v_{1\zeta}^{\delta 0} = \frac{i}{k_s} \nabla_{\parallel} \cdot \mathbf{v}_{1\parallel}^{\delta 0} = \frac{i}{k_s} \nabla_{\parallel} \cdot (\mathbf{V}_{1\parallel}^0 + \mathbf{v}_{1\parallel}^{d0}), \quad (2.28)$$

where  $\nabla_{\parallel}$  is the parallel divergence operator. Inserting this into Eq. (2.27) gives,

$$v_{1\zeta}^{d0} = V_{1\zeta}^0 - \frac{i}{k_s} \nabla_{\parallel} \cdot \left( \mathbf{V}_{1\parallel}^0 + \mathbf{v}_{1\parallel}^{d0} \right). \quad (2.29)$$

Using that at the surface  $\nabla_{\parallel} \cdot \mathbf{v}_{1\parallel}^{d0} = \nabla_{\parallel} \cdot \mathbf{v}_{1\parallel}^d = \nabla \cdot \mathbf{v}_1^d - \partial_{\zeta} v_{1\zeta}^d$ , and  $\mathbf{v}_1^d = \frac{1 - i\Gamma_{\text{fl}}}{i\omega\rho_0} \nabla p_1$ , we obtain:

$$\partial_{\zeta} p_1 = \frac{i\omega\rho_0}{1 - i\Gamma_{\text{fl}}} \left( V_{1\zeta}^0 - \frac{i}{k_s} \nabla_{\parallel} \cdot \mathbf{V}_{1\parallel}^0 \right) - \frac{i}{k_s} (k_c^2 p_1 + \partial_{\zeta}^2 p_1), \quad \text{at } \zeta = 0. \quad (2.30)$$

The final expression seen in Bach and Bruus, Ref. 78 Eq. 25, can be found by using the approximation given in that article  $(i/k_s) \nabla \cdot (\mathbf{v}_1^{d0} - \mathbf{V}_1^0) = (i/k_s) \nabla_{\parallel} \cdot (\mathbf{v}_{1\parallel}^{d0} - \mathbf{V}_{1\parallel}^0) + \mathcal{O}(\epsilon)$ , which is correct to the order of  $\epsilon$ , on Eq. (2.29). The boundary conditions implemented in the models in this thesis are those stated in Eq. (2.30), because they are easy to implement in COMSOL, and do not need the last approximation.

The equation for the effective boundary condition from the fluid onto the solid is also described in Bach and Bruus Ref. 78, and can be calculated by assuming continuous stress across the boundary. More specifically, this means that the stress in the solid, Eq. (2.5), should be equal to the stress in the fluid, Eq. (2.2), at the boundary. For the stress in the fluid, Eq. (2.2), the divergence terms are an order of  $\Gamma_{\text{fl}}$  smaller than the other terms, and therefore the remaining terms are dominated by the perpendicular derivative of the stress, such that  $\boldsymbol{\sigma}_{\text{sl}} \cdot \mathbf{e}_{\zeta} = -p_1 \mathbf{e}_{\zeta} + \eta_0 \partial_{\zeta} \mathbf{v}_1^{\delta}$ . Using Eq. (2.26), the fact that  $\partial_{\zeta} \mathbf{v}_1^{\delta} = ik_s \mathbf{v}_1^{\delta}$  at the boundary, and the definition of the bulk velocity,  $\mathbf{v}_1^d = \frac{1 - i\Gamma_{\text{fl}}}{i\omega\rho_0} \nabla p_1$ , the final solid boundary condition in contact with the fluid is,

$$\boldsymbol{\sigma}_{\text{sl}} \cdot \mathbf{e}_{\zeta} = -p_1 \mathbf{e}_{\zeta} + \eta_0 ik_s \left( \mathbf{V}_1^0 - \frac{1 - i\Gamma_{\text{fl}}}{i\omega\rho_0} \nabla p_1 \right). \quad (2.31)$$

### Effective boundary theory second order

Bach and Bruus Ref. 78 derived effective boundary conditions for the second-order time-averaged streaming  $\langle \mathbf{v}_2 \rangle$  that analytically integrate the contributions of the boundary layer, in order to decrease the necessary numerical resolution and therefore make computations many times faster. The derivation is carried out in detail in their article, along with numerical validation of their results. For the purpose of enabling a discussion of the assumptions made and the expected accuracy, necessary for justifying the use of the boundary conditions in this thesis, and especially in Section 5.4, a short summary is given here. The effective boundary conditions are derived in Bach and Bruus by splitting the fields,  $p_2$  and  $\mathbf{v}_2$  into short- and long-range fields. The divergence of the long-range second-order velocity is approximated by zero, from the second-order continuity equation,  $\nabla \cdot \mathbf{v}_2^d = \Gamma_{\text{fl}} k_0 |\mathbf{v}_1^d|^2 / (2c_{\text{fl}}) \approx 0$ , which gives the governing equation for the second-order long-range streaming given in Ref. 78 Eq. 52b,

$$\mathbf{0} = -\nabla \left( p_2^d - \langle \mathcal{L}_{ac}^d \rangle \right) + \eta_0 \nabla^2 \mathbf{v}_2^d + \frac{\Gamma \omega}{c_{fl}^2} \langle \mathbf{S}_{ac}^d \rangle, \quad (2.32)$$

where  $\langle \mathcal{L}_{ac}^d \rangle = \frac{1}{4} \kappa_0 |p_1|^2 - \frac{1}{4} \rho_0 |\mathbf{v}_1^d|^2$  is the time-averaged acoustic Lagrangian density and  $\langle \mathbf{S}_{ac}^d \rangle = c_0^2 \langle \rho_1 \mathbf{v}_1^d \rangle$  is the time-averaged acoustic energy flux density. The boundary conditions of the short-range velocity fields were found by Bach and Bruus by first analyzing individual terms and keeping those of lowest order in  $\epsilon$ , then doing a Taylor expansion of the first order bulk velocity field  $\mathbf{v}_1^d(\xi, \eta, \zeta) = \mathbf{v}_1^{d0}(\xi, \eta) + (\partial_\zeta \mathbf{v}_1^d(\xi, \eta, \zeta))|_{\zeta=0} \zeta$ , which is only applicable for  $\zeta \ll d$ , and finally integrating the boundary contribution on the perpendicular direction from the surface up to infinity. This boundary condition on the short-range fields can then be inserted into the equations of the boundary condition for the long-range fields,  $\mathbf{v}_2^d$ . Following the recommendation of the lead author of Bach and Bruus [78], the final boundary conditions for the long-range bulk fields are the same as their Eq. 55, but where some of the perpendicular components from their Eq. 54c have been kept instead of assumed to be small, which should increase the accuracy in some cases, so that the boundary condition is:

$$\begin{aligned} \mathbf{v}_2^{d0} = & -\frac{1}{2\omega} \text{Re} \left\{ \mathbf{v}_1^{\delta 0*} \cdot \nabla \left( \frac{1}{2} \mathbf{v}_1^{\delta 0} - i \mathbf{V}_1^{0*} \right) - i \mathbf{V}_1^{0*} \cdot \nabla \mathbf{v}_1^d \right. \\ & + \left[ \frac{2-i}{2} \nabla \cdot \mathbf{v}_1^{\delta 0*} + i \left( \nabla \cdot \mathbf{V}_1^{0*} - \partial_\zeta v_{1\zeta}^{d*} \right) \right] \mathbf{v}_1^{\delta 0} \left. \right\} \cdot (\mathbf{e}_\xi \mathbf{e}_\xi + \mathbf{e}_\eta \mathbf{e}_\eta) \\ & + \frac{1}{2\omega} \text{Re} \left\{ \nabla_{\parallel} \cdot \left( i \mathbf{v}_{1\parallel}^{\delta 0} V_{1\zeta}^{0*} \right) - \frac{1+i}{\delta} V_{1\zeta}^{0*} v_{1\zeta}^{\delta 0} \right. \\ & \left. + \left[ i \mathbf{V}_1^{0*} \cdot \nabla \left( \mathbf{v}_1^d + \mathbf{v}_1^{\delta 0} \right) \right] \cdot \mathbf{e}_\zeta \right\} \mathbf{e}_\zeta. \end{aligned} \quad (2.33a)$$

Under the assumption that the system is in resonance in the liquid with a high Q-factor of the standing wave such that  $\mathbf{V}_1^0 \ll \mathbf{v}_1^d$ , then from Eq. (2.33a) the expression can be approximated, as was shown in Bach and Bruus[78] in equation Eq. 61 from their paper, to be

$$\begin{aligned} \mathbf{v}_2^{d0} = & -\frac{1}{2\omega} \text{Re} \left\{ \mathbf{v}_1^{\delta 0*} \cdot \nabla \left( \frac{1}{2} \mathbf{v}_1^{\delta 0} \right) \right. \\ & + \left[ \frac{2-i}{2} \nabla \cdot \mathbf{v}_1^{\delta 0*} - i \left( \partial_\zeta v_{1\zeta}^{d*} \right) \right] \mathbf{v}_1^{\delta 0} \left. \right\} \cdot (\mathbf{e}_\xi \mathbf{e}_\xi + \mathbf{e}_\eta \mathbf{e}_\eta) \\ & + 0 \mathbf{e}_\zeta \mathbf{e}_\zeta. \end{aligned} \quad (2.34a)$$

This is a good assumption for paper II, since the Q-factor is high in the fluid, as the standing waves build up in the acoustical cavity, as but it is not a good assumption for paper III.

### 2.2.4 Radiation force

The radiation force in acoustofluidics is the force that a particle experiences when it is hit with an incoming pressure wave and scatters it. This scattered wave interacts with the incoming pressure wave, and through nonlinear terms in the Navier–Stokes equation, ends up exerting a force on the particles. In Settnes and Bruus, Ref. 130, this force was calculated for a spherical and compressible particle suspended in a viscous fluid, where the authors expanded the scattering field to the monopole and dipole terms, and derived the force[130],

$$\mathbf{F}_{\text{rad}} = -\pi a^3 \left[ \frac{2\kappa_0}{3} \text{Re}(f_0^* p_1^* \nabla p_1) - \rho_0 \text{Re}(f_1^* \mathbf{v}_1^* \cdot \nabla \mathbf{v}_1) \right], \quad (2.35)$$

where  $a$  is the particle radius, and  $f_0$  and  $f_1$  are the monopole and dipole scattering coefficients defined as [93, 130],

$$f_0 = 1 - \frac{\kappa_p}{\kappa_0}, \quad f_1 = \frac{2[1 - \gamma(\delta/a)](\rho_p - \rho_0)}{2\rho_p + \rho_0[1 - 3\gamma(\delta/a)]}, \quad (2.36)$$

where  $\kappa_p$  and  $\kappa_0$  are the compressibility of the particle and fluid respectively, while  $\rho_p$  and  $\rho_0$  are the density of the particle and fluid respectively, and where  $\gamma(\delta/a)$  is  $\gamma(\delta/a) = -\frac{3}{2}[1 + i(1 + \delta/a)]\delta/a$ , where  $\delta$  is the viscous boundary layer, as mentioned previously.

In the case of a small particle, ( $a \ll \lambda$ ), in the inviscid case,  $\delta = 0$ , the force can be approximated by the negative gradient of the Gorkov potential: [131][93]

$$U^{\text{rad}} = -\pi a^3 \left[ \frac{\kappa_0}{3} \text{Re}(f_0) |p_1|^2 - \frac{1}{2} \rho_0 \text{Re}(f_1) |\mathbf{v}_1|^2 \right], \quad (2.37a)$$

$$\mathbf{F}_{\text{rad}} = -\nabla U^{\text{rad}}, \quad (2.37b)$$

but in general, the equation that has been used in this thesis is Eq. (2.35). One of the parameters that can quickly convey the direction a particle will move in a classical 1D standing wave, based on the scattering coefficients, is the acoustic contrast factor[66]:

$$\Phi = \frac{1}{3} f_0 + \frac{1}{2} \text{Re}(f_1), \quad (2.38)$$

### 2.2.5 Particle velocity

The time-averaged particle velocity in a fluid can be calculated by applying Newton's momentum equation to all the forces that affect the particle. In this thesis we will limit ourselves to the acoustic radiation force, the drag force,  $\mathbf{F}_{\text{drag}}$ , and the buoyancy-corrected gravitation force,  $\mathbf{F}_{\text{grav}}$ , such that the total force on the particle is,

$$\mathbf{F}_{\text{tot}} = \mathbf{F}_{\text{rad}} + \mathbf{F}_{\text{drag}} + \mathbf{F}_{\text{grav}}, \quad (2.39)$$

where[93],

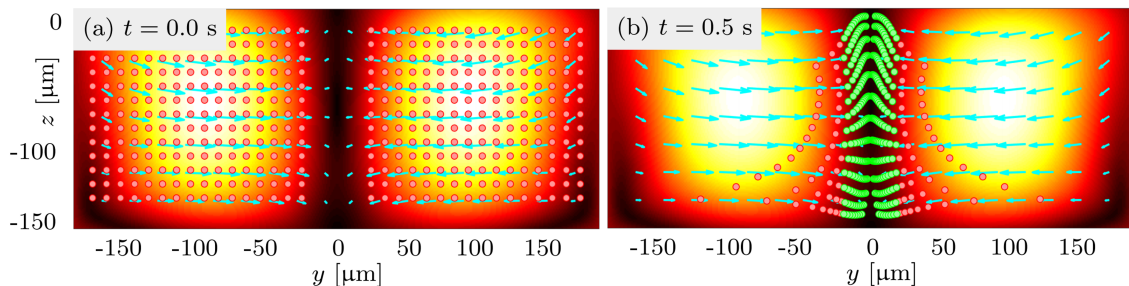


Figure 2.1: Example of particle focusing by the acoustic radiation force. In this simulation, 5- $\mu\text{m}$ -diameter polystyrene particles are focused in the center of a microfluidic channel filled with water and actuated at 1.946 MHz by a thin-film transducer shown in Fig. 4.6(a), with simulations explained further in Section 4.2 and paper Section 5.2. (a) show the original particle position and (b) show the particles after 0.5 s. The color plot shows the magnitude of the effective particle velocity,  $|\mathbf{v}_p|$ , from 0  $\mu\text{m}/\text{s}$  in black and 394  $\mu\text{m}/\text{s}$  in white, with the direction indicated by the cyan arrows. The particle trajectories are calculated by numerically integrating up  $\mathbf{v}_p$  from Eq. (2.41). The colors of the particles were changed from red to green for illustration purposes when they were within four particle diameters of the center line of the channel,  $y = 0$ . Adapted from supplementary material in Ref. 1.

$$\mathbf{F}_{\text{drag}} = 6\pi\eta_{\text{fl}}a(\mathbf{v}_2 - \mathbf{v}_p), \quad (2.40a)$$

$$\mathbf{F}_{\text{grav}} = \frac{4}{3}\pi a^3 \mathbf{g}(\rho_p - \rho_0), \quad (2.40b)$$

where  $\mathbf{g} = -9.82 \text{ N/kg } \mathbf{e}_z$ ,  $\mathbf{v}_p$  is the particle velocity. By inserting this into Newton's momentum equation and numerically integrating over time it is possible to calculate the time-dependent position of all the particles in the system. While it is completely feasible to do, especially for a few particles over a small time scale, when calculating for many particles this quickly becomes tedious since a fine time resolution is necessary because the large forces in Eq. (2.39) almost cancel out as soon as the particle has reached terminal velocity. Since we are usually working at low Reynolds numbers, the particle momentum plays a small role in the overall motion of the particle, and the particle motion quickly reaches a velocity such that there is force balance on the particle,  $\mathbf{F}_{\text{tot}} = 0$ . This means that the force field can be translated into an effective particle velocity field,

$$\mathbf{v}_p = \mathbf{v}_2 + (\mathbf{F}_{\text{rad}} + \mathbf{F}_{\text{grav}}) / (6\pi\eta_{\text{fl}}a), \quad (2.41)$$

which is much easier to numerically integrate, and therefore is much more effective when simulating many particles. This has been done several times in the literature, for example in Ref. 93 or 66, and was also used in paper II, in Section 5.2, for calculating the average focus times of 3,536 particles per device for several devices.

### 2.2.6 Acoustical energy density

The average acoustic energy density is one of those parameters that is usually given for a standing wave system because it is easy to reference and conveys a great deal of information about the system. It also adheres to scaling laws that make it easy to predict how the system will change with the average acoustic energy. The average acoustic energy density is:[80]

$$E_{\text{ac}}^{\text{fl}} = \frac{1}{V_{\text{fl}}} \int_{V_{\text{fl}}} \left( \frac{1}{4} \kappa_0 |p_1|^2 + \frac{1}{4} \rho_0 |\mathbf{v}_1^{\text{fl}}|^2 \right) dV, \quad (2.42)$$

where  $V_{\text{fl}}$  is the fluid volume over which one integrates to make the average. It can be viewed as the volume average of the time-averaged potential and kinetic energy in the system. Because of the linearity of the first-order equations, for any given frequency, the displacements scale proportionally with the applied electric potential, and the first-order pressure and velocity field therefore both scale with displacement. Therefore, the average acoustic energy density scales with the square of the applied electric potential. Since the acoustic radiation force and acoustic streaming are second-order effects, they scale with the square of the electric potential, and therefore are proportional to the average acoustic energy density. This has also been observed experimentally in Ref. 132.

## 2.3 Axisymmetric models

When a model is axisymmetric, the 3D calculations can be reduced to 2D because there is no angular dependence in the model, and it is easy to exploit this by an appropriate choice of coordinate system. Axisymmetric models were used in paper III, Section 5.3, and as an early result in the GHz acoustofluidics section.

The theory in the previous sections was formulated without reference to any specific coordinate system, with the exception of the solid mechanical equations in Voigt notation, in Section 2.1.1, which was formulated in Cartesian coordinates. In order to translate between the definitions, we define  $[x, y, z] = [r \cos(\phi), r \sin(\phi), z]$ , where we assume that the first-order scalar fields have no  $\phi$  dependence,

$$p_1(x, y, z) = p_1(r, z), \quad \varphi(x, y, z) = \varphi(r, z), \quad (2.43)$$

as well as that the first order vector fields  $\mathbf{u}_1$  and  $\mathbf{v}_1$  have no  $\phi$  dependence and no  $\phi$  component. Then:

$$\mathbf{u}_1(x, y, z) = u_{1,r}(r, z) \mathbf{e}_r + u_{1,z}(r, z) \mathbf{e}_z, \quad \mathbf{v}_1(x, y, z) = v_{1,r}(r, z) \mathbf{e}_r + v_{1,z}(r, z) \mathbf{e}_z. \quad (2.44)$$

We can look at the derivatives, defined as  $\nabla = \left( \mathbf{e}_r \partial_r + \mathbf{e}_\phi \frac{1}{r} \partial_\phi + \mathbf{e}_z \partial_z \right)$ . Since the unit vector for  $r$  and  $\phi$  depend on the position, their partial derivatives are  $\partial_\phi \mathbf{e}_r = \mathbf{e}_\phi$  and  $\partial_r \mathbf{e}_\phi = -\mathbf{e}_r$ , and therefore we must be careful when taking the derivatives.

By applying coordinate transformations to the equations Eq. (2.6) and Eq. (2.8), and assuming that the fields  $\mathbf{u}_1$  and  $\varphi$  are axisymmetric, it is possible to calculate the strain and electric field system in cylindrical coordinates, given in Voigt notation:

$$\begin{pmatrix} \sigma_{rr} \\ \sigma_{\phi\phi} \\ \sigma_{zz} \\ \sigma_{\phi z} \\ \sigma_{rz} \\ \sigma_{r\phi} \\ D_r \\ D_\phi \\ D_z \end{pmatrix} = \begin{pmatrix} C_{11} & C_{12} & C_{13} & 0 & 0 & 0 & 0 & 0 & -e_{31} \\ C_{12} & C_{11} & C_{13} & 0 & 0 & 0 & 0 & 0 & -e_{31} \\ C_{13} & C_{13} & C_{33} & 0 & 0 & 0 & 0 & 0 & -e_{33} \\ 0 & 0 & 0 & C_{44} & 0 & 0 & 0 & -e_{15} & 0 \\ 0 & 0 & 0 & 0 & C_{44} & 0 & -e_{15} & 0 & 0 \\ 0 & 0 & 0 & 0 & 0 & C_{66} & 0 & 0 & 0 \\ 0 & 0 & 0 & 0 & e_{15} & 0 & \varepsilon_{11} & 0 & 0 \\ 0 & 0 & 0 & e_{15} & 0 & 0 & 0 & \varepsilon_{11} & 0 \\ e_{31} & e_{31} & e_{33} & 0 & 0 & 0 & 0 & 0 & \varepsilon_{33} \end{pmatrix} \begin{pmatrix} \partial_r u_r \\ u_r/r \\ \partial_z u_z \\ 0 \\ \partial_r u_z + \partial_z u_r \\ 0 \\ -\partial_r \varphi \\ 0 \\ -\partial_z \varphi \end{pmatrix}, \quad (2.45)$$

for a hexagonal piezoelectric material. Non piezoelectric materials can be calculated the same way; however, the piezoelectric couplings coefficients simply are zero for this class of materials. For isotropic materials, there are the further requirements that  $C_{13} = C_{12}$ ,  $C_{33} = C_{11}$  and  $C_{66} = C_{44}$ .

Notice that the Voigt coupling matrix is unchanged under the transformation, because the hexagonal piezoelectric material coefficients are defined such that they are invariant under rotation in the plane. This is also why anisotropic materials such as silicon (100), where the parameters depend on orientation in the plane [133], cannot properly be simulated in axisymmetric simulations. Since silicon is such a stable in microelectromechanical systems (MEMS), if one needs to design an axisymmetric system that involves silicon then one can instead use silicon (111), since plates of silicon (111) behave as an isotropic material [134].

The fluid-mechanical equations in this chapter have been stated without reference to any specific coordinate system, and if they are applied with the appropriate derivative, they can be calculated in such a system. By carefully taking the derivative while considering the derivative of the basis functions, one can find the appropriate derivative in cylinder coordinates. For convenience, the gradient of a scalar and divergence of a vector are given as: [128]

$$\nabla A = \mathbf{e}_r \partial_r A + \mathbf{e}_\phi \frac{1}{r} \partial_\phi A + \mathbf{e}_z \partial_z A, \quad (2.46)$$

$$\nabla \cdot \mathbf{B} = \frac{1}{r} [\partial_r (r B_r) + \partial_\phi B_\phi + r \partial_z B_z]. \quad (2.47)$$



## Chapter 3

# Numerical modeling and validation of FEM in COMSOL

This chapter will briefly describe the numerical modeling that was used in this thesis in general terms. COMSOL[135] was used as a finite element method (FEM) solver to simulate the acoustofluidic and acoustomechanical systems that were investigated in the papers and in later sections. MATLAB[136] was sometimes used as a more flexible way of controlling COMSOL through the LiveLink package, as well as to post-process the results. None of the extra COMSOL packages were used, instead the weak-form solver that is built in to the fundamental COMSOL Multiphysics program was used. The description of the numerical FEM solver will be kept basic in Section 3.1 with the weak form formulation in Section 3.1.1 and boundary conditions in Section 3.1.2. The concrete COMSOL implementation will be described in Section 3.2, the use of the adaptive frequency stepping method in Section 3.2.2, and a short discussion in of the numerical validation, convergence analysis, comparison with experiments, axisymmetric comparison to the full 3D, and a discussion of thin-films and electrodes in sections Section 3.3 through Section 3.3.4.

### 3.1 Finite element method

The theory chapter, Chapter 2, presented the partial differential equations (PDEs) that we would like solve in various types of systems in order to understand or predict specific acoustofluidic phenomena. While it is possible to solve these equations analytically in limited, simplified, or very specific systems[77, 137] it is in general not possible, or at least very difficult and time consuming, to find the analytically solutions to the coupled PDE's in the theory chapter. Instead, a numerical solution to the equation can be sought. One such numerical method is the finite element method (FEM) which can be used for PDEs on a grid of points, referred to as a mesh in the thesis. The method works by solving for a large but finite number of elements with test functions which can be used to approximate any continuous function.

### 3.1.1 Weak form formulation

Let us first assume that the PDE's can be written in terms of a generalized flux tensor field,  $\mathbf{J}$ , a generalized force vector field,  $\mathbf{F}$ , and a solution,  $\mathbf{h}(\mathbf{r}, t)$ , such that,

$$\nabla \cdot \mathbf{J}[\mathbf{h}(\mathbf{r}, t)] - \mathbf{F}[\mathbf{h}(\mathbf{r}, t)] = 0, \quad (3.1)$$

then the task becomes to find the solution  $\mathbf{h}(\mathbf{r}, t)$ . In order to enable a computer to approximate  $\mathbf{h}(\mathbf{r}, t)$  in an automated way, the method expands it into a weighted sum over a complete set of polynomial functions. Each polynomial  $\Theta_n(\mathbf{r}, t)$  is called a test function and is defined piecewise on each element, and the task is now to find the weighting  $C_n$  of each element on each function.  $\mathbf{h}(\mathbf{r}, t) = \sum_n C_n \Theta_n(\mathbf{r}, t)$ . However, it is still difficult to efficiently determine the weighting, and there is also the problem of showing that solution is indeed a solution. The problem is equivalent to showing that the projection onto an arbitrary function is zero. This can be done by projecting the equation Eq. (3.1) onto every test function and integrating over the volume. We can require each integral over each test function to be zero, since the left-hand side of Eq. (3.1) should be equal to the right hand if we indeed have the correct solution. Therefore,

$$\sum_n \left\{ \int_{\Omega} \Theta_m(\mathbf{r}, t) \cdot \nabla \cdot \mathbf{J}[C_n \Theta_n(\mathbf{r}, t)] - \Theta_m(\mathbf{r}, t) \cdot \mathbf{F}[C_n \Theta_n(\mathbf{r}, t)] \right\} dV = 0, \quad (3.2)$$

where the sum has been taken out of the integral. By assuming that  $\mathbf{J}$  is linear and by using Gauss's theorem,

$$\sum_n \left\{ \oint_{\partial\Omega} \Theta_m \cdot \mathbf{J}(\Theta_n) \cdot \mathbf{n} dA + \int_{\Omega} -\nabla \Theta_m : \mathbf{J}(\Theta_n) - \Theta_m \cdot \mathbf{F}(\Theta_n) dV \right\} C_n = 0, \quad (3.3)$$

where moving the derivative to the test function is easier for the solver since the derivative of the test functions can be calculated analytically, and we have dropped the spatial and temporal dependence of the test functions for clarity. Now by only expanding to a finite order in the test functions, since higher-order polynomials will have a diminishing effect on the expansion if the elements that each test function spans are sufficiently small, we obtain a finite number of integrals, such that the problem of finding the coefficients becomes an inverse matrix problem,  $\sum_n K_{nm} C_n = 0$ , where  $K_{nm}$  is the integral over the  $n$  and  $m$  test functions which can be calculated, and therefore the  $C_n$  coefficients can be found through matrix operations.

### 3.1.2 Boundary conditions

The boundary integral in Eq. (3.3) enables us to implement boundary conditions on the problem. The two types of boundary conditions that are used in the thesis are the Neumann boundary condition, which in COMSOL is called the weak contribution, and the Dirichlet boundary condition. The Neumann boundary condition involves setting the flux

at the boundary to a specific value, and therefore it means setting the generalized flux,  $\mathbf{J}[\Theta_n] \cdot \mathbf{n} = \mathbf{N}(\Theta_n)$ , to the desired flux boundary condition, where  $\mathbf{N}(\Theta_n)$  is the flux condition on the boundary. The Dirichlet boundary condition sets the value of the function at that boundary to a specific value. Examples of how these boundary conditions are used in the thesis can be found in the COMSOL implementation Section 3.2.

## 3.2 COMSOL implementation

COMSOL is the software that is used to solve the PDEs given in the theory chapter Chapter 2, that is, Cauchy's equation Eq. (2.4), Maxwell's first equation, Eq. (2.7), and the pressure acoustic equation, Eq. (2.24b). It uses its own built-in FEM solver based on the method described in Section 3.1. To solve the physics for these specific systems, we use the weak form formulation, defined in the COMSOL Multiphysics base program under the name "weak form PDE," and find the generalized flux,  $\mathbf{J}$ , and the generalized force,  $\mathbf{F}$ , for each of the fields, as well as defining the boundary conditions on each domain. For the Cauchy equation, Eq. (2.4), the generalized flux and force are, under the assumption of time-harmonic first-order fields,

$$\nabla \cdot \boldsymbol{\sigma}_{\text{sl}} + \rho \omega^2 \mathbf{u}_1 = 0, \quad \mathbf{J} = \boldsymbol{\sigma}_{\text{sl}}, \quad \mathbf{F} = -\rho_{\text{sl}} \omega^2 \mathbf{u}_1, \quad (3.4)$$

with the definition of the stress in solids found in Eq. (2.6) and for piezoelectric materials in Eq. (2.6). For Maxwell's first equation, Eq. (2.7), the generalized flux and force are:

$$\nabla \cdot \mathbf{D} = 0, \quad \mathbf{J} = \mathbf{D}, \quad \mathbf{F} = 0, \quad (3.5)$$

where  $\mathbf{D}$  for a piezoelectric material is defined in Equation Eq. (2.8). For the pressure-acoustic equation, Eq. (2.24b), the generalized flux and force are:

$$\nabla \cdot \nabla p_1 + k_c^2 p_1 = 0, \quad \mathbf{J} = \nabla p_1, \quad \mathbf{F} = -k_c^2 p_1. \quad (3.6)$$

The boundary condition on the pressure from the solid is a weak contribution, or Neumann boundary condition, such that

$$N(p_1, \mathbf{V}_1) = \partial_\zeta p_1 = \frac{i\omega\rho_0}{1 - i\Gamma_{\text{fl}}} \left( V_{1\zeta}^0 - \frac{i}{k_s} \nabla_{\parallel} \cdot \mathbf{V}_{1\parallel}^0 \right) - \frac{i}{k_s} (k_c^2 p_1 + \partial_\zeta^2 p_1), \quad (3.7)$$

and the boundary condition on the solid from the fluid is also a Neumann boundary condition, such that

$$\mathbf{N}(p_1, \mathbf{V}_1) = \boldsymbol{\sigma}_{\text{sl}} \cdot \mathbf{e}_\zeta = -p_1 \mathbf{e}_\zeta + \eta_0 i k_s \left( \mathbf{V}_1^0 - \frac{1 - i\Gamma_{\text{fl}}}{i\omega\rho_0} \nabla p_1 \right). \quad (3.8)$$

The boundary conditions from the electric potential defined in equation, Eq. (2.15b), Eq. (2.15c), Eq. (2.15d) are defined as Dirichlet boundary conditions on the surface of the piezoelectric material in question, which simply implies defining the desired values at the surface in COMSOL. The remaining boundary condition is simply zero flux, which is the default boundary condition that is defined in COMSOL and which translates to  $\mathbf{N}(\Theta_n) = 0$ .

### 3.2.1 Material parameters

To model specific systems instead of generally studying the categories of *fluids* and *solids*, we require the parameter values for each material that is needed in order to simulate the systems. In this thesis, we use many different materials, and the parameter values come from many different sources. Although more materials were used during the PhD project than is presented in this thesis, the material parameters needed to reproduce the simulation as presented in this thesis, are summarized in the tables, Table 3.1 for water, Table 3.2 for Iodixanol concentrations, Table 3.3 for piezoelectric materials, and Table 3.4 for solids, with the references to the sources for all parameters.

Table 3.1: Parameter values for water as used in this thesis. The values are calculated based on polynomials that are fitted in temperature and are here presented at 25 C° and are from Ref. 117

Parameter	symbol	value	unit
Density	$\rho_0$	997	kg m <sup>-3</sup>
Speed of sound	$c_{fl}$	1497	m s <sup>-1</sup>
Compresibility	$\kappa_0$	448	TPa <sup>-1</sup>
Bulk viscosity	$\eta_{fl}^b$	2.485	mPa s
Dynamic viscosity	$\eta_{fl}$	0.890	mPa s
Dampening	$\Gamma_{fl}$	10.3	THz <sup>-1</sup> f

Table 3.2: Parameter of Iodixanol of varying concentrations. The polynomial fit is done in Ref. 28, and restated here for convenience, as these parameters plays a role in Paper III, Section 5.3.

Parameter	symbol	value	unit
Density	$\rho_0^{Iod}$	$1005 + 5.245x$	kg m <sup>-3</sup>
Speed of sound	$c_{fl}^{Iod}$	$1507 - 0.7308x + 8.053 \cdot 10^{-3}x^2 + 2.557 \cdot 10^{-5}x^3$	m s <sup>-1</sup>
Compresibility	$\kappa_{fl}^0$	$438.4 - 1.853x + 3.116 \cdot 10^{-3}x^2$	TPa <sup>-1</sup>
Dyn. viscosity	$\eta_{fl}^{Iod}$	$0.954 + 1.952 \cdot 10^{-2}x + 2.419 \cdot 10^{-4}x^2 + 2.173 \cdot 10^{-5}x^3$	mPa s
Iodixanol concen.	$x$	from $x = 0$ to $x = 60$	%

Table 3.3: Parameter values for the piezoelectric materials used in this thesis, where the relation  $C_{66} = \frac{1}{2}(C_{11} - C_{12})$  applies since the materials are hexagonal in structure to a fair approximation, with films being textured with grain boundaries randomly oriented in the film and bulk PZT being a ceramic that typically has randomly oriented grain structures that are polarized along the  $z$  axis.

Parameter	symbol	value	unit	parameter	symbol	value	unit
<i>Thin-film aluminum nitride, AlN [138–140]</i>							
Density	$\rho_{sl}$	3300	$\text{kgm}^{-3}$	Mech. dampening	$\Gamma_{sl}$	0.0005	
Elastic modulus	$C_{11}$	410.2	GPa	Elastic modulus	$C_{33}$	385.0	GPa
Elastic modulus	$C_{12}$	142.4	GPa	Elastic modulus	$C_{44}$	122.9	GPa
Elastic modulus	$C_{13}$	110.1	GPa	Elastic modulus	$C_{66}$	133.9	GPa
PZE coefficient	$e_{31,f}$	-1.05	$\text{C m}^{-2}$	PZE coefficient	$e_{15}$	-0.39	$\text{C m}^{-2}$
PZE coefficient	$e_{33}$	1.46	$\text{C m}^{-2}$	El. dampening	$\Gamma_{\varepsilon}$	0.0005	
Permittivity	$\varepsilon_{11}$	9	$\varepsilon_0$	Permittivity	$\varepsilon_{33}$	11	$\varepsilon_0$
<i>Thin-film aluminum scandium nitride, <math>\text{Al}_{0.6}\text{Sc}_{0.4}\text{N}</math> [138, 140]</i>							
Density	$\rho_{sl}$	3300	$\text{kgm}^{-3}$	Mech. dampening	$\Gamma_{sl}$	0.0005	
Elastic modulus	$C_{11}$	313.8	GPa	Elastic modulus	$C_{33}$	197.1	GPa
Elastic modulus	$C_{12}$	150.0	GPa	Elastic modulus	$C_{44}$	108.6	GPa
Elastic modulus	$C_{13}$	139.2	GPa	Elastic modulus	$C_{66}$	81.9	GPa
PZE coefficient	$e_{31,f}$	-2.65	$\text{C m}^{-2}$	PZE coefficient	$e_{15}$	-0.32	$\text{C m}^{-2}$
PZE coefficient	$e_{33}$	2.73	$\text{C m}^{-2}$	El. dampening	$\Gamma_{\varepsilon}$	0.0005	
Permittivity	$\varepsilon_{11}$	22	$\varepsilon_0$	Permittivity	$\varepsilon_{33}$	22	$\varepsilon_0$
<i>Bulk and thin-film lead zirconium titanate, PZT [141]</i>							
Density	$\rho_{sl}$	7700	$\text{kgm}^{-3}$	Mech. dampening	$\Gamma_{sl}$	0.005	
Elastic modulus	$C_{11}$	168	GPa	Elastic modulus	$C_{33}$	123	GPa
Elastic modulus	$C_{12}$	110	GPa	Elastic modulus	$C_{44}$	30.1	GPa
Elastic modulus	$C_{13}$	99.9	GPa	Elastic modulus	$C_{66}$	29.0	GPa
PZE coefficient	$e_{31,f}$	-14.7	$\text{C m}^{-2}$	PZE coefficient	$e_{31}$	-2.8	$\text{C m}^{-2}$
PZE coefficient	$e_{33}$	14.7	$\text{C m}^{-2}$	PZE coefficient	$e_{15}$	9.86	$\text{C m}^{-2}$
Permittivity	$\varepsilon_{11}$	828	$\varepsilon_0$	Permittivity	$\varepsilon_{33}$	700	$\varepsilon_0$
				El. dampening	$\Gamma_{\varepsilon}$	0.005	

Table 3.4: Parameter values of the most-used solids used in this thesis. Reference values for the different materials are given in the table. Some of the parameter values for Schott D263 and Pyrex are calculated by using Eq. (2.10a) and Eq. (2.10b), and using the relation for isotropic materials,  $C_{12} = C_{11} - 2C_{44}$ .

Parameter	symbol	value	unit	parameter	symbol	value	unit
<i>Glass, Schott D263</i> [142, 143]							
Density	$\rho_{sl}$	2510	$\text{kgm}^{-3}$				
Young's modulus	$E$	72.9	GPa	Poisson's ratio	$s$	0.208	
Elastic modulus	$C_{11}$	81.8	GPa	Elastic modulus	$C_{44}$	30.2	GPa
Elastic modulus	$C_{12}$	21.5	GPa	Mech. dampening	$\Gamma_{sl}$	0.0004	
Long. sound speed	$c_{lo}$	5710	$\text{m s}^{-1}$	Tran. sound speed	$c_{tr}$	3467	$\text{m s}^{-1}$
<i>Glass, Pyrex</i> [143, 144]							
Density	$\rho_{sl}$	2230	$\text{kgm}^{-3}$				
Young's modulus	$E$	62.8	GPa	Poisson's ratio	$s$	0.20	
Elastic modulus	$C_{11}$	69.8	GPa	Elastic modulus	$C_{44}$	26.2	GPa
Elastic modulus	$C_{12}$	17.4	GPa	Mech. dampening	$\Gamma_{sl}$	0.0004	
Long. sound speed	$c_{lo}$	5594	$\text{m s}^{-1}$	Tran. sound speed	$c_{tr}$	3425	$\text{m s}^{-1}$
<i>Silicon (100)</i> [133, 143]							
Density	$\rho_{sl}$	2329	$\text{kgm}^{-3}$	Mech. dampening	$\Gamma_{sl}$	0.0001	
Elastic modulus	$C_{11}$	165.7	GPa	Elastic modulus	$C_{44}$	79.6	GPa
Elastic modulus	$C_{12}$	63.9	GPa				

Table 3.5: Parameter values for 5- $\mu\text{m}$ -diameter polystyrene particles in water, with all parameters at 25 °C except for the speed of sound in polystyrene, which was measured at 20 °C. The parameter values are from Ref. 145, except that the scattering coefficients  $f_0$  and  $f_1$  are calculated from Eq. (2.36) using the particle radius  $a = 2.5 \mu\text{m}$ .

Parameter	symbol	Value	Unit
Density	$\rho_{ps}$	1050	$\text{kg m}^{-3}$
Compressibility	$\kappa_{ps}$	249	$\text{TPa}^{-1}$
Poisson's ratio	$\nu_{ps}$	0.35	
Speed of sound at 20 °C	$c_{ps}$	2350	$\text{ms}^{-1}$
Monopole coefficient, Eq. (2.36)	$f_0^{\text{ps}}$	0.44	
Dipole coefficient, Eq. (2.36)	$f_1^{\text{ps}}$	$0.034 + 0.0002 i$	

### 3.2.2 Adaptive frequency stepping

One of the methods used during the project was adaptive frequency stepping, a method for controlling COMSOL through Matlab and the LiveLink module, which was mentioned in Paper I, but not explained in detail. When doing frequency sweeps in high Q-factor systems, the peaks are very narrow and often spaced far apart in the frequency domain. This means that if the same resolution that is necessary to properly resolve the peaks is used everywhere, the time spent to make long sweeps in frequency would increase dramatically. As an example, with the adaptive stepping method used in paper I, a typical frequency sweep over the range 0.1-3 MHz was done with 450-500 points, where the lowest frequency step necessary to resolve the peaks was 15 Hz, and at large flat sections the frequency stepping increased to 16000 Hz. On a workstation with a 3.7-GHz Intel Core i9 7960X, the simulation processes took roughly 40 min with adaptive frequency stepping, but had the entire simulation been run at the minimum required resolution at 15 Hz, the frequency sweep would have taken roughly 4 days, without the higher-resolution solutions being different enough to notice with the naked eye.

While the method dramatically sped up the computation speed of long frequency sweeps, the procedure is not very complicated and is a standard tool in numerical com-

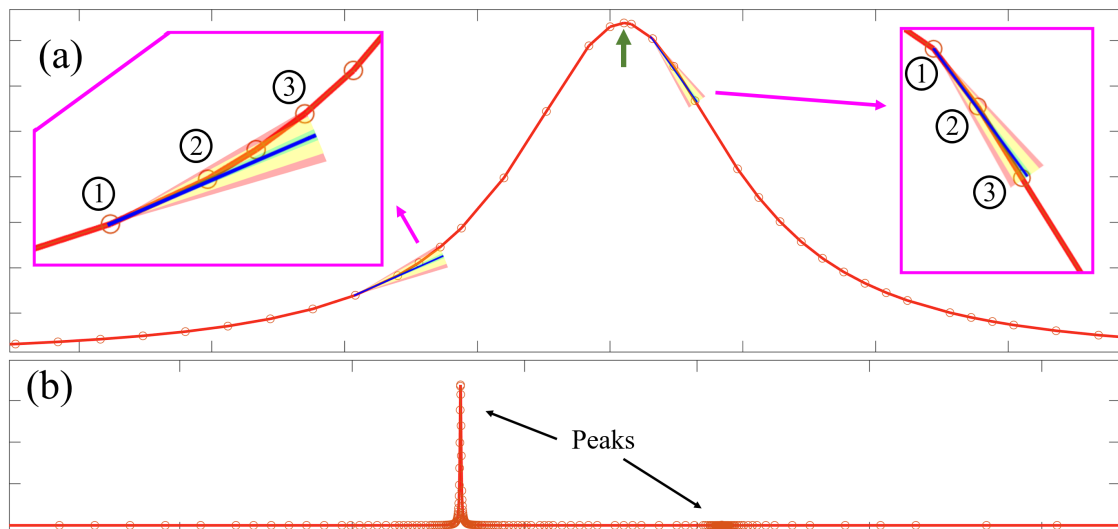


Figure 3.1: - Sketch of the adaptive frequency stepping method. (a) Sweep of a peak using the stepping method. The insert on the left is a zoom-in of the downstepping, since the linear interpolation from 1 and 2 was too far from 3, shown in red bars that is outside tolerance, and insert on the right shows upstepping since the interpolation within tolerance, shown as 3 being close enough to the interpolation. The green arrow on the center peak show the point that was simulated at the frequency estimated by fitting the points around the peak. (b) Show a zoom-out of the sweep where it can be seen that the peaks, a large one on the left and a small one on the right, are resolved much more finely than the area between peaks.

putations. The implementation in this case is to use COMSOL to do the simulation of a single frequency at a time controlled through Matlab by using the COMSOL-Matlab livelink module. This allows for more control in a coding friendly environment. At each frequency the desired parameter to be resolved is taken, typically through a COMSOL probe. The next frequency to be simulated is chosen by taking a step size and adding it to the last frequency. The probe value from the simulation at this new frequency is compared to a predicted probe value by using a linear interpretation of the last two frequencies. If the actual probe value at this frequency differs from the predicted probe value by a predefined maximum tolerance, then the frequency step was too large, the step size is decreased, and the last step is repeated. An example of this is seen in Fig. 3.1(a) in the insert to the left. If the difference between the predicted and simulated probe value is sufficiently small relative to some other predefined minimum tolerance, then the step size is increased for the next step (see insert on the right of Fig. 3.1(a)). By choosing the minimum and maximum tolerances for adjusting the step size up or down, one can design the smoothness of the returned probe values compared to the time the sweep will take to complete. One could use a higher-order interpolation in the prediction; however, while this would increase the predictability, it would need to be compensated by decreasing the tolerances correspondingly, and the end result would not change.

An additional process was employed to increase the precision of the peak value. After a frequency sweep had passed a peak by some number of points, say  $n$ , the peak was fitted to a Lorentzian distribution by taking the point from  $-n$  to  $n$  from the peak value, and from that fit the peak frequency was calculated and added to the frequency sweep in order to have a more precise peak value, seen on Fig. 3.1(a) as the point indicated by the green arrow.

On Fig. 3.1(b), we can see on a larger scale how the resolution of the sweep changes dramatically from resolving the peaks to resolving the large flat area in between. This method also finds small peaks, as seen in the large difference between the peak on the left and the one on the right.

### 3.3 Numerical validation

The numerical analysis was validated in various ways throughout the thesis. The axisymmetric simulations were compared with full 3D simulations, and a mesh convergence analysis was carried out, shown here on 2D axisymmetric simulations, where it is possible to increase the mesh drastically. The model of glass blocks with AlN thin film is also compared to the measured frequency sweeps in paper I, where 173 peaks are spread over 35 devices as presented in paper I, Section 5.1, and lastly, the convergence of the thin-film piezoelectric film and the effect of thin electrodes.

#### 3.3.1 Axisymmetric compared to full 3D

Models where the system is axisymmetric can be simulated by changing coordinate systems from Cartesian to cylindrical, where if it is completely axisymmetric it is easy to convert into 2D simulations which are equal to simulations done in full 3D in Cartesian coordinates.

This allow us to simulate systems that would otherwise not have been possible, because the simulation would have required too much random-access memory (RAM) or excessive time for a step that needed to be repeated many times, such as frequency sweeps or even parameter fitting on large frequency spectra. For a perfectly axisymmetric system, a solution calculated in full 3D should be equal to the results of axisymmetric simulations in 2D, which is what is tested in Fig. 3.2 by using a toy model for our investigations. We

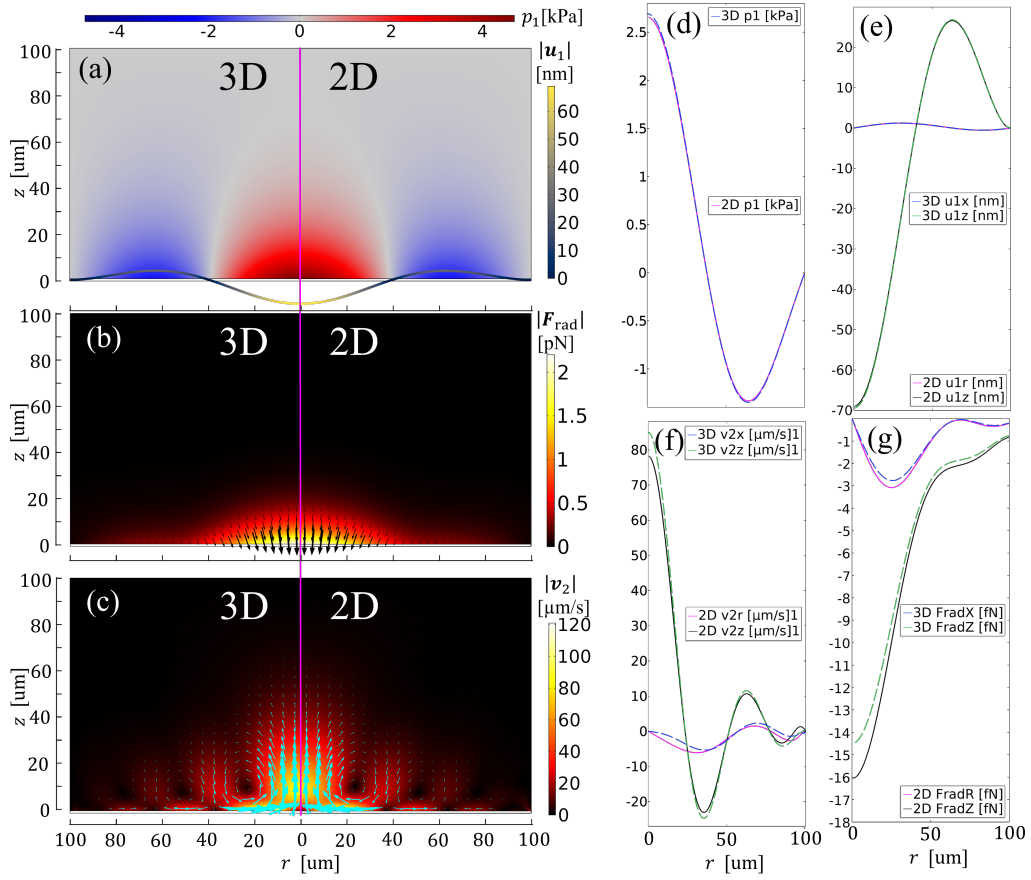


Figure 3.2: Shows the fields in both full 3D and 2D axisymmetric simulations for the second-order resonance mode of a 1- $\mu\text{m}$ -thick Pyrex membrane. (a)-(c) simulation cross section of a full 3D model on the left and a 2D axisymmetric model on the right, with color bars to the right. (a) Pressure field,  $p_1$ , and displacement field,  $\mathbf{u}_1$ . (b) Radiation force,  $F_{\text{rad}}$ . (c) Acoustic streaming,  $\mathbf{v}_2$ . (d)-(e) show line plots of the different fields, where (d), (f), and (g) are taken at the horizontal line  $z = 10 \mu\text{m}$  and (e) is taken at the horizontal line  $z = 0 \mu\text{m}$ . The line plots that correspond to 3D are dashed blue and green lines, and for 2D they are solid magenta and black lines. Figure 4(d) shows the line plot of the pressure field,  $p_1$ , (e) shows a line plot of the displacement components,  $u_{1,r}$  and  $u_{1,z}$ , (f) shows the streaming components,  $v_{2,r}$  and  $v_{2,z}$ , (g) shows the radiation force components,  $F_{\text{rad},r}$  and  $F_{\text{rad},z}$ . The first-order fields fit better than the second-order fields.

simulate a 1- $\mu\text{m}$ -thick circular membrane of Pyrex with water above it. The membrane is actuated with a displacement of  $\pm 1$  nm at its edge and the fluid above is contained with soft wall boundary conditions<sup>1</sup> on the edges at the top and sides. The simulations were performed at the resonance of the second harmonic of the membrane, which for the 3D model was 0.326 MHz and for the 2D system was at 0.325 MHz. With 3D models on the left and 2D models on the right of Fig. 3.2 (a)-(c), the pressure,  $p_1$ , and displacement field,  $\mathbf{u}_1$ , are shown and compared qualitatively in Fig. 3.2(a) and though line plots in (d) and (e). The radiation force,  $\mathbf{F}_{\text{rad}}$  is also compared in (b) with line plots of the components in (g), and the second-order acoustic streaming,  $\mathbf{v}_2$ , is compared in (c) with its line plot components in (f). The line plots are taken for all fields at the line  $z = 10 \mu\text{m}$ , in the radial direction in 2D and in the  $x$  direction in 3D, except the displacement field which is taken likewise but at  $z = 0 \mu\text{m}$ , which corresponds to the top of the Pyrex membrane. As shown in the figure, the simulated fields of the full 3D and axisymmetric 2D systems are very much alike, as one would expect them to be. There is no scaling to make the curves align: the curves shown represent the direct results of the simulation. The differences are discussed below.

The main difference between the two is the use of RAM and the computation time that it takes to simulate the systems. The first-order fields in 3D took 20 GB of RAM, 1.2 million degrees of freedom (DOF) and 8 minutes and 42 seconds to compute, whereas the 2D system took 3.0 GB of RAM, 159 thousand DOF, and 10 seconds to compute, and the mesh resolution, that is mesh elements per wavelength, was much higher for the 2D case compared to the 3D case. The real advantage came with the second-order fields, where the effective boundary theory was used for both 3D and 2D models. To compute the 3D system took 371 GB of RAM, 3.3 million DOF and 1 hour and 20 minutes to compute on a high-performance computing cluster (HPC) available at DTU, whereas the 2D simulations took 2.2 GB of RAM, 105 thousand DOF, and 5 seconds to compute. The second-order 3D fields set the resolution limit on the system to be calculated as it was not possible to request much more RAM on the available HPC cluster. The simulation time, usage of RAM and DOF are rough guidelines since the way COMSOL performs the simulations seems peculiar, and results are thus only reproducible within  $\pm 20\%$ .

In Fig. 3.2, we see that the first-order fields fit fairly well, and as one might expect, the difference between 3D and 2D becomes more pronounced in the second-order fields, as the difference from the first order fields will be squared due to the nature of the first- and second-order fields. While the overall structure is the same in 3D and 2D, the most pronounced difference lies in the differences in  $v_{2,r}$ , and the exact reason for this is not yet known, whether it lies in the model implementation or mesh resolution. If not in the model, then the most obvious possibility is the mesh resolution: that is, the 3D model does not converge to the same degree as the 2D model, and with the resolution that was possible in 3D it would not have been expected that the results would be accurate within more than 1%. Another possibility is the artificial actuation in the model, which was

<sup>1</sup>Soft wall boundary conditions in this case means that the pressure is set to zero at the edges by a Dirichlet boundary condition. This is equivalent to having a perfectly soft wall, hence the name, where the wall would move if any pressure were put on it, and therefore the pressure is zero to accommodate this change.

implemented as a harmonic displacement with an amplitude of 1  $\mu\text{m}$  at the edge of the Pyrex membrane, which borders the fluid domain. At this boundary, we should not expect the effective boundary condition to hold, since it is beyond the range of validity as stated in Bach and Bruus Ref. 78. In general, effective boundary conditions have been observed to be very robust to sharp corners, but in this extreme case the boundary conditions could introduce error that could cause the differences observed. Lastly, the 3D model and the 2D model in the simulations presented in Fig. 3.2 are two different iterations of the same model, with the difference that the 3D model it simulates the velocity field in the solid and calculates the displacement field in the solid, whereas the 2D model simulates the displacement field in the solid and calculates the velocity fields in the solid. While this procedure might introduce some differences, in general it seems to produce good agreement between the two models on Fig. 3.2.

The generally good agreement in Fig. 3.2 gives us confidence to use this model to simulate systems that require higher resolution than is possible in full 3D. The membrane modes in Paper III Section 5.3 are one such system, where at the frequencies in question and with the large water volume, it would not have been possible to simulate in full 3D even by going to the HPC cluster.

### 3.3.2 Mesh convergence analysis

The numerical simulations should be independent of the specific mesh for there to be any hope of the simulations being a correct simulation of a real-world physical device. To check this, we do a mesh convergence analysis of our numerical results to see if there is any mesh dependence. We say that the model has reached mesh convergence if the solved fields do not deviate by some fraction from higher mesh resolutions. If we do not have an analytical solution with which to compare, which we often do not, then we must evaluate the convergence trend by comparing to the highest mesh possible with the system we have access to. In order to quantify the difference between two solutions, we calculate the L2-norm difference divided by the L2 norm of the highest resolution, calculated as [122],

$$C(g_n) = \sqrt{\frac{\int_{\Omega} |g_n - g_{\text{ref}}|^2 dV}{\int_{\Omega} |g_{\text{ref}}|^2 dV}}, \quad (3.9)$$

where  $g_n$  is the  $n$ 'th solution of  $g$ , where  $g$  is a stand-in for one of the fields in the solution, in the convergence analysis and  $g_{\text{ref}}$  is the reference value of that field, often a best guess for the solution, which often translates to the highest possible resolution.

Sometimes convergence analysis and comparison to analytical models are insufficient, particularly if the model is incorrect to begin with. In such cases, comparison with experiment is the only solution, which will be discussed in Section 3.3.3.

### 3.3.3 Comparison with experiments

Some comparison with experiments were carried out, in particular in Paper I, Section 5.1, where we used the model to fit to 173 peaks spread over 35 devices of 9 different types.

Both the number of peaks spread across the different devices and geometries, as well as the overall fit, give us confidence that the solid-mechanical modeling does indeed fit the real devices. This is important since it shows that the modeling of the film seems to be consistent over a host of nominally equivalent devices as well as across some different device geometries. One of the critiques that still could be made is that we only look at the impedance spectra, and fit peaks to peaks, and thus do not know if the modes look the same in the real devices as they do in the simulations. However when one takes a look at the resultant modeling, seen as an animation in the supplemental material of Paper I, Ref. 2, it is difficult to see how the modes could look significantly different from the form given. With that in mind, as well as the fact that we are not fitting to few peaks individually but rather to the entire spectra and are seeing all the experimental peaks in the simulation as well, we suggest that the modes are the same.

This agreement with simulation and experiment in the solid-mechanical part in Paper I when actuated by a piezoelectric thin film is encouraging for the results of Paper II, Section 5.2. In some sense, the system is essentially a mechanical bulk resonator, where the fluid constitutes only roughly 1.2% of the total volume, and the film is less than 0.1% of the total volume. Therefore, having a good understanding of the thin film and mechanical system that governs roughly 99% of the device is a good place to start. The solid-mechanical part of the model in Paper I and Paper II is the same. The fluid-mechanical simulations in Paper II were compared to a device that was studied in the literature, which had a bulk PZT transducer attached. By using the same model for the thin-film driven device as was used to compare the bulk PZT devices to the literature, we hoped that this would be an indirect way of testing the thin-film device. The only step remaining is to compare to a real thin-film driven acoustofluidic bulk device, which we very much look forward to.

As a side note, simulations were compared to several different results published in peer-reviewed journals, besides that mentioned in the previous paragraph. This was intended to validate the models, both in terms of simulations and experiments, from other groups, in order to see if our model replicated what had already been published. However, this has not been included in this thesis.

### 3.3.4 Mesh of thin films and electrodes

A general heuristic is that the mesh should contain at least 6 nodes per wavelength[93], however since the wavelength is large in AlN or AlScN, because of the high speed of sound in, for example, and because the film is so thin, this would mean that a large number of mesh elements would never be necessary. Because of the small thickness of the film, the electric field is often very large, and although the field is usually linear when actuating it far away from the bulk resonance of the thin film, it can have large gradients at the boundary of the electrodes. The largest problems with the mesh in the film is that if one is not careful, elements with very large aspect ratios can be produced, which can happen when COMSOL tries to match the film-mesh with other parts of the system. One method that seemed to work consistently was to generate a mesh on the film surface, roughly four times as large as the desired final mesh in the solid that the film was deposited on, then

sweep the mesh through the film volume and refine it twice. This gives a mesh that at the surface interface between the film and the substrate is roughly the same size and four mesh elements in the thickness direction, which is more than the 6 nodal elements since the element order was always at least quadratic. In most simulations, however, there was no effect seen on the simulation by changing from having one mesh element in the thickness direction to four or more; however, since the film is such a small part of the system, it usually does not significantly affect the simulation time to have a higher resolution for the film, and therefore most of the time four elements were chosen.

Another part of the thin films that seemingly would affect the system is the electrodes on the film. While electrodes play an important role in practice, since the electrodes help define the polarization of the crystal structure, in simulations the electrodes usually play a smaller role. The electrodes are on the order of 100 nm, which with a typical thin film thickness of 1  $\mu\text{m}$  means that they are fairly large compared to the thin film. In the simulations, we assume that the electrodes do not change the electric field since they represent equipotential surfaces for the electric potential. They do contribute to the solid-mechanical resonance frequency, but for the large bulk systems presented in Papers I and II, they contribute so little to the changes in frequency that their presence or absence is usually not observable. This is because the frequency changes are small relative to other uncertainties in the system, either measurement uncertainties in Paper I, or fabrication or parameter uncertainties. Therefore, it is often not practical to include them. In both Paper I and Paper II, these electrodes were originally included, however after having investigated the minute effect they had on the system, we omitted them. The role that the electrodes have in practice for the growth of the film, its actuation, its attachment to the substrate has not been explored in this thesis.



## Chapter 4

# Summary of Results

The purpose of this section is to provide an overview of some of the results that have been produced in this thesis. The summary of results includes the three papers mentioned previously, a conference contribution, and two minor results that have not been published. The intention with this summary is to provide something between a paper abstract and an entire article, as well as having a chapter that gives information that for one reason or other did not make it into the papers. It is also a manner of conveying information which might be of interest to the reader but which did not fit into a traditional article format, such as motivation and underlying ideas, before going into a project, and in general aims to give a slightly different perspective. If the reader is so inclined, they are welcome to skip this section and go to the papers, all of which are self-contained.

### 4.1 Paper I

*Paper I* refers to the paper titled: *Fabrication, Characterization, and Simulation of Glass Devices with AlN Thin-Film Transducers for Excitation of Ultrasound Resonances* by *André G. Steckel, Henrik Bruus, Paul Muralt, and Ramin Matloub*. For a very quick summary, see the abstract of paper I in Section 5.1. Here we will give a slightly longer summary with a few details that were omitted to conform to the format of traditional scientific papers.

**Original idea:** The paper arises from the question of whether it would be possible to characterize the material parameters of a substrate by depositing a thin piezoelectric film on top of it and characterize its impedance spectra. It was assumed that to validate the results there would need to be an ensemble of different shapes and a host of nominally equivalent devices.

**Motivation:** There were several interesting points that could be addressed by this research, other than the main question of the possibility of the core concept. First, we had to test whether the solid-mechanical part of the modeling was correct. Without having access to acoustofluidic devices that showed a high degree of reproducibility, as they

always have either had large tolerances because of either the manufacturing process or unreproducible human handling, the device simulation-experiment correspondence has at best been phenomenologically equivalent, without exact one-to-one correspondence in the entire frequency domain. There was also the question of whether the model correctly simulated thin-film devices. Of course, the first step in that process was to show that the nominally equivalent devices indeed gave reproducible results, which they did. Lastly, we wanted to see whether it was possible to improve the accuracy of the material parameters on a glass type that might be used for acoustofluidic devices later in the project. No matter how good the model, if the material parameter values are not correct the final modeling will not be accurate.

**Design:** The design of the devices was to be compatible with the photolithography

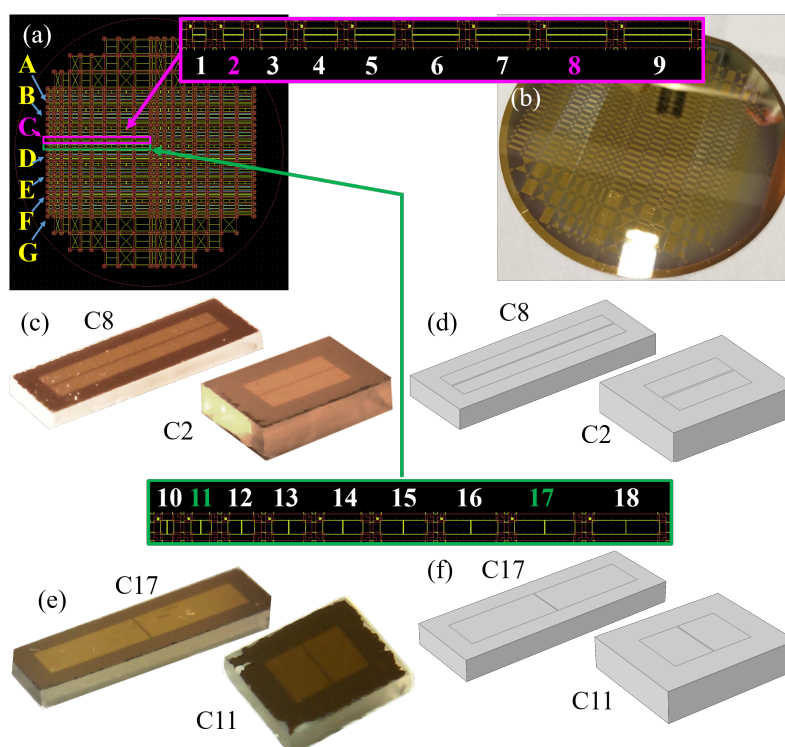


Figure 4.1: This figure shows the design of glass devices and electrode patterns. (a) is the mask of the top electrode on the 4-inch wafer. The purple and green boxes show zoom-in on devices that are designed with a split along the device (purple) and with the split across the device (green). Subfigure (b) shows the wafer before it was diced with the top electrode patterning in gold. Subfigure (c) shows images of the devices C8 and C2 after they were diced, with the modeling counterpart on (d). Subfigure (e) shows images of the devices C17 and C11 after they were diced, again with their model counterpart on the right in (f). Adapted from [2]

method in terms of the smallest sizes. The devices were also to be designed such that they could be diced with long straight cuts. Lastly, the closest distance the electrodes could be to the edges of the devices, without risking short circuits between the top and bottom electrodes when dicing the devices, was chosen to be 500  $\mu\text{m}$  for safety. Three main types of electrode designs were made, across nine different device lengths, with 14 repetitions of the set chosen. The electrodes were split along the length of the device, as well as along the width of the device, and unbroken top electrode, all of them with a fully covering bottom electrode. The fully covering top electrode should have had part of the top electrode and film removed later in the fabrication process, but this step was skipped, and therefore these devices were never tested, since it was not possible to access the bottom electrode for impedance measurements. At the edges of the wafer, the remaining space was used for devices of different dimensions and electrode shapes than the standard devices, with the idea that these devices would then be used as a validation of the parameters that were fitted to the other devices.

**Fabrication:** The fabrication of the devices was carried out at the clean-room facility Ecole Polytechnique Fédérale de Lausanne (EPFL) by Ramin Matloub, co-author of the paper. The devices were fabricated on 4-inch wafers of soda-lime-silica float glass upon which 10 nm of titanium were sputtered as an adhesion layer, after which 100 nm of platinum was sputtered, which was necessary for defining the crystal growth orientation of the 1- $\mu\text{m}$ -thick aluminum nitride (AlN) film. The platinum film also acts as a bottom electrode for the film. The AlN film is grown in a Wurtzite crystal structure in the (0001) orientation with randomly orientated grains in the plane, which does not matter as the hexagonal structure is isotropic in the plane. On top of that was placed 10 nm of chrome as an adhesion layer. Then 100 nm of gold was sputtered on top of the AlN film, followed by a photoresistor film which was used to etch the inverse of the top electrode design of the gold and chrome such that the gold patterns left became the top electrodes. The devices were then diced out from the wafer by a 120  $\mu\text{m}$  wide diamond circular saw. For the details of the fabrication, see Paper II.

**Characterization:** The characterization of the dimensions of the devices was carried out with an electronic micrometer and their electrical impedances were measured with a Agilent 4294A Precision Impedance Analyzer (Agilent Technologies AG, Basel, Switzerland), with details on the instruments and measured dimensions given in Paper I. For the impedance spectra, it was important that the connector leads be as short as possible, since even small parasitic inductances caused large changes to the impedance spectra. It also was important that the connections not affect the system, and therefore spring-loaded needle electrodes were chosen, as they would have the smallest impact while staying connected. The reflections from the surface on which the device was placed on were eliminated by placing the device on a piece of folded tissue paper. For the measurements, a box was built that plugged into the impedance analyzer that allowed for the smallest electrical leads, which had grounded coaxial electrodes in a four-point measurement setup. The box allowed for quick and easy changes of devices and for consistent measurements. Measurements were done from 0.1 to 10 MHz in steps of 500 Hz, which required a LabVIEW

program to control and collect the data. Each measurement took roughly 20 minutes. Of the devices that were available, 144 devices were tested, where some devices were discarded if they had a short circuit between the top and bottom electrodes on both top electrodes. That is to say, if only one of the top electrodes was shorted, the measurements were still taken, and were included in the 144 measurements, which gave different electrode impedance spectra than those that were not shorted. Of the 144 measurements, 35 measurements were included in Paper I, where they were analyzed further. The paper only focused on devices with top electrodes split along the length of the device, not those split across, and only on the measurements that did not have obvious faults, such as a device that had one of the top electrodes shorted, or if the connection was momentarily lost because someone walked by. It is apparent upon viewing the curves in Fig. 4.2 that

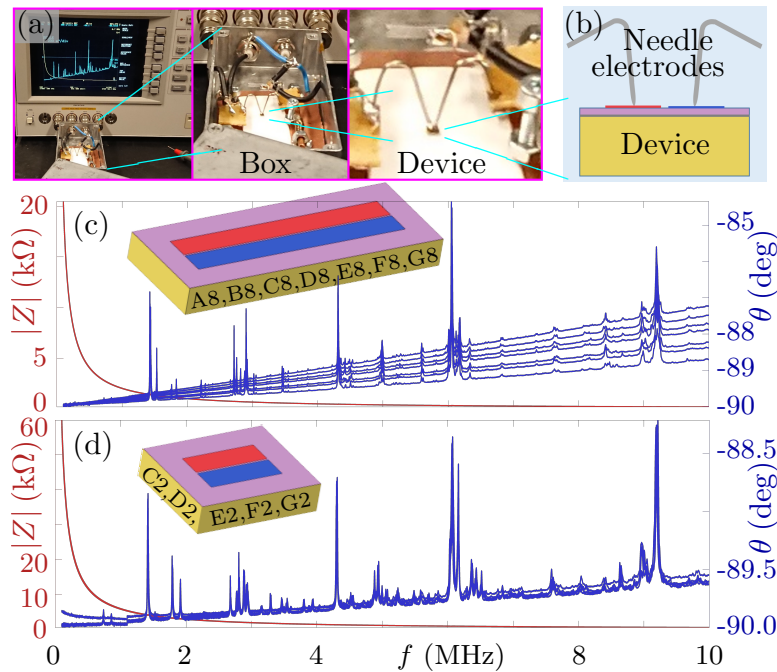


Figure 4.2: Impedance measurements on the devices A8-G8 and C2-G2. Subfigure (a) shows from the left the impedance measurement device, Agilent 4294A Precision Impedance Analyzer, the box made to perform the measurements in a consistent and reproducible manner, and a zoom-in on the device. Subfigure (b) shows a sketch of the device that shows the needle electrodes that were spring-loaded by torsioning a spring further up in the system. Subfigure (c) shows the impedance measurements of the devices A8-G8, with the absolute value of the impedance spectra in orange and the phase in blue. Notice that the phase plots do not lie on top of each other, as there is a slope that is different for each device, which is a result of not having discharged the electrodes. (d) Measurements of the impedance spectra of devices C2-G2. Notice that here the electrodes were short-circuited in order to discharge the film before each spectrum, such that the spectra now lies on top of each other. Adapted from [2]

the spectra shown on (c) seem to have similar peaks and the overall structures seem to be the same, but they all have different slopes. This was solved in Fig. 4.2 (d) by discharging the devices by short-circuiting the top electrodes before each spectrum with a conducting piece of metal. By looking on the spectra in Fig. 4.2, we see that the curves of many nominally identical devices lie on top of each other. This is important since reproducibility is one of the first characteristics that we wanted to show, and is a minimum requirement for having any chance of determining the parameters *in situ*.

**Simulations:** The simulations for the nine different geometries of the devices with the split along the device were performed according to the theory described in Chapter 2,

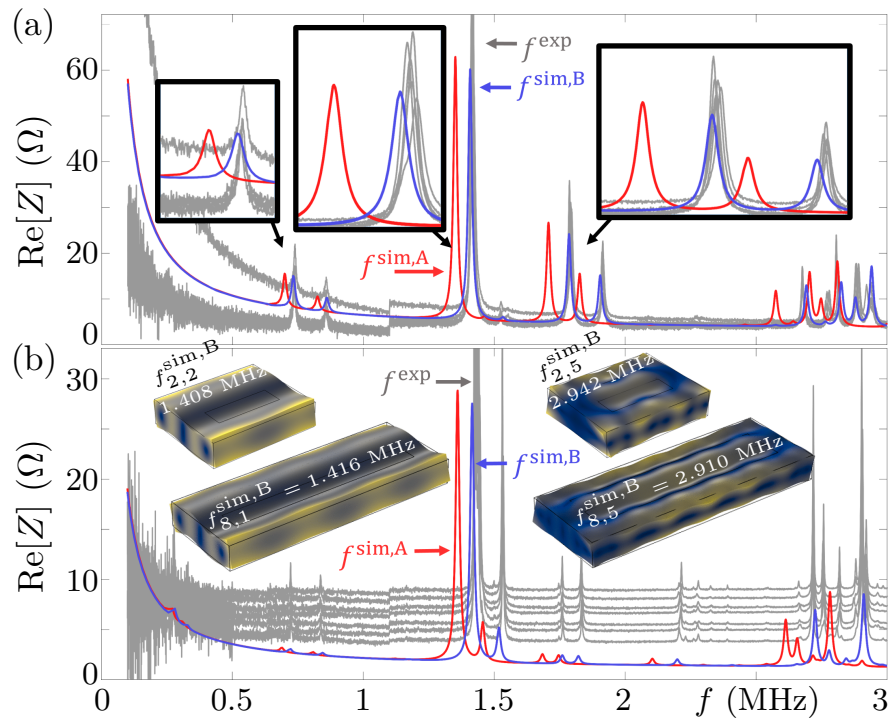


Figure 4.3: Simulations of glass devices and comparison of calculated to measured impedance spectra. (a) Measurements of the real value of the impedance spectra for devices C2-G2 in gray. Red curves show simulations with manufacturer parameter values and blue curves show simulations with fitted parameter values, the Young's modulus and Poisson's ratio, for the glass substrate. As is seen on the inserts, which are zoom-ins on the curves, the blue curve fits significantly better than the red curve. (d) The curves for measurements in gray for devices A8-G8, simulations using the original parameter values in red and the fitted parameter values in blue, with inserts showing two four modes in the simulations. The top two are from the spectra shown in (a) with the mode numbers (2,2) and (2,5), referring to the modes described in the table II in paper I. The bottom two inserts are for simulations shown in the spectra in (b). Adapted from [2]

but without the fluid. Adaptive frequency stepping, as described in Section 3.2.2, was also used. With the adaptive frequency stepping method, the frequency varied between 15 Hz and 16000 Hz and a typical sweep from 0.1 to 3 MHz was resolved with 450–500 points and took 40 min per device on a workstation with 128 GB of random-access memory (RAM) and an Intel Core i9 7960X processor at 3.7-GHz with 16 cores. Without adaptive frequency stepping, a device at the same maximum resolution would take roughly 4 days to simulate, and for all the nine geometries it would roughly take a month of computation time per simulation of all devices, of which there were multiple, since the parameter values were refined iteratively.

**Comparison with experiments:** The simulations produced curves that had the same overall structure as the measured impedance curves but whose resonance peaks seemed systematically too low, when using the manufacturer’s parameter values. This was quantified by comparing the five most prominent and identifiable resonance frequencies in the spectra of each device and comparing them to experiment. 45 simulation peaks were compared to 173 experimental peaks, and the peak values of the simulations were found to have  $(-4.6 \pm 0.1)\%$  of relative deviation from the experimental resonance peaks. The spectra of the original parameter values are the red curves in Fig. 4.3, where they can be seen to be consistently lower in frequency than the grey peaks.

**Parameter value correction:** By changing the Young’s modulus and Poission’s ratio from 70 GPa to  $(76 \pm 1)$  GPa and from 0.23 to  $(0.21 \pm 0.01)$ , respectively, the relative deviation between the fitted simulation and the experiments changed to  $(-0.5 \pm 0.1)\%$ . This was done by hand-fitting the parameter values, and this opens up the possibility for more precise and automatized methods in the full 0.1 to 10 MHz regime in the future, and thereby increasing the precision for *in situ* determination of the parameter values. Hopefully, a deeper exploration of the system would also provide a better understanding of its dampening. The spectra of the fitted parameter values can be seen on Fig. 4.3 in the blue curves.

**Conclusion and outlook:** In this paper, we showed that it is possible to actuate bulk substrate devices with a thin piezoelectric film and that by using the impedance spectra of these resonances in the bulk glass, we can find *in situ* parameters for the bulk substrate through simulations by matching the peaks.

## 4.2 Paper II

*Paper II* refers to the paper titled: *Numerical study of bulk acoustofluidic devices driven by thin-film transducers and whole-system resonance modes*, by André G. Steckel and Henrik Bruus. The abstract of paper II in Section 5.2, will give a quick overview of the article; this section is a slightly longer summary with a slightly different perspective than that presented in the article.

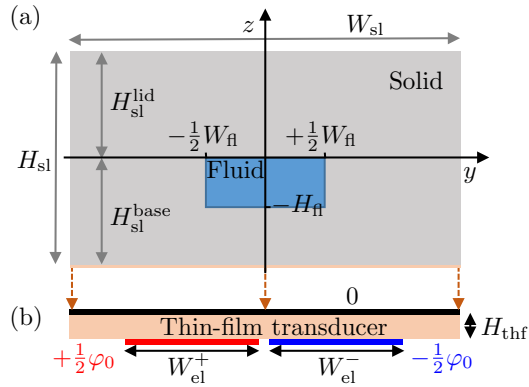


Figure 4.4: Sketch of a thin-film actuated acoustofluidic bulk device. (a) Sketch of the cross-section in the  $yz$ -plane of an acoustofluidic device with a purely elastic solid in gray, a fluid channel in blue, and a piezoelectric thin-film transducer in tan, which has been artificially enhanced to make it visible in (b). The thin-film transducer is much smaller than the device and typically less than 0.1% the device height. Subfigure (b) is a zoom-in on the thin-film transducer and from the top is the ground electrode in black, thin-film transducer in tan, and electrodes in red and blue, which are actuated with  $\frac{1}{2}\varphi$  and  $\pi$  out of phase with respect to each other. Adapted from [1]

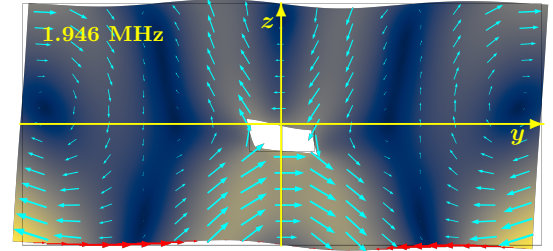


Figure 4.5: Cross-section of a simulation of the device, shown in Fig. 4.6, in the  $yz$ -plane at  $x = 0$  showing the underlying mechanism of thin-film transducer devices. The cyan arrows are displacement vectors, the color plot is the amplitude of the displacement field,  $u_1$ , going from 0 in dark blue to 15 nm in yellow, and the system displacement has been artificially scaled by 7000 to make it visible on the figure. The red arrows show the in-plane strain multiplied with the  $y$ -basis vector,  $\partial_y u_{1,y} e_y$ , in order to make the scalar visible. As seen from the direction and spacing of the arrows, the film is expanding on the left and contracting on the right. Adapted from [1]

**Motivation:** The idea of the paper is to show that it is possible to use 1- $\mu\text{m}$ -thick piezoelectric thin films to actuate acoustofluidic devices that are much larger than the thin film, where the system is driven at the whole-system resonance of the bulk part of the device. A sketch of such a device is shown on Fig. 4.4. This would solve problems with reproducibility, since the thin-film devices in Paper I showed that these devices were indeed electromechanically reproducible. It would also allow for large-scale lead-free manufacturing of acoustofluidic devices using roll-to-roll manufacturing. This would also permit the use of a different manufacturing technique when designing new acoustofluidic device, where this technique has advantages and disadvantages. The advantages were just mentioned; perhaps the most prominent disadvantage is the technological barrier to entry involved in depositing piezoelectric thin films.

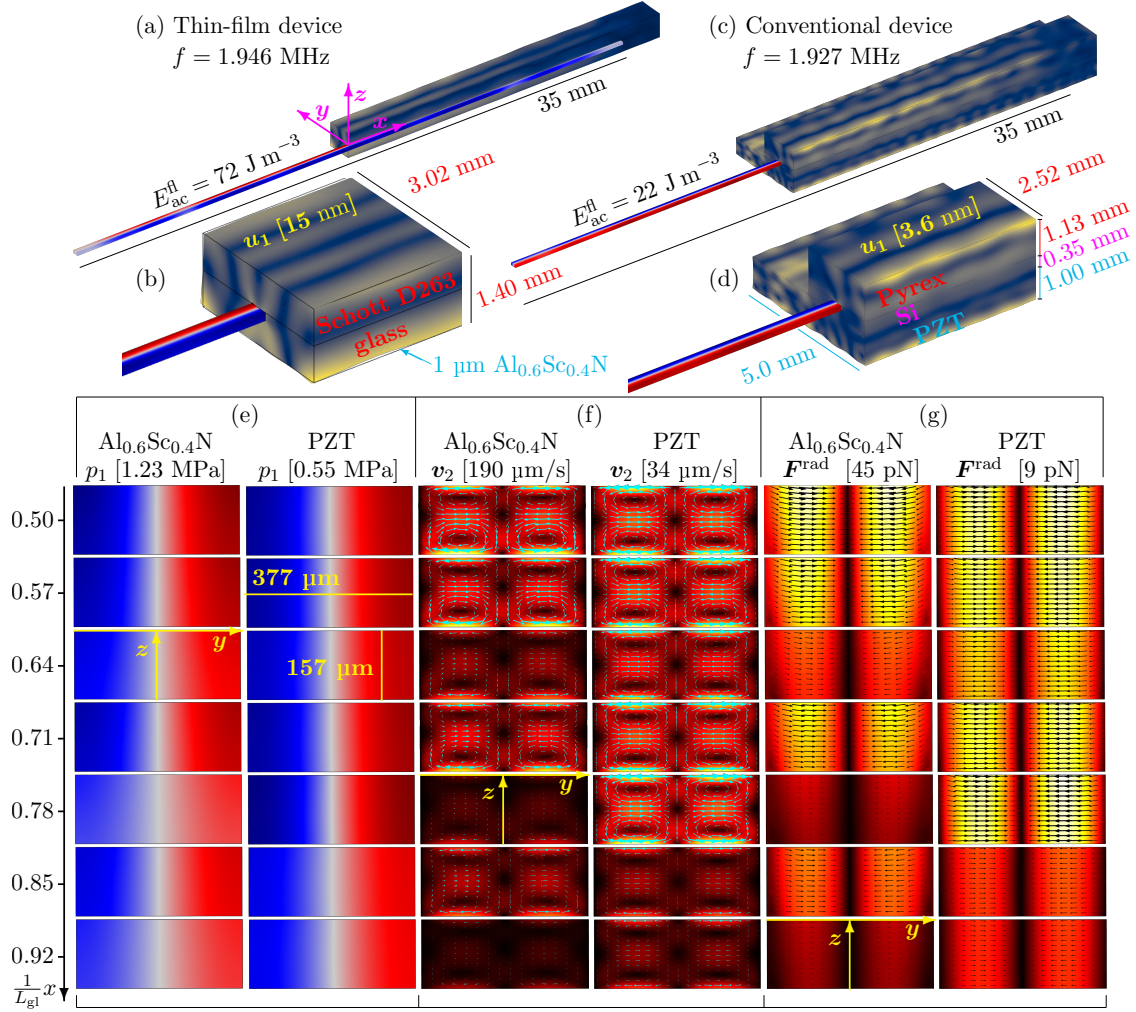


Figure 4.6: Comparison of a thin-film actuated device with a bulk actuated device in terms of first- and second-order fields. (a,b) Acoustofluidic device driven by a 1- $\mu\text{m}$ -thick  $\text{Al}_{0.6}\text{Sc}_{0.4}\text{N}$  thin-film, with displacement amplitude,  $|u_1|$ , shown in the color plot from 0 nm in dark blue to 15 nm in yellow, and a pressure field defined in (e). (c,d) Conventional device actuated by a 1-mm-thick PZT transducer, with displacement field as in (a,b) but going from 0 nm to 3.6 nm. (e)-(g) Fields are displayed for the thin-film device on the left and the bulk PZT device on the right, with cross section plots from the mid-point to  $0.92 \frac{x}{L_{gl}}$ , in seven equally spaced steps. (e) Pressure field from minimum, in blue, to maximum, in red, with symmetrized color scales and maximum amplitude in square brackets. (f) Acoustic streaming amplitude,  $|v_2|$ , from 0  $\mu\text{m/s}$  in black to max amplitude in squared brackets, in white, with intermediate colors of red and yellow. (f) Radiation force magnitude,  $|F^{rad}|$ , for 5- $\mu\text{m}$ -diameter polystyrene particles, from 0 pN, in black, to maximum in square brackets, in white, over red and yellow. Adapted from [1]

**Core concept:** There are three core concepts that make it possible for a piezoelectric thin film to actuate such a system: (1) The thin-film expansion perpendicular to the thin film due to the piezoelectric component  $e_{33}$  is negligible since the film is free to expand in that direction and is far from the thickness resonance of the film. However it will contribute to the piezoelectric component  $e_{13}$  which causes an in-plane expansion, and contraction, along the surface which cumulatively allows for actuation of the device. An example of this is seen in Fig. 4.5, where the in-plane strain pattern is displayed with red arrows. (2) Actuation of the device is possible if the strain pattern in the mode of the device, at that frequency, matches that of the stress generated by the electrode pattern in the thin film. Therefore, if a mode in the glass does not have a strain pattern in the film that can be matched to the electrodes, it would not be possible to actuate that mode. As an example of such a mode, one could imagine a vertical standing mode, which would not have a strain pattern in the in-plane direction of the film. A resonance only in the fluid and not the glass would not be actuated either because of the lack of a strain pattern and acoustic resonance in the glass. A mode that has a proper strain pattern, a good resonance in the glass, and fluid channel will be referred to as a whole-body resonance. Comparing it to a violin, the strings, the wood, or the design of the cavity inside does not individually make a good instrument; only when all the components work together will there be the desired effect. (3) The high mechanical quality factor (Q-factor) at resonance of materials such as glass and silicon, causes the device to act as an acoustical whole-body resonator, which builds up instead of dampening the waves. This allows for high strains and stresses in the film, which helps build up the internal resonances, perpetuating the cycle. The energy is lost both in the bulk of the device and in the fluid channel, where it drives the acoustofluidic action, but because the thin film constitutes such a small part of the device, the dampening in the film almost does not matter, as seen later in Fig. 4.7.

**Model:** The theory of the model is as described in Chapter 2 excluding the axisymmetric part, as all calculations are performed in Cartesian coordinates. The device was based on and compared to an acoustofluidic device developed and described by Augustsson *et al.* Ref. 146, which was taken to be a conventional acoustofluidic device driven by a bulk PZT transducer. The thin-film driven devices are made in glass of the type Shcott D263, since it is widely available, biocompatible, and the datasheets containing Young's modulus and Poisson's ratio are on their website[142]. The device could just as well have been made from silicon, for the purpose of demonstrating the concept, but that would have made it difficult to observe the internal acoustics. Constructing the device from a silicon base and glass lid, makes it more difficult to optimize the modes, by changing the dimensions of the device, and the modes will not be as clean as they are for a homogeneous device, and therefore not as illustrative. What is important is that the Q-factor in the system be high, which is both the case for silicon and glass[143], since if the dampening in the solid is low, then mechanical energy from the film deposit on the larger device surface will find its way to the water channel.

**Simulation:** The simulations were performed on a workstation with 128 GB of RAM and an Intel Core i9 7960X processor at 3.70 GHz with 16 cores. The numerical portion

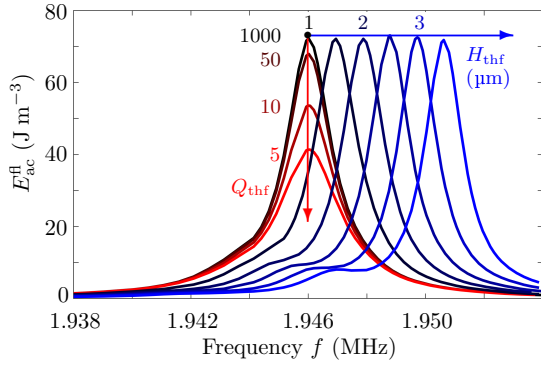


Figure 4.7: Simulations of the  $\text{Al}_{0.6}\text{Sc}_{0.4}\text{N}$  thin-film driven system in Fig. 4.6, shown in the black frequency spectra. The progressively redder curves show how the resonance peak changes when the mechanical quality factor of the thin film is changed in the simulation from 1000 to 5, where the energy changes only by half for this change. The progressively bluer curves show how the resonance changes when the thickness of the thin film is changed from 1  $\mu\text{m}$  to 3.5  $\mu\text{m}$ , where the frequency changes from 1.938 to 1.954 MHz. Adapted from [1]

was carried out in the finite element solver program COMSOL[147], and the mesh of the simulations was such that there was at least 12 nodal points per wavelength at 2 MHz with at least 18 in the fluid. Standard convergence analysis was performed and the variations in the acoustofluidic response was seen to be around 1% when comparing with the highest mesh resolution possible in our system.

**Comparison with traditional device:** When comparing the thin-film driven device with the conventional device at  $1\text{-}V_{\text{pp}}$ , the  $\text{Al}_{0.6}\text{Sc}_{0.4}\text{N}$  thin-film device performed on par with or sometimes even better than the conventional device, as seen in Fig. 4.6. The mode that was found in the conventional device was strong all the way through the channel, whereas the mode of the thin-film device was strongest in the center, and the pressure field gradually decreased towards the end of the device. This is however not a general trend for these devices, but rather particular to these specific modes, as other modes found were either more uniform across the lengths or more irregularities in the length direction for both types of devices. These modes were chosen because they showed good acoustofluidic action, and that the modes were uniform and robust to changes. By changing the materials of the thin film, we showed that the  $\text{AlN}$ ,  $\text{Al}_{0.6}\text{Sc}_{0.4}\text{N}$ , and the  $\text{PZT}$  thin films also could be used to actuate the device. While  $\text{PZT}$  gave the strongest response for  $1\text{-}V_{\text{pp}}$ , followed by  $\text{Al}_{0.6}\text{Sc}_{0.4}\text{N}$  and then  $\text{AlN}$ , the maximal electric field that is possible before the film experiences a breakdown is also important. A  $1\text{-}\mu\text{m}$ -thick  $\text{PZT}$  film can probably not even reach  $1\text{-}V_{\text{pp}}$ , whereas  $\text{Al}_{0.6}\text{Sc}_{0.4}\text{N}$  can reach higher, and  $\text{AlN}$  even higher, breakdown voltages that more than compensate for the lower piezoelectric coefficients, since the acoustical energy scales with the square of the applied voltage[132]. When comparing the different devices with respect to acoustical energy density per unit of piezoelectric factor  $e_{13,f}$  squared, they were comparable, and the product of the acoustical focusing time multiplied with the acoustical energy density was roughly the same across the devices, which is also seen in the similarity of acoustical modes in the devices.

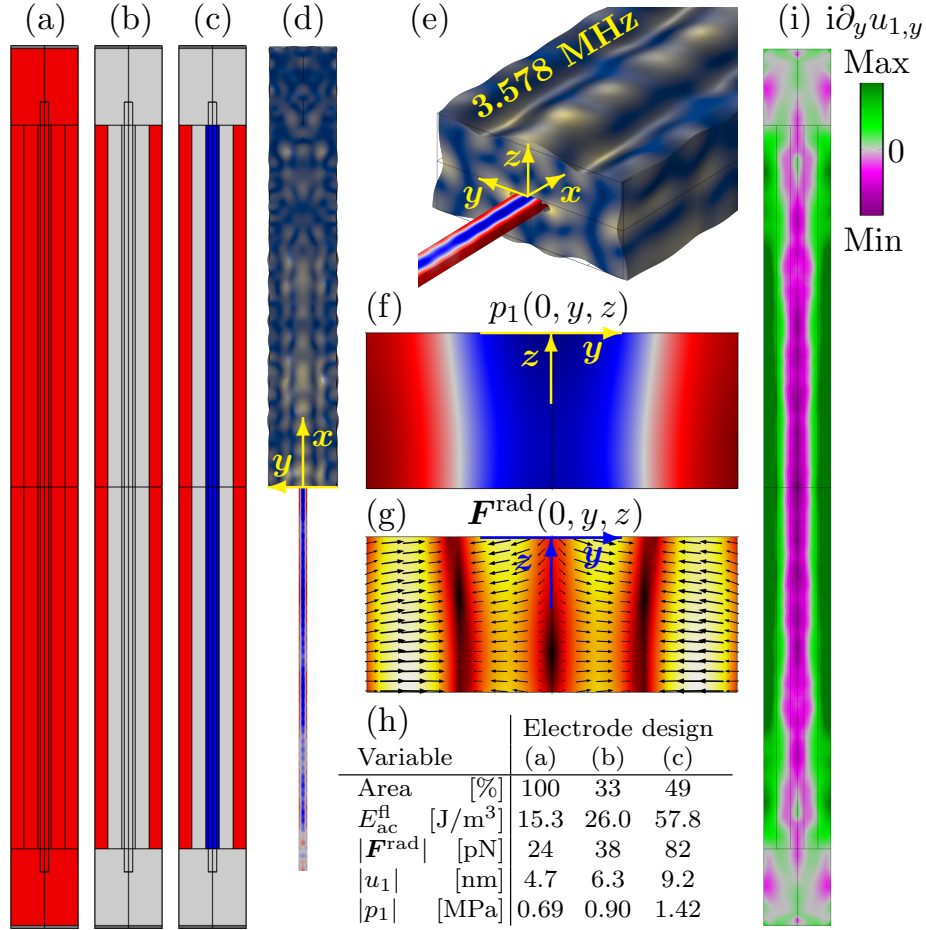


Figure 4.8: Simulations of full-wave standing pressure mode in the channel and the effect of electrode patterning. (a)-(c) Electrode pattern where red and blue are  $\pi$  out of phase and grey is not actuated. The electrode patterns are symmetric to be able to actuate the symmetric mode in the channel. (d)-(g) Simulation of the electrode pattern shown in (a) at a resonance of 3.578 MHz where the maximum displacement amplitude,  $|u_1|$ , pressure amplitude,  $|p_1|$ , radiation force magnitude,  $\mathbf{F}^{rad}$ , are given in (h). Furthermore, the table in (h) gives the percentage area covered by electrodes in (a)-(c) and the average acoustic energy density. The differences of the modes for the different electrode patterns are not visible to the unaided eye and look like the fields given (d)-(g), however the acoustofluidic action does increase for the more optimized electrode pattern in (b) and (c), which is summarized in the table in (h). In (i), it is shown the out of phase in-plane strain,  $i\partial_y u_{1,y}$ , with symmetrical color bar on the right, where the colors indicate where to place the positive electrode (green area), and negative electrode (purple area) for maximal efficiency. Adapted from [1]

**Film Q-factor and thickness:** An interesting aspect of the system is that since the PZE thin-film is such a small part of the system, the mechanical dampening of the film almost does not affect the system, as seen in Fig. 4.7. It is shown that a Q-factor of 50 in the  $\text{Al}_{0.6}\text{Sc}_{0.4}\text{N}$  thin-film only slightly changes the average acoustical energy density at resonance, and that it is only halved at a low Q-factor of 5, for films that typically have Q-factors above 1000[148, 149]. The thickness of the  $\text{Al}_{0.6}\text{Sc}_{0.4}\text{N}$  thin film did not seem to matter much for the specific mode, where the average acoustical energy remained high for the system when changing the film thickness from 1  $\mu\text{m}$  to 3.5  $\mu\text{m}$ , which changed the resonance frequency from 1.938 to 1954 MHz as seen in Fig. 4.7.

**Electrode shape:** By going to the standing-full-wave-horizontal mode of the device at 3.578 MHz, seen in Fig. 4.8, and changing the electrode shape so that it is symmetric and therefore enables symmetric modes in the device, we see the double nodal line mode in the horizontal direction, which would focus particles in two lines. At this frequency, the device mode has several wavelengths in the glass-width direction and therefore there might be some possibility of optimizing acoustofluidic action by changing the electrode coverage and polarization. Indeed, by actuating only roughly 33% of the outer sides of the electrode, the average acoustic energy density changes from  $15.3 \text{ J/m}^3$  to  $26.0 \text{ J/m}^3$ , and by again actuating some of the middle electrode, but now  $\pi$  out of phase from the first electrode, such that the coverage is now roughly 49%, the average acoustical energy density changes to  $57.8 \text{ J/m}^3$ , with the other fields following suit according to the scaling laws. This is because part of the electrode was working against itself with the full electrode, insofar as some parts were expanding while others were contracting. By only actuating the expanding part, the energy was increased, and by actuating the part that was contracting out of phase such that the film was also contracting, the effect was increased even more.

**Spatial modes and symmetry breaking:** Another feature of these systems are the clean modes enabled in the devices. Because there is such a high level of symmetry in the systems, driven almost purely by the bulk glass resonance, then it is easy to identify each individual mode. This is explained further in the paper, where the first standing half wave mode in the system was shown at 0.956 MHz, and the five subsequent modes show increasing modal numbered standing waves in the length direction. The modes, however, are not limited to systems that exhibit perfect symmetry, and it is also shown in the paper that even when moving the channel from the symmetry point in the center to the side, by 50 and 100  $\mu\text{m}$  in the  $y$ -direction, it is still possible to actuate the device and generate a standing field in the channel. **Conclusion and outlook:** The conclusion is that a 1- $\mu\text{m}$ -thick piezoelectric thin film does indeed seem able to actuate a bulk acoustofluidic device in a manner that is as good as a conventional device. There are many advantages to PZE thin-film driven devices, and by bringing this method of actuation to the attention of the acoustofluidic community, we hope that this will inspire our experimental colleagues to make the device and to test it in the future.

### 4.3 Paper III

This section is here for completeness, since the paper is still in preparation, and any details that the author of this thesis thought were missing from the article were added to the article if time allowed. Also, since the other articles were published at the time of this thesis, the corresponding summary sections provided the opportunity to add information, new understanding, or a different view on the subject. This section will therefore be very short and intended as a slightly more informal discussion than what was in the article.

**Original idea:** The original idea for the paper originated from the desire to use optimized electrode coverage of thin-films for applications in acoustofluidics, combined with the idea that the Bessel modes from a membrane must send out waves from the antinodes that through interference would create a pressure hot spot at some location above the membrane center. It was thought that this hot spot might enable trapping, however it soon became apparent, due to the boundary condition on the axisymmetric axis, that the pressure would be an anti-node, and therefore particles with positive acoustic contrast factor would not be focused on the center, but rather only particles with negative acoustic contrast factor would be focused. Therefore, by changing the fluid, it is possible to change the acoustic contrast factor of some cells; a fluid that has been used in the literature for managing this is Iodixanol[28].

**Model:** The model used in this paper is the same as in Chapter 2, specifically the axisymmetric equations of Section 2.3, which had a comparison between 3D and 2D axisymmetric models shown in Section 3.3.1. The specifics of the model with mesh, simulation time, and degrees of freedom are explained in greater detail in Paper III.

**Simulations and discussion:** The simulations in this paper were of two different geometries. Both geometries had a 1- $\mu\text{m}$ -thick  $\text{Al}_{0.6}\text{Sc}_{0.4}\text{N}$  thin film and a 10- $\mu\text{m}$ -thick membrane of silicon (111) in the axisymmetric model. The first geometry had a membrane diameter of 200- $\mu\text{m}$ , and the second had a membrane diameter of 1000- $\mu\text{m}$ . This was done for several reasons. Firstly, the fourth-order membrane mode of the smaller membrane was a clearer demonstration of the physical phenomenon. It showed that matching the electrode patterning with the out-of-phase in-plane strain increased the acoustofluidic action, and the in-plane strain was much clearer for the small membrane than higher-order modes of the larger membrane. Secondly, it also shows the phenomenon of the hot spot in the pressure field above the membrane, as well as how the waves in the  $r$ -direction were standing waves, and those in the  $z$ -direction were traveling waves. So, in most aspects the fundamentals of how the system works were visible for both the small and the larger membrane, but it was in general clearer for the small membrane. Thirdly, the dimension of this small membrane matched nicely with a recent result published in Ref. 150, where they had a roughly 200- $\mu\text{m}$  in diameter and 10- $\mu\text{m}$ -thick membrane of silicon, with AlN thin-film on top. The top electrodes, however, were not made to efficiently actuate the membrane, and in fact the membrane was actuated with a SAW actuator where the device was placed on top of the SAW device. This did however show that it is possible to fabri-

cate such devices, and that such devices are interesting for the acoustofluidic community. However, our device at these dimensions, and at the fourth-order membrane mode, had an actuation frequency of approximately 52 MHz, and at this frequency the wavelength in water was roughly the same length as the diameter of the MCF-7 cells that were to be investigated. This was not possible with the specific model for the radiation force that we were using, and therefore a larger membrane was used for the radiation force calculations since this lowered the frequency to about 18.5 MHz.

The simulations of the larger membrane then showed that the radiation force would have an anti-focus in the middle of the membrane for water and the cancer cells in question, MCF-7. However, when changing the suspension medium with different concentrations of Iodixanol, it was possible to turn the device into a trap. There was still a barrier that the cells had to overcome to enter the trap, and the trapping in the  $z$ -direction was not as good as in the radial direction. The barrier was shown to diminish when the density of the fluid was changed, was significantly lower when the cells were neutrally buoyant, and even had a hole in it when the density was lowered even further, and the streaming drag force was taken into account. The fluid with the modified density was purely theoretical, as no known fluid has such parameters, but it showed that there is further room for optimization. As a side note, while it was not shown in the paper, placing the thin film at the bottom of the membrane, instead of the top of the membrane, shows equally good acoustofluidic action, and the differences in the resulting fields were almost imperceptible. Whether it is possible to fabricate a device, with the film at the bottom, is a different question, but at least the system seems to be robust to such changes. Another element that was not mentioned in the paper was that by using a AlN thin film instead of a  $\text{Al}_{0.6}\text{Sc}_{0.4}\text{N}$  thin film, it was also possible to actuate the system, but it was necessary to account for the lower piezoelectric coefficient by using a higher actuation voltage to get the same results.

**Conclusion and outlook:** We showed that the higher-order membrane modes could be enhanced by choosing a top electrode pattern that matched the out-of-phase strain pattern in the film. We also showed that such a system could be turned into a trap for cancer cells if the suspension medium was changed. There was some discussion of how the trapping could be improved by changing the density of the medium, and also a discussion of what could be studied in the future. It would be interesting to consider devices that have an axial mode number different from zero in the membrane, as it might allow for there to be a pressure node in the central axis of the simulation, and therefore enable focusing of cells without a change of suspension medium.

## 4.4 Conference Paper I

**Original idea:** We wanted to investigate GHz acoustofluidics, since that is a field with a great deal of interesting and emerging research. Simulations of GHz acoustofluidics can be difficult because the large frequencies makes the wavelengths in the system very small. For

instance, at 1.5 GHz the wavelength in water is roughly 1  $\mu\text{m}$  and the viscous boundary layer has a size of 14 nm. This makes it difficult to simulate the system for any larger volume, and especially without the effective boundary conditions developed by Bach and Bruus 78. However, with these tools we did some simulations to try and understand the system.

**Model:** The model was based on the same model presented in Chapter 2, and the geometry was designed to match what has been published in the literature. Because of the small wavelengths, it was only possible to do 3D simulations of the actuator alone, whereas the simulations with fluids were done in 2D. A remark on the validity of the model is that the effective boundary conditions require that  $\epsilon = \frac{\delta}{d} \ll 1$ , and for the simulations at 1.5 GHz,  $\epsilon \approx 0.087$ . As the effective boundary layer theory throws away terms in the order of  $\epsilon$ , we should not expect the model of the system to be correct to at least an upper bound of  $\epsilon$ .

**Simulations:** The simulations show that the system has a complicated structure, because of the many wavelengths in the system. The solid-mechanical resonator shows that if the clamping on the system happens to be close to the actuation, then thin-film bulk resonances become very simple, and this was done in order to replicate what was done in the literature, and at least some freedom is needed in order for there to be a reasonable resonance. If, however, there was no PML layer, then the mode was very complicated. In the 2D simulations of a cross section of the device with a fairly small water channel of only 40  $\mu\text{m}$  high, the waves were almost damped in the system, which will be investigated further in Section 4.6. It was seen that this generated fairly high streaming of 3.5 mm  $\text{s}^{-1}$ , at a resonance of 1.545 GHz.

**Conclusion and outlook:** The results are early and rough, but they give a glimpse into how complicated the systems can appear due to being a many-wavelength system. The field has much to offer in terms of future investigations.

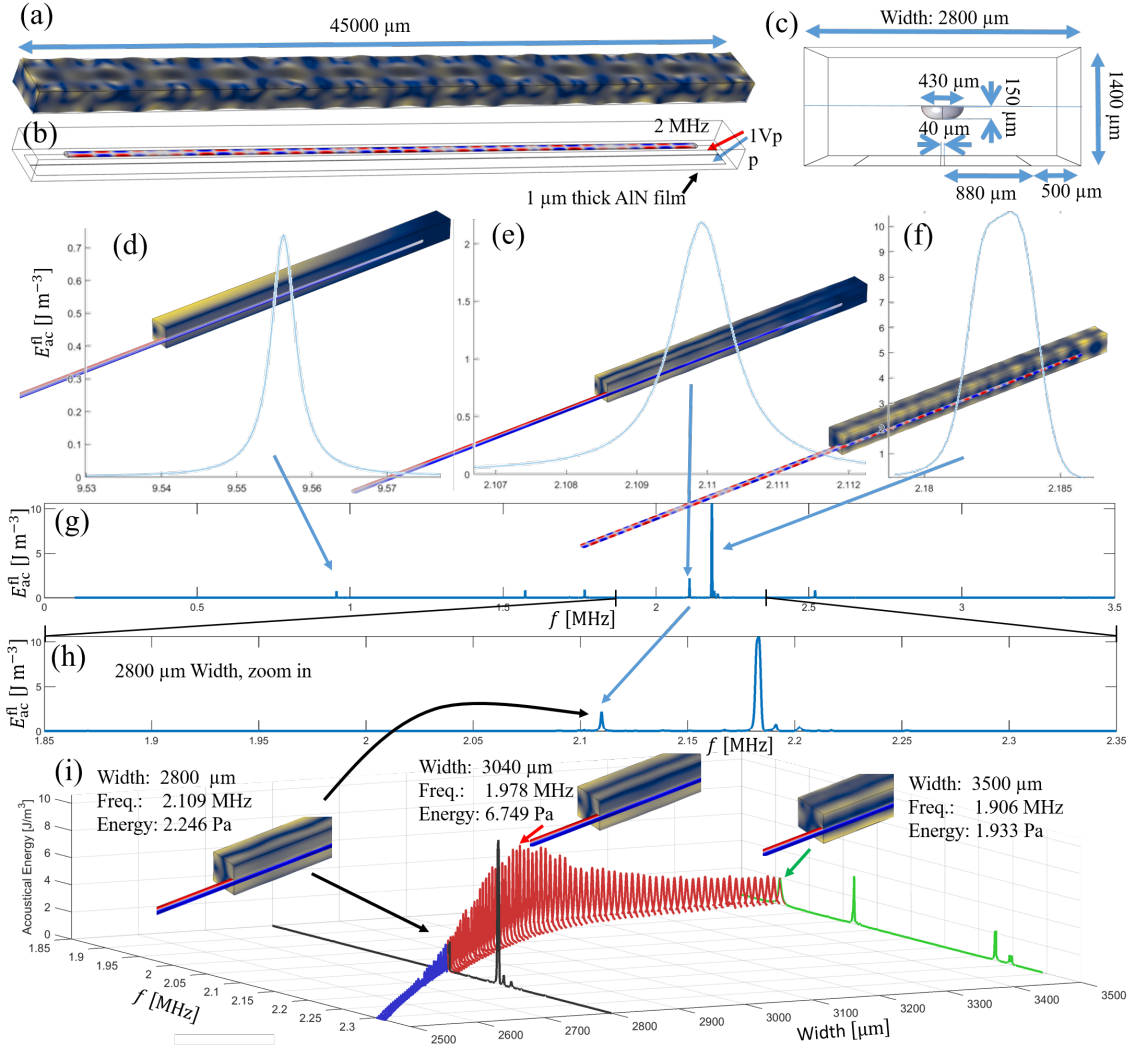


Figure 4.9: Simulations and optimization of the width of the device in Fig. 6 of Paper II. (a) the displacement field, and (b) the pressure field not at resonance but simply at 2 MHz, with a 1- $\mu$ m-thick AlN thin-film device actuated with 1 V<sub>pp</sub>, with dimensions in the sketch of (c). (d) - (f) show zoom-in on three peaks in the spectra that is seen in (g), with acoustic energy density,  $E_{ac}^{fl}$ , plotted against frequency,  $f$ . (h) shows a zoom-in on the spectra from 1.85 MHz to 2.35 MHz, and which is also shown as the in black spectra in (i). In (i) the peak in (e) was followed when changing width of the device from 2500  $\mu$ m to 3500  $\mu$ m where a peak for that mode was found at a width of 3040  $\mu$ m.

## 4.5 Minor results I - Optimization of device width

This section presents some minor results that came before Paper II and was the reason for why the width of the device in Paper II ended being 3020  $\mu\text{m}$  for the  $\text{Al}_{0.6}\text{Sc}_{0.4}\text{N}$  device in Paper II. The fitting of the width shows the strength of controlling COMSOL through MATLAB by using the LiveLink, as well as using the frequency stepping method, since simulations such as these otherwise would have taken too long.

**Original idea:** The idea was to take the device of Paper II, and do a long frequency sweep with the antisymmetric actuation, see if there was a strong and robust mode, and then change the width while following the mode in frequency to see if there was a maximum acoustical energy for that mode.

**Simulations:** On Fig. 4.9(a)-(b) is seen as a typical off-resonance behavior, taken at 2 MHz. At off resonance the system the modes are usually very messy and not very strong. It is only when on-resonance for a mode that corresponds well with the electrode pattern, that there is any significant acoustic response. These strong modes are typically cleaner looking, but there are examples where this is not true, as seen in the later discussion of (f). Because of the high Q-factor of the glass, which constitutes the bulk of the device, the width of the peaks is very narrow. A traditional frequency sweep, with constant step size, would have taken months to simulate. This is because of the frequency resolution needed to resolve the fine peaks over so long a frequency span, where each step takes several minutes. Even with the frequency stepping method it still took a few days, and the long sweep seen on Fig. 4.9(g), for the dimensions in (c), which is the same system as in Paper II, Section 5.2, Fig. 6. Select peaks are shown in Fig. 4.9(d)-(f), which are zoom-ins on the long sweep, and where the peak in (d) is the mode zero in Fig. 6 of Paper II, and mode (e) is the mode that eventually ends up as the primary mode in the system. Mode Fig. 4.9(f) is an example of a mode that is not very clean-looking. When looking at it in detail, the mode pattern at the electrode interface is homogeneous, but internally the mode has a great deal of complexity in the length direction. The resonance peak in the frequency spectra in (f) also looks lopsided, and it is believed that this is the result of two modes being close to each other. The mode seems to split into two modes very easily when changing the dimension, and in general was much more sensitive to small variations than the other modes. Therefore, although the mode has a high acoustic energy, it has not been chosen as a candidate for optimizing the width. The peak chosen for optimization was Fig. 4.9(e), and the zoom-in on the spectra in (g) can be seen on (h). The resonance spectra in (h) are seen on (i) as the black-lined frequency sweep. The width of the device was then changed slightly, a frequency sweep around the peak center of the previous width was performed, and the cycle repeated, such that the peak was followed and recorded. First the sweep was done from a width of 2800  $\mu\text{m}$  to 2500  $\mu\text{m}$ , seen on (i) as the blue curves, and it was observed that the average acoustical energy density in the channel fell. Then it was increased from 2800  $\mu\text{m}$  to 3500  $\mu\text{m}$ , and a maximum was found at a width of 3040  $\mu\text{m}$ . When changing to  $\text{Al}_{0.6}\text{Sc}_{0.4}\text{N}$  it was observed that the best width was 3020  $\mu\text{m}$ , which became the width that was used in Paper II, as the main example. However, it is worth noting that it is a fairly wide maximum, and therefore hopefully also robust to manufacturing tolerances.

## 4.6 Minor results II - GHz acoustofluidic dampening

When investigating GHz acoustofluidics, as shown in conference paper I, Section 5.4, we went slightly further than what was described in the paper. Two small results are included herein for the purposes of illustration. The mechanism behind the dampening was investigated, as shown on Fig. 4.10, and a system in the GHz regime simulated with the axisymmetric model is shown in Fig. 4.11. The system pressure,  $p_1$  and displacement,  $\mathbf{u}_1$  are shown on Fig. 4.10(a) and the resulting streaming is seen on Fig. 4.10(b). At GHz frequencies the system behaves differently, as the dampening in the system,  $\Gamma_{fl} \propto \omega$ , is proportional to frequency, and therefore the term in the streaming that is responsible for the Eckart streaming,  $\frac{\Gamma_{fl}\omega}{c_0^2} \langle \mathbf{S}_{ac}^d \rangle$  is proportional to frequency squared. Therefore, the streaming in these systems is very much driven by the bulk dampening in the system. This can be seen by looking at figure Fig. 4.10 (c) and (d), where the negative of the divergence of the time averaged acoustic energy flux density,  $-\nabla \cdot \langle \mathbf{S}_{ac}^d \rangle$ , is shown in the color plot, and the time averaged acoustic energy flux density,  $\langle \mathbf{S}_{ac}^d \rangle$ , which is proportional to the Eckart

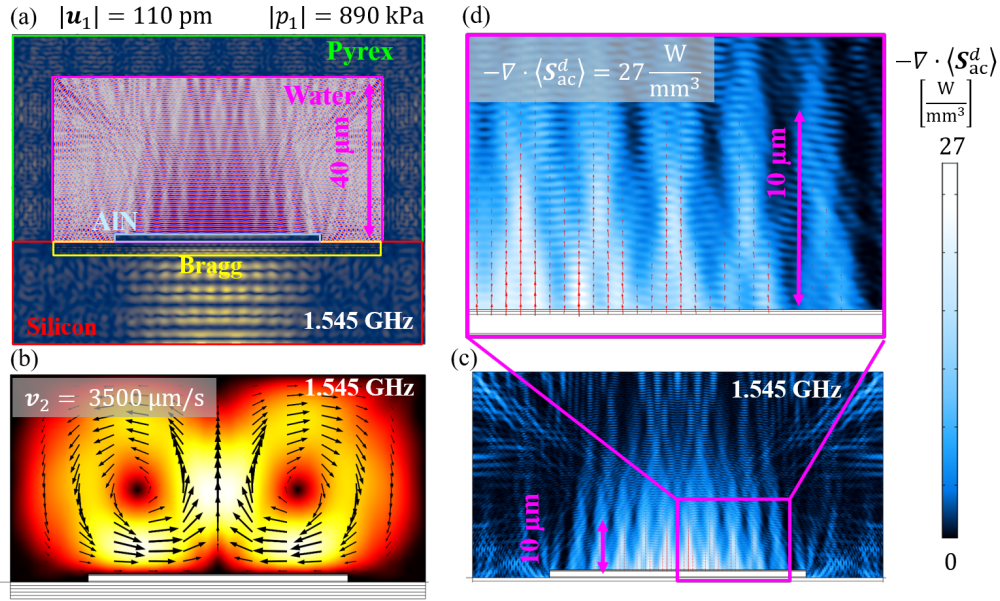


Figure 4.10: Simulations of GHz acoustics, pressure, displacement, streaming and dampening. (a) displacement amplitude,  $|\mathbf{u}_1|$ , seen as the color plot from 0 pm in dark blue to 110 pm in yellow and the pressure,  $p_1$ , going from  $-890$  kPa in dark blue to  $+890$  kPa in dark red with zero as grey. The dimensions are in Section 5.4. The streaming is seen on (b) going from  $0 \mu\text{m s}^{-1}$  in black to  $3500 \mu\text{m s}^{-1}$  in white, with red and yellow as intermediate colors. On (c), and the zoom-in in (d), is seen the negative of the divergence of the time averaged acoustic energy flux density,  $-\nabla \cdot \langle \mathbf{S}_{ac}^d \rangle$ , as the color scale with the colorbar on the right, and the red arrows are the time averaged acoustic energy flux density,  $\langle \mathbf{S}_{ac}^d \rangle$ .

streaming, is plotted with red arrows. As is seen, most of the dampening is happening in the length scale of  $10\ \mu\text{m}$ , and if one compares the streaming with the Eckart streaming term it is seen that this must be the way the system would stream. There is conservation of fluid, such that the Eckart streaming is pushing the fluid up in the center and it rolls around and flows back again. This is not a purely damped traveling wave, since in this system there are also reflections from the fluid channel ceiling. Therefore there are some standing wave patterns that are seen on the zoom-in on Fig. 4.10(d), where the dampening also has a wave pattern.

The system is small compared to the usual devices used in this thesis, since they are typically in the lower end of the MHz regime, whereas here we are in the GHz regime, and therefore the wavelengths in fluid and the solid are much smaller. This means that the resolution must be high as well, as the same rule apply for mesh elements, and nodal points per wavelength remain the same as always. This means that it is not possible to simulate the system in full 3D, with our current systems, however it is possible to simulate in axisymmetric 2D, and then interpolate into 3D, and an early example of this is seen on Fig. 4.11.

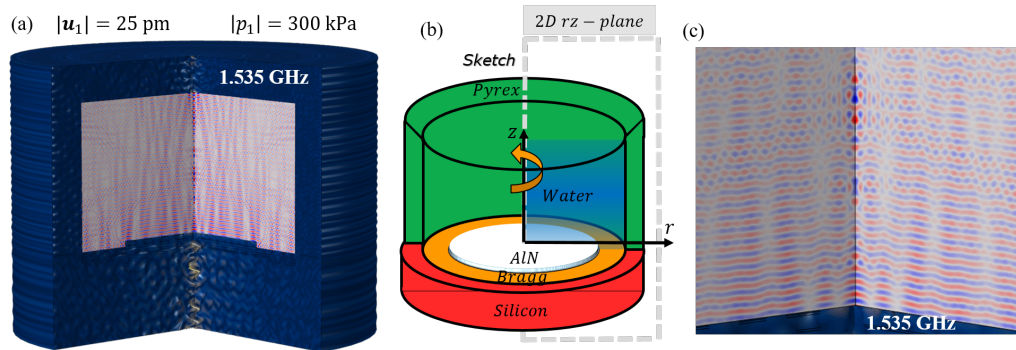


Figure 4.11: Early results of the simulation of GHz acoustics, pressure, and displacement in an axisymmetric system. (a) The pressure,  $p_1$ , ranges from  $-300\ \text{kPa}$  in dark blue to  $+300\ \text{kPa}$  in dark red and the displacement amplitude,  $|\mathbf{u}_1|$ , seen in the color plot, range from  $0\ \text{pm}$  in dark blue to  $25\ \text{pm}$  in yellow. (b) Sketch of the system, adapted from Ref. [3]. (c) Zoom-in on the fluid shown in (a).



## Chapter 5

# Publications

During the PhD project, two peer-reviewed journal papers were published, and one is submitted to a journal and awaits peer review. These papers represent a large portion of the work done in the PhD and are attached in this chapter.

Of the several conference papers written during this PhD, one was not connected to a paper, and has been added to this chapter. It was presented orally to the 2020 Acoustofluidics Conference, and appears in the conference book.

During the PhD project a patent publication was also submitted: Patent application André G. Steckel, Henrik Bruus, and Thomas Laurell, [*Title under Non-disclosure agreement until August 2022*], patent application number 21154133.9, submitted 28 January 2021.

## 5.1 Paper I: Phys. Rev. Appl. 16, (2021)

*Fabrication, Characterization, and Simulation of Glass Devices with AlN Thin-Film Transducers for Excitation of Ultrasound Resonances.* [2]

**DOI:** [10.1103/PhysRevApplied.16.014014](https://doi.org/10.1103/PhysRevApplied.16.014014)

**Authors:** [André G. Steckel](#), Henrik Bruus, Paul Muralt, and Ramin Matloub.

**Journal:** Physical Review Applied **16**, (2021)

## Fabrication, Characterization, and Simulation of Glass Devices with AlN Thin-Film Transducers for Excitation of Ultrasound Resonances

André G. Steckel,<sup>1,\*</sup> Henrik Bruus<sup>1,†</sup> Paul Muralt,<sup>2,3,‡</sup> and Ramin Matloub<sup>3,§</sup>

<sup>1</sup>*Department of Physics, Technical University of Denmark, DTU Physics Building 309, Kongens Lyngby DK-2800, Denmark*

<sup>2</sup>*Materials Science, EPFL, Station 12, Lausanne 1015, Switzerland*

<sup>3</sup>*PIEMACS Sàrl, EPFL Innovation Parc, Bâtiment C, Lausanne 1015, Switzerland*



(Received 16 November 2020; revised 2 April 2021; accepted 27 May 2021; published 7 July 2021)

We present the fabrication of 570- $\mu\text{m}$ -thick millimeter-sized soda-lime-silicate float-glass blocks with a 1- $\mu\text{m}$ -thick AlN thin-film piezoelectric transducer sandwiched between thin metallic electrodes and deposited on the top surface. The electromechanical properties are characterized by electrical-impedance measurements in the frequency range from 0.1 to 10 MHz with a peak-to-peak voltage of 0.5 V applied to the electrodes. We measure the electrical-impedance spectra of 35 devices, all of width 2 mm, but with nine different lengths ranging from 2 to 6 mm and with two to seven copies of each individual geometry. Each impedance spectrum exhibits many resonance peaks, and we carefully measure the five most prominent ones in each spectrum. We compare the resulting 173 experimental resonance frequencies with simulation results from a finite-element-method model that we develop. When we use the material parameters from the manufacturer, we obtain an average relative deviation of the 173 simulated resonance frequencies from the experimental values of  $(-4.6 \pm 0.1)\%$ . When we optimize the values of the Young's modulus and Poisson's ratio of the float glass in the simulation, this relative deviation decreases to  $(-0.5 \pm 0.1)\%$ . Our results suggest a method for an accurate *in situ* determination of the acoustic parameters at ultrasound frequencies of any elastic solid onto which a thin-film transducer can be attached.

DOI: [10.1103/PhysRevApplied.16.014014](https://doi.org/10.1103/PhysRevApplied.16.014014)

### I. INTRODUCTION

Aluminum nitride (AlN) is one of the most commonly used materials in integrated thin-film piezoelectric transducers for actuating microelectromechanical systems (MEMS). Because of their low dielectric and mechanical loss tangents, their structural and chemical stability, and their compatibility with standard silicon-based CMOS microfabrication techniques, AlN sputtered thin films are commercially used in thin-film bulk-wave acoustic-resonator filters [1]. The academic literature reports applications of AlN thin-film transducers as rf filters [2], contour-mode resonators [3], switches [4,5], suspended microchannel resonators [6], and accelerometers [7].

Detailed studies of AlN-thin-film-actuated high-tone bulk acoustic resonators with high quality factors have been performed in the 0.3–3 GHz range on 350- $\mu\text{m}$ -thick substrates of sapphire, crystal quartz, fused silica, and silicon [8], and on 30- $\mu\text{m}$ -thick Si membranes [9,10].

Because AlN is a nonferroelectric polar material, reorientation of the polar axis is not possible. The material growth process therefore has to provide a textured structure that includes the alignment of the polar directions [11], since otherwise the random orientations of the grains constituting the AlN thin film would result in a zero average piezoelectric effect. In the work presented here, we therefore follow the process developed in our previous work on pure [12] and Sc-doped [13,14] AlN films, and select Pt/Ti as the seed layer for the bottom electrode stack as it promotes nucleation of (002)-oriented AlN grains.

Over the past few years, piezoelectric thin films made of nonferroelectric polar materials, such as zinc oxide (ZnO) and AlN, have found a broad range of lab-on-a-chip applications such as biosensing, particle or cell concentrating, sorting, patterning, pumping, mixing, nebulization, and jetting. Integrated devices with acoustic transducers, sensors, and microfluidic channels have been fabricated by depositing such piezoelectric films onto a wide range of materials

\*angust@fysik.dtu.dk

†bruus@fysik.dtu.dk

‡paul.muralt@epfl.ch

§ramin.matloub@piemacs.ch

Published by the American Physical Society under the terms of the [Creative Commons Attribution 4.0 International](https://creativecommons.org/licenses/by/4.0/) license. Further distribution of this work must maintain attribution to the author(s) and the published article's title, journal citation, and DOI.

beyond the usual silicon substrates, such as ceramics, diamond, glass, and, more recently, also polymers, metallic foils, and flexible glass, for making flexible devices. Such thin-film acoustic-wave devices have great potential for implementing integrated, disposable, or bendable lab-on-a-chip devices into various sensing and actuating applications [15]. To advance such applications, we focus in the present work on AlN thin-film transducers deposited on glass substrates and driven in the 0.1–10 MHz range.

The deposition of AlN thin films and the control of their texture are more difficult than in the case of ZnO films [16], and their integration into MEMS is not a trivial task, as they tend to have a high in-plane stress with a sharp transition around zero stress [17]. However, the thermal conductivity of AlN is more than 3 times larger than of ZnO, which enables the operation of AlN films at a higher power level, an important feature for applications in rf technology. AlN films are normally sputter deposited at moderate temperatures (typically 200–400 °C) to achieve optimal performance, although “room temperature” deposition with a local temperature near the target of around 150 °C is sometimes used [18]. Also, the deposition conditions, especially the amount of oxygen or moisture in the vacuum chamber, have significant effects on the growth and microstructure of AlN films. Growing AlN films thicker than a few micrometers is particularly challenging because of the potentially large film stress and the tendency to form microcracks.

In the present work, we use our titanium-seed-layer technique [12] to improve the fabrication of AlN thin-film transducers deposited on glass substrates for future use in biosensing and lab-on-a-chip applications. In Sec. II, we describe the design of the devices, followed in Sec. III by a presentation of the fabrication and characterization processes. In Sec. IV, we then present the characterization of the acoustic properties of the devices by measuring electrical-impedance spectra in the frequency range from 0.1 to 10 MHz. A numerical model and its finite-element-method implementation is described in Sec. V. A comparison of the simulation results with the results of the experiments presented in Sec. VI shows such good agreement that our numerical handling of the measured impedance spectra can be turned into an improved *in situ* determination of the acoustic properties of the glass substrate. Finally, concluding remarks are presented in Sec. VII.

## II. DEVICE DESIGN

Figure 1 shows the design of the devices under study. This design is chosen to ease the microfabrication, the experimental characterization, and the subsequent validation of a finite-element method model of the system. All devices consist of a simple box-shaped 570- $\mu\text{m}$ -thick and 2-mm-wide block of soda-lime-silicate (SLS) float glass [19] of length  $L$  diced from a wafer.  $L$  is in the range

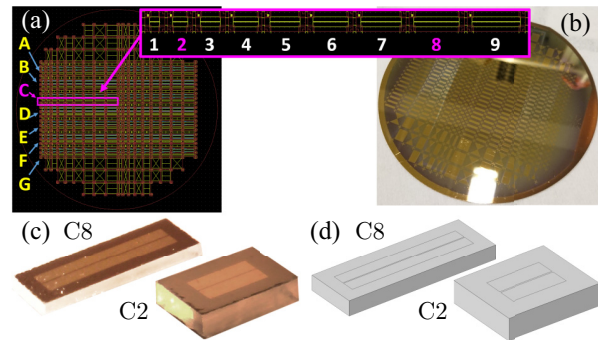


FIG. 1. (a) Design of the electrode mask for the lithography step in the fabrication process that defines the gold electrodes on the top surface of the glass wafer. The relevant devices are taken from rows A–G and columns 1–9. The inset shows row C, columns 1–9. Devices with the same column index are nominally identical. (b) Photograph of the fabricated wafer before dicing it into individual devices. (c) Microscope images of the actual devices C2 and C8. (d) Rendering of the two 2-mm-wide and 0.57-mm-high devices C2 (2.5 mm long) and C8 (5.5 mm long), showing the outline of the 1-mm-wide top electrode split into two halves by a 40- $\mu\text{m}$ -wide gap.

from 2 to 6 mm in steps of 0.5 mm, thus resulting in nine groups of nominally identical devices. A 1- $\mu\text{m}$ -thick AlN thin-film piezoelectric transducer, sandwiched between submicrometer-thick metal electrodes, is deposited on the top surface of the glass block. To ease the dicing process and to avoid short-circuiting between the two electrodes, the top electrode of the transducer has its width reduced to  $W_{\text{TE}} = 1$  mm and its length to  $L_{\text{TE}} = L - 1$  mm. Moreover, to allow antisymmetric voltage actuation, the top electrode is split in half by a 40- $\mu\text{m}$ -wide gap perpendicular to the length direction. As listed in Table I, there are up to seven nominally identical copies, A, B, C, D, E, F, and G, in each group of devices.

TABLE I. A list of the 35 devices under study. The rectangular glass blocks are all 0.57 mm thick and have a nominal width  $W = 2$  mm and a length  $L$  in the range from 2 to 6 mm. The deposited AlN thin-film piezoelectric transducer is 1  $\mu\text{m}$  thick and is sandwiched between a 0.1- $\mu\text{m}$ -thick bottom and a 0.15- $\mu\text{m}$ -thick top metal electrode. The top electrode has a total width  $W_{\text{TE}} = 1$  mm and length  $L_{\text{TE}} = L - 1$  mm. All devices with the same column index are nominally identical.

Device column	Device row	$L$ (mm)	$L_{\text{TE}}$ (mm)
1	C, D, G	2.0	1.0
2	C, D, E, F, G	2.5	1.5
3	A, B, C, G	3.0	2.0
4	A, B, D	3.5	2.5
5	A, B, C	4.0	3.0
6	B, C	4.5	3.5
7	A, B, C, D, E	5.0	4.0
8	A, B, C, D, E, F, G	5.5	4.5
9	C, D, E	6.0	5.0

### III. FABRICATION AND CHARACTERIZATION OF THE PIEZOELECTRIC THIN-FILM TRANSDUCER

The device fabrication is based on a 4-in. SLS float-glass wafer (Schott Suisse SA, Yverdon). This glass has a low thermal expansion, a high thermal-shock resistance, and an ability to withstand temperatures up to 490 °C for long periods, so by not raising the process temperature above 300 °C, we ensure high quality and reproducibility in our fabrication process. Following a microfabrication process similar to the one described in Ref. [12], and sketched in Fig. 2, the first step is cleaning of the glass substrate with isopropyl alcohol and acetone to remove organic contamination. Additional plasma cleaning is performed immediately before the deposition of the bottom electrode in the deposition tool. We prepare textured Ti, Pt, and AlN thin films using a dedicated cluster sputtering chamber (Pfeiffer Vacuum), and then sputter-deposit 10 nm of Ti at 300 °C to serve as an adhesion layer between the glass substrate and the Pt bottom electrode. Next, the 100-nm-thick Pt electrode is deposited with the same tool in a different chamber, also at 300 °C, without breaking the vacuum. Subsequently, 1 μm of (0001)-textured AlN is deposited using a dedicated reactive pulsed direct-current magnetron sputtering chamber at 300 °C, and on top of the AlN film 10 nm of Cr and 150 nm of Au are sputter deposited as the top electrode, with Cr being used as the adhesion layer between the AlN and Au. In the next process step, standard photolithography is exploited to transfer the intended pattern onto the top electrode, and this pattern is realized by ion-beam etching (Veeco). Finally, the wafer is diced into smaller chips ready for use, as shown in Fig. 1(c).

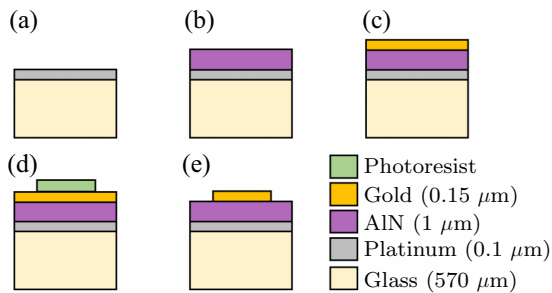


FIG. 2. Sketch of the fabrication process, where a stack consisting of a bottom electrode, an AlN thin film, and the top electrode is deposited on a glass block. (a) Deposition of a 10-nm-thick Ti adhesion layer (not shown) followed by a 100-nm-thick platinum layer. (b) Deposition of the 1-μm-thick AlN film. (c) Deposition of a 10-nm-thick Cr adhesion layer (not shown) followed by a 150-nm-thick gold layer. (d) Deposition and development of photoresist. (e) Patterning of the top electrode by ion-beam etching of the exposed gold, followed by removal of the photoresist.

After fabrication and dicing, the quality of the resulting devices is checked by visual inspection with a microscope, and their dimensions are measured using an electronic micrometer (RS Pro 705-1229, RS Components). By measuring all available devices, the average height and width are found to be  $(571 \pm 1) \mu\text{m}$  and  $(2031 \pm 2) \mu\text{m}$ , respectively, and the average lengths of devices 1–9 are determined to be  $(2011 \pm 1)$ ,  $(2512 \pm 1)$ ,  $(3013 \pm 1)$ ,  $(3514 \pm 1)$ ,  $(4016 \pm 1)$ ,  $(4500 \pm 1)$ ,  $(5016 \pm 1)$ ,  $(5509 \pm 1)$ , and  $(6018 \pm 1) \mu\text{m}$ , respectively. The uncertainties represent one standard deviation of several repeated measurements, and the relative uncertainty ranges from 0.2% for the height down to below 0.1% for the longest length.

### IV. MEASURED ELECTRICAL IMPEDANCE

The electrical impedance of the 35 devices listed in Table I is measured as a function of frequency from 0.1 to 3 MHz in steps of 500 Hz using an Agilent 4294A Precision Impedance Analyzer (Agilent Technologies AG, Basel, Switzerland) with a 0.5-V<sub>pp</sub> ac voltage applied in

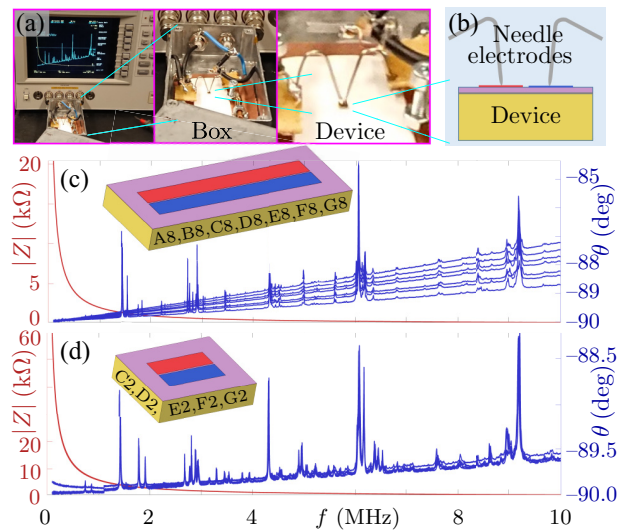


FIG. 3. (a) Three photographs of the spectrum analyzer and the attached metal box that provides electrical shielding of the device, but here with its lid removed to reveal the device mounted inside. An enlargement of the interior of the metal box shows the coaxial connectors and the wires leading to the device. A further enlargement shows the spring-loaded electrodes attached to the device. (b) End-view sketch of the spring-loaded electrodes attached to the device, consisting of a glass block (beige) and an AlN thin-film transducer (purple) with a split top electrode (red and blue). (c) Impedance spectra, showing the magnitude  $|Z(f)|$  (red curves) and the phase  $\theta(f)$  (blue curves) for the seven nominally identical devices A8, B8, C8, D8, E8, F8, and G8 shown in the inset. The phase curves differ, as the devices are not discharged initially. (d) As part (c) but for the five nominally identical devices C2, D2, E2, F2, and G2. Here, the phase curves are nearly identical, as the devices are discharged initially.

antiphase between the two halves of the split top electrode. The bottom electrode is left floating.

To reduce the electrical noise, each device under study is placed in a grounded metal box, from where it is connected with short coaxial cables to the impedance analyzer by pressing spring-loaded needle electrodes onto each half of the split top electrode; see Figs. 3(a) and 3(b). The setup is also designed to minimize undesired parasitic components: the parasitic inductance in the system is reduced to somewhere around  $L_{\text{ext}} = (28 \pm 15)$  nH, the parasitic resistance is roughly  $R_{\text{ext}} = (5 \pm 3)$   $\Omega$ , and the parasitic capacitance is negligible compared with the intrinsic capacitance  $C_{\text{dev}}$  of the device formed by the electrodes separated by the thin AlN film, ranging from 18 pF for the smallest device to 86 pF for the largest. This design ensures that the resonance frequency  $f_{\text{ext}} = (1/2\pi)(L_{\text{ext}}C_{\text{dev}})^{-1/2}$  involving the external inductance is pushed up in value, such that  $100 \text{ MHz} \lesssim f_{\text{ext}} \lesssim 220 \text{ MHz}$ , much larger than 10 MHz, and therefore does not interfere with the intrinsic resonances of the device under study. Finally, the device under

study is placed on a folded soft piece of tissue paper to acoustically isolate it from the environment.

Examples of the 35 recorded impedance spectra  $Z(f) = |Z|e^{i\theta}$  are shown in Figs. 3(c) and 3(d), where we plot the magnitude  $|Z(f)|$  and the phase  $\theta(f)$ . We first note that the intrinsic resonances of the devices are most clearly visible in the phase plots  $\theta(f)$ . Because of the parasitic impedances of the system, the base level of  $\theta(f)$  shows a linear increase from the  $-90^\circ$  of an ideal capacitor in the dc limit to a value between  $-89.7^\circ$  and  $-87.8^\circ$  at 10 MHz. The device resonances appear as sharp peaks in the phase curve, with a width of around 0.01 times the resonance frequency itself and with an amplitude ranging from  $0.1^\circ$  to  $3.5^\circ$ . This technique is a variant of standard resonant ultrasound spectroscopy (RUS) [20–22]. However, in contrast to conventional RUS, the ultrasound transducers in our case are an integrated but tiny part of the structures to be characterized.

Next, we note that the positions and amplitudes of the resonance peaks are nearly identical for samples with

TABLE II. For each of the nine device geometries, labeled by the column index  $k = 1-9$  in Table I, five resonance peaks ( $k, n$ ) of increasing frequency with  $n = 1-5$  are selected from the impedance spectrum for comparing the simulations with the measurements. Peaks (4, 1) and (4, 2), marked with asterisks, are not measured on device B in column  $n = 4$ . The experimental value  $f_{k,n}^{\text{exp}}$  is the average resonance frequency of peak  $n$  over all devices (row indices A–G in Table I) with column index  $k$ . The simulation result  $f_{k,n}^{\text{sim,A}}$  is the corresponding resonance frequency obtained from the numerical modeling described in Sec. V using the parameter values given in the literature. The simulation result  $f_{k,n}^{\text{sim,B}}$  is obtained by using the optimized values listed in Table IV of the Young’s modulus and Poisson’s ratio for the glass block. Finally, for  $X = \text{A or B}$ ,  $\Delta_{k,n}^X = (f_{k,n}^{\text{sim,X}} - f_{k,n}^{\text{exp}})/f_{k,n}^{\text{exp}}$  is the relative deviation of the simulation result from the experimental value for resonance peak  $n$  and device geometry  $k$ .

Peak $k, n$	$f_{k,n}^{\text{exp}}$ (MHz)	$f_{k,n}^{\text{sim,A}}$ (MHz)	$f_{k,n}^{\text{sim,B}}$ (MHz)	$\Delta_{k,n}^{\text{A}}$ (%)	$\Delta_{k,n}^{\text{B}}$ (%)	Peak $k, n$	$f_{k,n}^{\text{exp}}$ (MHz)	$f_{k,n}^{\text{sim,A}}$ (MHz)	$f_{k,n}^{\text{sim,B}}$ (MHz)	$\Delta_{k,n}^{\text{A}}$ (%)	$\Delta_{k,n}^{\text{B}}$ (%)
1, 1	0.943	0.886	0.927	-6.0	-1.6	5, 4	2.712	2.607	2.722	-3.9	0.4
1, 2	1.424	1.355	1.411	-4.9	-0.9	5, 5	2.901	2.774	2.903	-4.4	0.1
1, 3	2.065	1.954	2.045	-4.1	-1.0	6, 1	1.425	1.353	1.410	-5.0	-1.1
1, 4	2.717	2.613	2.722	-5.4	0.2	6, 2	1.537	1.465	1.531	-4.7	-0.4
1, 5	2.896	2.764	2.894	-4.5	-0.1	6, 3	1.606	1.531	1.595	-4.7	-0.7
2, 1	0.737	0.699	0.732	-5.2	-0.7	6, 4	2.741	2.634	2.742	-3.9	0.0
2, 2	1.418	1.351	1.408	-4.7	-0.7	6, 5	2.910	2.784	2.913	-4.3	0.1
2, 3	1.791	1.707	1.786	-4.7	-0.3	7, 1	0.321	0.314	0.322	-2.3	0.3
2, 4	1.915	1.826	1.904	-4.6	-0.5	7, 2	1.440	1.366	1.421	-5.2	-1.3
2, 5	2.942	2.811	2.942	-4.5	-0.0	7, 3	1.561	1.480	1.542	-5.2	-1.2
3, 1	0.612	0.580	0.607	-5.2	-0.8	7, 4	2.733	2.626	2.735	-3.9	0.1
3, 2	1.403	1.336	1.395	-4.8	-0.5	7, 5	2.905	2.777	2.905	-4.4	0.0
3, 3	1.489	1.420	1.480	-4.6	-0.6	8, 1	1.438	1.361	1.416	-5.4	-1.6
3, 4	1.752	1.668	1.741	-4.8	-0.6	8, 2	1.533	1.456	1.518	-5.0	-1.0
3, 5	2.735	2.632	2.739	-3.7	0.2	8, 3	1.834	1.746	1.821	-4.8	-0.7
4, 1*	0.522	0.494	0.519	-5.4	-0.7	8, 4	2.718	2.613	2.726	-3.9	0.3
4, 2*	0.544	0.525	0.547	-3.4	0.7	8, 5	2.903	2.782	2.910	-4.2	0.2
4, 3	1.431	1.360	1.416	-5.0	-1.0	9, 1	1.429	1.358	1.415	-4.9	-1.0
4, 4	1.667	1.587	1.656	-4.8	-0.6	9, 2	1.511	1.436	1.498	-4.9	-0.9
4, 5	2.725	2.621	2.729	-3.8	0.2	9, 3	1.765	1.679	1.751	-4.9	-0.8
5, 1	1.429	1.358	1.415	-4.9	-1.0	9, 4	2.089	1.993	2.082	-4.6	-0.3
5, 2	1.609	1.533	1.599	-4.8	-0.6	9, 5	2.744	2.638	2.748	-3.8	0.1
5, 3	2.104	1.998	2.088	-5.0	-0.7						

nominally identical geometry from different parts of the wafer [see Fig. 1(a)], for the approximately 30 peaks that can be easily identified in the range from 0.1 to 10 MHz. About 40% of the devices selected from columns 1–9 and rows A–G have a short circuit between one or both of the top electrodes and the bottom electrode, so they are discarded from the study. This is the reason that all seven fabricated devices are listed for only column 8 in Table I. We find that the slope of the base level of the phase spectra  $\theta(f)$  can vary even for nominally identical devices, as seen in Fig. 3(d). It turns out that this variance is due to spurious charging effects, perhaps due to the floating electrode. This effect can be avoided by briefly short-circuiting the electrodes with a piece of metallic wire, and thus discharging the system. After discharging, the phase spectra become nearly identical for all devices with the same geometry; see Fig. 3(e). When these precautions are taken, the impedance spectra exhibit a large degree of repeatability and reproducibility.

For each of the nine different device geometries among our 35 selected devices, labeled by the column index  $k = 1$ –9 in Table I, we measure the resonance frequencies of the five most prominent isolated nonoverlapping resonance peaks, labeled by  $n = 1$ –5, in the impedance-phase spectra  $\theta(f)$ . This results in  $5 \times 35 - 2 = 173$  resonance frequencies (for device 4B, we did not measure all five peaks, but only the three highest). In Table II, we list the experimentally determined values of the resonance frequencies, but to avoid showing all 173 of them, we show only the average resonance frequency  $f_{k,n}^{\text{exp}}$  of peak  $n$  over all devices (row indices A–G in Table I) with column index  $k$ , which results in  $9 \times 5 = 45$  entries.

TABLE III. Material parameters at 25 °C for the AlN thin-film transducer and the SLS float-glass substrate. The frequency-dependent damping coefficients  $\Gamma_{\text{sl}}(f)$  and  $\Gamma_{\varepsilon}(f)$  in the solid and dielectric domain are obtained by fitting to the measured width of the resonance peaks and to the background level, respectively, for devices C2–G2. The longitudinal and transverse sound speed are called  $c_{\text{lo}}$  and  $c_{\text{tr}}$ , respectively. Since we have a thin film, we use  $e_{31,f} = e_{31} - (C_{13}/C_{33})e_{33}$  instead of  $e_{31}$  [24].  $\epsilon_0$  is the vacuum permittivity. The tiny metal electrodes are not simulated in this study.

Parameter	Value	Parameter	Value
<i>Thin-film aluminum nitride, AlN</i> [15,25]			
$\rho$	3300 kg m <sup>-3</sup>	$\Gamma_{\text{sl}}$	0.0005
$C_{11}$	410.2 GPa	$C_{33}$	385.0 GPa
$C_{12}$	142.4 GPa	$C_{44}$	122.9 GPa
$C_{13}$	110.1 GPa	$C_{66}$	133.9 GPa
$e_{31,f}$	-1.05 C m <sup>-2</sup>	$e_{15}$	-0.39 C m <sup>-2</sup>
$e_{33}$	1.46 C m <sup>-2</sup>	$\Gamma_{\varepsilon}(f)$	-[(1.43 MHz + 0.98f)/1 GHz]
$\epsilon_{11}$	9.2 $\epsilon_0$	$\epsilon_{33}$	10.1 $\epsilon_0$
<i>SLS float-glass substrate</i> [19]			
$\rho$	(2522 ± 15) kg m <sup>-3</sup>	(Measured at EPFL)	
$E$	(70 ± 2) GPa	$s$	0.23 ± 0.01
$C_{11}$	81.1 GPa	$C_{44}$	28.4 GPa
$c_{\text{lo}} = \sqrt{C_{11}/\rho}$	5672 m s <sup>-1</sup>	$C_{12}$	24.2 GPa
$c_{\text{tr}} = \sqrt{C_{44}/\rho}$	3359 m s <sup>-1</sup>	$\Gamma_{\text{sl}}(f)$	$f^{-1}$ 0.018 MHz

## V. MODELING AND NUMERICAL SIMULATION

We want to compare the experimental results for the impedance spectra and resonance frequencies with a numerical simulation. We therefore use the three-dimensional model for acoustofluidic systems recently developed by Skov *et al.* [23]. This model couples the mechanical displacement field  $\mathbf{u}$  and the electric potential  $\varphi$  in a system driven by a time-harmonic electric potential  $\tilde{\varphi} = \varphi_0 e^{-i\omega t}$ , with angular frequency  $\omega = 2\pi f$  and frequency  $f$ , applied to the interfaces between the metal electrodes and the piezoelectric AlN thin-film transducer. This time-harmonic boundary condition excites time-harmonic fields: the electric potential  $\tilde{\varphi}(\mathbf{r}, t)$  in the AlN thin-film transducer and the displacement  $\tilde{\mathbf{u}}(\mathbf{r}, t)$  in all solids of the system, where

$$\tilde{\varphi}(\mathbf{r}, t) = \varphi(\mathbf{r})e^{-i\omega t}, \quad \tilde{\mathbf{u}}(\mathbf{r}, t) = \mathbf{u}(\mathbf{r})e^{-i\omega t}. \quad (1)$$

Fields with a tilde are time-harmonic, whereas those without a tilde are complex-valued amplitudes.

The motion of an elastic solid with a given density  $\rho$  (in the model this is the glass, the metal electrodes, or the AlN thin-film transducer) is described by the displacement field  $\mathbf{u}$ , whereas the electrodynamics is described by the electric displacement field  $\mathbf{D}$ . The governing equations for  $\mathbf{u}$  and  $\mathbf{D}$  are Cauchy's elastodynamic equation and Maxwell's quasi-electrostatic equation,  $\nabla \cdot \mathbf{D} = 0$ :

$$-\rho\omega^2(1 + i\Gamma_{\text{sl}})\mathbf{u} = \nabla \cdot \boldsymbol{\sigma}, \quad \nabla \cdot [-(1 + i\Gamma_{\varepsilon})\boldsymbol{\varepsilon} \cdot \nabla\varphi] = 0. \quad (2)$$

Here,  $\Gamma_{sl}, \Gamma_\varepsilon \ll 1$  are weak damping coefficients,  $\boldsymbol{\varepsilon}$  is the dielectric tensor, and  $\boldsymbol{\sigma}$  is the stress tensor, which is coupled to  $\mathbf{u}$  through a stress-strain relation depending on the material-dependent elastic moduli  $C_{ik}$ .

For the isotropic glass and metal electrodes, the electric field is unimportant, whereas the relation between the stress tensor  $\sigma_{ik}$  and the strain components  $\frac{1}{2}(\partial_i u_k + \partial_k u_i)$  is given in the compact Voigt representation as

$$\begin{pmatrix} \sigma_{xx} \\ \sigma_{yy} \\ \sigma_{zz} \\ \sigma_{yz} \\ \sigma_{xz} \\ \sigma_{xy} \end{pmatrix} = \begin{pmatrix} C_{11} & C_{12} & C_{12} & 0 & 0 & 0 \\ C_{12} & C_{11} & C_{12} & 0 & 0 & 0 \\ C_{12} & C_{12} & C_{11} & 0 & 0 & 0 \\ 0 & 0 & 0 & C_{44} & 0 & 0 \\ 0 & 0 & 0 & 0 & C_{44} & 0 \\ 0 & 0 & 0 & 0 & 0 & C_{44} \end{pmatrix} \begin{pmatrix} \partial_x u_x \\ \partial_y u_y \\ \partial_z u_z \\ \partial_y u_z + \partial_z u_y \\ \partial_x u_z + \partial_z u_x \\ \partial_x u_y + \partial_y u_x \end{pmatrix}. \quad (3)$$

Here,  $C_{ik}$  are the elastic moduli, which are listed for SLS float glass in Table III, and  $C_{12} = C_{11} - 2C_{44}$ .

In the piezoelectric AlN film, the stress tensor  $\boldsymbol{\sigma}$  and the electric displacement field  $\mathbf{D}$  are given by the strain tensor  $\frac{1}{2}[\nabla \mathbf{u} + (\nabla \mathbf{u})^T]$ , the electrical field  $-\nabla \varphi$ , the electromechanical coupling coefficients  $e_{ik}$ , the elastic moduli  $C_{ik}$ , and the electric permittivities  $\varepsilon_{ik}$  as

$$\begin{pmatrix} \sigma_{xx} \\ \sigma_{yy} \\ \sigma_{zz} \\ \sigma_{yz} \\ \sigma_{xz} \\ \sigma_{xy} \\ D_x \\ D_y \\ D_z \end{pmatrix} = \begin{pmatrix} C_{11} & C_{12} & C_{13} & 0 & 0 & 0 & 0 & 0 & -e_{31} \\ C_{12} & C_{11} & C_{13} & 0 & 0 & 0 & 0 & 0 & -e_{31} \\ C_{13} & C_{13} & C_{33} & 0 & 0 & 0 & 0 & 0 & -e_{33} \\ 0 & 0 & 0 & C_{44} & 0 & 0 & 0 & -e_{15} & 0 \\ 0 & 0 & 0 & 0 & C_{44} & 0 & -e_{15} & 0 & 0 \\ 0 & 0 & 0 & 0 & 0 & C_{66} & 0 & 0 & 0 \\ 0 & 0 & 0 & 0 & e_{15} & 0 & \varepsilon_{11} & 0 & 0 \\ 0 & 0 & 0 & e_{15} & 0 & 0 & 0 & \varepsilon_{11} & 0 \\ e_{31} & e_{31} & e_{33} & 0 & 0 & 0 & 0 & 0 & \varepsilon_{33} \end{pmatrix} \begin{pmatrix} \partial_x u_x \\ \partial_y u_y \\ \partial_z u_z \\ \partial_y u_z + \partial_z u_y \\ \partial_x u_z + \partial_z u_x \\ \partial_x u_y + \partial_y u_x \\ -\partial_x \varphi \\ -\partial_y \varphi \\ -\partial_z \varphi \end{pmatrix}. \quad (4)$$

Here, the symmetry of AlN leads to  $C_{12} = C_{11} - 2C_{66}$ .

In terms of volume (mass) ratios, the device consists of 99.8% (99.5%) glass, 0.2% (0.3%) AlN film, and 0.0% (0.2%) metal electrodes. We find that within the numerical uncertainties, the simulation results are unchanged when the metal electrodes and prestress effects in the AlN film are left out. So, to reduce the memory requirements and to speed up the computation times, we leave out the prestress and the tiny metal electrodes in our modeling. Consequently, the boundary conditions for the electric potential  $\varphi$  are as follows: (1) on the interface between the bottom electrode and the AlN film, the potential is grounded,  $\varphi = 0$ ; (2) on the interface between one half of the split electrode and the AlN film,  $\varphi = +\frac{1}{2}V_0$ ; (3) on the interface between the other half of the split electrode and the AlN film, the potential is in antiphase,  $\varphi = -\frac{1}{2}V_0$ ; (4) on the side walls of the AlN film, with normal vector  $\mathbf{n}$ , the no-free-charge condition applies,  $\mathbf{n} \cdot \nabla \varphi = 0$ . For the mechanical displacement field in the solids, a nonstress condition is applied to all external surfaces,  $\mathbf{n} \cdot \boldsymbol{\sigma} = \mathbf{0}$ .

Once a solution for  $\mathbf{u}$  and  $\varphi$  is obtained, the electrical impedance  $Z$  can be computed in the model as the ratio of the total voltage drop  $V_0$  to the integral over the electrical

current density  $\mathbf{J}$  through the surface  $\partial\Omega_{1/2}$  of one of the halves of the split electrode:

$$Z = \frac{V_0}{I} = \frac{V_0}{\int_{\partial\Omega_{1/2}} \mathbf{J} \cdot \mathbf{n} da}. \quad (5)$$

As there are no free charges in the system, the only contribution to the current density  $\mathbf{J}$  is the polarization current density  $\mathbf{n} \cdot \mathbf{J} = \mathbf{e}_z \cdot \mathbf{J}_{\text{pol}} = \partial_t P_z = -i\omega(D_z + \varepsilon_0 \partial_z \varphi)$ . We compute  $D_z$  from Eq. (4) and obtain, as in Ref. [26],

$$Z = \frac{(i/\omega)V_0}{\int_{\partial\Omega_{1/2}} [e_{31}(\partial_x u_x + \partial_y u_y) + e_{33}\partial_z u_z + (\varepsilon_0 - \varepsilon_{33})\partial_z \varphi] da}. \quad (6)$$

We implement the model of the AlN-thin-film-actuated glass-block devices in the finite-element-method software package COMSOL Multiphysics 5.4 [27] following the procedure described in Ref. [23]. The coupled field equation [Eq. (2)] for the elastic-solid displacement  $\mathbf{u}$  and the electric potential  $\varphi$  is implemented together with the constitutive equations [Eqs. (3) and (4)] using the weak-form

interface ‘‘PDE Weak Form.’’ Examples of COMSOL scripts with a PDE-weak-form implementation of acoustofluidics are available in Ref. [23] and as Supplemental Material in Ref. [28].

The system geometry described in Sec. II is meshed fairly coarsely because we study the low end of the spectrum, mainly  $f < 3$  MHz, where the wavelengths are larger than 1.1 mm. The mesh of the glass block is a free tetrahedral mesh with a maximum element size of 0.2 mm, whereas the AlN thin film is modeled as a swept structured mesh with three mesh layers in the thickness direction and the same element size along the surface as for the glass. We use quadratic Lagrangian test functions and the mesh convergence test described in Ref. [29] to verify that the numerical resolution is satisfactory.

We use an adaptive-step-size algorithm to compute the impedance spectra. Close to a resonance peak, the step size goes down to 15 Hz, but far from resonance peaks, it increases to 1600 Hz. The resonance frequency is determined as the position of the maximum of a Lorentzian fit containing the 11 closest points. A typical short 0.1–3-MHz spectrum contains 450–500 points, whereas a long 0.1–10-MHz spectrum contains 2500–2800 points. A short and a long spectrum take around 0 h 40 min and 2 h 50 min, respectively, to compute on our HP-G4 workstation with a 3.7-GHz Intel Core i9 7960X-2.8 16-core processor and a memory of 128 GB RAM.

The spatial form of the acoustic mode corresponding to a given simulated resonance peak is revealed by plotting the displacement field  $|\mathbf{u}|$ . In the Supplemental Material [30], movies of each of the 45 resonance peaks  $(k, n)$  listed in Table II are presented.

## VI. COMPARING SIMULATION WITH EXPERIMENTAL RESULTS

We use the numerical model of Sec. V to simulate electrical-impedance spectra  $Z^{\text{sim}}(f)$  through Eq. (6). In the following, we compare these simulation results with the experimental spectra  $Z^{\text{exp}}(f)$  described in Sec. IV.

Two examples of such a comparison in the frequency range from 0.1 to 3 MHz are seen in Figs. 4(a) and 4(b) for device geometries 2 and 8, respectively, where we plot the resistive part  $\text{Re}[Z]$  of the electrical impedance as an alternative way to reveal the resonance peaks, instead of using the phase spectra  $\theta(f)$  as in Figs. 3(c) and 3(d). The single red curve in each plot shows the simulation results obtained with the parameter values listed in Table III, whereas the family of gray curves shows the experimental results for all available devices with the relevant geometry. It is seen that the experimental impedance spectra are reproduced fairly well by the simulation regarding the positions of the resonance peaks and their relative heights. We note that, similarly to Fig. 3, the off-resonance levels of the experimental curves (gray) for the real part  $\text{Re}[Z]$

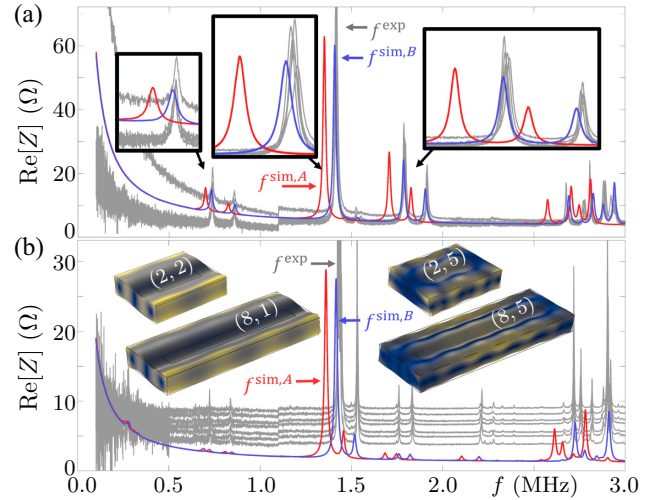


FIG. 4. (a) Resistive real part  $\text{Re}[Z]$  of the impedance as a function of frequency  $f$  measured for the five devices C2–G2 of Fig. 3(d) (gray curves,  $f^{\text{exp}}$ ), and simulated numerically using the parameter values from the literature listed in Table III (red curve,  $f^{\text{sim,A}}$ ) and using the fitted parameter values listed in Table IV (blue curve,  $f^{\text{sim,B}}$ ). (b) Similar plot of  $\text{Re}[Z]$  versus  $f$ , but for the seven devices A8–G8 of Fig. 3(c). The insets are color plots of the displacement field  $|\mathbf{u}|$  for four selected resonance peaks  $(k, n)$  from 0 (blue) to maximum (yellow). Movies of the modes of all the simulated resonance peaks in Table II are given in the Supplemental Material [30].

coincide for the devices C2–G2 in Fig. 4(a), which are discharged, while they are displaced for the devices A8–G8 in Fig. 4(b), which are not discharged. Moreover, we note that in Fig. 4(a), we fit the off-resonance level in the numerical model for  $Z$  in Eq. (6) using  $\Gamma_\varepsilon(f)$  given in Table III.

The agreement between the experiments and simulations is quantified in Table II, where it is seen that for the 173 resonance peaks in our study, the relative deviation  $\Delta_{k,n}^A$  of each simulated resonance frequency  $f_{k,n}^{\text{sim,A}}$  deviates by only a few percent from the experimental value  $f_{k,n}^{\text{exp}}$ . The mean value and the standard deviation of the mean value of all relative deviations  $\Delta_{k,n}^A$  are  $(-4.6 \pm 0.1)\%$ , which is a fairly good result. However, the simulation results show a statistically significant systematic underestimate of the resonance frequency. This is also clear from the insets in Fig. 4(a) showing enlargements of four resonance peaks: in all cases, the measured (gray) peaks for the seven nominally identical devices fall on top of each other, with variations much smaller than the peak width, whereas, in contrast, the simulated (red) peaks are shifted downward in frequency by a few peak widths.

This systematic shift of the simulated resonance peaks leads us to investigate whether a fitting of the two most significant but not so accurately determined material parameters, the Young’s modulus  $E$  and Poisson’s ratio  $s$  of the SLS float-glass substrate, could lead to better numerical

TABLE IV. Fitted values for Young's modulus  $E'$ , Poisson's ratio  $s'$ , and the damping coefficient  $\Gamma_{sl}$  of SLS float glass for improving the agreement between the experiments and simulations. The values of  $C'_{11}$ ,  $C'_{12}$ ,  $C'_{44}$ ,  $c'_{tr}$ , and  $c'_{lo}$  are functions of  $E'$  and  $s'$  [33].

Parameter	Value	Parameter	Value
$E'$	$(76 \pm 1)$ GPa	$s'$	$(0.21 \pm 0.01)$
$C'_{11}$	85.5 GPa	$C'_{44}$	31.4 GPa
$C'_{12}$	22.7 GPa	$\Gamma_{sl}(f)$	$f^{-1}$ 0.018 MHz
$c'_{lo} = \sqrt{C'_{11}/\rho}$	5824 m s <sup>-1</sup>	$c'_{tr} = \sqrt{C'_{44}/\rho}$	3529 m s <sup>-1</sup>

agreement with the experiments. Indeed, by using a simple stepping procedure, we find that such an improvement is obtained with the substitution

$$E = 70 \text{ GPa} \xrightarrow{\text{fit}} (76 \pm 1) \text{ GPa}, \quad s = 0.23 \xrightarrow{\text{fit}} 0.21 \pm 0.01. \quad (7)$$

This procedure extends the methods for obtaining the electromechanical coefficients of piezoelectric transducers [31,32] to determining the elastic coefficients of any elastic solid driven by vanishingly small thin-film transducers. The parameter values obtained for the best fitting to the experimental data are summarized in Table IV, and the resonance frequencies obtained from the simulation based on these values are denoted by  $f_{k,n}^{\text{sim,B}}$ .

The improved agreement between the simulations and experiments is seen qualitatively in Fig. 4, where the blue curves representing  $f_{k,n}^{\text{sim,B}}$  more accurately reproduce the gray experimental impedance spectra. The improved agreement is also evident from the insets in Fig. 4(a), where the blue curve  $f_{k,n}^{\text{sim,B}}$  now falls on top of the gray experimental curves to within a fraction of the peak width. Quantitatively, the improved agreement between the experiments and simulations is seen in Table II, where the relative deviation  $\Delta_{k,n}^{\text{B}}$  of each simulated resonance frequency  $f_{k,n}^{\text{sim,B}}$  deviates by less than one percent from the experimental value  $f_{k,n}^{\text{exp}}$ . The mean value and the standard deviation of the mean value of all relative deviations are  $\Delta_{k,n}^{\text{B}} = (-0.5 \pm 0.1)\%$ , or 9 times better than the first result,  $(-4.6 \pm 0.1)\%$ , obtained using the manufacturers' parameters.

The improved numerical agreement with the experiments using the fitted values of the Young's modulus and Poisson's ratio for the glass substrate suggests that our numerical-fitting simulation algorithm may be used as a starting point for developing a method for an improved *in situ* determination of acoustic parameters in the 0.1–10 MHz range, and possibly at higher frequencies. At the present stage, we do not know whether the relative deviation of roughly 5% between the literature values in Table III and the fitted values in Table IV is within the uncertainty generated by sample-to-sample variations in

the SLS float glass or whether it is a direct result of the fabrication process involving the deposition of the AlN thin-film transducers at 300 °C, which is, however, still in the specified range for stable properties of the float glass studied. The improved agreement between the simulations and experiments also suggests that using impedance measurements coupled with simulations is a promising way to investigate the resonance modes, since there is little ambiguity about which peaks are which. Also, from the measurements shown in Fig. 4, it is clear that by combining simulations with more varied device geometries it will be possible to predict particularly desired resonance frequencies with good accuracy and, consequently, to design appropriate device geometries.

## VII. CONCLUSION

We present the fabrication of 570- $\mu\text{m}$ -thick millimeter-sized SLS float-glass blocks with a 1- $\mu\text{m}$ -thick AlN thin-film piezoelectric transducer sandwiched between thin metallic electrodes and deposited on the top surface. The electromechanical properties of the devices are characterized by electrical-impedance measurements in the frequency range from 0.1 to 10 MHz with a peak-to-peak voltage of 0.5 V applied to the electrodes.

We measure the electrical-impedance spectra for 35 different device geometries, all of width 2 mm, but with nine different lengths ranging from 2 to 6 mm and with two to seven copies of each individual geometry. Each impedance spectrum exhibits many resonance peaks, and we carefully measure the five most prominent ones in each spectrum. Comparing the resulting 173 experimental resonance frequencies with the result of a finite-element-method simulation, using material parameter values from the manufacturer, results in an average relative deviation of the 173 simulated resonance frequencies from the experimental values of  $(-4.6 \pm 0.1)\%$ .

We show that by using the Young's modulus and Poisson's ratio of the SLS float glass as fitting parameters in the simulation, we can reduce the relative deviation of the 173 simulated resonance frequencies from the experimental values by a factor of 9 to  $(-0.5 \pm 0.1)\%$ . Given a more sophisticated automated fitting procedure, ideally involving more resonance peaks and devices with different electrode configurations for better excitation of other resonance modes than those obtained with the current devices, this result suggests that our numerical fitting procedure could lead to an improved method for *in situ* determination of the acoustic parameters at ultrasound frequencies of any elastic solid to which a thin-film transducer can be attached.

## ACKNOWLEDGMENTS

This work was supported by the BioWings project funded by the European Union's Horizon 2020 Future

and Emerging Technologies (FET) program, Grant No. 801267.

- [1] R. Ruby, in *2017 IEEE 30th International Conference on MicroElectro Mechanical Systems (MEMS)* (IEEE, New York, 2017), p. 308.
- [2] M. Dubois and P. Muralt, Properties of aluminum nitride thin films for piezoelectric transducers and microwave filter applications, *Appl. Phys. Lett.* **74**, 3032 (1999).
- [3] G. Piazza, P. J. Stephanou, and A. P. Pisano, Piezoelectric aluminum nitride vibrating contour-mode MEMS resonators, *J. Microelectromech. Syst.* **15**, 1406 (2006).
- [4] U. Zaghoul and G. Piazza, Highly scalable NEMS relays with stress-tuned switching voltage using piezoelectric buckling actuators, *IEEE Trans. Electron. Device* **61**, 3520 (2014).
- [5] N. Sinha, G. E. Wabiszewski, R. Mahameed, V. V. Felmetsger, S. M. Tanner, R. W. Carpick, and G. Piazza, Piezoelectric aluminum nitride nanoelectromechanical actuators, *Appl. Phys. Lett.* **95**, 053106 (2009).
- [6] A. De Pastina, D. Maillard, and L. Villanueva, Fabrication of suspended microchannel resonators with integrated piezoelectric transduction, *Microelectron. Eng.* **192**, 83 (2018).
- [7] R. H. Olsson III, K. E. Wojciechowski, M. S. Baker, M. R. Tuck, and J. G. Fleming, Post-CMOS-compatible aluminum nitride resonant MEMS accelerometers, *J. Microelectromech. Syst.* **18**, 671 (2009).
- [8] H. Zhang, W. Pang, H. Yu, and E. S. Kim, High-tone bulk acoustic resonators on sapphire, crystal quartz, fused silica, and silicon substrates, *J. Appl. Phys.* **99**, 124911 (2006).
- [9] J. Masson, G. Martin, R. Boudot, Y. Gruson, S. Ballandras, A. Artieda, P. Muralt, B. Belgacem, and L. Chomeloux, in *2007 IEEE International Frequency Control Symposium Joint with the 21st European Frequency and Time Forum* (IEEE, New York, 2007), p. 741.
- [10] T. Fujikura, O. Matsuda, D. M. Profunser, O. B. Wright, J. Masson, and S. Ballandras, Real-time imaging of acoustic waves on a bulk acoustic resonator, *Appl. Phys. Lett.* **93**, 261101 (2008).
- [11] P. Muralt, Recent progress in materials issues for piezoelectric MEMS, *J. Am. Ceram. Soc.* **91**, 1385 (2008).
- [12] K. M. Howell, W. Bashir, A. De Pastina, R. Matloub, P. Muralt, and L. G. Villanueva, Effect of AlN seed layer on crystallographic characterization of piezoelectric AlN, *J. Vac. Sci. Technol., A* **37**, 021504 (2019).
- [13] R. Matloub, A. Artieda, C. Sandu, E. Milyutin, and P. Muralt, Electromechanical properties of  $\text{Al}_{0.9}\text{Sc}_{0.1}\text{N}$  thin films evaluated at 2.5 GHz film bulk acoustic resonators, *Appl. Phys. Lett.* **99**, 092903 (2011).
- [14] R. Matloub, M. Hadad, A. Mazzalai, N. Chidambaram, G. Moulard, C. S. Sandu, T. Metzger, and P. Muralt, Piezoelectric  $\text{Al}_{1-x}\text{Sc}_x\text{N}$  thin films: A semiconductor compatible solution for mechanical energy harvesting and sensors, *Appl. Phys. Lett.* **102**, 152903 (2013).
- [15] Y. Q. Fu, J. K. Luo, N. T. Nguyen, A. J. Walton, A. J. Flewitt, X. T. Zu, Y. Li, G. McHale, A. Matthews, E. Iborra, H. Du, and W. I. Milne, Advances in piezoelectric thin films for acoustic biosensors, acoustofluidics and lab-on-chip applications, *Prog. Mater. Sci.* **89**, 31 (2017).
- [16] J.-B. Lee, D.-H. Cho, D.-Y. Kim, C.-K. Park, and J.-S. Park, Relationships between material properties of piezo-electric thin films and device characteristics of film bulk acoustic resonators, *Thin Solid Films* **516**, 475 (2007).
- [17] M. Dubois and P. Muralt, Stress and piezoelectric properties of aluminum nitride thin films deposited onto metal electrodes by pulsed direct current reactive sputtering, *J. Appl. Phys.* **89**, 6389 (2001).
- [18] C. K. Lee, F. Placido, S. Cochran, and K. J. Kirk, in *Proceedings, 2002 IEEE Ultrasonics Symposium, 2002, Vol. 2* (IEEE, New York, 2002), p. 1119.
- [19] Float glass substrates, [soda-lime-silicate glass:  $\text{SiO}_2$  (70.8%),  $\text{Na}_2\text{O}$  (13.9%),  $\text{CaO}$  (8.4%),  $\text{MgO}$  (4.4%),  $\text{Al}_2\text{O}_3$  (1.5%),  $\text{K}_2\text{O}$  (0.4%),  $\text{SO}_3$  (0.3%),  $\text{Fe}_2\text{O}_3$  (0.08%)], SCHOTT, SCHOTT Suisse SA, 2 Rue Galilée, Yverdon, Switzerland, [https://www.epfl.ch/research/facilities/cmi/wp-content/uploads/2020/05/float\\_glass.pdf](https://www.epfl.ch/research/facilities/cmi/wp-content/uploads/2020/05/float_glass.pdf) (accessed 16 November 2020).
- [20] A. Migliori, J. Sarrao, W. Visscher, T. Bell, M. Lei, Z. Fisk, and R. Leisure, Resonant ultrasound spectroscopic techniques for measurement of the elastic-moduli of solids, *Physica B* **183**, 1 (1993).
- [21] M. Radovic, E. Lara-Curzio, and L. Riester, Comparison of different experimental techniques for determination of elastic properties of solids, *Mater. Sci. Eng. A-Struct.* **368**, 56 (2004).
- [22] A. Cachiaras, L. Gilde, J. Swab, P. Patel, and G. Quinn, Soda-lime-silicate float glass: A property comparison, US Army Research Laboratory, ARL, Aberdeen Proving Ground, MD 21005-5069, USA (2017), <https://www.researchgate.net/publication/320871872> (accessed 16 November 2020).
- [23] N. R. Skov, J. S. Bach, B. G. Winkelmann, and H. Bruus, 3D modeling of acoustofluidics in a liquid-filled cavity including streaming, viscous boundary layers, surrounding solids, and a piezoelectric transducer, *AIMS Math.* **4**, 99 (2019).
- [24] P. Muralt, J. Conde, A. Artieda, F. Martin, and M. Cantoni, Piezoelectric materials parameters for piezoelectric thin films in GHz applications, *Int. J. Microw. Wirel. Technol.* **1**, 19 (2009).
- [25] M. A. Caro, S. Zhang, T. Riekkinen, M. Ylilampi, M. A. Moram, O. Lopez-Acevedo, J. Molarius, and T. Laurila, Piezoelectric coefficients and spontaneous polarization of  $\text{ScAlN}$ , *J. Phys.-Condens. Matter* **27**, 245901 (2015).
- [26] N. R. Skov, P. Sehgal, B. J. Kirby, and H. Bruus, Three-Dimensional Numerical Modeling of Surface-Acoustic-Wave Devices: Acoustophoresis of Micro- and Nanoparticles Including Streaming, *Phys. Rev. Appl.* **12**, 044028 (2019).
- [27] COMSOL Multiphysics 5.4 (2018), <http://www.comsol.com>.
- [28] P. B. Muller and H. Bruus, Theoretical study of time-dependent, ultrasound-induced acoustic streaming in microchannels, *Phys. Rev. E* **92**, 063018 (2015).

- [29] P. B. Muller, R. Barnkob, M. J. H. Jensen, and H. Bruus, A numerical study of microparticle acoustophoresis driven by acoustic radiation forces and streaming-induced drag forces, *Lab Chip* **12**, 4617 (2012).
- [30] See Supplemental Material at <http://link.aps.org/supplemental/10.1103/PhysRevApplied.16.014014> for movies of the time-dependent displacement field  $|\mathbf{u}|$  for each of the 45 resonance peaks  $(k, n)$  listed in column  $f_{k,n}^{\text{sim, B}}$  of Table II.
- [31] T. Lahmer, M. Kaltenbacher, B. Kaltenbacher, R. Lerch, and E. Leder, FEM-based determination of real and complex elastic, dielectric, and piezoelectric moduli in piezoceramic materials, *IEEE Trans. Ultrason. Ferroelectr. Freq. Control* **55**, 465 (2008).
- [32] C. Y. Kiyono, N. Perez, and E. C. N. Silva, Determination of full piezoelectric complex parameters using gradient-based optimization algorithm, *Smart Mater. Struct.* **25**, 025019 (2016).
- [33] J. T. Karlsen and H. Bruus, Forces acting on a small particle in an acoustical field in a thermoviscous fluid, *Phys. Rev. E* **92**, 043010 (2015).



## 5.2 Paper II: J. Acoust. Soc. Amer. 150, 634-645 (2021)

*Numerical study of bulk acoustofluidic devices driven by thin-film transducers and whole-system resonance modes.* [1]

As well as supplemental material:

*Supplementary material: Numerical study of bulk acoustofluidic devices driven by thin-film transducers and whole-system resonance modes.*

**DOI:** [10.1121/10.0005624](https://doi.org/10.1121/10.0005624)

**Authors:** [André G. Steckel](#) and Henrik Bruus.

**Journal:** Journal of the Acoustical Society of America, **150**, 634-645 (2021)

# Numerical study of bulk acoustofluidic devices driven by thin-film transducers and whole-system resonance modes<sup>a)</sup>

André G. Steckel and Henrik Bruus<sup>b)</sup>

Department of Physics, Technical University of Denmark, DTU Physics Building 309, DK-2800 Kongens Lyngby, Denmark

## ABSTRACT:

In bulk acoustofluidic devices, acoustic resonance modes for fluid and microparticle handling are traditionally excited by bulk piezoelectric (PZE) transducers. In this work, it is demonstrated by numerical simulations in three dimensions that integrated PZE thin-film transducers, constituting less than 0.1% of the bulk device, work equally well. The simulations are performed using a well-tested and experimentally validated numerical model. A water-filled straight channel embedded in a mm-sized bulk glass chip with a 1- $\mu\text{m}$ -thick thin-film transducer made of  $\text{Al}_{0.6}\text{Sc}_{0.4}\text{N}$  is presented as a proof-of-concept example. The acoustic energy, radiation force, and microparticle focusing times are computed and shown to be comparable to those of a conventional bulk silicon-glass device actuated by a bulk lead-zirconate-titanate transducer. The ability of thin-film transducers to create the desired acoustofluidic effects in bulk acoustofluidic devices relies on three physical aspects: the in-plane-expansion of the thin-film transducer under the applied orthogonal electric field, the acoustic whole-system resonance of the device, and the high  $Q$ -factor of the elastic solid, constituting the bulk part of the device. Consequently, the thin-film device is remarkably insensitive to the  $Q$ -factor and resonance properties of the thin-film transducer.

© 2021 Author(s). All article content, except where otherwise noted, is licensed under a Creative Commons Attribution (CC BY) license (<http://creativecommons.org/licenses/by/4.0/>). <https://doi.org/10.1121/10.0005624>

(Received 30 January 2021; revised 16 June 2021; accepted 24 June 2021; published online 29 July 2021)

[Editor: Kedar Chitale]

Pages: 634–645

## I. INTRODUCTION

An increasing number of microscale ultrasound acoustofluidic devices are used for applications within clinical diagnostics, biology, and forensic sciences.<sup>1–5</sup> Examples include but are not limited to rapid sepsis diagnostics by detection of bacteria in blood,<sup>6</sup> enrichment of prostate cancer cells in blood,<sup>7</sup> high-throughput cytometry and multiple-cell handling,<sup>8,9</sup> cell synchronization,<sup>10</sup> single-cell patterning and manipulation,<sup>11,12</sup> and size-independent sorting of cells.<sup>13</sup> Furthermore, acoustofluidics has been used for massively parallel force microscopy on biomolecules,<sup>14</sup> acoustic tweezing,<sup>15–18</sup> and noncontact microfluidic trapping and particle enrichment.<sup>19</sup>

Most applications rely on one of two basic methods for exciting the ultrasound field. One method is based on surface acoustic waves, excited by interdigitated metallic electrodes positioned on the surface of a piezoelectric (PZE) substrate. The other method relies on bulk acoustic waves excited in liquid-filled acoustic microchannels embedded in acoustically hard bulk devices by an attached bulk transducer that makes up 10%–50% volume-per-volume (v/v) of the device<sup>20</sup> or in microchannels with a thin silicon-membrane lid driven by a lead-zirconate-titanate (PZT) thin film that makes up around 15% v/v of the actuated

membrane, which is excited while leaving the bulk part of the device inert.<sup>21</sup>

Recently, the bulk-acoustic-wave method has been extended by the concept of whole-system ultrasound resonances (WSUR) in which the resonant acoustic modes are defined by the whole system and not just the microcavities.<sup>22,23</sup> In this paper, we extend the WSUR concept by substituting the large bulk PZE transducer by a tiny PZE thin-film transducer integrated on the surface of the device and constituting less than 0.1% v/v of the resulting globally actuated device, a volume ratio 2 orders of magnitude smaller than any previous device.

Integrated thin-film PZE transducers have been used extensively for actuating electromechanical systems and are often made of aluminum nitride (AlN). Thin-film transducers made of AlN are structurally and chemically stable, have a low dielectric and mechanical loss, and are compatible with standard silicon-based complementary metal-oxide semiconductor (CMOS) microfabrication techniques. Academic applications of AlN thin-film transducers include radio-frequency (RF) filters,<sup>24</sup> suspended microchannel resonators,<sup>25</sup> contour mode resonators,<sup>26</sup> switches,<sup>27,28</sup> and accelerometers.<sup>29</sup> AlN thin films have been deposited on substrates of sapphire, crystal quartz, fused silica, and silicon,<sup>30</sup> and 30- $\mu\text{m}$ -thick Si membranes.<sup>31,32</sup> Commercially, AlN-sputtered thin films are used in thin-film bulk-wave acoustic resonator filters.<sup>33</sup> However, hitherto thin-film transducers have not yet been applied in generic MHz bulk

<sup>a)</sup>This paper is part of a special issue on Theory and Applications of Acoustofluidics.

<sup>b)</sup>Electronic mail: bruus@fysik.dtu.dk, ORCID: 0000-0001-5827-2939.

acoustofluidic devices other than the aforementioned specialized silicon-membrane device.<sup>21</sup>

In this paper, based on a well-tested and experimentally validated numerical model,<sup>23,34,35</sup> we demonstrate by three-dimensional (3D) numerical simulations that generic bulk glass chips with integrated PZE thin-film transducers constituting less than 0.1% v/v of the system, as sketched in Fig. 1, form devices with an acoustofluidic response on par with that obtained in a conventional silicon-glass device actuated by a bulk-PZT transducer using equivalent model assumptions. This result offers several advantages for the practical application of thin-film transducers within acoustofluidics: Thin-film devices do not depend on resonance properties of the thin-film transducer itself, they require no gluing, and can be fabricated by well-controlled reproducible microfabrication techniques subject to parallel mass-fabrication processes. We use 3D modeling to capture the axial variations observed experimentally even in straight, rectangular acoustofluidic channels.<sup>36</sup>

The paper is organized as follows: In Sec. II, we briefly summarize the theory and numerical model used throughout the paper. In Sec. III, we present a proof-of-concept example showing that a thin-film acoustofluidic bulk device performs on par with a conventional bulk-transducer bulk device. In Sec. IV, we discuss the physical principle of the thin-film transduction process; robustness of the device to the material, thickness, and quality factor of the thin-film transducer; role of the shape of the thin-film-transducer electrodes, spatial regularity, and sensitivity of the device to shifts in the channel position away from exact centering in the glass chip. Finally, in Sec. V, we present our conclusions.

## II. THEORY

Throughout this work, we use the theory and numerical model developed by Skov *et al.*,<sup>34</sup> including the effective

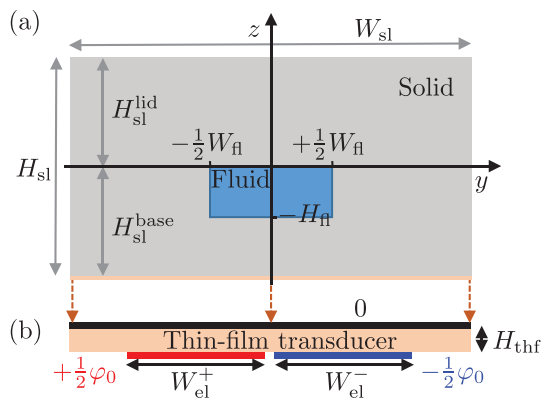


FIG. 1. (Color online) (a) A sketch of the  $yz$ -plane cross section of the long, straight thin-film driven device consisting of an elastic solid (gray) of width  $W_{sl}$  and height  $H_{sl}$ , an embedded fluid-filled microchannel (blue) of width  $W_{fl}$  and height  $H_{fl}$ , and an attached thin-film transducer (beige) of width  $W_{sl}$  and small height  $H_{thf} \approx 0.001H_{sl}$ . (b) A zoom-in on the thin-film transducer (beige) showing its grounded top electrode (black, of width  $W_{sl}$  and potential zero) and split-bottom electrode (red “+” and blue “-” of width  $W_{el}^+$  and potential  $\pm \frac{1}{2}\varphi_0$ ), made to excite the antisymmetric half-wave-like resonance mode.

boundary layer theory for the fluid domain by Bach and Bruus,<sup>37</sup> as briefly summarized in this section. This model is well-tested and experimentally validated for acoustofluidic devices,<sup>23,34,35</sup> and although it was originally stated for bulk-PZT transducers, the model is trivially extended to describe other types of PZE transducers, including thin-film transducers.

### A. Governing equations for the time-harmonic fields

We consider a time-harmonic electric potential  $\tilde{\varphi}(\mathbf{r}, t)$ , which excites the PZE transducer and induces a displacement field  $\tilde{\mathbf{u}}_1(\mathbf{r}, t)$  in the solids that, in turn, leads to an acoustic pressure  $\tilde{p}_1(\mathbf{r}, t)$  in the fluid channel. All of these fields  $\tilde{F}(\mathbf{r}, t)$  separate into a complex-valued amplitude  $F(\mathbf{r})$  and complex time-harmonic phase factor with frequency  $f$ ,

$$\tilde{F}(\mathbf{r}, t) = F(\mathbf{r}) e^{-i\omega t}, \quad \omega = 2\pi f. \quad (1)$$

The phase factor  $e^{-i\omega t}$  cancels out in the following linear governing equations, leaving just the amplitude fields.

The first-order perturbation theory implies that the acoustic pressure  $p_1$  in the fluid is governed by the Helmholtz equation with a damping coefficient  $\Gamma_{fl}$ ,<sup>34</sup>

$$\nabla^2 p_1 = -\frac{\omega^2}{c_{fl}^2} (1 + i\Gamma_{fl}) p_1, \quad \Gamma_{fl} = \left( \frac{4}{3}\eta_{fl} + \eta_{fl}^b \right) \omega \kappa_{fl}, \quad (2)$$

where  $c_{fl}$  is the speed of sound,  $\rho_{fl}$  is the density,  $\kappa_{fl} = (\rho_{fl} c_{fl}^2)^{-1}$  is the isentropic compressibility, and  $\eta_{fl}$  and  $\eta_{fl}^b$  are the dynamic and bulk viscosity of the fluid, respectively; see Table S1 in the supplementary material.<sup>38</sup> The pressure gradient governs the acoustic fluid velocity  $\mathbf{v}_1^{fl}$ ,

$$\mathbf{v}_1^{fl} = -i \frac{1 - i\Gamma_{fl}}{\omega \rho_{fl}} \nabla p_1. \quad (3)$$

For the linear PZE transducer (of either  $Al_{1-x}Sc_xN$ ,  $AlN$ , or  $PZT$ ), the electrical potential  $\varphi$  is governed by Gauss’s law for a linear dielectric without free charges,<sup>34</sup>

$$\nabla \cdot \mathbf{D} = 0, \quad (4)$$

where  $\mathbf{D}$  is the electric displacement field, including a purely electric part  $-(1 + i\Gamma_\varepsilon)\boldsymbol{\varepsilon} \cdot \nabla\varphi$ , in which  $\Gamma_\varepsilon$  is a small damping coefficient, and  $\boldsymbol{\varepsilon}$  is the dielectric tensor. The governing equation for the mechanical displacement field  $\mathbf{u}_1$  in a linear elastic solid (including the PZE) with density  $\rho_{sl}$  is the weakly damped Cauchy equation,<sup>34,39</sup>

$$-(1 + i\Gamma_{sl})\rho_{sl}\omega^2 \mathbf{u}_1 = \nabla \cdot \boldsymbol{\sigma}_{sl}, \quad (5)$$

where  $\Gamma_{sl}$  is a small damping coefficient. Using the Voigt notation, the linear electromechanical coupling in the PZE, which relates the stress and electric displacement to the strain and electric field, is given by

$$\begin{pmatrix} \sigma_{xx} \\ \sigma_{yy} \\ \sigma_{zz} \\ \sigma_{yz} \\ \sigma_{xz} \\ \sigma_{xy} \\ D_x \\ D_y \\ D_z \end{pmatrix} = \begin{pmatrix} C_{11} & C_{12} & C_{13} & 0 & 0 & 0 & 0 & 0 & -e_{31} \\ C_{12} & C_{11} & C_{13} & 0 & 0 & 0 & 0 & 0 & -e_{31} \\ C_{13} & C_{13} & C_{33} & 0 & 0 & 0 & 0 & 0 & -e_{33} \\ \hline 0 & 0 & 0 & C_{44} & 0 & 0 & 0 & -e_{15} & 0 \\ 0 & 0 & 0 & 0 & C_{44} & 0 & -e_{15} & 0 & 0 \\ 0 & 0 & 0 & 0 & 0 & C_{66} & 0 & 0 & 0 \\ \hline 0 & 0 & 0 & 0 & e_{15} & 0 & \varepsilon_{11} & 0 & 0 \\ 0 & 0 & 0 & e_{15} & 0 & 0 & 0 & \varepsilon_{11} & 0 \\ e_{31} & e_{31} & e_{33} & 0 & 0 & 0 & 0 & 0 & \varepsilon_{33} \end{pmatrix} \begin{pmatrix} \partial_x u_x \\ \partial_y u_y \\ \partial_z u_z \\ \partial_y u_z + \partial_z u_y \\ \partial_x u_z + \partial_z u_x \\ \partial_x u_y + \partial_y u_x \\ -\partial_x \varphi \\ -\partial_y \varphi \\ -\partial_z \varphi \end{pmatrix}. \quad (6)$$

The remaining three components of the stress tensor are given by the symmetry relation  $\sigma_{ik} = \sigma_{ki}$ . Similarly, the Cauchy equation (5) governs  $\mathbf{u}_1$  in a purely elastic solid, but now the stress-strain relation (6) includes only the first six rows and first six columns as  $\mathbf{D}$  and  $\varphi$  do not couple to  $\boldsymbol{\sigma}_{sl}$  and  $\mathbf{u}_1$ . The parameter values are listed in Table SII of the supplementary material.<sup>38</sup>

### B. Governing equations for the steady time-averaged fields

The nonlinearity of the governing equations results in higher order responses to the time-harmonic actuation. Here, we are only interested in the steady time-averaged second-order response and define  $F_2(\mathbf{r}) = \langle \tilde{F}_2(\mathbf{r}, t) \rangle = (\omega/2\pi) \int_0^{2\pi/\omega} \tilde{F}_2(\mathbf{r}, t) dt$ . A time-average of a product of two first-order fields is also a second-order term, which is written as  $\langle \text{Re}[\tilde{A}_1(t)] \text{Re}[\tilde{B}_1(t)] \rangle = \frac{1}{2} \text{Re}[A_1 B_1^*]$ , where the asterisk denotes complex conjugation. The acoustic streaming  $\mathbf{v}_2$  is such a time-averaged field. It is a steady-state, incompressible Stokes flow driven by the slip velocity stated in Sec. II C and time-averaged acoustic dissipation body force proportional to  $\Gamma_{fl}$ ,<sup>37</sup>

$$\eta_{fl} \nabla^2 \mathbf{v}_2 = \nabla p_2 - \frac{\Gamma_{fl} \omega}{2c_{fl}^2} \text{Re}[p_1^* \mathbf{v}_1^{\text{fl}}], \quad \nabla \cdot \mathbf{v}_2 = 0. \quad (7)$$

The spatial average  $E_{ac}^{\text{fl}}$  of the time-averaged acoustic energy density in the fluid volume  $V_{fl}$  is given as the sum of the kinetic and compressional energy densities,

$$E_{ac}^{\text{fl}} = \frac{1}{V_{fl}} \int_{V_{fl}} \left[ \frac{1}{4} \rho_{fl} |\mathbf{v}_1^{\text{fl}}|^2 + \frac{1}{4} \kappa_{fl} |p_1|^2 \right] dV, \quad (8)$$

where  $\rho_{fl}$  and  $\kappa_{fl}$  are the fluid density and compressibility, respectively.

The acoustic radiation force  $\mathbf{F}^{\text{rad}}$  acting on a single particle with radius  $a$ , density  $\rho_{ps}$ , and compressibility  $\kappa_{ps}$  suspended in the fluid is minus the gradient of the acoustic potential  $U^{\text{rad}}$ ,<sup>40,41</sup>

$$\mathbf{F}^{\text{rad}} = -\nabla U^{\text{rad}}, \quad (9a)$$

$$U^{\text{rad}} = \pi a^3 \left( \frac{1}{3} f_0 \kappa_{fl} |p_1|^2 - \frac{1}{2} f_1 \rho_{fl} |\mathbf{v}_1^{\text{fl}}|^2 \right), \quad (9b)$$

$$f_0 = 1 - \frac{\kappa_{ps}}{\kappa_{fl}}, \quad f_1 = \frac{2(\rho_{ps} - \rho_{fl})}{2\rho_{ps} + \rho_{fl}}, \quad (9c)$$

where  $f_0$  and  $f_1$  are the so-called acoustic monopole and dipole scattering coefficients, respectively.

To further quantify the quality of the acoustophoretic response in the fluid volume  $V_{fl}$  of a standing half-wave-like pressure wave, which by  $\mathbf{F}^{\text{rad}}$  focuses microparticles in the vertical nodal plane  $y=0$ , we use the figure of merit  $R$  in  $V_{fl}$ , introduced by Moiseyenko and Bruus,<sup>22</sup>

$$R = \frac{\int_{V_{fl}} -\text{sign}(y) F_y^{\text{rad}} dV}{\int_{V_{fl}} |F_z^{\text{rad}}| dV}. \quad (10)$$

$R$  is large when the focusing force  $-\text{sign}(y) F_y^{\text{rad}}$  with the appropriate sign is large and the magnitude  $|F_z^{\text{rad}}|$  of the vertical force is small. Essentially,  $R$  expresses how many times larger the average horizontal focusing force component is compared to the vertical focusing force component.

Another quantitative measure is the time  $t_{\text{foc}}$  it takes, on average, after turning on the acoustic field to focus by acoustophoresis a dilute suspension of microparticles of radius  $a$  into the narrow region  $|y| < 8a$ , centered around the vertical nodal plane  $y=0$  from their initial positions. We consider  $N$  particles that start from the evenly distributed positions  $\mathbf{r}_i$ ,  $i = 1, 2, \dots, N$ , outside of the narrow region. The equation of motion for a single particle with velocity  $\mathbf{v}_p$  suspended in a fluid with a streaming velocity  $\mathbf{v}_2$  is the force balance between the Stokes drag force and acoustic radiation force,  $\mathbf{v}_p(\mathbf{r}) = \mathbf{v}_2(\mathbf{r}) + (1/6\pi\eta_{fl}a) \mathbf{F}^{\text{rad}}(\mathbf{r})$ .<sup>42</sup> The time,  $t_{fi}$ , when a given particle reaches the narrow region,  $|y_f| = 8a$ , is found by numerical integration of the trajectory as detailed in the

supplementary material.<sup>38</sup> The average focus time for the homogeneous particle distribution is, therefore, defined by

$$t_{\text{foc}} = \frac{1}{N} \sum_{i=1}^N t_{fi}. \quad (11)$$

Quantitatively, for a given actuation voltage, a good acoustophoretic resonance mode is characterized by having a large  $E_{\text{ac}}$ , large  $R$ , and small  $t_{\text{foc}}$ .

### C. Boundary conditions fluids, solids, and PZE

The boundary conditions of the fields on all boundaries and interfaces of the model are specified as follows. On the surfaces facing the surrounding air, we assume zero stress on the solid and PZE as well as zero free surface charge density on the PZE. On the surfaces with electrodes, the PZE has a specified alternating current (ac)-voltage amplitude. On the internal solid-PZE and solid-fluid surfaces, the stress and displacement are continuous except for the latter in the form of the effective boundary conditions derived by Bach and Bruus.<sup>37</sup> These boundary conditions include, analytically, the shallow viscous boundary layer of thickness  $\delta_{\text{fl}} = \sqrt{2\eta_{\text{fl}}/(\rho_{\text{fl}}\omega)} \approx 0.5 \mu\text{m}$ , which, therefore, does not need to be resolved numerically, the complex-valued shear-wave number  $k_s = (1 + i)\delta_{\text{fl}}^{-1}$  of the fluid (fl), and the velocity  $\mathbf{v}_1^{\text{sl}} = -i\omega\mathbf{u}_1$  of the solid (sl),

$$\text{sl-air} : \quad \boldsymbol{\sigma}_{\text{sl}} \cdot \mathbf{n} = \mathbf{0}, \quad \mathbf{n} \text{ is the surface normal}, \quad (12a)$$

$$\text{sl-fl} : \quad \boldsymbol{\sigma}_{\text{sl}} \cdot \mathbf{n} = -p_1 \mathbf{n} + ik_s \eta_{\text{fl}} (\mathbf{v}_1^{\text{sl}} - \mathbf{v}_1^{\text{fl}}), \quad (12b)$$

$$\mathbf{v}_1 \cdot \mathbf{n} = \mathbf{v}_{\text{sl}} \cdot \mathbf{n} + \frac{i}{k_s} \nabla_{\parallel} \cdot (\mathbf{v}_{\text{sl}} - \mathbf{v}_1)_{\parallel} \quad (12c)$$

$$\text{PZE-air} : \quad \mathbf{D} \cdot \mathbf{n} = \mathbf{0}, \quad (12d)$$

$$\text{top elec.} : \quad \varphi = 0, \quad (12e)$$

$$\text{bot elec.} : \quad \varphi = \pm \frac{1}{2} \varphi_0. \quad (12f)$$

Further, at fluid–solid interfaces, the slip velocity  $\mathbf{v}_2^{\text{bc}}$ , driving the streaming, takes into account both the motion of the surrounding elastic solid and Reynolds stress induced in a viscous boundary layer in the fluid,<sup>37</sup>

$$\mathbf{v}_2 = \mathbf{v}_2^{\text{bc}}, \quad \mathbf{n} \cdot \mathbf{v}_2^{\text{bc}} = 0, \quad (13a)$$

$$\begin{aligned} (\mathbf{1} - \mathbf{nn}) \cdot \mathbf{v}_2^{\text{bc}} = & -\frac{1}{8\omega} \nabla_{\parallel} |\mathbf{v}_{1\parallel}^{\text{fl}}|^2 \\ & - \text{Re} \left[ \left( \frac{2-i}{4\omega} \nabla_{\parallel} \cdot \mathbf{v}_{1\parallel}^{\text{fl}*} + \frac{i}{2\omega} \partial_{\perp} v_{1\perp}^{\text{fl}*} \right) \mathbf{v}_{1\parallel}^{\text{fl}} \right], \end{aligned} \quad (13b)$$

where the subscript “ $\parallel$ ” indicates the derivative or vector components parallel to the surface and, likewise, “ $\perp$ ” indicates the perpendicular components. Equation (13) is the special case of the slip velocity  $\mathbf{v}_2^{\text{bc}}$ , which is only valid near the acoustic resonance, where  $|\mathbf{v}_1^{\text{fl}}|$  in the bulk is much larger than  $|\mathbf{v}_1^{\text{sl}}|$  of the walls at the fluid–solid interface.

Finally, we use the symmetry at the  $yz$ - and  $xz$ -planes to reduce the model to one-quarter the size in the domain  $x > 0$  and  $y > 0$ , allowing for finer meshing and/or faster computations. We apply the symmetric boundary conditions at the  $yz$ -plane  $x = 0$  and anti-symmetry at the  $xz$ -plane  $y = 0$  for the first-order fields and symmetric boundary conditions at both planes for the second-order fields,

$$\text{Symmetry, } x = 0 : \quad (14a)$$

$$\partial_x \varphi = 0, \quad \partial_x p_1 = 0, \quad \partial_x p_2 = 0,$$

$$v_{1,x}^{\text{sl}} = 0, \quad \partial_x v_{1,y}^{\text{sl}} = 0, \quad \partial_x v_{1,z}^{\text{sl}} = 0, \quad (14b)$$

$$v_{2,x}^{\text{fl}} = 0, \quad \partial_x v_{2,y}^{\text{fl}} = 0, \quad \partial_x v_{2,z}^{\text{fl}} = 0, \quad (14c)$$

$$\text{Anti-symmetry, } y = 0 : \quad (14d)$$

$$\varphi = 0, \quad p_1 = 0, \quad \partial_y p_2 = 0,$$

$$v_{1,x}^{\text{sl}} = 0, \quad \partial_y v_{1,y}^{\text{sl}} = 0, \quad v_{1,z}^{\text{sl}} = 0, \quad (14e)$$

$$\partial_y v_{2,x}^{\text{fl}} = 0, \quad v_{2,y}^{\text{fl}} = 0, \quad \partial_y v_{2,z}^{\text{fl}} = 0. \quad (14f)$$

## III. MAIN RESULTS COMPARING A THIN-FILM AND A BULK-TRANSDUCER DEVICE

### A. The two main model devices

As a proof of concept that a tiny thin-film transducer is able to drive a bulk acoustofluidic device as well as a conventional bulk transducer, we study the two devices shown in Figs. 2(a) and 2(c), which both contain a water-filled microchannel of length  $L_{\text{fl}} = 35 \text{ mm}$ , width  $W_{\text{fl}} = 0.377 \text{ mm}$ , and height  $H_{\text{fl}} = 0.157 \text{ mm}$ , chosen as a typical channel size used in the literature<sup>1</sup> and specifically studied experimentally and theoretical in Ref. 43. We emphasize that both devices are simulated on equal footing using the same model approach with the same assumptions on damping and lack of clamping. Also, both devices are made of acoustically hard materials with high acoustic impedances relative to water, namely, 13.2 for silicon and 8.4 for glass.

The thin-film device consists of a rectangular glass block of  $L_{\text{gl}} = 40 \text{ mm}$ , width  $W_{\text{gl}} = 3.02 \text{ mm}$ , and height  $H_{\text{gl}} = 1.4 \text{ mm}$ . An  $\text{Al}_{0.6}\text{Sc}_{0.4}\text{N}$  thin-film transducer of length  $L_{\text{thf}} = L_{\text{gl}}$ , width  $W_{\text{thf}} = W_{\text{gl}}$ , and height  $H_{\text{thf}} = 1 \mu\text{m}$  is deposited on the bottom surface of the  $xy$ -plane, thus, occupying only 0.07% of the total device volume. To excite the half-wave-like pressure wave, an antisymmetric voltage actuation is effective<sup>23</sup> and made possible by splitting the bottom electrode in half by a 40- $\mu\text{m}$ -wide gap along the  $x$  axis. The microchannel is centered along the  $x$ - and  $y$  axes, but its top aligns with the center of the glass height  $\frac{1}{2}H_{\text{gl}}$  to mimic that the glass block consists of two glass slabs of equal height bonded together except that the microchannel is etched into the top surface of the bottom slab; see Fig. 1. This specific device is chosen because in a recent study, we successfully modeled and experimentally validated a similar thin-film-glass-block device without the microchannel.<sup>44</sup>

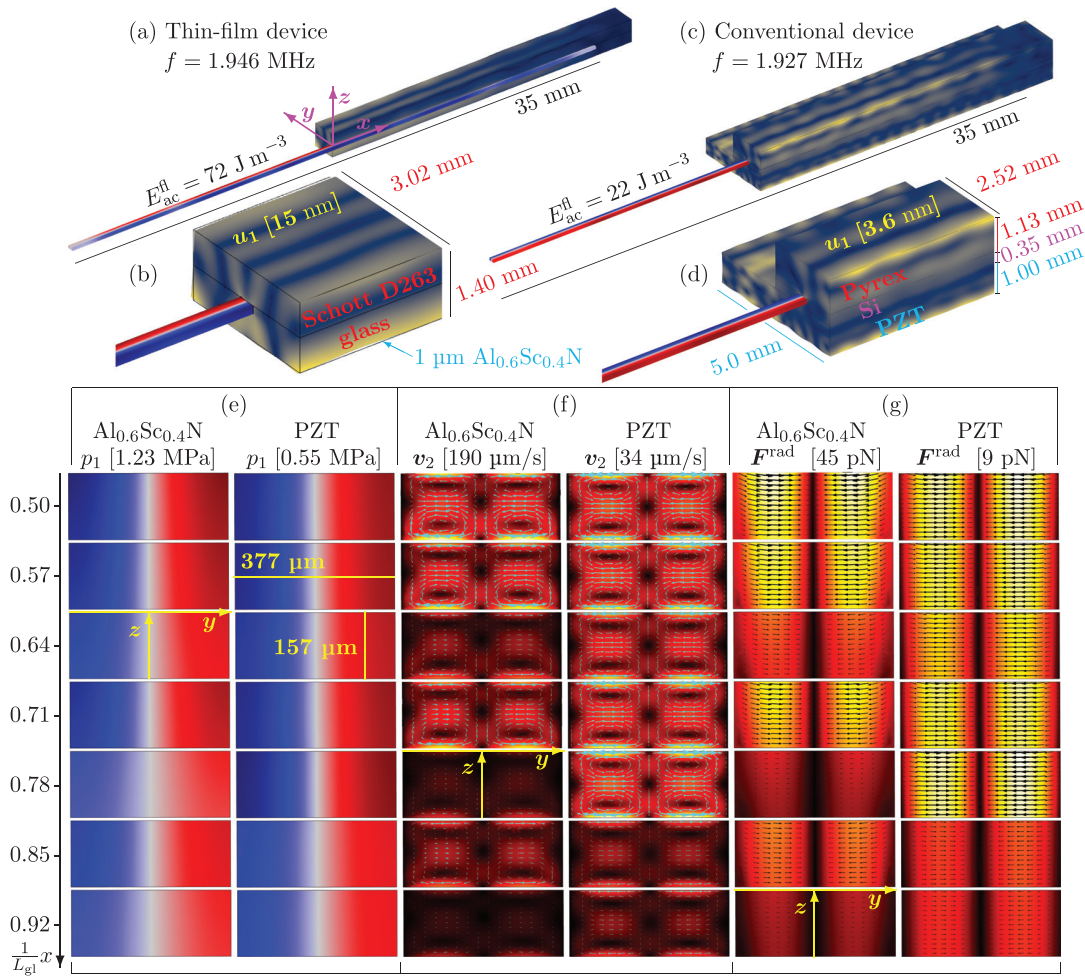


FIG. 2. (Color online) (a),(b) A bulk glass chip driven by a 1- $\mu\text{m}$ -thick  $\text{Al}_{0.6}\text{Sc}_{0.4}\text{N}$  thin-film transducer (not visible) actuated at resonance  $f = 1.946$  MHz with  $1 V_{\text{pp}}$ . The 3D color plots are  $u_1$  from 0 (blue) to 15 nm (yellow) and  $p_1$  from  $-1.23$  MPa (blue) to  $+1.23$  MPa (red). (c),(d) A conventional Si-glass chip driven by a bulk PZT actuated at resonance  $f = 1.927$  MHz with  $1 V_{\text{pp}}$ . The color plots are  $u_1$  from 0 (blue) to 3.6 nm (yellow) and  $p_1$  from  $-0.55$  MPa (blue) to  $+0.55$  MPa (red). (e) The color plots of  $p_1$  from  $-p_{\text{max}}$  (blue, value in the square bracket) to  $+p_{\text{max}}$  (red) of the  $\text{Al}_{0.6}\text{Sc}_{0.4}\text{N}$ -driven device on the left and PZT-driven device on the right in seven cross sections from  $x/L_{\text{sl}} = 0.5$  to  $0.92$  in steps of  $0.07$  are shown. (f) The color plots as in (e) but for the streaming velocity magnitude  $v_2$  from zero (black) to  $v_2^{\text{max}}$  (white, value in the square bracket) and with vectors showing  $v_2$ . (g) The color and vector plot as in (f) but for the radiation force  $F^{\text{rad}}$  from zero (black) to  $F_{\text{max}}^{\text{rad}}$  (white, value in the square bracket) for suspended 5- $\mu\text{m}$ -diameter polystyrene particles. See the animations of the modes in the supplementary material (Ref. 38).

The bulk-transducer device has been studied extensively both experimentally and numerically in the literature.<sup>36,42,43</sup> It consists of a silicon substrate of length  $L_{\text{sl}} = 40$  mm, width  $W_{\text{sl}} = 2.52$  mm, and height  $H_{\text{sl}} = 0.35$  mm into which the centered microchannel is etched and onto which is bonded a Pyrex glass lid of the same length and width but with the height  $H_{\text{py}} = 1.13$  mm. This silicon-glass chip is placed off-center on a nominal 2-MHz PZT transducer of  $L_{\text{pzt}} = 40$  mm, width  $W_{\text{pzt}} = 5$  mm, and height  $H_{\text{pzt}} = 1$  mm such that the rightmost side walls align. In the actual device, the transducer is glued to the chip, but here we neglect the glue layer and assume an ideal bonding instead. Note that the fraction of the total volume occupied by the bulk-PZT transducer is large,  $V_{\text{pzt}}/V_{\text{tot}} = 57\%$  v/v.

Using these dimensions and the material parameters listed in Tables SI and SII of the supplementary material,<sup>38</sup> we implement these two 3D device models in the commercial finite-element software COMSOL Multiphysics 5.4,<sup>45</sup> closely following the implementation method described in

Ref. 34. We use tetrahedral meshes chosen to have at least 12 nodal points per wavelength at 2 MHz in all domains (18 in the fluid domain) except in the  $z$ -direction of the thin-film, where the thickness is much smaller than the wavelength. So here, a swept mesh was used to ensure at least four nodal points. Performing a standard mesh convergence analysis,<sup>34</sup> we found deviations in the acoustofluidic responses of about 1% when comparing to the highest mesh resolution possible in our setup. We observed no changes by adding additional nodal points in the thin-film thickness direction. All simulations were run on a workstation with a 16-core processor Intel i9-7960X at 3.70 GHz boost clock and 128 GB random access memory (Intel, Santa Clara, CA).

## B. Mode analysis of the two devices

The first step in our analysis is to identify good acoustic resonance modes in the two devices, which we actuate in a

comparable manner with a peak-to-peak voltage of  $\varphi_0 = 1$  V. In the thin-film device, the voltage amplitude of the ac-voltage on the “positive” (“negative”) half of the bottom electrode is set to  $+\frac{1}{2}\varphi_0$  ( $-\frac{1}{2}\varphi_0$ ,  $180^\circ$  out of phase) relative to the grounded top electrode. Similarly, the voltage amplitude on the top electrode in the bulk-PZT device is set to  $+\frac{1}{2}\varphi_0$  relative to the grounded bottom electrode. The frequency of the actuation voltage is then swept from 0.1 to 3.5 MHz while monitoring the acoustic energy density  $E_{ac}^{fl}$ , Eq. (8), in the water. The frequency steps in the sweep are adaptive, ranging from  $\Delta f = 16$  kHz when the local curvature in  $E_{ac}^{fl}(f)$  is small (far from resonance peaks) down to  $\Delta f = 0.03$  kHz when it is large (near resonance peaks).

As expected, the strongest resonance peak in  $E_{ac}^{fl}$  happens near the hard-wall standing half-wave resonance  $f_0 = c_{fl}/2W_{wa} = 2$  MHz. This main resonance is located at  $f_{thf} = 1.946$  MHz with a maximum energy density of  $E_{ac}^{fl}(f_{thf}) = 72 \text{ J m}^{-3}$  for the thin-film device and at  $f_{pzt} = 1.927$  MHz with a  $E_{ac}^{fl}(f_{pzt}) = 22 \text{ J m}^{-3}$ . The amplitude  $p_1$  of the pressure and  $u_1$  of the displacement field for these main resonance modes in the two devices are shown in Figs. 2(a)–2(d). One immediate conclusion is that the quality of the resulting resonant pressure mode in the two devices is comparable: a nearly perfect antisymmetric wave across the channel with only weak variations along the channel. The pressure amplitude of 1.23 MPa in the thin-film device is 2.2 times larger than the 0.55-MPa amplitude in the bulk-PZT device.

When inspecting the displacement field in Figs. 2(a)–2(d), it is seen that it has a more regular mode with a larger 15-nm amplitude in the thin-film device [Figs. 2(a) and 2(b)] compared to the more complex resonance mode with a smaller 3.6-nm amplitude in the larger volume of the bulk-PZT device [Figs. 2(c) and 2(d)]. Figure 2(e) shows the pressure in seven vertical channel –cross sections, equally spaced along the channel from its center to its end, showing the abovementioned weak axial variations in  $p_1$  for both devices. Clearly on a qualitative level, the tiny 0.07% v/v thin-film transducer is seen to deliver a comparable, and perhaps even better, acoustic response in the device compared with the conventional large 57% v/v bulk-PZT transducer.

As a first rough quantitative comparison, we sample  $p_1$  in 700 equidistant points along a straight line parallel to the  $x$  axis through the edge point  $(0, \frac{1}{2}W_{fl}, -\frac{1}{2}H_{fl})$ . We find the following regression lines with standard deviations:  $p_1(x, \frac{1}{2}W_{fl}, -\frac{1}{2}H_{fl}) = (1.15 - 0.83\frac{2x}{L_{fl}} \pm 0.16)$  MPa for the thin-film and  $(0.56 - 0.23(2x/L_{fl}) \pm 0.05)$  MPa for the bulk-PZT device. The former pressure is nearly twice as large as the latter at the center  $x = 0$ , namely, 1.15 versus 0.56 MPa, but they both end at the same value at the channel end  $x = \frac{1}{2}L_{fl}$ , namely, 0.32 versus 0.33 MPa. Clearly, the pressure is higher in the thin-film device, but the pressure variations are also three times larger, namely, 0.16 versus 0.05 MPa compared to the bulk-PZT device. In the following, for further quantitative comparison, we study the acoustic radiation force  $F^{rad}$  and related focusing time  $t_{foc}$  that it

takes to focus 5- $\mu$ m-diameter particles in the vertical pressure nodal plane  $y = 0$ .

### C. The acoustic radiation force and streaming at resonance

The acoustic modes  $p_1$  and  $u_1$  are the basic fields giving rise to the steady time-averaged responses used for applications in acoustofluidic devices, namely, the acoustic streaming  $v_2$  in the fluid and the radiation force  $F^{rad}$  acting on the suspended microparticles. In Figs. 2(f) and 2(g), these responses are shown in the same seven cross sections as were used in Fig. 2(e). Being second-order responses, the amplitudes of  $v_2$  and  $F^{rad}$  become  $2.2^2 \approx 5$  larger in the thin-film than in the bulk-PZT device, where 2.2 is the aforementioned ratio in the pressure amplitudes. Similarly, the axial variations in  $v_2$  and  $F^{rad}$  are nearly five times larger in the thin-film than they are in the bulk-PZT device.

For a more complete quantitative comparison of the acoustophoretic response, we compute the acoustic energy density  $E_{ac}$  [Eq. (8)], the figure of merit  $R$  [Eq. (10)], and the focusing time  $t_{foc}$  [Eq. (11)] for suspended 5- $\mu$ m-diameter microparticles for the two main resonance modes in Fig. 2. As detailed in the supplementary material,<sup>38</sup>  $t_{foc}$  for a given mode is given by the average of the focus time of 3536 individual particle trajectories computed by numerical integration. The respective values are listed in Table I, and they support the result of the qualitative comparison of the shape of the pressure, streaming, and force fields: The time-averaged response of the  $Al_{0.6}Sc_{0.4}N$  thin-film device is comparable in terms of  $E_{ac}$ ,  $R$ , and  $t_{foc}$  to that of the bulk-PZT device. It supports the usual quadrupolar Rayleigh streaming pattern, and the radiation force points toward the vertical center plane along the axis, which can, thus, serve as a plane for particle focusing. Whereas  $R$  is  $22.7/7.1 = 3.2$  times smaller,  $E_{ac}^{fl}$  is  $72/22 = 3.3$  times larger and  $t_{foc}$  is  $1.73/0.53 = 3.3$  times faster in the thin-film device compared to the bulk-PZT device. From this first example, it is, therefore, clear that the thin-film bulk device would work as an excellent acoustofluidic device and thin-film transducers can be used on generic bulk chips without fabricating the

TABLE I. The quantitative comparison of the quality of the resonance modes of three thin-film (thf) and one bulk (bulk) device:  $Al_{0.6}Sc_{0.4}N$  (thf) and Pz26 (bulk) of Fig. 2, as well as AlN (thf) and Pz26 (thf) discussed in Sec. IV B. Listed are the resonance frequency  $f_{res}$ , the figure of merit, Eq. (10), the acoustic energy density  $E_{ac}$ , Eq. (8), and the focusing time  $t_{foc}$ , Eq. (11), for 5- $\mu$ m-diameter microparticles. See the animations of the resonance modes in the supplementary material (Ref. 38).

Response	AlN thf	$Al_{0.6}Sc_{0.4}N$ thf	Pz26 thf	Pz26 bulk
$f_{res}$ (MHz)	1.948	1.946	1.942	1.927
$R$ (-)	6.7	7.1	8.5	22.7
$E_{ac}^{fl}$ ( $\text{J m}^{-3}$ )	7.3	72	$2.1 \times 10^3$	22
$t_{foc}$ (s)	5.4	0.52	0.016	1.73
$E_{ac}^{fl} t_{foc}$ ( $\text{J s m}^{-3}$ )	39.4	37.4	34.2	38.1
$E_{ac}^{fl}/e_{31}^2 f$ ( $\text{m F}^{-1}$ ; Ref. 38)	7.0	10.3	9.9	—

delicate and expensive membrane devices.<sup>21</sup> In the following, we investigate further the physical characteristics of the thin-film bulk device.

#### IV. PHYSICAL ASPECTS OF ACOUSTOFLUIDIC BULK DEVICES DRIVEN BY THIN-FILM TRANSDUCERS

In this section, we use the numerical model to study various physical aspects of acoustofluidic devices with thin-film transducers. The study includes the physical principle of the thin-film transduction process; the robustness of the device to the material, thickness, and quality factor of the thin-film transducer; the role of the thin-film-transducer electrode shape; the spatial regularity; and the sensitivity of the device to shifts in the channel position away from the exact centering in the glass chip.

##### A. The physics of thin-film actuation of bulk devices

The ability of the thin-film transducer to create the desired acoustophoretic microparticle focusing by radiation force or mixing by acoustic streaming in a bulk acoustofluidic device relies on three physical aspects of the system: the in-plane-expansion of the thin-film transducer under the action of the orthogonal applied electric field, the acoustic whole-system resonance of the device, and the high  $Q$ -factor of the elastic solid, constituting the bulk part of the device.

Traditional bulk PZE transducers typically work by exciting a standing half-wave in the transducer thickness direction, which is also the direction of both the polarization and applied electrical field. This gives a large mechanical displacement because of the large longitudinal PZE coefficient  $e_{33}$ . This thickness mode is fairly easy to compute and design for, and it is also relatively good at transferring acoustical power into a device attached to the transducer by the large displacement component along the surface normal. Conventional bulk PZE transducers with a millimeter-thickness typically have good resonances in the low-MHz regime.

In contrast, the half-wave transducer resonances of the thin-film transducers are pushed up into the GHz regime as a result of the micrometer-sized thickness, which is much higher than the low-MHz frequencies typically used in bulk acoustofluidics. Therefore, the transduction studied in this work is dominated by the transverse PZE coefficient  $e_{31f}$ . The large electric field on the order of MV/m that results from applying, say, a potential difference of  $1 V_{pp}$  across a  $1\text{-}\mu\text{m}$ -thick thin-film transducer, generates a large strain that accumulates along the millimeter-sized transducer-glass interface, which is the first of the three physical prerequisites. When this strain pattern has a sufficiently compatible overlap with that of a given resonance mode in the large glass block, the system will be excited at a frequency near this resonance mode frequency. This is the second physical prerequisite. We emphasize that this transduction mechanism does not rely on exciting any resonances in the thin-film transducer but instead on exciting resonances in the whole system, of which the transducer is only a minute part.

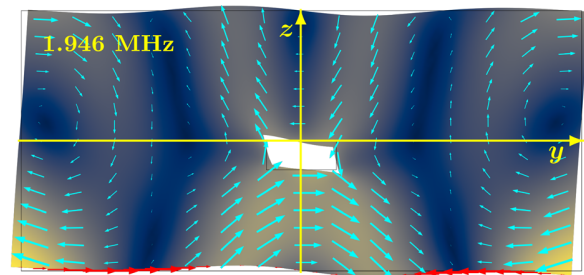


FIG. 3. (Color online) The 3D numerical simulation in the  $yz$ -plane at  $x=0$  of the displacement field  $u_1$  (enhanced by a factor of 7000 for clarity) in the  $\text{Al}_{0.6}\text{Sc}_{0.4}\text{N}$  thin-film device of Fig. 2(a) at the whole-system resonance  $f_{\text{thf}} = 1.946\text{ MHz}$ . The vector plot of  $u_1$  (cyan vectors) and color plot of its magnitude  $u_1$  from 0 (dark blue) to 15 nm (light yellow) is shown. The mode is excited by the  $\text{Al}_{0.6}\text{Sc}_{0.4}\text{N}$  thin-film transducer driven by a  $1\text{-}V_{pp}$  ac-voltage at the frequency  $f = 1.946\text{ MHz}$ . The in-plane strain  $\partial_y u_{1,y} e_y$  (red vectors) generated by the transducer on the transducer-glass interface shows expansion on the left and contraction on the right side in a way that is compatible with the strain field of the whole-system resonance mode. See the animations of the modes in the supplementary material (Ref. 38).

The thin-film transduction mechanism is exemplified in Fig. 3 (and in the corresponding animation in the supplementary material<sup>38</sup>) by the mode  $f_{\text{thf}}$  in the thin-film device [Fig. 2(a)]. The in-plane strain  $(\partial_y u_{1,y})e_y$  on the transducer-glass interface generated by the antisymmetrically driven split-bottom-electrode thin-film transducer corresponds to an expansion on the left side and a contraction on the right side. This strain pattern is compatible with that of the whole-system resonance mode, which, therefore, is excited with a large 15-nm displacement amplitude. The resulting antisymmetric oscillatory displacement field of the glass block pushes on the water in the channel, which leads to an antisymmetric pressure wave  $p_1$  [Fig. 2(e)] with the desired acoustofluidic properties shown in Figs. 2(f) and 2(g).

The third and last physical prerequisite is the high-quality factor of the whole system as an acoustic resonator. Because the thin-film transducer in our main example constitutes only a 0.07% v/v, the quality factor is completely dominated by that of the glass block, which has a high value,  $Q \sim 10^3$ , in a typical glass.<sup>39</sup>

##### B. The robustness of the device to the material, thickness, and quality factor of the thin-film transducer

The above thin-film transduction method implies that the functionality of the thin-film acoustofluidic device is robust to changes in several characteristic properties of the thin-film transducer, essentially because of its small volume fraction of the whole system. In the following, we study three such properties, namely, the material, thickness, and quality factor of the thin-film transducer.

We simulate three types of PZE materials. One is the commonly used PZT, having large PZE coefficients. One drawback of this material is its lead content, which is being out-phased for health and environmental reasons, and another is the difficulty in fabricating the material with a sufficiently low dissipation. Whereas other materials have

lower PZE coefficients than PZT, they may be fabricated with higher purity and less dissipation. The lead-free AlN is a choice for its simpler and better well-controlled high-quality depositing on a variety of substrates, which allows for higher break-down voltages that may compensate for the lower PZE coefficient.  $\text{Al}_{1-x}\text{Sc}_x\text{N}$  offers a PZE coefficient between the values of PZT and AlN with many of the same advantages as AlN, but it has a more complex fabrication process and alower break-down voltage.

In the first three columns of Table I, the simulation results of these different PZE materials are listed, while keeping all other quantities fixed in the model: AlN,  $\text{Al}_{0.6}\text{Sc}_{0.4}\text{N}$ , and PZT Pz26, and maintaining this order when referring to the numerical results in the following. In spite of the very different material parameters listed in Table SII of the supplemental material,<sup>38</sup> the resulting acoustofluidic response of the main resonance  $f_{\text{thf}}$  is nearly the same shape-wise, and only the amplitudes vary. Within 0.3%, the resonance frequencies are identical,  $f_{\text{thf}} = 1.948, 1.946,$  and  $1.942$  Mz, whereas the field amplitudes reflect the difference in the PZE coefficients and are for the pressure  $|p_1| = 0.44, 1.20,$  and  $3.50$  MPa, the displacement  $|u_1| = 5.1, 15,$  and  $38$  nm, and the acoustic energy density  $E_{\text{ac}}^{\text{fl}} = 7.3, 72,$  and  $2.1 \times 10^3 \text{ J m}^{-3}$ . Besides the obvious difference in the amplitude, the computed whole-system resonance is nearly the same in all three cases, showing a nearly ideal antisymmetric pressure wave in the microchannel. This is also reflected in the last two rows of Table I, which show how well the scaling laws  $t_{\text{foc}}^{-1} \propto E_{\text{ac}}^{\text{fl}} \propto e_{31,f}^2$  are obeyed in the three cases.

The thin-film device is also insensitive to the quality factor of the thin-film transducer, which, in terms of the damping coefficient  $\Gamma_{\text{sl}}$  in the Cauchy equation (5), is given by  $Q = \frac{1}{2} \Gamma_{\text{sl}}^{-1}$ . For two reasons, we expect a weak dependency on  $Q$ . The tiny volume of the transducer implies that the  $Q$ -factor of the system is completely dominated by that of the glass block. Consequently, as the transduction mechanism does not rely on the resonance properties of the thin-film transducer, the strong  $Q$ -dependence that is usually associated with the resonant modes in the transducer is absent. The simulation results shown in Fig. 4 confirm this expectation. Here, the acoustic energy density  $E_{\text{ac}}^{\text{fl}}$  in the microchannel of the thin-film device [Fig. 2(a)] at the resonance  $f_{\text{thf}} = 1.946$  MHz is shown as a function of  $Q$  from the original value of 1000 down to an appalling low value of 5. The resonant behavior reflected in  $E_{\text{ac}}^{\text{fl}}(f)$  is maintained, and the change in  $Q$  by a factor of 200 results in a drop of the peak value of  $E_{\text{ac}}^{\text{fl}}$  by a factor of only 2, from 72 to  $40 \text{ J m}^{-3}$ .

Finally, the simulation results in Fig. 4 also show that the main resonance mode  $f_{\text{thf}}$  is maintained when changing the thickness by a factor of 3.5 from  $H_{\text{thf}} = 1$  to  $3.5 \mu\text{m}$ , numbers typical for the current AlN and  $\text{Al}_{1-x}\text{Sc}_x\text{N}$  thin-film fabrication technology. The amplitude of the resonance peak in  $E_{\text{ac}}^{\text{fl}}$  is nearly constant ( $72 \pm 1$ )  $\text{J m}^{-3}$  from the thinnest to thickest film.

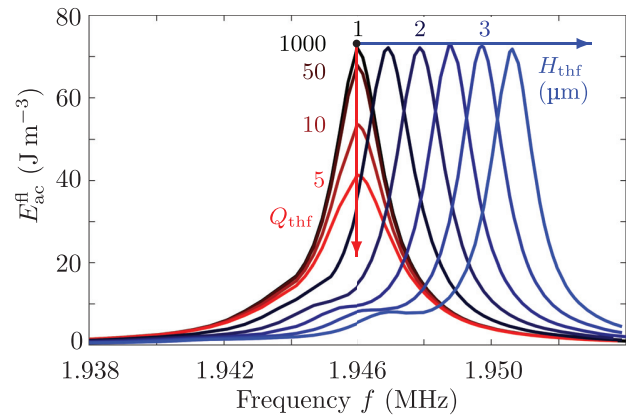


FIG. 4. (Color online) The 3D simulations of the acoustic energy density  $E_{\text{ac}}^{\text{fl}}$  of the resonance mode for the system shown in Fig. 2(a) versus the frequency from 1.938 to 1.954 MHz as a function of the thin-film  $Q$ -factor  $Q_{\text{thf}}$ , decreasing from 1000, 50, and 10 to 5 (red arrow), and as a function of the thin-film thickness  $H_{\text{thf}}$ , increasing from 1 to  $3.5 \mu\text{m}$  in steps of  $0.5 \mu\text{m}$  (blue arrow).

### C. Enhancing the acoustic response of the device by shaping the electrodes of the thin-film transducer

Thin-film transducers are fabricated by standard microfabrication deposition techniques, and this implies several distinct advantages. The lateral shape of the transducer or its electrode can be chosen freely by photolithography techniques; the attachment of the transducer to the glass chip is reproducible, stable, and strong, and the less controlled use of glue, known from standard bulk-transducer technology,<sup>46</sup> is avoided. Commercially, microfabrication techniques open up for volume production with relatively cheap unit prices, a necessary prerequisite for widespread single-use applications in biotechnology and medicine, where the cross-contamination arising from the multiple use of the same device is a no go.

An illustrative example of how the shape of the metal electrodes on the surface of the thin-film transducer may enhance the acoustic response is shown in Fig. 5. Here, the thin-film device of Fig. 2(a) is used as a starting point, but instead of the split-bottom electrode used for antisymmetric excitations, the bottom electrode is used for symmetric excitations in the three different cases of Figs. 5(a)–5(c), keeping all other parameters fixed: (a) an un-split electrode, (b) a large-gap split electrode, and (c) a two-gap split electrode. The aim is to excite with varying strength the symmetric full-wavelength-like pressure mode having two vertical nodal planes, which obeys the symmetry condition  $p_1(x, -y, z) = p_1(x, y, z)$ . Indeed, such a symmetric whole-system resonance is located at  $f = 3.578$  MHz as shown in Figs. 5(d)–5(g). As listed in Fig. 5(h), the strength of the mode depends on the electrode design. By reducing the electrode coverage from 100% in case (a) to 33% in case (b), the acoustic energy density can be increased by a factor of 2. Another factor of 2 is obtained by having the 49% electrode coverage of case (c), which includes an excitation voltage of  $+\varphi_0$  on the outer electrodes and  $-\varphi_0$  on the center electrode.

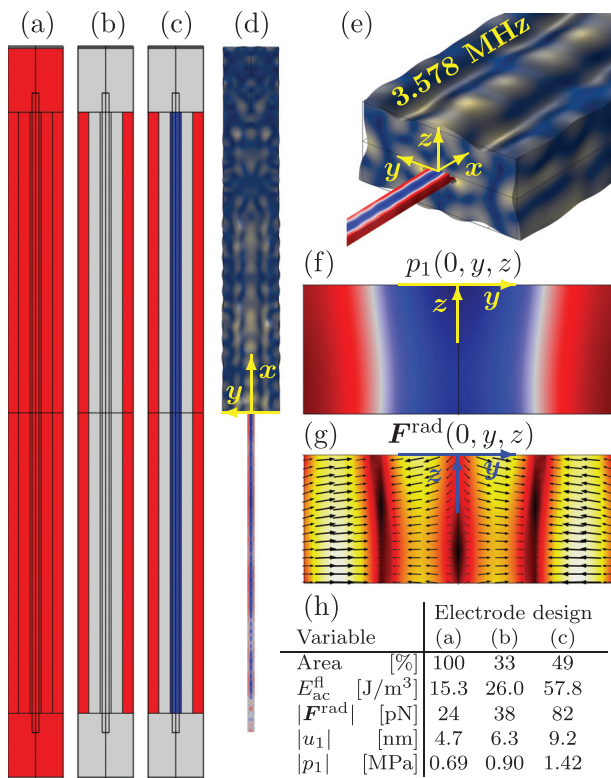


FIG. 5. (Color online) Simulations of the device in Fig. 2(a) but now exciting the symmetric full-wave-like resonance mode at  $f = 3.578$  MHz. [(a)–(c)] Three designs of a symmetric bottom electrode for exciting this mode, where red is actuated by  $\varphi = +\varphi_0$ , blue is actuated by  $\varphi = -\varphi_0$ , and gray marks no electrode. The top electrode is grounded,  $\varphi = 0$ . [(d)–(g)] The 3D simulations of  $u_1$ ,  $p_1$ , and  $F^{rad}$  in the device with electrode design (c) using the same plot format as in Fig. 2 but with the color scales given in (h), together with the acoustic energy density  $E_{ac}$  and the area (in %) covered by the bottom electrode for all three electrode designs. See the supplementary material for animations of the resonance mode in all three cases (Ref. 38).

The explanation of this result is found in the spatial form of the whole-system resonance mode. By inspection, we see that the displacement field at the glass-transducer interface forms a wave with in-plane contractions and expansions. The PZE coefficient  $e_{31f}$  in the transducer implies the presence of an electric field with a vertical component that changes sign along the in-plane direction. This tendency is counteracted by the fully covering bottom electrode, which imposes a unidirectional electrical field. Consequently, by removing the central part of the bottom electrode (or adding the anti-phase central part), this constraining boundary condition is relaxed (or changed into a supporting condition) while the remaining side parts of the electrode are still capable of exciting the whole-system resonance mode. This example offers a glimpse of the opportunities for design improvements by performing a shape optimization of the electrodes or perhaps the entire thin-film transducer.

#### D. Spatially regular modes in the thin-film device

Intuitively, the simplicity of the thin-film device consisting essentially of just a glass block should lead to simpler

modes with regular spatial dependencies. As mentioned above, the presence of a bulky PZT transducer leads to the excitation of whole-system resonance modes with a more irregular wave pattern in the displacement fields. Also, experimentally, this has been observed as hot spots in the pressure field along an otherwise perfectly shaped rectangular microchannel.<sup>36</sup>

In Fig. 6(a), we show six different whole-system resonance modes at lower frequencies near 1 MHz in a thin-film device with a  $1\text{-}\mu\text{m}$ -thick split-bottom-electrode AlN thin-film transducer mounted on the bottom of a rectangular Schott D263 glass block (Schott Suisse SA, Yverdon, Switzerland) of length  $L_{sl} = 45$  mm, width  $W_{sl} = 2.8$  mm, and height  $H_{sl} = 1.4$  mm. The microchannel of the system has length  $L_n = 40$  mm, width (at its top)  $W_n = 0.43$  mm, and height  $H_n = 0.15$  mm. To mimic the shape obtained by the isotropic etching in the glass, the side walls are modeled as quarter circles as shown in Fig. 6(b). The quarter circles increase the resonance frequency, but by increasing the channel width, we maintain a usual half-wave-like resonance mode close to 2 MHz as in Fig. 2(a). The frequencies of the resonance modes near 1 MHz are far from this 2 MHz and, thus, we would not expect these modes to be very strong. However, a clear spectrum with well-separated resonance

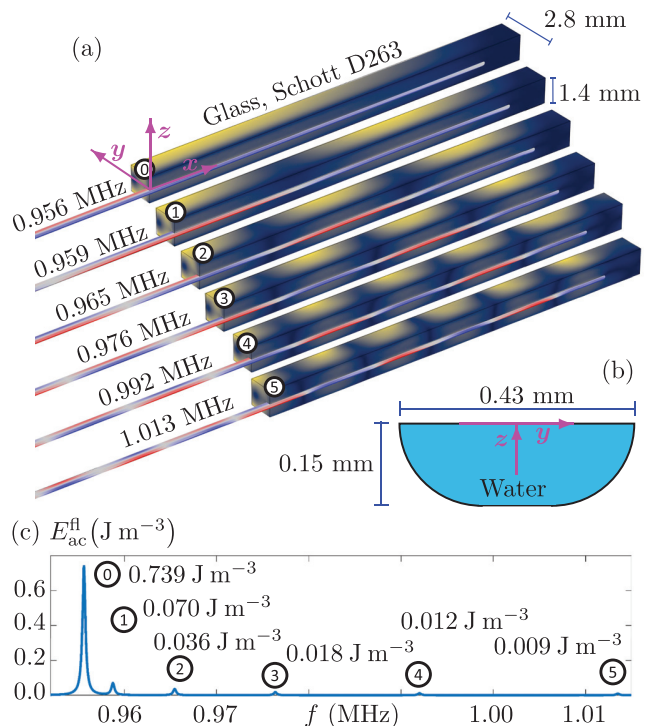


FIG. 6. (Color online) The simulation of the low-frequency modes near 1 MHz in a thin-film device with a  $1\text{-}\mu\text{m}$ -thick split-bottom-electrode AlN thin-film transducer. The system is symmetric around the vertical center plane at  $x = 0$  and antisymmetric around the vertical center plane at  $y = 0$ . (a) The lowest six resonance modes  $n = 0, 1, \dots, 5$  with  $2n$  nodal planes along the  $x$  axis and one nodal plane along the  $y$  axis. The plot format is the same as in Fig. 2(a). (b) The cross-sectional shape of the microchannel in the vertical  $yz$ -plane. (c) The acoustic energy density spectrum  $E_{ac}^{fl}(f)$  identifying the six resonance modes. See the supplementary material for animations of the six resonance modes (Ref. 38).

modes appears as shown in Fig. 6(c), yet another example of whole-system resonances excited by the thin-film transducer.

The antisymmetric actuation of the split-bottom electrode, combined with the geometrical symmetry, dictates that the system is symmetric around the vertical plane, at  $x=0$ , across the device, and antisymmetric around the vertical plane, at  $y=0$ , along the device. In Fig. 6(a), one immediately notices the spatial regularity of both the displacement field  $u_1$  and pressure field  $p_1$  in the six displayed modes. Both fields have the required symmetry along the  $x$  axis and anti-symmetry along the  $y$  axis, and both fields exhibit one nodal plane along the transverse  $y$  direction and, respectively,  $2n$  nodal planes with  $n = 0, 1, 2, \dots, 5$  along the axial  $x$  direction. In Fig. 6(c), the spectrum  $E_{ac}^{fl}(f)$  in the frequency range from 0.952 to 1.015 MHz is shown, which allows for the identification of the six resonance frequencies  $f_{n,1,0}$ , where the indices refer to the number of nodal planes in each direction. Of the six modes, the  $n=0$ -mode without nodes along the  $x$  axis has an axial structure that matches the  $x$ -independent voltage boundary condition better than the other modes, and indeed it has the highest energy density. As the number  $n$  of  $x$  axis nodes increases, the corresponding mode exhibits an increasing number of nodes and, hence, an increasing mismatch with the  $x$ -independent voltage boundary condition. This explains the monotonically decreasing peak value of  $E_{ac}^{fl}$  for the increasing values of  $n$  shown in Fig. 6(b).

### E. Device sensitivity to breaking of geometrical symmetries

As a final point, we discuss the consequences of breaking the perfect anti-symmetry of the thin-film device imposed in Figs. 2, 3, and 6. Using the microfabrication techniques, many geometrical features can be defined with accuracies down between 1 and 10  $\mu\text{m}$ ; however, it can be problematic to reach such accuracies when dicing up a full-sized wafer into the individual devices. For microelectronics, this is not problematic if the integrated circuits are sufficiently removed from the edges. However, for acoustofluidic devices, the whole substrate influences the whole-system resonances. For this reason, it is interesting to investigate the sensitivity of a

given acoustofluidic device given shifts in the position of the microchannel relative to the edges of the substrate.

In Fig. 7, we study the acoustic response to a shift in the center axis of the microchannel in the thin-film device of Fig. 2(a) from the ideal symmetric position at  $y=0$  to 50 and 100  $\mu\text{m}$ . The whole-system-resonance mode is not degraded significantly by this shift, which adds to the robustness in the experimental applications. A contributing factor to this robustness is that the water-filled channel only constitutes 1.2% of the total volume of the device. We notice that the main antisymmetric form of the acoustic pressure is largely unaffected by the shift, and the acoustic energy density  $E_{ac}^{fl}$  remains high in the range from 55 to 78  $\text{J m}^{-3}$ . However, as the shift increases, more pronounced axial inhomogeneities develop. Such inhomogeneities may imply a degradation in the functionality for stop-flow applications; however, as is well known experimentally from the measurements on several acoustofluidic devices in flow-through applications, such axial inhomogeneities averages out, and the device would work essentially without degradation.<sup>20</sup>

### V. CONCLUSION AND OUTLOOK

In this paper, based on a well-tested and experimentally validated numerical model,<sup>23,34,35</sup> we have shown by 3D numerical simulations in Sec. III, including Fig. 2 and Table I, that bulk glass chips with integrated PZE thin-film transducers constituting less than 0.1% v/v of the device have an acoustofluidic response on par with that obtained in a conventional silicon-glass device actuated by a PZT transducer, quantified by  $E_{ac}^{fl}$ ,  $R$ , and  $t_{foc}$ . The analysis in Sec. IV A demonstrated that the ability of the thin-film transducer to induce the desired acoustofluidic response in a bulk device relies on three physical aspects of the system: the in-plane-expansion of the thin-film transducer under the action of the orthogonal applied electric field, the acoustic whole-system resonances of the device, and the high  $Q$ -factor of the elastic solid, constituting the bulk part of the device.

We have pointed out some of the advantages of using thin-film transducers. Among them is the low sensitivity of the thin-film device to the material, thickness, and quality

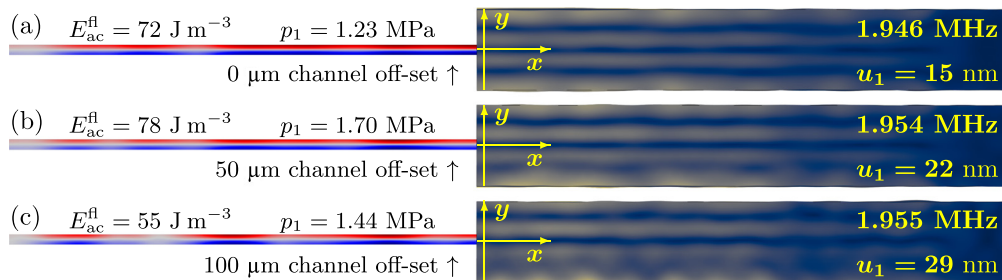


FIG. 7. (Color online) (a) The resonance mode at  $f = 1.946 \text{ MHz}$  of the device shown in Fig. 2(a), and using the same plot format, with the acoustic energy density  $E_{ac} = 72 \text{ J m}^{-3}$  and maximum pressure amplitude  $p_1 = \pm 1.23 \text{ MPa}$  in the fluid, and maximum displacement amplitude  $u_1 = 15 \text{ nm}$  in the solid. (b) The same as that in (a) but with the channel offset 50  $\mu\text{m}$  in the  $y$  direction and with resonance frequency  $f = 1.954 \text{ MHz}$ ,  $E_{ac} = 78 \text{ J m}^{-3}$ ,  $p_1 = \pm 1.70 \text{ MPa}$ , and  $u_1 = 22 \text{ nm}$ . (c) The same as that in (a) but with the channel offset by 100  $\mu\text{m}$  in the  $y$  direction and with resonance frequency  $f = 1.955 \text{ MHz}$ ,  $E_{ac} = 55 \text{ J m}^{-3}$ ,  $p_1 = \pm 1.44 \text{ MPa}$ , and  $u_1 = 29 \text{ nm}$ . See the supplementary material for animations of the three resonance modes (Ref. 38).

factor of the thin-film transducer discussed in Sec. IV B. Another advantage is that thin-film devices can be produced by clean-room microfabrication techniques, similar to the ones employed in the fabrication of surface acoustic waves. These techniques make it possible to shape the transducer electrodes, and in Sec. IV C, we discussed how to exploit this design freedom to boost the acoustofluidic response in the example of Fig. 5 by a factor of 4 by carefully shaping the transducer electrodes and reducing their area. We have also exploited the advantage of the microfabrication techniques that the thin-film transducers are integrated in the devices without involving the use of glue or glycerol coupling layers, which are used in the conventional bulk-transducer technique, although they are hard to control and often result in diminished reproducibility.

The performance of the thin-film and bulk-PZT bulk devices have been compared on equal footing using the same model approach and the same assumptions on damping and lack of clamping. More accurate simulation predictions for both types of devices would require better knowledge of the material parameters, the actual damping mechanisms in all elements of the devices, and modeling of the specific clamping and tubing of the device to the measurement setup. The influence of these factors on the functionality of especially the thin-film device will be part of future studies in close collaboration with experimental colleagues.

In an application perspective, the use of thin-film transducers offers new possibilities in the field of acoustofluidics. The fact that the thin-film transducer constitutes such a low volume fraction implies not only that the device is relatively insensitive to the quality of the thin film but also that the core part of the acoustofluidic system, namely, the microchannel, constitutes a relatively larger part of the system and is, thus, easier to control. The AlN-based thin-film transducers can be fabricated with high breakdown voltages ( $\sim 20$  V/ $\mu\text{m}$ ), which more than compensates for its lower coupling coefficient  $e_{31f}$ , and lower the dissipation and heat production.

We hope that this theoretical analysis will inspire our experimental colleagues in the field to investigate the new application aspects offered by the thin-film acoustofluidic devices.

## ACKNOWLEDGMENTS

This work was supported by the *BioWings* project funded by the European Union's Horizon 2020 *Future and Emerging Technologies* (FET) programme Grant No. 801267.

<sup>1</sup>A. Lenshof, C. Magnusson, and T. Laurell, "Acoustofluidics 8: Applications in acoustophoresis in continuous flow microsystems," *Lab Chip* **12**, 1210–1223 (2012).

<sup>2</sup>M. Gedge and M. Hill, "Acoustofluidics 17: Surface acoustic wave devices for particle manipulation," *Lab Chip* **12**, 2998–3007 (2012).

<sup>3</sup>E. K. Sackmann, A. L. Fulton, and D. J. Beebe, "The present and future role of microfluidics in biomedical research," *Nature* **507**(7491), 181–189 (2014).

<sup>4</sup>T. Laurell and A. Lenshof, eds., *Microscale Acoustofluidics* (Royal Society of Chemistry, Cambridge, UK, 2015).

<sup>5</sup>M. Antfolk and T. Laurell, "Continuous flow microfluidic separation and processing of rare cells and bioparticles found in blood—A review," *Anal. Chim. Acta* **965**, 9–35 (2017).

<sup>6</sup>P. Ohlsson, M. Evander, K. Petersson, L. Mellhammar, A. Lehmusvuori, U. Karhunen, M. Soikkeli, T. Seppa, E. Tuunainen, A. Spangar, P. von Lode, K. Rantakokko-Jalava, G. Otto, S. Scheduling, T. Soukka, S. Wittfooth, and T. Laurell, "Integrated acoustic separation, enrichment, and microchip polymerase chain reaction detection of bacteria from blood for rapid sepsis diagnostics," *Anal. Chem.* **88**(19), 9403–9411 (2016).

<sup>7</sup>P. Augustsson, C. Magnusson, M. Nordin, H. Lilja, and T. Laurell, "Microfluidic, label-free enrichment of prostate cancer cells in blood based on acoustophoresis," *Anal. Chem.* **84**(18), 7954–7962 (2012).

<sup>8</sup>R. Zmijan, U. S. Jonnalagadda, D. Carugo, Y. Kochi, E. Lemm, G. Packham, M. Hill, and P. Glynne-Jones, "High throughput imaging cytometer with acoustic focussing," *RSC Adv.* **5**(101), 83206–83216 (2015).

<sup>9</sup>M. Ohlin, I. Iranmanesh, A. E. Christakou, and M. Wiklund, "Temperature-controlled mpa-pressure ultrasonic cell manipulation in a microfluidic chip," *Lab Chip* **15**(16), 3341–3349 (2015).

<sup>10</sup>P. Thevoz, J. D. Adams, H. Shea, H. Bruus, and H. T. Soh, "Acoustophoretic synchronization of mammalian cells in microchannels," *Anal. Chem.* **82**(7), 3094–3098 (2010).

<sup>11</sup>D. J. Collins, B. Morahan, J. Garcia-Bustos, C. Doerig, M. Plebanski, and A. Neild, "Two-dimensional single-cell patterning with one cell per well driven by surface acoustic waves," *Nat. Commun.* **6**, 8686 (2015).

<sup>12</sup>F. Guo, Z. Mao, Y. Chen, Z. Xie, J. P. Lata, P. Li, L. Ren, J. Liu, J. Yang, M. Dao, S. Suresh, and T. J. Huang, "Three-dimensional manipulation of single cells using surface acoustic waves," *Proc. Natl. Acad. Sci. U.S.A.* **113**(6), 1522–1527 (2016).

<sup>13</sup>P. Augustsson, J. T. Karlsen, H.-W. Su, H. Bruus, and J. Voldman, "Iso-acoustic focusing of cells for size-insensitive acousto-mechanical phenotyping," *Nat. Commun.* **7**, 11556 (2016).

<sup>14</sup>G. Sitters, D. Kamsma, G. Thalhammer, M. Ritsch-Marte, E. J. G. Peterman, and G. J. L. Wuite, "Acoustic force spectroscopy," *Nat. Meth.* **12**(1), 47–50 (2015).

<sup>15</sup>B. W. Drinkwater, "Dynamic-field devices for the ultrasonic manipulation of microparticles," *Lab Chip* **16**, 2360–2375 (2016).

<sup>16</sup>D. J. Collins, C. Devendran, Z. Ma, J. W. Ng, A. Neild, and Y. Ai, "Acoustic tweezers via sub-time-of-flight regime surface acoustic waves," *Sci. Adv.* **2**(7), e1600089 (2016).

<sup>17</sup>H. G. Lim, Y. Li, M.-Y. Lin, C. Yoon, C. Lee, H. Jung, R. H. Chow, and K. K. Shung, "Calibration of trapping force on cell-size objects from ultrahigh-frequency single-beam acoustic tweezer," *IEEE Trans. Ultrason. Ferr.* **63**(11), 1988–1995 (2016).

<sup>18</sup>D. Baresch, J.-L. Thomas, and R. Marchiano, "Observation of a single-beam gradient force acoustical trap for elastic particles: Acoustical tweezers," *Phys. Rev. Lett.* **116**, 024301 (2016).

<sup>19</sup>B. Hammarström, B. Nilson, T. Laurell, J. Nilsson, and S. Ekström, "Acoustic trapping for bacteria identification in positive blood cultures with MALDI-TOF MS," *Anal. Chem.* **86**(21), 10560–10567 (2014).

<sup>20</sup>A. Lenshof, M. Evander, T. Laurell, and J. Nilsson, "Acoustofluidics 5: Building microfluidic acoustic resonators," *Lab Chip* **12**, 684–695 (2012).

<sup>21</sup>P. Reichert, D. Deshmukh, L. Lebovitz, and J. Dual, "Thin film piezoelectrics for bulk acoustic wave (BAW) acoustophoresis," *Lab Chip* **18**(23), 3655–3667 (2018).

<sup>22</sup>R. P. Moiseyenko and H. Bruus, "Whole-system ultrasound resonances as the basis for acoustophoresis in all-polymer microfluidic devices," *Phys. Rev. Appl.* **11**, 014014 (2019).

<sup>23</sup>W. N. Bodé, L. Jiang, T. Laurell, and H. Bruus, "Microparticle acoustophoresis in aluminum-based acoustofluidic devices with PDMS covers," *Micromachines* **11**(3), 292 (2020).

<sup>24</sup>M. Dubois and P. Muralt, "Properties of aluminum nitride thin films for piezoelectric transducers and microwave filter applications," *Appl. Phys. Lett.* **74**(20), 3032–3034 (1999).

<sup>25</sup>A. De Pastina, D. Maillard, and L. Villanueva, "Fabrication of suspended microchannel resonators with integrated piezoelectric transduction," *Microelectron. Eng.* **192**, 83–87 (2018).

<sup>26</sup>G. Piazza, P. J. Stephanou, and A. P. Pisano, "Piezoelectric aluminum nitride vibrating contour-mode MEMS resonators," *J. Microelectromech. Syst.* **15**(6), 1406–1418 (2006).

- <sup>27</sup>U. Zaghoul and G. Piazza, “Highly scalable NEMS relays with stress-tuned switching voltage using piezoelectric buckling actuators,” *IEEE Trans. Electron. Dev.* **61**(10), 3520–3528 (2014).
- <sup>28</sup>N. Sinha, G. E. Wabiszewski, R. Mahameed, V. V. Felmetzger, S. M. Tanner, R. W. Carpick, and G. Piazza, “Piezoelectric aluminum nitride nanoelectromechanical actuators,” *Appl. Phys. Lett.* **95**(5), 053106 (2009).
- <sup>29</sup>R. H. Olsson III, K. E. Wojciechowski, M. S. Baker, M. R. Tuck, and J. G. Fleming, “Post-CMOS-compatible aluminum nitride resonant MEMS accelerometers,” *J. Microelectromech. Syst.* **18**(3), 671–678 (2009).
- <sup>30</sup>H. Zhang, W. Pang, H. Yu, and E. S. Kim, “High-tone bulk acoustic resonators on sapphire, crystal quartz, fused silica, and silicon substrates,” *J. Appl. Phys.* **99**(12), 124911 (2006).
- <sup>31</sup>J. Masson, G. Martin, R. Boudot, Y. Gruson, S. Ballandras, A. Artieda, P. Muralt, B. Belgacem, and L. Chomeloux, “On the dispersive behaviour of AlN/Si high overtone bulk acoustic resonators,” in *2007 IEEE International Frequency Control Symposium Joint with the 21st European Frequency and Time Forum* (2007), pp. 741–744.
- <sup>32</sup>T. Fujikura, O. Matsuda, D. M. Profunser, O. B. Wright, J. Masson, and S. Ballandras, “Real-time imaging of acoustic waves on a bulk acoustic resonator,” *Appl. Phys. Lett.* **93**(26), 261101 (2008).
- <sup>33</sup>R. Ruby, “The ‘how & why’ a deceptively simple acoustic resonator became the basis of a multi-billion dollar industry,” in *2017 IEEE 30th International Conference on Micro Electro Mechanical Systems (MEMS)* (2017), pp. 308–313.
- <sup>34</sup>N. R. Skov, J. S. Bach, B. G. Winckelmann, and H. Bruus, “3D modeling of acoustofluidics in a liquid-filled cavity including streaming, viscous boundary layers, surrounding solids, and a piezoelectric transducer,” *AIMS Math.* **4**, 99–111 (2019).
- <sup>35</sup>N. R. Skov, P. Sehgal, B. J. Kirby, and H. Bruus, “Three-dimensional numerical modeling of surface-acoustic-wave devices: Acoustophoresis of micro- and nanoparticles including streaming,” *Phys. Rev. Appl.* **12**, 044028 (2019).
- <sup>36</sup>P. Augustsson, R. Barnkob, S. T. Wereley, H. Bruus, and T. Laurell, “Automated and temperature-controlled micro-PIV measurements enabling long-term-stable microchannel acoustophoresis characterization,” *Lab Chip* **11**(24), 4152–4164 (2011).
- <sup>37</sup>J. S. Bach and H. Bruus, “Theory of pressure acoustics with viscous boundary layers and streaming in curved elastic cavities,” *J. Acoust. Soc. Am.* **144**, 766–784 (2018).
- <sup>38</sup>See supplementary material at <https://www.scitation.org/doi/suppl/10.1121/10.0005624> for details on the values of the material parameters, focus time  $t_{\text{foc}}$ , and animations of the resonance modes.
- <sup>39</sup>P. Hahn and J. Dual, “A numerically efficient damping model for acoustic resonances in microfluidic cavities,” *Phys. Fluids* **27**, 062005 (2015).
- <sup>40</sup>L. P. Gorkov, “On the forces acting on a small particle in an acoustical field in an ideal fluid,” *Sov. Phys.-Dokl.* **6**(9), 773–775 (1962) [Dokl. Akad. Nauk SSSR **140**, 88–91 (1961)].
- <sup>41</sup>M. Settnes and H. Bruus, “Forces acting on a small particle in an acoustical field in a viscous fluid,” *Phys. Rev. E* **85**, 016327 (2012).
- <sup>42</sup>R. Barnkob, P. Augustsson, T. Laurell, and H. Bruus, “Measuring the local pressure amplitude in microchannel acoustophoresis,” *Lab Chip* **10**(5), 563–570 (2010).
- <sup>43</sup>P. B. Muller, M. Rossi, A. G. Marin, R. Barnkob, P. Augustsson, T. Laurell, C. J. Kähler, and H. Bruus, “Ultrasound-induced acoustophoretic motion of microparticles in three dimensions,” *Phys. Rev. E* **88**(2), 023006 (2013).
- <sup>44</sup>A. G. Steckel, H. Bruus, P. Muralt, and R. Matloub, “Fabrication, characterization, and simulation of glass devices with AlN thin-film transducers for excitation of ultrasound resonances,” *Phys. Rev. Appl.* **16**, 014014 (2021).
- <sup>45</sup>COMSOL Multiphysics 5.4 (2018), available at <http://www.comsol.com> (Last viewed 16 June 2021).
- <sup>46</sup>W. N. Bodé and H. Bruus, “Numerical study of the coupling layer between transducer and chip in acoustofluidic devices,” *J. Acoust. Soc. Am.* **149**(5), 3096–3105 (2021).

# Supplementary material: Numerical study of bulk acoustofluidic devices driven by thin-film transducers and whole-system resonance modes

André G. Steckel<sup>1, a)</sup> and Henrik Bruus<sup>1, b)</sup>  
*Department of Physics, Technical University of Denmark,  
 DTU Physics Building 309, DK-2800 Kongens Lyngby, Denmark*

(Dated: 16 May 2021)

## S1. MATERIAL PARAMETERS

The devices modeled in the main manuscript consists of water, one of two types of glass, and one of three types of piezoelectric transducer.

The parameters for water are taken from Muller and Bruus,<sup>1</sup> where each parameter is given as a fifth-order polynomial in the temperature. In this work we use the values computed for 25 °C as listed in Table S1.

TABLE S1. Parameter values of water at 25 °C used in the numerical simulations.<sup>1</sup>

Parameter	Value	Parameter	Value
$\rho_{\text{fl}}$	997 kg m <sup>-3</sup>	$\eta_{\text{fl}}^{\text{b}}$	2.485 mPa s
$c_{\text{fl}}$	1497 m s <sup>-1</sup>	$\Gamma_{\text{fl}}$	10.3 THz <sup>-1</sup> f
$\kappa_{\text{fl}}$	448 TPa <sup>-1</sup>	$\eta_{\text{fl}}$	0.890 mPa s

The parameter values used for the solids in the devices are listed in Table S2. For each type of piezoelectric material we list the density  $\rho_{\text{sl}}$ , the damping coefficient  $\Gamma_{\text{sl}}$ , and the nonzero values for the elastic constants  $C_{ik}$ , the piezoelectric coupling constants  $e_{ik}$ , and dielectric constants  $\epsilon_{ik}$ . For each type of glass we list the density  $\rho_{\text{sl}}$ , the damping coefficient  $\Gamma_{\text{sl}}$ , and the nonzero values for the elastic constants  $C_{ik}$ . Moreover, we supplement these values with the values of Young's modulus  $E$ , Poisson's ratio  $s$ , the longitudinal sound speed  $c_{\text{lo}}$ , and the transverse sound speed  $c_{\text{tr}}$ , related as follows:

$$C_{11} = \rho c_{\text{lo}}^2 = \frac{1-s}{(1+s)(1-2s)} E, \quad (1a)$$

$$C_{44} = \rho c_{\text{tr}}^2 = \frac{1}{2(1+s)} E. \quad (1b)$$

A PZE film behave different from its bulk counterpart as the film is free to expand in the perpendicular

TABLE S2. Parameters of the solids at 25 °C used in the numerical simulations.  $\epsilon_0$  is the vacuum permittivity, and for the two glasses is listed the Young's modulus  $E$ , the Poisson ratio  $s$ , and the longitudinal  $c_{\text{lo}}$  and transverse  $c_{\text{tr}}$  sound speeds. For glass  $C_{44} = \frac{1}{2}(C_{11} - C_{12})$ , and all PZE in this work have  $C_{66} = \frac{1}{2}(C_{11} - C_{12})$ .

Parameter	Value	Parameter	Value
<i>Thin-film aluminum nitride, AlN<sup>2-4</sup></i>			
$\rho_{\text{sl}}$	3300 kg m <sup>-3</sup>	$\Gamma_{\text{sl}}$	0.0005
$C_{11}$	410.2 GPa	$C_{33}$	385.0 GPa
$C_{12}$	142.4 GPa	$C_{44}$	122.9 GPa
$C_{13}$	110.1 GPa	$C_{66}$	133.9 GPa
$e_{31,f}$	-1.05 C m <sup>-2</sup>	$e_{15}$	-0.39 C m <sup>-2</sup>
$e_{33}$	1.46 C m <sup>-2</sup>	$\Gamma_{\epsilon}$	0.0005
$\epsilon_{11}$	9 $\epsilon_0$	$\epsilon_{33}$	11 $\epsilon_0$
<i>Thin-film aluminum scandium nitride, Al<sub>0.6</sub>Sc<sub>0.4</sub>N<sup>2,4</sup></i>			
$\rho_{\text{sl}}$	3300 kg m <sup>-3</sup>	$\Gamma_{\text{sl}}$	0.0005
$C_{11}$	313.8 GPa	$C_{33}$	197.1 GPa
$C_{12}$	150.0 GPa	$C_{44}$	108.6 GPa
$C_{13}$	139.2 GPa	$C_{66}$	81.9 GPa
$e_{31,f}$	-2.65 C m <sup>-2</sup>	$e_{15}$	-0.32 C m <sup>-2</sup>
$e_{33}$	2.73 C m <sup>-2</sup>	$\Gamma_{\epsilon}$	0.0005
$\epsilon_{11}$	22 $\epsilon_0$	$\epsilon_{33}$	22 $\epsilon_0$
<i>Bulk and thin-film lead zirconium titanate, PZT<sup>5</sup></i>			
$\rho_{\text{sl}}$	7700 kg m <sup>-3</sup>	$\Gamma_{\text{sl}}$	0.005
$C_{11}$	168 GPa	$C_{33}$	123 GPa
$C_{12}$	110 GPa	$C_{44}$	30.1 GPa
$C_{13}$	99.9 GPa	$C_{66}$	29.0 GPa
$e_{31,f}$	-14.7 C m <sup>-2</sup>	$e_{31}$	-2.8 C m <sup>-2</sup>
$e_{33}$	14.7 C m <sup>-2</sup>	$e_{15}$	9.86 C m <sup>-2</sup>
$\epsilon_{11}$	828 $\epsilon_0$	$\epsilon_{33}$	700 $\epsilon_0$
<i>Glass, Schott D263<sup>6</sup></i>			
$\rho_{\text{sl}}$	2510 kg m <sup>-3</sup>	$\Gamma_{\text{sl}}$	0.005
$E$	72.9 GPa	$s$	0.208
$C_{11}$	81.8 GPa	$C_{44}$	30.2 GPa
$C_{12}$	21.5 GPa	$\Gamma_{\text{sl}}$	0.0004
$c_{\text{lo}}$	5710 m s <sup>-1</sup>	$c_{\text{tr}}$	3467 m s <sup>-1</sup>
<i>Glass, Pyrex<sup>7,8</sup></i>			
$\rho_{\text{sl}}$	2230 kg m <sup>-3</sup>	$\Gamma_{\text{sl}}$	0.0004
$E$	62.8 GPa	$s$	0.20
$C_{11}$	69.8 GPa	$C_{44}$	26.2 GPa
$C_{12}$	17.4 GPa	$\Gamma_{\text{sl}}$	0.0004
$c_{\text{lo}}$	5594 m s <sup>-1</sup>	$c_{\text{tr}}$	3425 m s <sup>-1</sup>
<i>Silicon substrate<sup>8,9</sup></i>			
$\rho_{\text{sl}}$	2329 kg m <sup>-3</sup>	$\Gamma_{\text{sl}}$	0.0001
$C_{11}$	165.7 GPa	$C_{44}$	79.6 GPa
$C_{12}$	63.9 GPa		

a) [angust@fysik.dtu.dk](mailto:angust@fysik.dtu.dk)

b) [bruus@fysik.dtu.dk](mailto:bruus@fysik.dtu.dk)

TABLE S3. Parameter values used in the numerical simulations for 5- $\mu\text{m}$ -diameter polystyrene tracer particles suspended in water. The values are from Ref. 12, from which the scattering coefficients  $f_0$  and  $f_1$  are computed using the particle radius  $a = 2.5 \mu\text{m}$ .

Parameter	symbol	Value
Density	$\rho_{\text{ps}}$	$1050 \text{ kg m}^{-3}$
Compressibility	$\kappa_{\text{ps}}$	249 TPa
Poisson's ratio	$\nu_{\text{ps}}$	0.35
Speed of sound at 20°C	$c_{\text{ps}}$	$2350 \text{ ms}^{-1}$
Monopole coefficient, Eq. (10c)	$f_0$	0.44
Dipole coefficient, Eq. (10c)	$f_1$	$0.034 + 0.0002i$

( $z$ ) direction. The model thus uses the effective coupling coefficient  $e_{31,f}$ , given by the bulk parameter  $e_{33}$  as,<sup>10,11</sup>

$$e_{31,f} = e_{31} - \frac{C_{13}}{C_{33}} e_{33}. \quad (2)$$

Finally, the parameter values used for the polystyrene tracer particles in the focus time simulations are listed in Table S3.

## S2. THE FOCUS TIME OF MICROPARTICLES

In this section we describe the numerical determination of the average acoustophoretic focus time  $t_{\text{foc}}$ , Eq. (11), for a dilute suspension of microparticles in the half-wave-like resonance in the thin-film and bulk-PZT devices of Fig. 2(a) and Table I. The simulation closely follows the method presented by Muller *et al.*<sup>13</sup>

Acoustophoretic motion of suspended microparticles is due to the acoustic radiation force and the drag force from the acoustic streaming. Due to the low Reynolds number, the inertial forces can be neglected, and the equation of motion for a single particle with velocity  $\mathbf{v}_p$  suspended in a fluid with a streaming velocity  $\mathbf{v}_2$  is the force balance between the Stokes drag force and the acoustic radiation force,  $\mathbf{v}_p(\mathbf{r}) = \mathbf{v}_2(\mathbf{r}) + \frac{1}{6\pi\eta_{\text{fl}}a} \mathbf{F}^{\text{rad}}(\mathbf{r})$ .<sup>14</sup>

We use standard 5- $\mu\text{m}$ -diameter polystyrene particles (radius  $a = 2.5 \mu\text{m}$ ) as tracer particles, and their parameter values are listed in Table S3. Initially, the particles are placed in the 17 equidistant vertical cross-section planes in the mid-section of the microchannel from  $x = 0$  to  $\frac{1}{4}L_{\text{fl}} = 8.25 \text{ mm}$  in steps of 0.5 mm. Within each plane the particles are placed in a uniform  $10 \mu\text{m} \times 10 \mu\text{m}$  square grid as shown in Fig. S1(a), no closer than  $6a = 15 \mu\text{m}$  from the walls to reduce the effect of wall-particle interactions,<sup>12</sup> and no closer than  $8a = 25 \mu\text{m}$  to the center, where the particles are to be focused. We thus consider a total of  $N = 17 \times 16 \times 13 = 3,536$  particles.

The acoustic wave is turned on at time  $t = 0$ , and the time  $t_{fi}$  it takes a single particle starting at the initial position  $\mathbf{r}_i$  to reach the final position  $\mathbf{r}_f = (x_f, y_f, z_f)$  is

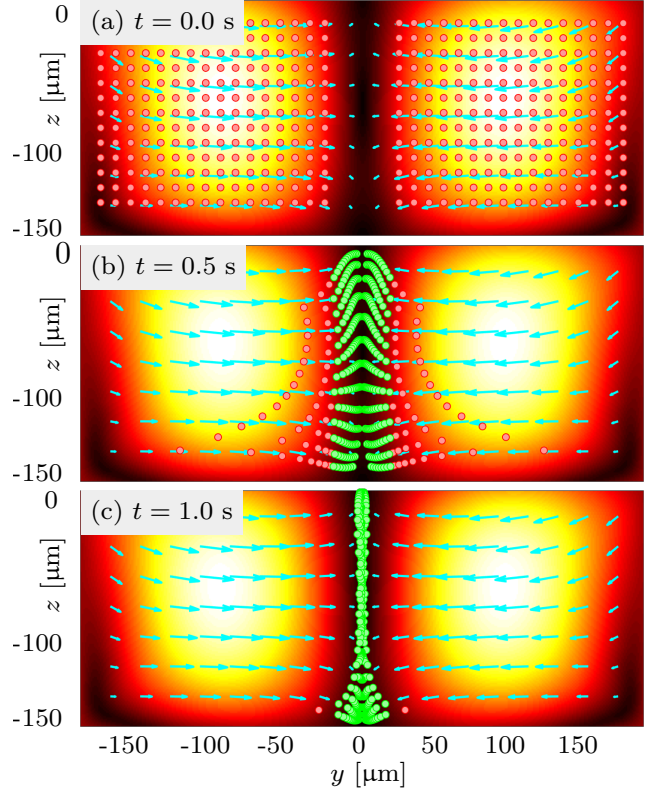


FIG. S1. The simulated acoustophoretic motion of 5- $\mu\text{m}$ -diameter polystyrene particles in the center plane,  $x = 0$ , of the  $\text{Al}_{0.6}\text{Sc}_{0.4}\text{N}$ -thin-film-driven device Fig. 2(a). The particle positions are shown at the times (a)  $t = 0.0 \text{ s}$ , (b)  $t = 0.5 \text{ s}$ , and (c)  $t = 1.0 \text{ s}$ . The particles are colored red before and green after reaching the center region  $|y| < 8a$ , where they are considered to be focused. The vectors represent the local particle speed  $\mathbf{v}_p$ , and the color plot is its magnitude from 0 (black) to  $394 \mu\text{m/s}$  (white).

computed by numerical integration of  $d\mathbf{r} = \mathbf{v}_p dt$ ,

$$\mathbf{r}_f = \mathbf{r}_i + \int_0^{t_{fi}} d\mathbf{r}(t), \quad \text{with } d\mathbf{r}(t) = \frac{\mathbf{F}^{\text{rad}}(\mathbf{r}(t))}{6\pi\eta_{\text{fl}}a} dt. \quad (3)$$

The numerical integration is performed in MATLAB. When the given particle reaches the boundary  $|y| = 8a$  of the narrow region centered around the vertical nodal plane  $y = 0$ , it is considered to be focused, and the time  $t_{fi}$  it took to reach this point is recorded. The average focus time for the homogeneous particle distribution is therefore defined by

$$t_{\text{foc}} = \frac{1}{N} \sum_{i=1}^N t_{fi}. \quad (4)$$

The acoustophoretic focusing of the suspended microparticles is illustrated in Fig. S1 and in the corresponding

animation entitled `SuppPubmm7.gif` in the supplementary files.

### S3. TIME-HARMONIC ANIMATIONS FOR FIG. 2

- `SuppPubmm1a.gif`: Time-harmonic animation of Fig. 2(a) where the magnitude of the real part of the displacement,  $|\text{Re}(u_1)|$ , is shown from 0 (dark blue) to 15 nm (yellow). The real part of the pressure field,  $\text{Re}(p_1)$ , is shown from  $-1.23$  MPa (blue) to 1.23 MPa (red). The simulation is done for a quarter of the device by symmetry reduction, and subsequently the pressure field has been extended through mirroring of the solution anti-symmetrically in the  $y$ -direction and symmetrically in the  $x$ -direction to make the mode visible.
- `SuppPubmm1b.gif`: Time-harmonic animation of Fig. 2(c) where the magnitude of the real part of the displacement,  $|\text{Re}(u_1)|$ , is shown from 0 (dark blue) to 3.6 nm (yellow). The real part of the pressure field,  $\text{Re}(p_1)$ , is shown from  $-0.55$  MPa (blue) to 0.55 MPa (red). The simulation is done in a symmetry-reduced half of the device, and subsequently the pressure field has been extended through mirroring of the solution symmetrically in the  $x$ -direction to make the mode visible.

### S4. TIME-HARMONIC ANIMATIONS FOR FIG. 3

- `SuppPubmm2.gif`: Time-harmonic animation of Fig. 3 where the magnitude of the real part of the displacement,  $|\text{Re}(u_1)|$ , is shown from 0 (dark blue) to 15 nm (yellow). The real part of the displacement,  $\text{Re}(u_1)$  is shown as the cyan arrows, and  $\text{Re}(\partial_y u_{1,y})$  is shown as red arrows. The simulation is done for a quarter of the device by symmetry reduction, and subsequently the pressure field has been extended through mirroring of the solution anti-symmetrically in the  $y$ -direction. The displacement motion of the solid has been scaled up by a factor of 7,000 to become visible.

### S5. TIME-HARMONIC ANIMATIONS FOR FIG. 5

- `SuppPubmm3a.gif`: Time-harmonic animation of Fig. 5(d) but for the electrode design shown in Fig. 5(a), where the magnitude of the real part of the displacement,  $|\text{Re}(u_1)|$ , is shown from 0 (dark blue) to 4.7 nm (yellow). The real part of the pressure field,  $\text{Re}(p_1)$ , is shown from  $-0.69$  MPa (blue) to 0.69 MPa (red). The simulation is done in a symmetry-reduced quarter of the device. Subsequently the displacement field has been through mirroring of the solution symmetrically in the  $y$ -direction, and the pressure field has been extended through mirroring of the solution symmetrically in both the  $y$ -direction and the  $x$ -direction to make the mode visible. The displacement motion of the

solid has been scaled up by a factor of 36,000 to become visible.

- `SuppPubmm3b.gif`: Time-harmonic animation of Fig. 5(d) but for the electrode design shown in Fig. 5(b), where the magnitude of the real part of the displacement,  $|\text{Re}(u_1)|$ , is shown from 0 (dark blue) to 6.3 nm (yellow). The real part of the pressure field,  $\text{Re}(p_1)$ , is shown from  $-0.90$  MPa (blue) to 0.90 MPa (red). The simulation is done in a symmetry-reduced quarter of the device. Subsequently the displacement field has been through mirroring of the solution symmetrically in the  $y$ -direction, and the pressure field has been extended through mirroring of the solution symmetrically in both the  $y$ -direction and the  $x$ -direction to make the mode visible. The displacement motion of the solid has been scaled up by a factor of 24,000 to become visible.
- `SuppPubmm3c.gif`: Time-harmonic animation of Fig. 5(d) but for the electrode design shown in Fig. 5(c), where the magnitude of the real part of the displacement,  $|\text{Re}(u_1)|$ , is shown from 0 (dark blue) to 9.2 nm (yellow). The real part of the pressure field,  $\text{Re}(p_1)$ , is shown from  $-1.42$  MPa (blue) to 1.42 MPa (red). The simulation is done in a symmetry-reduced quarter of the device. Subsequently the displacement field has been through mirroring of the solution symmetrically in the  $y$ -direction, and the pressure field has been extended through mirroring of the solution symmetrically in both the  $y$ -direction and the  $x$ -direction to make the mode visible. The displacement motion of the solid has been scaled up by a factor of 16,000 to become visible.

### S6. TIME-HARMONIC ANIMATIONS FOR FIG. 6

For the simulations shown in Fig. 6(a) all these simulations is of a quarter of the device, with appropriate boundary conditions, where the pressure field has been extended through mirroring of the solution symmetrically in both the  $y$ -direction and the  $x$ -direction to make the mode visible.

- `SuppPubmm4a.gif`: Time-harmonic animation of Fig. 6(a) mode (0), where the magnitude of the real part of the displacement,  $|\text{Re}(u_1)|$ , is shown from 0 (dark blue) to maximum (yellow). The real part of the pressure field,  $\text{Re}(p_1)$ , is shown from minimum in blue to maximum in red.
- `SuppPubmm4b.gif`: Time-harmonic animation of Fig. 6(a) mode (1), where the magnitude of the real part of the displacement,  $|\text{Re}(u_1)|$ , is shown from 0 (dark blue) to maximum (yellow). The real part of the pressure field,  $\text{Re}(p_1)$ , is shown from minimum in blue to maximum in red.
- `SuppPubmm4c.gif`: Time-harmonic animation of Fig. 6(a) mode (2), where the magnitude of the real

part of the displacement,  $|\text{Re}(u_1)|$ , is shown from 0 (dark blue) to maximum (yellow). The real part of the pressure field,  $\text{Re}(p_1)$ , is shown from minimum in blue to maximum in red.

- **SuppPubmm4d.gif**: Time-harmonic animation of Fig. 6(a) mode (3), where the magnitude of the real part of the displacement,  $|\text{Re}(u_1)|$ , is shown from 0 (dark blue) to maximum (yellow). The real part of the pressure field,  $\text{Re}(p_1)$ , is shown from minimum in blue to maximum in red.
- **SuppPubmm4e.gif**: Time-harmonic animation of Fig. 6(a) mode (4), where the magnitude of the real part of the displacement,  $|\text{Re}(u_1)|$ , is shown from 0 (dark blue) to maximum (yellow). The real part of the pressure field,  $\text{Re}(p_1)$ , is shown from minimum in blue to maximum in red.
- **SuppPubmm4f.gif**: Time-harmonic animation of Fig. 6(a) mode (5), where the magnitude of the real part of the displacement,  $|\text{Re}(u_1)|$ , is shown from 0 (dark blue) to maximum (yellow). The real part of the pressure field,  $\text{Re}(p_1)$ , is shown from minimum in blue to maximum in red.

#### S7. TIME-HARMONIC ANIMATIONS FOR FIG. 7

- **SuppPubmm5a.gif**: Time-harmonic animation of Fig. 7(a) where the magnitude of the real part of the displacement,  $|\text{Re}(u_1)|$ , is shown from 0 (dark blue) to 15 nm (yellow). The real part of the pressure field,  $\text{Re}(p_1)$ , is shown from  $-1.23$  MPa (blue) to  $1.23$  MPa (red). The simulation is done in a symmetry-reduced half of the device, and subsequently the pressure field has been extended through mirroring of the solution symmetrically in the  $x$ -direction to make the mode visible.
- **SuppPubmm5b.gif**: Time-harmonic animation of Fig. 7(b) where the magnitude of the real part of the displacement,  $|\text{Re}(u_1)|$ , is shown from 0 (dark blue) to 22 nm (yellow). The real part of the pressure field,  $\text{Re}(p_1)$ , is shown from  $-1.70$  MPa (blue) to  $1.70$  MPa (red). The simulation is done in a symmetry-reduced half of the device, and subsequently the pressure field has been extended through mirroring of the solution symmetrically in the  $x$ -direction to make the mode visible.
- **SuppPubmm5c.gif**: Time-harmonic animation of Fig. 7(a) where the magnitude of the real part of the displacement,  $|\text{Re}(u_1)|$ , is shown from 0 (dark blue) to 29 nm (yellow). The real part of the pressure field,  $\text{Re}(p_1)$ , is shown from  $-1.44$  MPa (blue) to  $1.44$  MPa (red). The simulation is done in a symmetry-reduced half of the device, and subsequently pressure field has been extended through mirroring of the solution symmetrically in the  $x$ -direction to make the mode visible.

#### S8. TIME-HARMONIC ANIMATIONS FOR TABLE I

- Column one **SuppPubmm6a.gif**: Time-harmonic animation of simulation used for table I AlN results. Same dimensions as Fig. 2(a) but were the thin-film is made of AlN and actuated at 1.948 MHz. The magnitude of the real part of the displacement,  $|\text{Re}(u_1)|$ , is shown from 0 (dark blue) to 5.1 nm (yellow). The real part of the pressure field,  $\text{Re}(p_1)$ , is shown from  $-0.44$  MPa (blue) to  $0.44$  MPa (red). The simulation is done for a quarter of the device by symmetry reduction, and subsequently the pressure field has been extended through mirroring of the solution anti-symmetrically in the  $y$ -direction and symmetrically in the  $x$ -direction to make the mode visible.
- Column two **SuppPubmm1a.gif**: Time-harmonic animation of Fig. 2(a) where the magnitude of the real part of the displacement,  $|\text{Re}(u_1)|$ , is shown from 0 (dark blue) to 15 nm (yellow). The real part of the pressure field,  $\text{Re}(p_1)$ , is shown from  $-1.23$  MPa (blue) to  $1.23$  MPa (red). The simulation is done for a quarter of the device by symmetry reduction, and subsequently the pressure field has been extended through mirroring of the solution anti-symmetrically in the  $y$ -direction and symmetrically in the  $x$ -direction to make the mode visible.
- Column three **SuppPubmm6b.gif**: Time-harmonic animation of simulation used for table I PZT thin-film results. Same dimensions as Fig. 2(a) but were the thin-film is made of AlN and actuated at 1.948 MHz. The magnitude of the real part of the displacement,  $|\text{Re}(u_1)|$ , is shown from 0 (dark blue) to 71 nm (yellow). The real part of the pressure field,  $\text{Re}(p_1)$ , is shown from  $-6.26$  MPa (blue) to  $6.26$  MPa (red). The simulation is done for a quarter of the device by symmetry reduction, and subsequently the pressure field has been extended through mirroring of the solution anti-symmetrically in the  $y$ -direction and symmetrically in the  $x$ -direction to make the mode visible.
- Column four **SuppPubmm1b.gif**: Time-harmonic animation of Fig. 2(c) where the magnitude of the real part of the displacement,  $|\text{Re}(u_1)|$ , is shown from 0 (dark blue) to 3.6 nm (yellow). The real part of the pressure field,  $\text{Re}(p_1)$ , is shown from  $-0.55$  MPa (blue) to  $0.55$  MPa (red). The simulation is done for a quarter of the device by symmetry reduction, and subsequently the pressure field has been extended through mirroring of the solution symmetrically in the  $x$ -direction to make the mode visible.

- <sup>1</sup>P. B. Muller and H. Bruus, “Numerical study of thermoviscous effects in ultrasound-induced acoustic streaming in microchannels,” *Phys. Rev. E* **90**(4), 043016 (2014) doi: [10.1103/PhysRevE.90.043016](https://doi.org/10.1103/PhysRevE.90.043016).
- <sup>2</sup>M. A. Caro, S. Zhang, T. Riekkinen, M. Ylilammi, M. A. Moram, O. Lopez-Acevedo, J. Molarius, and T. Laurila, “Piezoelectric coefficients and spontaneous polarization of ScAlN,” *J. Phys.-Condens. Mat.* **27**(24), 245901 (2015) doi: [10.1088/0953-8984/27/24/245901](https://doi.org/10.1088/0953-8984/27/24/245901).
- <sup>3</sup>A. Iqbal and F. Mohd-Yasin, “Reactive sputtering of aluminum nitride (002) thin films for piezoelectric applications: A review,” *Sensors* **18**(6), 1797 (2018) doi: [10.3390/s18061797](https://doi.org/10.3390/s18061797).
- <sup>4</sup>R. H. Olsson, Z. Tang, and M. D’Agati, “Doping of aluminum nitride and the impact on thin film piezoelectric and ferroelectric device performance,” in *2020 IEEE Custom Integrated Circuits Conference (CICC)* (2020), pp. 1–6, doi: [10.1109/CICC48029.2020.9075911](https://doi.org/10.1109/CICC48029.2020.9075911).
- <sup>5</sup>Meggitt A/S, Porthusvej 4, DK-3490 Kvistgaard, Denmark, *Ferroperm matrix data*, <https://www.meggittferroperm.com/materials/>, accessed 2 May 2021.
- <sup>6</sup>SCHOTT, SCHOTT Suisse SA, 2 Rue Galilée, Yverdon, Switzerland, *Borosilicate glass substrates*, <https://www.epfl.ch/research/facilities/cmi/wp-content/uploads/2020/05/D263T.d.pdf>, accessed 2 May 2021.
- <sup>7</sup>CORNING, Houghton Park C-8, Corning, NY 14831, USA, *Glass Silicon Constraint Substrates*, <http://www.valleydesign.com/Datasheets/Corning%20Pyrex%207740.pdf>, accessed 2 May 2021.
- <sup>8</sup>P. Hahn and J. Dual, “A numerically efficient damping model for acoustic resonances in microfluidic cavities,” *Physics of Fluids* **27**, 062005 (2015) doi: [10.1063/1.4922986](https://doi.org/10.1063/1.4922986).
- <sup>9</sup>M. A. Hopcroft, W. D. Nix, and T. W. Kenny, “What is the Young’s modulus of silicon,” *J. Microelectromech. Syst.* **19**, 229–238 (2010) doi: [10.1109/JMEMS.2009.2039697](https://doi.org/10.1109/JMEMS.2009.2039697).
- <sup>10</sup>P. Reichert, D. Deshmukh, L. Lebovitz, and J. Dual, “Thin film piezoelectrics for bulk acoustic wave (BAW) acoustophoresis,” *Lab Chip* **18**(23), 3655–3667 (2018) doi: [10.1039/c8lc00833g](https://doi.org/10.1039/c8lc00833g).
- <sup>11</sup>P. Muralt, J. Conde, A. Artieda, F. Martin, and M. Cantoni, “Piezoelectric materials parameters for piezoelectric thin films in ghz applications,” *Int. J. Microw. Wirel. T.* **1**(1), 19–27 (2009) doi: [10.1017/S1759078709000038](https://doi.org/10.1017/S1759078709000038).
- <sup>12</sup>R. Barnkob, P. Augustsson, T. Laurell, and H. Bruus, “Acoustic radiation- and streaming-induced microparticle velocities determined by microparticle image velocimetry in an ultrasound symmetry plane,” *Phys. Rev. E* **86**, 056307 (2012) doi: [10.1103/PhysRevE.86.056307](https://doi.org/10.1103/PhysRevE.86.056307).
- <sup>13</sup>P. B. Muller, R. Barnkob, M. J. H. Jensen, and H. Bruus, “A numerical study of microparticle acoustophoresis driven by acoustic radiation forces and streaming-induced drag forces,” *Lab Chip* **12**, 4617–4627 (2012) doi: [10.1039/C2LC40612H](https://doi.org/10.1039/C2LC40612H).
- <sup>14</sup>R. Barnkob, P. Augustsson, T. Laurell, and H. Bruus, “Measuring the local pressure amplitude in microchannel acoustophoresis,” *Lab Chip* **10**(5), 563–570 (2010) doi: [10.1039/b920376a](https://doi.org/10.1039/b920376a).

### 5.3 Paper III: Manuscript in preparation

*Numerical study of acoustic cell trapping above elastic membrane disks driven in higher-harmonic modes by thin-film transducers with patterned electrodes.* [3]

**ArXiv:** [arxiv.org/abs/2112.12567](https://arxiv.org/abs/2112.12567),

**Authors:** André G. Steckel and Henrik Bruus.

**Journal:** Submitted, under review.

# Numerical study of acoustic cell trapping above elastic membrane disks driven in higher-harmonic modes by thin-film transducers with patterned electrodes

André G. Steckel\* and Henrik Bruus†

Department of Physics, Technical University of Denmark,  
DTU Physics Building 309, DK-2800 Kongens Lyngby, Denmark

(Dated: 23 December 2021)

Excitations of MHz acoustic modes are studied numerically in 10- $\mu\text{m}$ -thick silicon disk membranes with a radius of 100 and 500  $\mu\text{m}$  actuated by an attached 1- $\mu\text{m}$ -thick (AlSc)N thin-film transducer. It is shown how higher-harmonic membrane modes can be excited selectively and efficiently by appropriate patterning of the transducer electrodes. When filling the half-space above the membrane with a liquid, the higher-harmonic modes induce acoustic pressure fields in the liquid with interference patterns that result in the formation of a single, strong trapping region located 50 - 100  $\mu\text{m}$  above the membrane, where a single suspended cell can be trapped in all three spatial directions. The trapping strength depends on the acoustic contrast between the cell and the liquid, and as a specific example it is shown by numerical simulation that by using a 60% iodixanol solution, a cancer cell can be held in the trap.

## I. INTRODUCTION

Recently, the concept of thin-film-actuated devices has been introduced in the field of microscale acoustofluidics at MHz ultrasound frequencies. In 2018, Reichert *et al.* demonstrated experimentally and numerically, how to generate useful acoustofluidic responses in microchannels with a thin silicon-membrane lid driven by a lead-zirconate-titanate (PZT) thin-film transducer [1]. In this case, the transducer makes up around 15% by volume ( $v/v$ ) of the actuated membrane, which is excited while leaving the bulk part of the device inert. In 2021, we successfully modeled and experimentally validated the excitation by aluminum scandium nitride (AlSc)N thin-film transducers of MHz-modes in millimeter-sized glass-block devices without microchannels [2]. In this system, the transducer is only 0.2%  $v/v$ . In a follow-up study [3], which constitutes the theoretical foundation of our present work, we demonstrated by numerical simulation, how thin-film transducers can induce acoustofluidic responses in bulk microfluidic devices on par with those obtained by using conventional bulk PZT transducers. In Ref. [3], we also studied the robustness and pointed out several advantages of using thin-film transducers: the low sensitivity of the thin-film device to the material, the thickness, and the quality factor of the thin-film transducer, and that the microfabrication techniques, by which the thin-film devices can be produced, also allow for careful shaping of the transducer electrodes, a design freedom that may be used to boost the acoustofluidic response of the device.

In this work, we follow up on the latter idea, and present a numerical study of how proper shaping of the electrodes on circular thin-film-driven membranes can increase the excitation amplitudes of the higher-harmonic

vibration eigenmodes in the membrane. When placing such membranes in the bottom wall of a cavity containing a liquid, we show that specific higher harmonics of the order  $n \gtrsim 10$  in the membrane induce acoustic pressure fields in the liquid with interference patterns that result in the formation of a single, strong trapping region located 50 - 100  $\mu\text{m}$  above the membrane, where a single suspended cell can be trapped in all three spatial directions. The choice of this model system is motivated by the increasing use of disk-shaped membranes in acoustofluidic applications, such as capacitive micro-machined ultrasonic transducers (CMUT) for imaging, inkjet printing, and testing [4], thin-film resonators for mixing and biosensing [5, 6], and silicon-membrane devices for particle manipulation [7].

In the field of acoustofluidics, electrode shaping is of course used extensively when dealing with surface acoustic waves (SAW), as the electrodes directly define these waves [8]. However, when dealing with bulk acoustic waves (BAW), the topic of this work, electrode shaping is rarely used, and not at all for the above-mentioned membrane devices. A simple split-electrode configuration with an applied anti-symmetric driving voltage, has been used on experiments on bulk piezoelectric (PZE) transducers [9, 10] and on thin-film transducers [1] to obtain a strong excitation of anti-symmetric modes for optimal particle focusing. Such systems has also been studied in numerical simulations [3, 11–13]. Furthermore, in a combined experimental and numerical study, Hammarström *et al.* used a square-shaped back and a full front electrode on a bulk PZE transducer to create a dynamically-defined array of particle traps in the liquid just above the transducer [14].

In the field of microelectromechanical system (MEMS), shaping of PZE-transducer electrodes has been studied in much more detail. For example the development of energy harvesting MEMS devices involving shaping of electrodes is an active research field [15–19]. A particular thorough study is the combined experimental and theoretical work on the excitation and detection of more

\* angust@fysik.dtu.dk

† bruus@fysik.dtu.dk

than 50 permitted arbitrary modes in disc-, plate-, ring-, and beam-shaped PZT-on-silicon resonators by electrode shaping [20]. It is this kind of selective excitation of chosen resonance modes that we in the present work extend from solid-state MEMS to acoustofluidic devices for particle handling.

The contents of the paper is as follows. In Section II we introduce our model system, a disk-shaped silicon-membrane-based microscale acoustofluidic system driven at MHz-frequencies by an (AlSc)N PZE thin-film transducer with patterned electrodes for selective excitation of higher-harmonic resonance modes, a system chosen for its compatibility with standard MEMS fabrication techniques. A brief summary is given of the basic theory and modeling developed in our previous work [3]. It includes time-harmonic perturbation theory, the electromechanical theory of the elastic membrane and the linear PZE transducer, acoustics and time-averaged acoustic streaming of the liquid, boundary conditions, and the numerical implementation in the software COMSOL Multiphysics [21]. In Section III, we present the main result of the paper, the selective enhanced excitation by electrode shaping of higher-harmonic membrane resonance modes for acoustofluidic applications. In Section IV, we present an application example by showing how specific higher-harmonics membrane modes may induce the above-mentioned trapping of a single suspended cell. In Section V, we discuss the possibility of size-dependent cell trapping and the advantages and disadvantages of the presented method of trapping, and finally in Section VI we present our main conclusions.

## II. MODEL SYSTEM, THEORY, AND NUMERICAL IMPLEMENTATION

The model system, sketched in Fig. 1, consists of a thin disk-shaped silicon membrane completely covered by a (AlSc)N thin-film PZE transducer on one of its surfaces. The ground electrode of the transducer is always fully covering the transducer, whereas the excitation electrode may be divided into several pieces each with individual alternate-current (AC) excitation voltages. Below the membrane is air (treated as vacuum), and above it a liquid. The system is axisymmetric, so that we use cylindrical coordinates  $(r, \phi, z)$  through the paper with the  $z$  axis perpendicular to the membrane through its center.

The basic theory and modeling for such a thin-film PZE-transducer-driven acoustofluidic system, was developed in a perturbation scheme involving the acoustic first-order fields and the steady time-averaged second-order fields in our previous work [3], founded on the theory for bulk PZE-transducer-driven systems [22] taking the acoustic boundary layers into account analytically through effective boundary conditions [23]. Numerical simulations based on this theory have been validated experimentally for several different microscale acoustofluidic systems [2, 9, 10, 22]. In the following we briefly

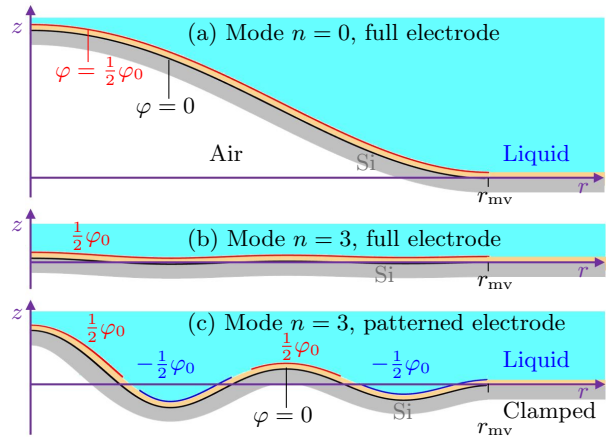


FIG. 1. The axisymmetric model in the  $r$ - $z$  plane consisting of a thin silicon membrane (gray) clamped for  $r > r_{mv}$  and fully covered with a thin-film (AlSc)N PZE transducer (beige) on its top surface. The grounded transducer electrode (black) covers the entire transducer, but the excitation electrode (red and blue) may be either fully covering or divided into several sections each with the indicated excitation voltage. Below the membrane is air (white, treated as vacuum) and above is a liquid (cyan). (a) The fundamental resonance mode ( $n = 0$ ) of the membrane with a large amplitude as the fully-covering excitation electrode (red) is compatible with the mode shape. (b) The third-harmonic ( $n = 3$ ) resonance mode of the membrane with a small amplitude as the fully covering excitation electrode (red) is incompatible with the mode shape. (c) The third-harmonic ( $n = 3$ ) resonance mode of the membrane with a large amplitude due to the specific patterning of the excitation electrode (red and blue) into four pieces with specific excitation voltages.

summarize this basic theory and its numerical implementation and adapt the previous cartesian-coordinate formulation into the cylindrical coordinates of the present axisymmetric system. We do not study azimuthal variations, so the full three-dimensional (3D) problem is independent of  $\phi$  and is thus reduced to a two-dimensional (2D) problem in the radial and axial coordinates  $r$  and  $z$ , respectively.

### A. First-order acoustic fields

Using first-order perturbation theory and complex-valued fields [3], the time-harmonic electric potential  $\tilde{\varphi}_1(\mathbf{r}, t)$  applied to the PZE thin-film excites a time-harmonic acoustic displacement field  $\tilde{\mathbf{u}}_1(\mathbf{r}, t)$ ,

$$\tilde{\varphi}_1(\mathbf{r}, t) = \varphi_1(\mathbf{r}) e^{-i\omega t}, \quad \tilde{\mathbf{u}}_1(\mathbf{r}, t) = \mathbf{u}_1(\mathbf{r}) e^{-i\omega t}, \quad (1)$$

where  $\omega = 2\pi f$  is the angular frequency,  $f$  the frequency,  $\mathbf{r}$  the spatial coordinate, and  $t$  the time.

We convert the cartesian coordinates  $\mathbf{r} = (x, y, z)$  of Refs. [2, 3, 22] into cylindrical coordinates  $\mathbf{r} = (r \cos \phi, r \sin \phi, z)$ , and assuming  $\phi$ -independent excita-

tion voltages, we have,

$$\varphi_1(\mathbf{r}) = \varphi_1(r, z), \quad \mathbf{u}_1(\mathbf{r}) = u_r(r, z)\mathbf{e}_r + u_z(r, z)\mathbf{e}_z. \quad (2)$$

The governing equations of  $\mathbf{u}_1$  and  $\varphi_1$  are the weakly damped Cauchy elastodynamic equation and the quasi-static Gauss equation for a charge-free linear dielectric,

$$-\rho\omega^2(1 + i\Gamma_{\text{sl}})\mathbf{u}_1 = \nabla \cdot \boldsymbol{\sigma}_{\text{sl}}, \quad \nabla \cdot \mathbf{D} = 0, \quad (3)$$

where  $\boldsymbol{\sigma}_{\text{sl}}$  is the Cauchy stress tensor,  $\Gamma_{\text{sl}}$  is the damping coefficient of the solid, and  $\mathbf{D} = -(1 + i\Gamma_\varepsilon)\boldsymbol{\varepsilon} \cdot \nabla\varphi_1$  is the electric displacement field with  $\Gamma_\varepsilon$  and  $\boldsymbol{\varepsilon}$  being the dielectric damping coefficient and tensor, respectively. For a purely mechanical solid, the stress tensor is defined in Voigt notation as,

$$\boldsymbol{\sigma}_{\text{sl}} = \mathbf{C} \cdot \mathbf{S}_{\text{sl}}, \quad (4)$$

where  $\mathbf{C}$  is the elastic moduli tensor of rank two which relates the strain tensor  $\mathbf{S}_{\text{sl}}$  to the stress tensor  $\boldsymbol{\sigma}_{\text{sl}}$ . In cylindrical coordinates, the Voigt notation-form of  $\mathbf{C}$ ,  $\mathbf{S}_{\text{sl}}$  and  $\boldsymbol{\sigma}_{\text{sl}}$  is,

$$\mathbf{C} = \begin{pmatrix} C_{11} & C_{12} & C_{13} & 0 & 0 & 0 \\ C_{12} & C_{11} & C_{13} & 0 & 0 & 0 \\ C_{13} & C_{13} & C_{33} & 0 & 0 & 0 \\ 0 & 0 & 0 & C_{44} & 0 & 0 \\ 0 & 0 & 0 & 0 & C_{44} & 0 \\ 0 & 0 & 0 & 0 & 0 & C_{66} \end{pmatrix}, \quad (5a)$$

$$\mathbf{S}_{\text{sl}} = \left( \partial_r u_{1r}, \frac{1}{r} u_{1r}, \partial_z u_{1z}, 0, \partial_r u_{1z} + \partial_z u_{1r}, 0 \right)^T, \quad (5b)$$

$$\boldsymbol{\sigma}_{\text{sl}} = \left( \sigma_{rr}, \sigma_{\phi\phi}, \sigma_{zz}, \sigma_{\phi z}, \sigma_{rz}, \sigma_{r\phi} \right)^T. \quad (5c)$$

Here, the column vectors  $\mathbf{S}_{\text{sl}}$  and  $\boldsymbol{\sigma}_{\text{sl}}$  are written as the transpose ‘‘T’’ of the row vectors. Moreover,  $\mathbf{C}$  is written for the lowest symmetry in our problem, the hexagonal crystal structure of (AlSc)N, and we note that it has the same form in cartesian as in cylindrical coordinates when the polarization axis is parallel to the  $z$  axis. Whereas neither the displacement nor the electric field has a component in the azimuthal  $\phi$ -direction, the strain and stress do have a nonzero  $\phi\phi$ -component. Finally, we note that for silicon (111) the above form for  $\mathbf{C}$  still applies, but with the symmetry constraints  $C_{13} = C_{12}$ ,  $C_{33} = C_{11}$ , and  $C_{66} = C_{44}$ . Other orientations of silicon crystal are not isotropic in the  $r$ - $\phi$  plane and thus cannot be modeled as an axisymmetric system [24, 25].

In this work, our PZE transducer is taken to be (AlSc)N which has a hexagonal piezoelectric crystal structure [26] with the material parameters listed in Table I. For PZE materials, the stress and electric displacement fields are coupled to the electric and strain fields though the piezoelectric coupling tensor,

$$\boldsymbol{\sigma}_{\text{sl}} = \mathbf{C} \cdot \mathbf{S}_{\text{sl}} - \mathbf{e}^T \cdot \mathbf{E}, \quad (6a)$$

$$\mathbf{D} = \mathbf{e} \cdot \mathbf{S}_{\text{sl}} + \boldsymbol{\varepsilon} \cdot \mathbf{E}, \quad (6b)$$

where the electric field defined as  $\mathbf{E} = -\nabla\varphi_1$ , and where in the Voigt notation for the hexagonal crystal structure,  $\mathbf{e}$  and  $\boldsymbol{\varepsilon}$  are the following tensors,

$$\mathbf{e} = \begin{pmatrix} 0 & 0 & 0 & 0 & 0 & e_{15} \\ 0 & 0 & 0 & 0 & e_{15} & 0 \\ e_{31} & e_{31} & e_{33} & 0 & 0 & 0 \end{pmatrix}, \quad \boldsymbol{\varepsilon} = \begin{pmatrix} \varepsilon_{11} & 0 & 0 \\ 0 & \varepsilon_{11} & 0 \\ 0 & 0 & \varepsilon_{33} \end{pmatrix}. \quad (7)$$

The mechanical displacement in the solids couple into the adjacent liquid or fluid as pressure waves. For a fluid with density  $\rho_{\text{fl}}$ , dynamic viscosity  $\eta_{\text{fl}}$ , bulk viscosity  $\eta_{\text{fl}}^b$ , compressibility  $\kappa_{\text{fl}}$ , and sound speed  $c_{\text{fl}}$ , and damping coefficient  $\Gamma_{\text{fl}}$ , the acoustic pressure  $p_1$  is governed by the weakly damped Helmholtz equation, and the acoustic velocity  $\mathbf{v}_1^d$  is derived from  $p_1$ ,

$$\tilde{p}_1 = p_1(\mathbf{r}) e^{-i\omega t}, \quad \tilde{\mathbf{v}}_1^d = \mathbf{v}_1^d(\mathbf{r}) e^{-i\omega t}, \quad (8a)$$

$$\nabla^2 p_1 = -\frac{\omega^2}{c_{\text{fl}}^2} (1 + i\Gamma_{\text{fl}}) p_1, \quad \kappa_{\text{fl}} = (\rho_{\text{fl}} c_{\text{fl}}^2)^{-1}, \quad (8b)$$

$$\mathbf{v}_1^d = -i \frac{1 - i\Gamma_{\text{fl}}}{\omega \rho_{\text{fl}}} \nabla p_1, \quad \Gamma_{\text{fl}} = \left( \frac{4}{3} \eta_{\text{fl}} + \eta_{\text{fl}}^b \right) \omega \kappa_{\text{fl}}. \quad (8c)$$

In our  $\phi$ -independent axisymmetric case we have

$$p_1(\mathbf{r}) = p_1(r, z), \quad \mathbf{v}_1^d(\mathbf{r}) = v_{1r}^d(r, z)\mathbf{e}_r + v_{1z}^d(r, z)\mathbf{e}_z. \quad (9)$$

## B. Second-order time-averaged fields

The nonlinearities in the fluid dynamics induce second-order terms in the perturbation theory from products of first-order terms [3]. Here, we focus on the time-averaged values of such fields,  $\mathbf{F}_2 = \langle \tilde{\mathbf{F}}_2(\mathbf{r}, t) \rangle = \frac{\omega}{2\pi} \int_0^{\frac{2\pi}{\omega}} \tilde{\mathbf{F}}_2(\mathbf{r}, t) dt$ , in particular the steady streaming velocity  $\mathbf{v}_2$  and the acoustic radiation force  $\mathbf{F}^{\text{rad}}$  on suspended particles. For the time-averaged product of two first-order fields  $A_1$  and  $B_1$  we use the well-known expression  $\langle \text{Re} [\tilde{A}_1(\mathbf{r}, t)] \text{Re} [\tilde{B}_1(\mathbf{r}, t)] \rangle = \frac{1}{2} \text{Re} [A_1(\mathbf{r}) B_1^*(\mathbf{r})]$ . The acoustic streaming  $\mathbf{v}_2$  is an incompressible Stokes flow with a non-negligible time-average Eckart-streaming bulk force

$$\eta_{\text{fl}} \nabla^2 \mathbf{v}_2 = \nabla \mathcal{P}_2 - \frac{\Gamma_{\text{fl}} \omega}{2c_{\text{fl}}^2} \text{Re} [p_1^* \mathbf{v}_1^d], \quad \nabla \cdot \mathbf{v}_2 = 0, \quad (10)$$

where  $\mathcal{P}_2$  is the pressure redefined to include the excessive pressure [23]. The expression for the acoustic radiation force  $\mathbf{F}^{\text{rad}}$  acting on a suspended particle of radius  $a$ , density  $\rho_{\text{pt}}$ , and compressibility  $\kappa_{\text{pt}}$  is [27],

$$\mathbf{F}^{\text{rad}} = -\pi a^3 \left\{ \frac{2\kappa_{\text{fl}}}{3} \text{Re} [f_0^* p_1^* \nabla p_1] - \rho_{\text{fl}} \text{Re} [f_1^* \mathbf{v}_1^{d*} \cdot \nabla \mathbf{v}_1^d] \right\}, \quad (11a)$$

$$f_0 = 1 - \frac{\kappa_{\text{pt}}}{\kappa_{\text{fl}}}, \quad f_1 = \frac{2(1 - \gamma)(\rho_{\text{pt}} - \rho_{\text{fl}})}{2\rho_{\text{pt}} + (1 - 3\gamma)\rho_{\text{fl}}}, \quad (11b)$$

where  $f_0$  and  $f_1$  are the monopole and dipole scattering coefficients,  $\delta$  is the width of the acoustic boundary layer, and  $\gamma$  is a correction factor,

$$\delta = \sqrt{\frac{2\eta_{\text{fl}}}{\omega\rho_{\text{fl}}}}, \quad \gamma = -\frac{3}{2} \left[ 1 + i \left( 1 + \frac{\delta}{a} \right) \right] \frac{\delta}{a}. \quad (12)$$

The total force  $\mathbf{F}^{\text{pt}}$  acting on a suspended particle moving with speed  $\mathbf{v}_{\text{pt}}$  at position  $\mathbf{r}$  is the sum of the radiation force  $\mathbf{F}^{\text{rad}}$ , the Stokes drag force  $\mathbf{F}^{\text{drag}}$ , and the buoyancy-corrected gravitational force  $\mathbf{F}^{\text{grav}}$  from the gravitational acceleration  $\mathbf{g}$ ,

$$\mathbf{F}^{\text{pt}} = \mathbf{F}^{\text{rad}} + \mathbf{F}^{\text{drag}} + \mathbf{F}^{\text{grav}}, \quad (13a)$$

$$\mathbf{F}^{\text{drag}} = 6\pi\eta_{\text{fl}}a(\mathbf{v}_2 - \mathbf{v}_{\text{pt}}), \quad \mathbf{F}^{\text{grav}} = \frac{4}{3}\pi a^3(\rho_{\text{pt}} - \rho_{\text{fl}})\mathbf{g}. \quad (13b)$$

### C. Boundary conditions

In the following we state the boundary conditions that we apply to the first-order acoustic and time-averaged second-order steady fields. On the axis  $r = 0$ , we have the usual axisymmetry conditions,

$$\partial_r p_1 = 0, \quad \partial_r u_{1z} = 0, \quad u_{1r} = 0, \quad \partial_r \varphi_1 = 0, \quad (14a)$$

$$\partial_r p_2 = 0, \quad \partial_r v_{2z} = 0, \quad v_{2r} = 0, \quad \text{at } r = 0. \quad (14b)$$

We control the electric potential  $\varphi_1$  on the transducer electrodes. At the ground electrode,  $\varphi_1 = 0$  always, whereas the excited electrodes have a peak-to-peak AC voltage amplitude of  $\varphi_0$ , so there  $\varphi = \frac{1}{2}\varphi_0 e^{i\Delta}$  with  $\Delta$  being a phase. Here, we work only with in-phase  $\Delta = 0$  (positive) and anti-phase  $\Delta = \pi$  (negative) excitation voltages, so at the electrode surfaces we have

$$\varphi_1 = 0, \quad \text{on ground electrodes}, \quad (15a)$$

$$\varphi_1 = +\frac{1}{2}\varphi_0, \quad \text{on positive electrodes}, \quad (15b)$$

$$\varphi_1 = -\frac{1}{2}\varphi_0, \quad \text{on negative electrodes}. \quad (15c)$$

At interfaces away from the electrodes, we assume a zero-free-charge condition on  $\varphi_1$ . On freely vibrating interfaces, we assume a zero-stress condition on  $\mathbf{u}_1$ ,

$$\mathbf{D} \cdot \mathbf{n} = 0, \quad \boldsymbol{\sigma}_{\text{sl}} \cdot \mathbf{n} = \mathbf{0}, \quad \text{at the solid-air interface}, \quad (16)$$

At the solid-fluid interface, we use the effective boundary conditions for the continuity of the first-order velocity and stress, developed in a coordinate-free form by Bach and Bruus [23], where the acoustic boundary layer in the fluid has been accounted for analytically. Here we state these boundary conditions for our case with  $\phi$ -

independent axisymmetric first-order fields,

$$\begin{aligned} \partial_z p_1 &= \frac{i\omega\rho_0}{1 - i\Gamma_{\text{fl}}} \left[ -i\omega u_{1z} - \frac{i}{k_s r} \partial_r (-i\omega r u_{1r}) \right] \\ &\quad - \frac{i}{k_s} (k_c^2 p_1 + \partial_z^2 p_1), \end{aligned} \quad (17a)$$

$$\boldsymbol{\sigma}_{\text{sl}} \cdot \mathbf{e}_z = -p_1 \mathbf{e}_z + ik_s \eta_0 \left( -i\omega \mathbf{u}_1 + \frac{1}{\omega\rho_0} \boldsymbol{\nabla} p_1 \right), \quad (17b)$$

$$k_c^2 = (1 + i\Gamma_{\text{fl}}) \frac{\omega^2}{c_{\text{fl}}^2}, \quad k_s = \frac{1 + i}{\delta}. \quad (17c)$$

as well as the second-order streaming  $\mathbf{v}_2$ ,

$$\begin{aligned} v_{2r}^{d0} &= -\frac{1}{2\omega} \text{Re} \left\{ \frac{1}{2} v_{1r}^{\delta 0*} \partial_r v_{1r}^{\delta 0} + \frac{1}{2} v_{1z}^{\delta 0*} \partial_z v_{1r}^{\delta 0} \right. \\ &\quad + \frac{2-i}{2} \left( \partial_r v_{1r}^{\delta 0*} + \frac{1}{r} v_{1r}^{\delta 0*} + \partial_z v_{1z}^{\delta 0*} \right) v_{1r}^{\delta 0} \\ &\quad + i \left( \partial_r u_{1r}^{0*} + \frac{1}{r} u_{1r}^{0*} + \partial_z u_{1z}^{0*} - \partial_z v_{1z}^{d*} \right) v_{1r}^{\delta 0} \\ &\quad \left. - i (v_{1r}^{\delta 0*} + v_{1z}^{\delta 0*}) \partial_z u_{1r} - i \mathbf{u}_1^{0*} \cdot \boldsymbol{\nabla} v_{1r}^d \right\}, \end{aligned} \quad (18a)$$

$$\begin{aligned} v_{2z}^{d0} &= -\frac{1}{2\omega} \text{Re} \left\{ i v_{1r}^{\delta 0*} \partial_r u_{1z}^{0*} + u_{1r}^{0*} \partial_r (v_{1z}^d + v_{1z}^{\delta 0}) \right. \\ &\quad \left. + u_{1z}^{0*} \partial_z (v_{1z}^d + v_{1z}^{\delta 0}) \right\} \end{aligned} \quad (18b)$$

Here,  $\mathbf{v}_1^{\delta 0} = \mathbf{u}_1^0 - \mathbf{v}_1^{d0}$ , which together with all terms containing the factor  $k_s$  originates from the boundary layer of width  $\delta$ .

Finally, when we consider systems without a lid, the acoustic waves transmitted from the membrane into the fluid will propagate toward infinity ( $r \rightarrow \infty$  and  $z \rightarrow \infty$ ) until damped out. To keep a finite-sized computational domain, we therefore follow Refs. [22, 28] and limit the physical domain of the fluid to the region  $0 < r < r_{\text{fl}}$  and  $0 < z < z_{\text{fl}}$ , then add so-called perfectly matched layers (PML) around this domain for  $r_{\text{fl}} < r < r_{\text{PML}}$  or  $z_{\text{fl}} < z < z_{\text{PML}}$ , in which all outgoing waves from the membrane are damped out, and from which no incoming waves are sent toward the membrane,

For  $r_{\text{fl}} < r < r_{\text{PML}}$  or  $z_{\text{fl}} < z < z_{\text{PML}}$  :

$$\chi(r, z) = \quad (19a)$$

$$K_{\text{PML}} \left( \theta[r - r_{\text{fl}}] \left[ \frac{r - r_{\text{fl}}}{r_{\text{PML}} - r_{\text{fl}}} \right]^2 + \theta[z - z_{\text{fl}}] \left[ \frac{z - z_{\text{fl}}}{z_{\text{PML}} - z_{\text{fl}}} \right]^2 \right),$$

$$\partial_r \rightarrow [1 + i\chi(r, z)]\partial_r, \quad \partial_z \rightarrow [1 + i\chi(r, z)]\partial_z. \quad (19b)$$

$$dr \rightarrow \frac{dr}{1 + i\chi(r, z)}, \quad dz \rightarrow \frac{dz}{1 + i\chi(r, z)}. \quad (19c)$$

Here,  $\theta$  is the Heaviside step function, and  $K_{\text{PML}}$  is a constant chosen, such that the outgoing waves are damped in the PML without reflections at  $r = r_{\text{fl}}$  and  $z = z_{\text{fl}}$ .

The choice of boundary conditions at the outer surface of the PML are not crucial due to the strong damping provided in the PML. We use the Dirichlet condition  $p_1 = 0$  there, but changing to Neumann condition  $\mathbf{n} \cdot \boldsymbol{\nabla} p_1 = 0$  leads to negligible relative deviation in the result, less than  $10^{-5}$  measured in terms of the L2-norm.

TABLE I. Material parameter values used in the model. The iodixanol solution is computed from the interpolation polynomials given in Ref. [30]. For the MCF-7 cells, the radius is chosen as the center value 10  $\mu\text{m}$  in the observed range of 8.1-12.2  $\mu\text{m}$  given in Ref. [31], and the scattering coefficients  $f_0$  and  $f_1$  are computed from Eq. (11b) using data from Ref. [32].

Parameter	Value	Parameter	Value
<i>Thin-film aluminum scandium nitride, Al<sub>0.6</sub>Sc<sub>0.4</sub>N [33, 34]</i>			
$\rho_{\text{sl}}$	3300 kg m <sup>-3</sup>	$\Gamma_{\text{sl}}$	0.0005
$C_{11}$	313.8 GPa	$C_{33}$	197.1 GPa
$C_{12}$	150.0 GPa	$C_{44}$	108.6 GPa
$C_{13}$	139.2 GPa	$C_{66}$	81.9 GPa
$e_{31,f}$	-2.65 C m <sup>-2</sup>	$e_{15}$	-0.32 C m <sup>-2</sup>
$e_{33}$	2.73 C m <sup>-2</sup>	$\Gamma_{\varepsilon}$	0.0005
$\varepsilon_{11}$	22 $\varepsilon_0$	$\varepsilon_{33}$	22 $\varepsilon_0$
<i>Membrane silicon, Si (111) [25, 35, 36]</i>			
$\rho_{\text{sl}}$	2329 kg m <sup>-3</sup>		
$E$	168.9 GPa	$s$	0.262
$C_{11}$	207.5 GPa	$C_{44}$	73.7 GPa
$C_{12}$	66.9 GPa	$\Gamma_{\text{sl}}$	0.0001
$c_{\text{lo}}$	5594 m s <sup>-1</sup>	$c_{\text{tr}}$	3425 m s <sup>-1</sup>
<i>Water [29]</i>			
$\rho_{\text{fl}}$	997 kg m <sup>-3</sup>	$\eta_{\text{fl}}$	0.890 mPa s
$c_{\text{fl}}$	1497 m s <sup>-1</sup>	$\eta_{\text{fl}}^{\text{b}}$	2.485 mPa s
$\kappa_{\text{fl}}$	448 TPa <sup>-1</sup>	$\Gamma_{\text{fl}}$	10.3 THz <sup>-1</sup> f
<i>Iodixanol 60% solution [30]</i>			
$\rho_{\text{fl}}^{\text{Idx,60\%}}$	1320 kg m <sup>-3</sup>	$c_{\text{fl}}^{\text{Idx,60\%}}$	1498 m s <sup>-1</sup>
$\eta_{\text{fl}}^{\text{Idx,60\%}}$	7.690 mPa s	$\kappa_{\text{fl}}^{\text{Idx,60\%}}$	338 TPa <sup>-1</sup>
<i>Cancer cell MCF-7 [31, 32]</i>			
$\rho_{\text{MCF-7}}$	1055 kg m <sup>-3</sup>	$\rho_{\text{MCF-7}}$	373 TPa <sup>-1</sup>
$a_{\text{MCF-7}}$	10 $\mu\text{m}$		
$f_0^{\text{Wa}}$	0.167	$f_1^{\text{Wa}}$	0.037 + 0.00002i
$f_0^{\text{Idx,60\%}}$	-0.104	$f_1^{\text{Idx,60\%}}$	-0.153 + 0.0010i

#### D. Numerical implementation in COMSOL

As in Ref. [3], we implement the model in the commercial finite-element software COMSOL 5.5 [21], closely following the implementation method described in Ref. [22]. The fields  $p_1$ ,  $\mathbf{u}_1$ ,  $\varphi_1$ ,  $p_2$ , and  $\mathbf{v}_2$  are all computed with quartic-order polynomial test functions. The mesh is defined to ensure at least 20 mesh elements per wavelength, and typically more, resulting in more than 80 nodal points per wavelength in the physical domain, and 10 elements per wavelength in the PML domain. In the bulk fluid we use a triangular mesh, and in both the membrane and the thin-film transducer, a structured mesh is used with at least four mesh elements in the thickness direction. At the symmetry axis  $r = 0$  is added a boundary layer of 15 elements, growing up from a smallest element of 0.005 times the bulk mesh size. This mesh ensured a successful mesh-convergence analysis similar to that presented in Ref. [29].

The materials used in the model are as follows: the PZE thin-film transducer is Al<sub>0.6</sub>Sc<sub>0.4</sub>N, the silicon membrane is Si-(111), the liquid is either pure water or a 60%

aqueous solution of iodixanol, and the cell is a MCF-7 breast-cancer cell. All material parameter values used in the model are listed in Table I including references to the literature.

We carried out the numerical simulations of the model on a workstation with a 16-cores Intel i9-7960X processor at 3.70 GHz boost clock frequency and 128 GB of random access memory (RAM). At any given frequency, a simulation of the first-order fields  $p_1$ ,  $\mathbf{u}_1$ , and  $\varphi_1$  comprised of 1.4 million degrees of freedom, used 14 GB RAM, and took 50 s, whereas the second-order fields  $p_2$  and  $\mathbf{v}_2$  comprised of 2.7 million degrees of freedom, used 27 GB RAM, and took 180 s.

### III. EXCITATION OF HIGHER-HARMONIC MEMBRANE MODES BY ELECTRODE PATTERNING

We now introduce the excitation of higher-harmonic membrane modes in acoustofluidics. As already indicated in Fig. 1, we show that only by patterning the excitation electrode to be compatible with the shape of the target higher-harmonic membrane mode, this mode can be excited with a sufficiently large amplitude.

#### A. Membrane modes and patterned electrodes

In Fig. 2 we show the main effect of patterning the excitation electrodes appropriately for a 10- $\mu\text{m}$ -thick Si-disk membrane covered uniformly by a 1- $\mu\text{m}$ -thick (AlSc)N thin-film transducer. The inner part  $r < r_{\text{mv}} = 100 \mu\text{m}$  of the membrane is free to vibrate, whereas the surrounding ring  $r_{\text{mv}} < r < r_{\text{mc}} = 300 \mu\text{m}$  is clamped. Above the membrane is placed a cylindrical domain of water of radius  $r_{\text{mc}}$  and height  $z_{\text{fl}} = 200 \mu\text{m}$ , and outside this domain is placed a PML domain of thickness 100  $\mu\text{m}$ .

In Fig. 2(a), the ground and excitation electrode are fully covering the transducer, and a peak-to-peak voltage  $\varphi_0 = 1 \text{ V}$  is applied to the latter. A frequency sweep reveals the  $\phi$ -independent vibration resonance modes  $n$  of the membrane disk,  $n = 0, 1, 2, 3, \dots$ , with resonance frequencies  $f_n = 2.16, 10.5, 19.7, 52.0 \text{ MHz}$  and a monotonically decreasing maximum displacement amplitude  $u_{1z,n}^{\text{max}} = 0.75, 0.24, 0.08, 0.02 \text{ nm}$  for  $n = 0, 1, 2, 3$ . Animations of modes  $n = 0$  and  $n = 3$  are given in the Supplemental Material [37].

This decreasing mode amplitude is partly explained by the uniformity across the thin-film-transducer surface of the applied perpendicular voltage drop  $\varphi_0$ , see Fig. 2(d,g), which by the electromechanical coupling matrix  $\mathbf{e}$  promotes a uniform stretching or compression of the thin film at any given time. This works well for the fundamental mode  $n = 0$  at 2.16 MHz, where the film is either stretching across the entire membrane at any given time, or contracting, although not uniformly, resulting in a perpendicular displacement  $u_{1z}$  that is either posi-

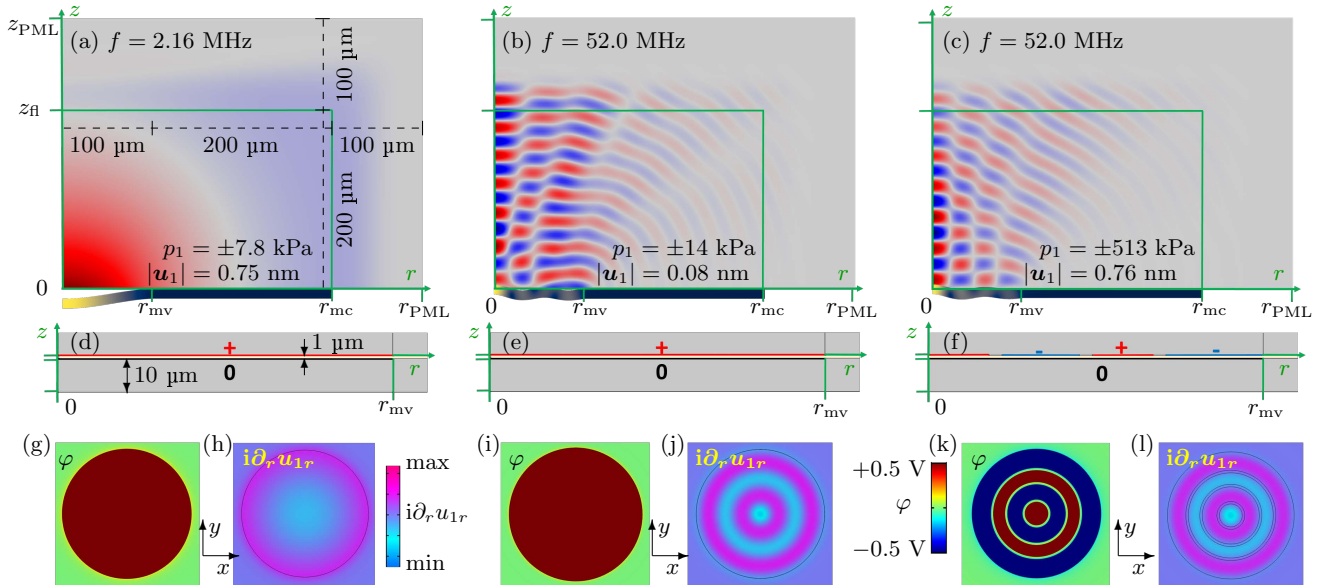


FIG. 2. Simulation of the resonance modes  $n$  for a 10- $\mu\text{m}$ -thick silicon Si (111) membrane of radius  $r_{\text{mv}} = 100 \mu\text{m}$  placed below a half-space filled with a fluid and actuated by an attached 1- $\mu\text{m}$ -thick  $\text{Al}_{0.6}\text{Sc}_{0.4}\text{N}$  thin-film PZE transducer with a peak-to-peak AC voltage  $\varphi_0 = 1 \text{ V}_{\text{pp}}$ . The fluid domain is surrounded by a 100- $\mu\text{m}$  wide PML domain. (a) Color plot of the pressure  $\text{Re}[p_1]$  from  $-7.8$  (blue) to  $+7.8$  kPa (red) and of the displacement amplitude  $|u_1|$  from 0 (blue) to  $0.75$  nm (yellow) for the  $n = 0$  fundamental mode at  $2.16$  MHz, excited by the uniform excitation electrode shown in (d) the  $r$ - $z$  plane and (g) the  $x$ - $y$  plane. (b) The same as (a) but for the  $n = 3$  harmonic mode at  $52.0$  MHz with pressure amplitude  $\pm 14$  kPa and displacement amplitude  $0.08$  nm, excited by the uniform excitation electrode shown in (e) the  $r$ - $z$  plane and (i) the  $x$ - $y$  plane. (c) The same as (b) but with pressure amplitude  $\pm 513$  kPa and displacement amplitude  $0.75$  nm, and with the patterned excitation electrode shown in (f) the  $r$ - $z$  plane and (k) the  $x$ - $y$  plane. (h), (j), and (l) Color plot of the out-of-phase in-plane strain  $\text{Re}[i\partial_r u_{1r}]$  from min (cyan) to max (magenta) for the membrane modes shown respectively in (a), (b), and (c) for which the vertical displacement  $\text{Re}[iu_{1z}]$  for clarity has been enhanced by a factor 15000, 30000, and 6000, respectively. Animations of panels (a) and (c) are given in the Supplemental Material [37].

tive across the entire membrane, or negative, as shown in Fig. 2(a). For the third harmonic mode  $n = 3$  at  $52.0$  MHz, the oscillating displacement  $u_{1z}$  changes sign 3 times along the radial direction as shown in Fig. 2(b), and this counteracts uniform stretching/contraction promoted by the uniform potential shown in Fig. 2(e,i), and as a result the excitation amplitude is decreased. Clearly, by arranging for a non-uniform potential following the non-uniform mechanical displacement, we could hope to restore a large excitation amplitude. But how?

The clue is the out-of-phase in-plane strain  $i\partial_r u_{1r}$  for mode  $n = 0$  and  $3$  shown in Fig. 2(h,j), respectively. This field indicates how the membrane would move were it free to vibrate in a given resonance mode. For  $n = 0$  at  $2.16$  MHz, the strain indicates a contraction (cyan) in a large center part of the membrane, which the uniform applied potential supports, only counteracting the expansion indicated by the strain in a minor peripheral part (magenta). In contrast, for mode  $n = 3$  at  $52$  MHz, the strain indicates four ring-shaped domains respectively exhibiting contraction, expansion, contraction, expansion, which is not compatible with the applied uniform potential, as each full contraction-expansion period is nearly canceled by the potential.

To make the potential for  $n = 3$  compatible with the strain pattern, we therefore split the excitation electrode into the same 3 ring-shaped domains (plus the central disk) defined by the strain with alternating excitation voltages  $+\frac{1}{2}\varphi_0$ ,  $-\frac{1}{2}\varphi_0$ ,  $+\frac{1}{2}\varphi_0$ , and  $-\frac{1}{2}\varphi_0$ , shown in Fig. 2(f,k). If these rings should be contacted by wires in the same layer [20] or by conducting vias to wires in a second layer, we leave to the experts of MEMS technology to figure out, here we just assume it possible in practise. The resulting acoustic response for the same applied voltage amplitude is shown in Fig. 2(c). Here we see that the resonance frequency remains  $f_3 = 52.0$  MHz, and that the displacement amplitude for the patterned electrode is  $u_{1z,3}^{\text{max,p}} = 0.75$  nm, one and half order of magnitude higher than that of the uniform electrode,  $u_{1z,3}^{\text{max,u}} = 0.02$  nm, and equal to the uniform-electrode mode-0 amplitude  $u_{1z,0}^{\text{max,u}} = 0.76$  nm.

## B. Traveling and standing pressure waves induced by higher-harmonic membrane modes

Let us now turn to the resulting acoustic pressure field  $p_1$  in the liquid above the membrane vibrating in its res-

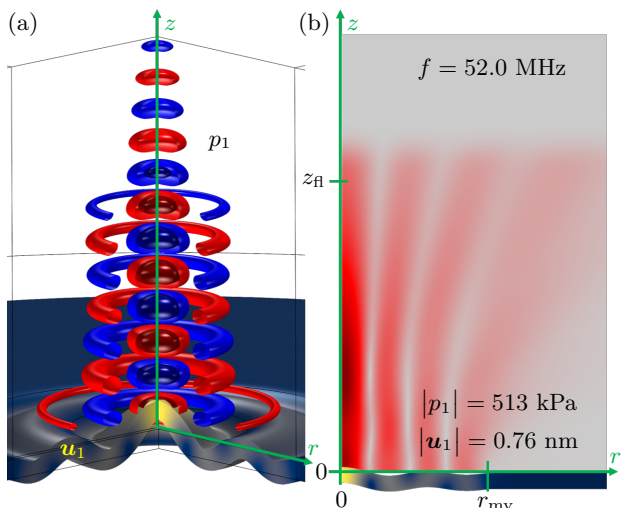


FIG. 3. (a) 3D contour plot of instantaneous isobars at  $-250$ ,  $-125$ ,  $125$ , and  $250$  kPa equivalent to Fig. 2(c) of the acoustic pressure  $p_1$  in the liquid above the membrane excited to resonance mode  $n = 3$  at  $52.0$  MHz by the patterned 3-ring electrode shown in Fig. 2(f,k). The displacement amplitude is enhanced by a factor 20,000 to be visible. An animation of  $p_1$  and  $\mathbf{u}_1$  is given in the Supplemental Material [37]. (b) A color plot similar to Fig. 2(c), but for the absolute value  $|p_1|$ .

onance modes  $n = 0$  and  $3$ . In Fig. 2(a) we see that a strong pressure wave is emitted from the antinode part of the vibrating membrane at  $2.16$  MHz in mode  $n = 0$  and absorbed in the PML domain. In Fig. 2(b), and more clearly in Fig. 2(c), we also see partial waves being emitted from each of the four antinodes in mode  $n = 3$  at  $52.0$  MHz. There is an important qualitative difference between the fundamental mode  $n = 0$  and any higher-harmonic mode  $n$ . The former emits only one partial wave, and thus  $p_1$  is devoid of interference patterns, whereas the latter emits  $n + 1$  partial waves from  $n + 1$  ring-shaped parts of the membrane surface. These partial waves interfere and give rise to a complex interference pattern stretching out in the bulk of the liquid above the membrane, such as seen in Fig. 2(c). This has profound implications for the acoustofluidic properties of the system, which we investigate further in Section IV.

In Fig. 3(a) is shown a 3D contour plot of instantaneous isobars equivalent to Fig. 2(c) of the acoustic pressure  $p_1$  in the liquid above the membrane excited to resonance mode  $n = 3$  at  $52.0$  MHz by the patterned electrode shown in Fig. 2(f,k). The pressure pattern consists of ring-shaped waves propagating upward in the  $z$  direction, while exhibiting standing waves in the radial direction.

This particular mixture of standing radial and traveling axial waves is clearly revealed by studying the color plot Fig. 3(b) of the absolute value  $|p_1|$  of the acoustic pressure. Following an outward radial path from  $r = 0$  at any given fixed height  $z = z_0$ , reveals regular oscillations in  $|p_1(r, z_0)|$  between nearly zero minima and large max-

ima, a characteristic of a standing radial wave. The most pronounced oscillation happens at height  $z_0 = 60$   $\mu\text{m}$ , and here we find the ratio  $\max |p_1| / \min |p_1| \approx 140$ , which corresponds to a nearly ideal standing wave.

When inspecting the pressure nodal surfaces (gray) in  $|p_1|$  in Fig. 3(b), we see that they form two nearly perfect and one deformed coaxial cylinder centered on the  $z$ -axis, but with a tendency to widen out as the distance to the membrane increases. Following any vertical path upward parallel to the  $z$ -axis,  $|p_1|$  is mainly monotonically decreasing, which is the characteristic of a nearly ideal damped traveling wave. One exception to this behavior is found along the  $z$ -axis, where a local maximum in  $|p_1(0, z)|$  is found for  $z \approx 60$   $\mu\text{m}$  above the center of the membrane. Here we estimate the ratio  $\max |p_1| / \min |p_1| \approx 1.3$ , which corresponds to a 1.0:0.3 mixture of a traveling and a standing wave. We shall see in Section IV that this small component of a standing wave along  $z$  together with the large standing wave component along  $r$  spawns a particle trap in all three spatial directions at some distance above the center of the vibrating silicon membrane.

### C. The effect of introducing a rigid lid

So far, we have assumed ideally absorbing surroundings by introducing the PML. As a result the pressure waves are traveling away from the membrane without being reflected back. In actual acoustofluidic systems, such a behavior is approximately realized by using soft PDMS rubber walls, as demonstrated recently by Skov *et al.* in a combined experimental and numerical study [38]. They also showed how replacing the soft lid with the other extreme, a hard glass lid, the traveling wave field was replaced by a standing wave field. Here, we briefly examine this latter case, by replacing the top PML in our model by a rigid lid placed at  $z = z_{fl}$  with a hard-wall boundary condition,  $\partial_z p_1 = 0$ , for the acoustic pressure. We keep the PML at the side to mimic an infinitely broad system.

The results of the rigid-lid simulation of  $p_1$  is shown in Fig. 4, where a vertical standing-wave behavior is clearly seen as horizontal nodal lines in the color plot of  $|p_1|$  in Fig. 4(b). However, since the PML at the side still allows for the waves to propagate away from the membrane, now predominantly in the radial direction, neither the membrane modes nor the maximum pressure amplitudes are much affected by replacing the PML lid with the rigid lid, as seen when comparing Figs. 3(b) and 4(b). The smooth behavior of  $|p(0, z)|$  is now overlaid with minor oscillations, but there is still a global pressure maximum along the  $z$ -axis.

Close to the membrane, the admixture of the vertical standing wave component is strong for the rigid-lid system, but still traveling waves are seen, as revealed by the animations of Figs. 2(c) and 4(b) given in the Supplemental Material [37]. As the characteristics of the pressure

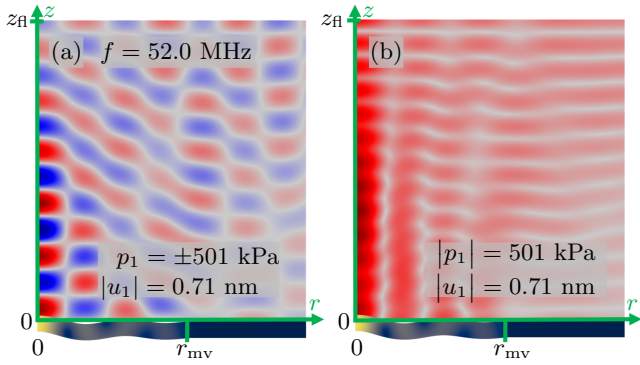


FIG. 4. The small membrane of Figs. 2 and 3 but with a hard-wall lid at  $z = z_{\text{fl}}$  instead of PML. (a) Same as Fig. 2(c) for the pressure  $p_1$ . An animation of  $p_1$  and  $\mathbf{u}_1$  is given in the Supplemental Material [37]. (b) Same as Fig. 3(b) for the magnitude  $|p_1|$  of the pressure  $p_1$ .

field are not strongly affected by the lid boundary condition, we continue using the previous case of an ideally absorbing lid in the following.

#### IV. CELL TRAPPING BY HIGHER-HARMONIC MEMBRANE MODES

We choose to illustrate the possibilities offered by the use of higher-harmonic membrane modes in acoustofluidics application with the example of trapping of a single suspended biological cell. Particle trapping is a central problem in the field studied by many groups. Examples are microparticle trapping in acoustic tweezers [39–44] and in disposable capillary tubes [28, 45], nanoparticle by using seed particles [46–48], and short and long term trapping [49, 50]. Trapping and the associated focusing has been created by various methods, including standing bulk [51, 52], traveling bulk [53], and surface [38, 54, 55] acoustic waves. An important focus area in the field is the trapping and focusing of biological cells in general [50, 56–58] and of circulating tumor cells in particular [30, 59, 60], in some cases accomplished by tuning the acoustic properties of the suspension medium tune relative to those of the given cells [30, 61].

##### A. Design of the membrane for cell trapping

In the following numerical simulation analysis of cell trapping, we choose as our model cell the breast cancer cell MCF-7 with the known acoustic parameters listed in Table I and here assumed to be spherical with a radius  $a_{\text{MCF-7}} = 10 \mu\text{m}$ . To facilitate acoustic trapping of such a cell, we prefer to work with an acoustic wavelength in the fluid larger than the cell,  $\lambda_0 \gtrsim 8a_{\text{MCF-7}} \approx 80 \mu\text{m}$ , or  $f_0 \lesssim 20 \text{ MHz}$ , a limit in which the long-wavelength limit expression (11a) of the acoustic radiation force on a

suspended particle is valid. Furthermore, for membrane mode  $n$  with radial wavelength  $\lambda_r^{(n)} \approx 2r_{\text{mv}}/(n + \frac{1}{2})$ , the mode frequency scales as  $f^{(n)} \propto [\lambda_r^{(n)}]^{-2}$ , and since  $f^{(n)} \propto \lambda_0^{-1}$  in the fluid, we can at membrane resonance write  $[\lambda_r^{(n)}]^2 = \lambda_0 L$ , where  $L$  is a parameter of dimension length characteristic for the given system. We find numerically that  $L \approx 110 \mu\text{m}$  in our system with a 10- $\mu\text{m}$ -thick silicon-membrane pushing on water. Combined with the long-wavelength criterion, we obtain  $\lambda_r^{(n)} = \sqrt{\lambda_0 L} \gtrsim \sqrt{8a_{\text{MCF-7}} L} \approx 94 \mu\text{m}$ . Finally, to ensure the formation of a trapping point on the  $z$ -axis, we must demand that  $\lambda_0 < \alpha \lambda_r^{(n)}$  (where  $\alpha \approx 1$  is a constant we have not been able to compute) because if not, the acoustic wave in the fluid propagates at an angle away from the  $z$ -axis. We thus conclude that all above criteria are satisfied if  $8a_{\text{MCF-7}} \lesssim \lambda_0 \lesssim \alpha^2 L$  (equivalent to  $12 \text{ MHz} \lesssim f_0 \lesssim 20\alpha^2 \text{ MHz}$ ) and  $\lambda_r^{(n)} \gtrsim 94 \mu\text{m}$ .

Consequently, as a proof of concept, we use the design shown in Fig. 5, consisting of a 10- $\mu\text{m}$ -thick silicon Si (111) disk membrane of radius  $r_{\text{mv}} = 500 \mu\text{m}$  driven in its  $n = 10$  harmonic mode with  $\lambda_r^{(10)} \approx 95 \mu\text{m}$  and

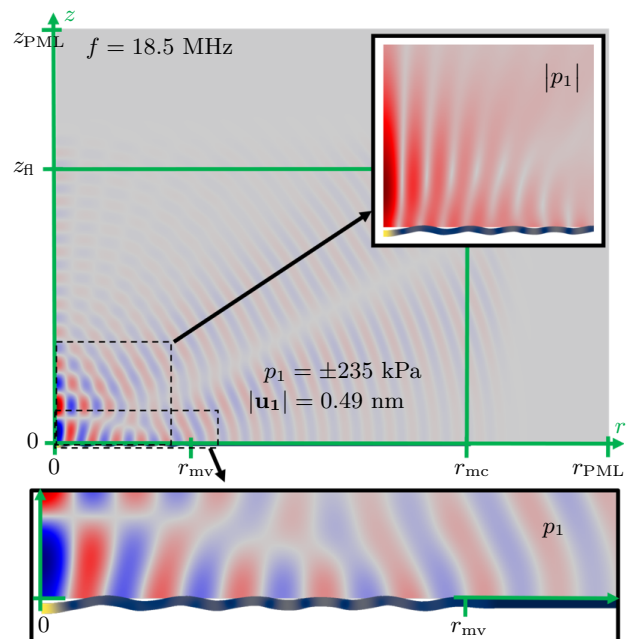


FIG. 5. A membrane device as in Fig. 2(c), but with  $r_{\text{mv}} = 500 \mu\text{m}$ ,  $r_{\text{mc}} = 1500 \mu\text{m}$ ,  $z_{\text{fl}} = 1000 \mu\text{m}$ , and with the excitation electrode is divided into 10 (instead of 3) ring-shaped segments each 44  $\mu\text{m}$  wide, separated by 4- $\mu\text{m}$ -wide gaps (not shown), and excited with alternating voltages  $\pm \frac{1}{2} \varphi_0$  as in Fig. 2(f,k). Color plots of the pressure  $\text{Re}[p_1]$  from  $-235$  (blue) to  $+235$  kPa (red) and of  $|\mathbf{u}_1|$  from 0 (blue) to 0.49 nm (yellow) for the  $n = 10$  higher-harmonic mode at 18.5 MHz. The top inset is a color plot of  $|p_1|$ . The bottom inset shows details of  $p_1$  and  $|\mathbf{u}_1|$ . An animation of  $p_1$  and  $\mathbf{u}_1$  is given in the Supplemental Material [37].

an estimated resonance frequency  $f^{(10)} \approx Lc_0/[\lambda_r^{(10)}]^2 \approx 18.2$  MHz. Similar to Fig. 2(f,k) of mode  $n = 3$ , the mode  $n = 10$  is excited by patterning the excitation electrode of the 1- $\mu\text{m}$ -thick  $\text{Al}_{0.6}\text{Sc}_{0.4}\text{N}$  transducer into ten ring-shaped segments. A 1  $V_{\text{pp}}$  AC voltage is applied to these segments with alternating phases  $+\frac{1}{2}\varphi_0$  and  $-\frac{1}{2}\varphi_0$ , resulting in a strong excitation of resonance mode  $n = 10$  at  $f = 18.5$  MHz, close to the prediction  $f^{(10)}$ . All the features seen in Fig. 5 of the disk-membrane displacement field  $\mathbf{u}_1$  and of the pressure field  $p_1$  in the liquid are the same as in Fig. 2(c), and the amplitudes are relatively large being  $|\mathbf{u}_1| = 0.49$  nm and  $|p_1| = 235$  kPa. Of particular interest for trapping, we notice a local maximum in  $|p_1(0, z)|$  in the inset of Fig. 5 near  $z = 100$   $\mu\text{m}$ , similar to the one at  $z = 60$   $\mu\text{m}$  shown in Fig. 3(b).

### B. Characterizing the cell trap

To characterize the cell trap, we study the total force  $\mathbf{F}^{\text{pt}}$  (13a) that acts on a MCF-7 cell suspended in water. In Fig. 6(a,b) is shown the contour plots of the radial and axial components  $F_r^{\text{pt}}$  and  $F_z^{\text{pt}}$  of  $\mathbf{F}^{\text{pt}}$ . To set the scale, we note that in this case, the buoyancy-corrected gravitational force is  $F_{\text{wa}}^{\text{grav}} = 2.3$  pN and the Stokes drag force is  $F_{\text{wa}}^{\text{drag}}(10 \mu\text{m/s}) = 1.7$  pN assuming that the velocity of the cell relative to water is 10  $\mu\text{m/s}$ . Firstly, we note that  $\mathbf{F}^{\text{pt}}$  with a magnitude above 70 pN is completely dominated by the radiation force  $\mathbf{F}^{\text{rad}}$ , secondly that  $F_r^{\text{pt}} \gtrsim F_z^{\text{pt}}$ , and thirdly that using pure water,  $\mathbf{F}^{\text{pt}}$  expels the cell from the primary nodal plane, instead of trapping it, as indicated by the black arrows.

This anti-trapping is a well-known result in trapping theory for a particle more heavy and rigid than the fluid in a single traveling wave [44]. To change the system into a trap, we need to tune the acoustic properties of the fluid to reverse the signs of the scattering coefficients  $f_0$  and  $f_1$ . This can be done by using the density modifier iodixanol as demonstrated in Refs. [30, 62–64].

In Fig. 6(c,d) is shown that indeed by using a 60% aqueous iodixanol solution that is heavier than pure water, the particle force  $\mathbf{F}^{\text{pt}}$  is reversed: the orange regions of  $F_r^{\text{pt}} > 0$  in Fig. 6(a) turns into the cyan regions of  $F_r^{\text{pt}} < 0$  in Fig. 6(c), and *vice versa*. Also, the yellow regions of  $F_z^{\text{pt}} > 0$  in Fig. 6(b) turns into the magenta regions of  $F_z^{\text{pt}} < 0$  in Fig. 6(d), and *vice versa*. The characteristic forces for the solution are  $F_{I60\%}^{\text{grav}} = -11$  pN and  $F_{I60\%}^{\text{drag}}(10 \mu\text{m/s}) = 15$  pN. In Fig. 6(c) we see that radial force  $F_r^{\text{pt}}$  points toward the  $z$  axis for  $r_{\text{mv}} \lesssim 20$   $\mu\text{m}$ , reaching a maximum amplitude of 234 pN at the height  $z_{\text{trap}} \approx 70$   $\mu\text{m}$ . However, the axial component  $F_z^{\text{pt}}$  is an order of magnitude smaller, and when plotting  $F_z^{\text{pt}}(0, z)$  along the  $z$ -axis, we find that although it has the desired upward direction  $F_z^{\text{pt}}(0, z) > 0$  for  $z < z_{\text{trap}}$ , it is still positive at its minimum at  $z = z_{\text{trap}}$ ,  $F_z^{\text{pt}}(0, z_{\text{trap}}) \approx +5$  pN. The setup is thus not a trap at all, because as the numer-

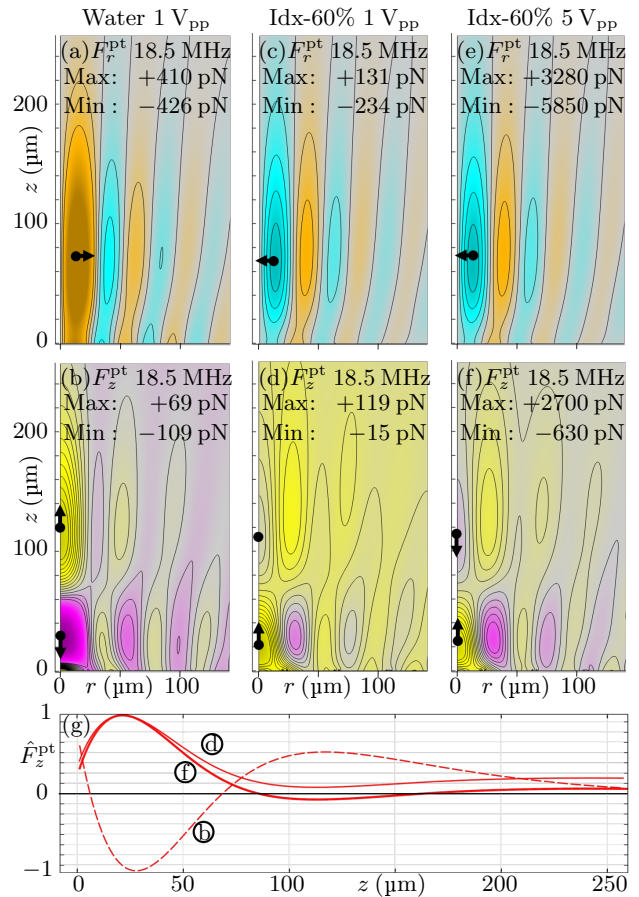


FIG. 6. Contour plots of the simulated components  $F_r^{\text{pt}}$  and  $F_z^{\text{pt}}$  of the force  $\mathbf{F}^{\text{pt}}$  acting on MCF-7 cells in the system shown in Fig. 5, but for different liquids and voltage amplitudes: (a,b) Water at 1  $V_{\text{pp}}$ , (c,d) 60% iodixanol at 1  $V_{\text{pp}}$ , and (e,f) 60% iodixanol at 5  $V_{\text{pp}}$ , using the parameters in Table I. The contour lines for  $F_r^{\text{pt}}$  are from  $-200$  to  $100$  pN in steps of  $50$  pN in (a,c), but from  $-5$  to  $2.5$  nN in steps of  $1.25$  nN in (e). The contour lines for  $F_z^{\text{pt}}$  are from  $-20$  to  $50$  pN in steps of  $5$  pN in (b,d), but  $-0.5$  to  $1.25$  nN in steps of  $0.125$  nN in (f). The black arrows indicate the components direction. (g) Line plot of the normalized vertical force component  $\hat{F}_z^{\text{pt}}$  along the  $z$ -axis for case (b), (d), and (f).

ical simulation reveals, at  $z_{\text{trap}}$  we have  $F_z^{\text{rad}} = -20$  pN,  $F_z^{\text{drag}} = +14$  pN, and  $F_z^{\text{grav}} = +11$  pN, such that  $F_z^{\text{pt}} = (-20 + 14)$  pN +  $11$  pN =  $5$  pN  $> 0$  pN.

A trap is achieved simply by enhancing the AC voltage amplitude from the 1  $V_{\text{pp}}$  to 5  $V_{\text{pp}}$ . This enhances the magnitude of the voltage-dependent second-order forces  $\mathbf{F}^{\text{rad}}$  and  $\mathbf{F}^{\text{drag}}$  by a factor  $5^2 = 25$ , leaving the gravitation force unchanged. Changing from 1  $V_{\text{pp}}$  to 5  $V_{\text{pp}}$ , we thus expect the weakest point in the trap to attain the value  $\mathbf{F}^{\text{pt}} = (-234 \times 25, (-20 + 14) \times 25 + 11)$  pN =  $(-5850, -119)$  pN, and this is exactly what is obtained, as shown in Fig. 6(e,f). So using an appropriate tuning of density of the liquid and of the excitation voltage, our

system is able to trap the MCF-7 cell in a trapping point located on the  $z$ -axis approximately  $70 \mu\text{m}$  above the membrane as revealed by the red thick line in Fig. 6(g).

As shown in Fig. 6(e), radial trapping occurs once the cell enters the cyan region where  $F_r^{\text{pt}} < 0$ . However, we notice that this region is surrounded by barrier-like orange region with  $F_r^{\text{pt}} > 0$ , which repels the cell. This barrier could make it difficult for the cell to enter the trapping region in the first place, however once trapped, the barrier prevents more particles to enter the trap. This aspect is discussed further in Section V. To gain a better understanding of how the trap is loaded, we study in the steady acoustic streaming in the following.

### C. Steady acoustic streaming in the trap

In the system with an acoustic wave propagating upward from a vibrating membrane, the acoustic streaming is dominated by the bulk-driven Eckart streaming due to the force density (10)  $\mathbf{f} = -\frac{\Gamma_{\text{fl}}\omega}{2c_{\text{fl}}^2} \text{Re}[p_1^* \mathbf{v}_1^d]$  from the upward traveling acoustic wave, whereas the Rayleigh boundary-driven streaming is negligible. In Fig. 7 is shown the simulated streaming for the 60% iodixanol solution at 18.5 MHz and  $5 V_{\text{pp}}$  corresponding to Fig. 6(e,f). The dominant feature is the toroidal vortex centered at  $(r, z) = (200, 140) \mu\text{m}$ , which drags in particles down toward the membrane near  $r = 300 \mu\text{m}$  and then sends them upward along the lower part of the  $z$ -axis, exactly where the trapping point is located. The flow velocity there is  $247 \mu\text{m/s}$  corresponding to a Stokes drag force on a trapped cell of  $F^{\text{drag}} = 358 \text{ pN}$ , which is

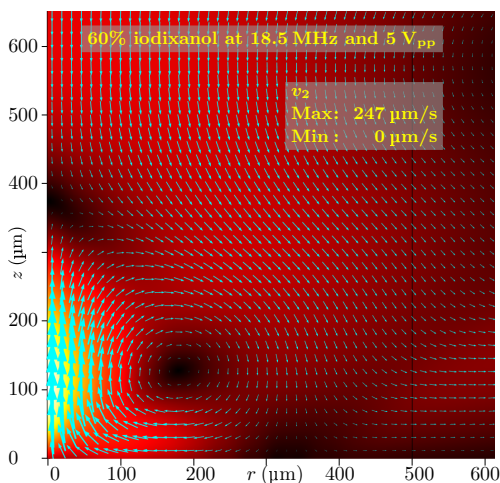


FIG. 7. Vector plot (cyan arrows) of the steady streaming  $\mathbf{v}_2$  and a color plot of  $|\mathbf{v}_2|$  from 0 (black) to  $247 \mu\text{m/s}$  (white) in a 60% iodixanol solution at  $f = 18.5 \text{ MHz}$  and  $5 V_{\text{pp}}$  corresponding to Fig. 6(e,f) of the membrane driven in mode  $n = 10$ . Bulk-driven Eckart streaming dominates over boundary-driven Rayleigh streaming.

a factor of 1.4 lower than the dominant radiation force,  $F_z^{\text{rad}} = 500 \text{ pN}$ . The trap thus work well for the large cancer cells, but less so for smaller cells, and we can estimate the critical cell radius  $a_{\text{cr}}$ , below which the cell is not trapped as  $a_{\text{cr}} = \sqrt{F_z^{\text{drag}}(10 \mu\text{m})/F_z^{\text{rad}}(10 \mu\text{m})} 10 \mu\text{m} = 8.5 \mu\text{m}$ . [65]

## V. DISCUSSION OF THE RESULTS

In the following, we discuss various aspects of the higher-harmonic membrane trap, its advantages and disadvantages. Some of these aspects are particular to the specific type of trap, while other apply to single-cell traps in general.

*Arrays of traps.* One distinct advantage of the membrane trap is its relatively small size, which permits the fabrication of arrays of single-cell traps for parallel analysis that can be turned on and off in a controlled manner. The design with  $(r_{\text{mv}}, n) = (500 \mu\text{m}, 10)$  analyzed in Fig. 5 allows for placing one trap per  $\text{mm}^2$ , a density that can be increased by identifying membrane modes with the desired properties for smaller values of  $r_{\text{mv}}$ .

*Improved loading by turning the trap upside down.* In Section IV C, it was mentioned how the toroidal streaming vortex of the membrane trap helped loading the trap. Given that  $\mathbf{F}^{\text{grav}}$  points upward, a further improvement of the loading process can be achieved by placing the membrane trap above the liquid instead of below. In this case cells would sediment upward toward the membrane, even when the acoustics is turned off. By subsequent actuation of the acoustics, the cells would be in a good position to be carried into the trap by the toroidal vortex. A further advantage of the inverted trap geometry is that trapping can be obtained at lower excitation voltages and for smaller particles due to a favorable interplay between  $\mathbf{F}^{\text{grav}}$  and  $\mathbf{F}^{\text{drag}}$  [66]. Turning the trap described in Section IV B upside down reduces the critical trapping radius  $a_{\text{cr}}$  by 30%.

*Reduction of the radial force barrier.* If the repelling force barrier surrounding the trap region poses a problem, as mentioned in Section IV B, it would be possible to reduce and perhaps even remove it by careful further tuning of the liquid. As studied by Qiu *et al.* [64], a range of carrier fluids with different acoustic properties can be created using solutions of Ficoll or iodixanol. In Fig. 8 we show the result of a purely theoretical computation of  $\mathbf{F}^{\text{pt}}$  for the 60% iodixanol solution of Fig. 6(c,d), were we assume it possible to keep all parameters constant, while lowering the density from its actual value,  $\rho_{\text{fl}}^{\text{Idx}, 60\%} = 1320 \text{ kg m}^{-3}$ , to match that of the MCF-7 cell,  $\rho_{\text{MCF-7}} = 1055 \text{ kg m}^{-3}$ , and even lower to  $930 \text{ kg m}^{-3}$ . Were it possible to find a liquid with these parameters, we see in Fig. 8(a,c), how the force barrier is strongly reduced in the neutral buoyant case, and nearly vanished in the low-density case of in Fig. 8(b,d).

*Creating an axial pressure node by breaking the ax-*

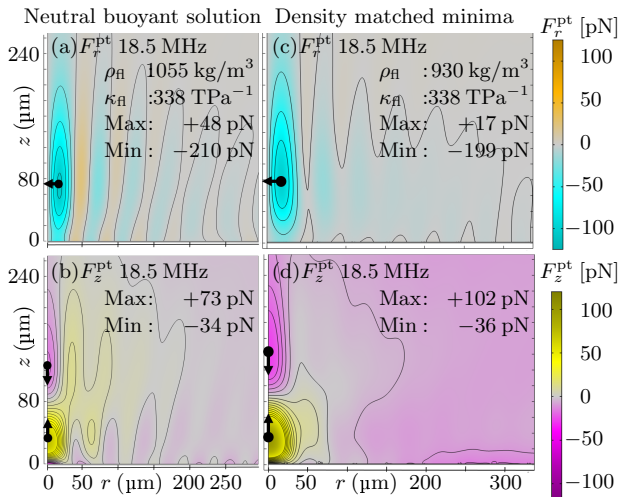


FIG. 8. Color plots of  $F_r^{\text{pt}}$  and  $F_z^{\text{pt}}$  in a 60% iodixanol solution at 18.5 MHz and  $1 V_{\text{pp}}$  as in Fig. 6(c,d), but assuming theoretically a reduction in the density from its actual value  $\rho_{\text{f}}^{\text{Idx},60\%} = 1320 \text{ kg m}^{-3}$ , while keeping all other parameters constant. (a) The neutral buoyant case  $\rho_{\text{f}}^{\text{Idx},60\%} = \rho_{\text{MCF-7}} = 1055 \text{ kg m}^{-3}$ . (b) A low-density case  $\rho_{\text{f}}^{\text{Idx},60\%} = 930 \text{ kg m}^{-3}$ .

*isymmetry.* The anti-trapping of cells in water shown in Fig. 6(a,b) is removed in Bessel-beam traps by breaking the axisymmetry and create a pressure node along the  $z$ -axis [44]. It would be interesting to study if a similar effect could be achieved in the membrane trap. It may be done by creating segments in the excitation electrode both in the radial and azimuthal direction, and then excite a rotating higher-harmonic mode by running the excitation voltage with appropriate phase shifts in the azimuthal direction as in Ref. [67].

*Sign-change of the radiation force for shorter wave lengths.* The anti-trapping of the membrane trap may be circumvented in a different way by working in the regime where the acoustic wavelength  $\lambda_0$  is comparable to the cell radius  $a$ . In this regime diffraction effects may change the sign of the radiation force [68]. A recent numerical study on suspended white blood cell has shown such a sign reversal to occur for  $a \approx 0.4\lambda_0$  [69]. This points to a way of getting the membrane trap to work without tuning of the suspension medium, and would perhaps therefore also work for a standard isotonic saline solution.

*Trapping of smaller-sized particles.* Given the relatively strong bulk-driven Eckart streaming in the membrane trap, it is not easy to reduce the critical radius from the above-mentioned value of  $a_{\text{cr}} = 8.5 \mu\text{m}$ . Several of the methods proposed in the literature are for systems dominated by boundary-driven Rayleigh streaming [53, 70, 71]. Perhaps only the method of trapped large seed particles would be a way to trap

smaller particles in the membrane trap [46].

## VI. CONCLUSION

In this paper, we have shown in a numerical study, how the concept of selective and efficient excitation of higher-harmonic disk membrane modes can be applied to acoustofluidic systems. The physical mechanism is based on the actuation of 1- $\mu\text{m}$ -thick piezoelectric  $\text{Al}_{0.6}\text{Sc}_{0.4}\text{N}$  thin-film transducers by patterning the excitation electrodes to match the out-of-phase strain pattern in the transducer at specific mode. As a proof of concept, we have shown that the  $n = 3$  higher-harmonic mode in an axisymmetric 200- $\mu\text{m}$ -diameter, 10- $\mu\text{m}$ -thick silicon membrane actuated at a frequency 52 MHz, emits pressure waves from each anti-node which results in interference patterns in the pressure field in a liquid placed above the membrane. When the condition that the wavelength in the liquid is smaller than that of the node spacing in the membrane mode, the interference pattern in the liquid can create a global pressure maximum in some distance above the membrane.

Our main example demonstrated how the global pressure maximum can be associated with the appearance of a single-cell trap, if the suspending liquid is tuned such that the cells have a negative acoustic contrast factor. In our model, this tuning was achieved by using a 60% iodixanol solution. To lower the operating frequency and obtain a wave length larger than the cell, the  $n = 10$  higher-harmonic mode in 1000- $\mu\text{m}$ -diameter, 10- $\mu\text{m}$ -thick membrane was excited at 18.5 MHz using appropriately patterned excitation electrodes. We showed numerically that MCF-7 cancer cells could be trapped approximately 70  $\mu\text{m}$  above the center of the membrane. Several aspects of the trap was discussed arrays of traps, an inverted setup, reduction of the radial force barrier in the trap, the creation of an axial pressure mode, and the sign-change of the radiation force at shorter wave lengths.

Our analysis demonstrate the higher-harmonic MHz acoustic modes can be excited selectively and efficiently in acoustofluidic systems by appropriate patterning of transducer electrodes in thin-film transducers. Such modes may prove useful in practical applications, such as the single-cell trap analyzed in our main example.

## ACKNOWLEDGEMENTS

This work was supported by the *BioWings* project funded by the European Union's Horizon 2020 *Future and Emerging Technologies* (FET) programme, grant No. 801267.

- 
- [1] P. Reichert, D. Deshmukh, L. Lebovitz, and J. Dual, Thin film piezoelectrics for bulk acoustic wave (BAW) acoustophoresis, *Lab Chip* **18**, 3655 (2018).
- [2] A. G. Steckel, H. Bruus, P. Mural, and R. Matloub, Fabrication, characterization, and simulation of glass devices with AlN thin-film transducers for excitation of ultrasound resonances, *Phys. Rev. Applied* **16**, 014014, 1 (2021).
- [3] A. G. Steckel and H. Bruus, Numerical study of bulk acoustofluidic devices driven by thin-film transducers and whole-system resonance modes, *J. Acoust. Soc. Am.* **150**, 634 (2021).
- [4] K. Brenner, A. S. Ergun, K. Firouzi, M. F. Rasmussen, Q. Stedman, and B. P. Khuri-Yakub, Advances in capacitive micromachined ultrasonic transducers, *Micromachines* **10**, 152, (27 pp) (2019).
- [5] W. Cui, H. Zhang, H. Zhang, Y. Yang, M. He, H. Qu, W. Pang, D. Zhang, and X. Duan, Localized ultrahigh frequency acoustic fields induced micro-vortices for sub-milliseconds microfluidic mixing, *Appl. Phys. Lett.* **109**, 253503 (6 pp) (2016).
- [6] W. Cui, L. Mu, X. Duan, W. Pang, and M. A. Reed, Trapping of sub-100 nm nanoparticles using gigahertz acoustofluidic tweezers for biosensing applications, *Nanoscale* **11**, 14625 (2019).
- [7] J. Qian, R. Yang, H. Begum, and J. E.-Y. Lee, Reconfigurable acoustofluidic manipulation of particles in ring-like rich patterns enabled on a bulk micromachined silicon chip, in *2021 21st International Conference on Solid-State Sensors, Actuators and Microsystems (Transducers)* (IEEE, 2021) pp. 365–368.
- [8] P. Delsing, A. N. Cleland, M. J. A. Schuetz, J. Knoerzer, G. Giedke, J. I. Cirac, K. Srinivasan, M. Wu, K. C. Balram, C. Bauerle, T. Meunier, C. J. B. Ford, P. V. Santos, E. Cerda-Mendez, H. Wang, H. J. Krenner, E. D. S. Nysten, M. Weiss, G. R. Nash, L. Thevenard, C. Gourdon, P. Rovillain, M. Marangolo, J.-Y. Duquesne, G. Fischer-auer, W. Ruile, A. Reiner, B. Paschke, D. Denysenko, D. Volkmer, A. Wixforth, H. Bruus, M. Wiklund, J. Reboud, J. M. Cooper, Y. Fu, M. S. Brugger, F. Rehfeldt, and C. Westerhausen, The 2019 surface acoustic waves roadmap, *J. Phys. D Appl. Phys.* **52**, 353001 (40pp) (2019).
- [9] W. N. Bodé, L. Jiang, T. Laurell, and H. Bruus, Microparticle acoustophoresis in aluminum-based acoustofluidic devices with PDMS covers, *Micromachines* **11**, 292 (2020).
- [10] F. Lickert, M. Ohlin, H. Bruus, and P. Ohlsson, Acoustophoresis in polymer-based microfluidic devices: Modeling and experimental validation, *J. Acoust. Soc. Am.* **149**, 4281 (2021).
- [11] M. Bora and M. Shusteff, Efficient coupling of acoustic modes in microfluidic channel devices, *Lab Chip* **15**, 3192 (2015).
- [12] R. P. Moiseyenko and H. Bruus, Whole-system ultrasound resonances as the basis for acoustophoresis in all-polymer microfluidic devices, *Phys. Rev. Applied* **11**, 014014 (2019).
- [13] A. Tahmasebipour, L. Friedrich, M. Begley, H. Bruus, and C. Meinhart, Toward optimal acoustophoretic microparticle manipulation by exploiting asymmetry, *J. Acoust. Soc. Am.* **148**, 359 (2020).
- [14] B. Hammarström, N. R. Skov, K. Olofsson, H. Bruus, and M. Wiklund, Acoustic trapping based on surface displacement of resonance modes, *J. Acoust. Soc. Am.* **149**, 1445 (2021).
- [15] F. Wein, M. Kaltenbacher, and M. Stingl, Topology optimization of a cantilevered piezoelectric energy harvester using stress norm constraints, *Struct. Multidiscip. O.* **48**, 173 (2013).
- [16] S. Du, Y. Jia, S.-T. Chen, C. Zhao, B. Sun, E. Arroyo, and A. A. Seshia, A new electrode design method in piezoelectric vibration energy harvesters to maximize output power, *Sensor. Actuat. A-Phys.* **263**, 693 (2017).
- [17] H. Fu, G. Chen, and N. Bai, Electrode coverage optimization for piezoelectric energy harvesting from tip excitation, *SENSORS* **18** (2018), 10.3390/s18030804.
- [18] Z. Yang, S. Zhou, J. Zu, and D. Inman, High-performance piezoelectric energy harvesters and their applications, *Joule* **2**, 642 (2018).
- [19] A. Luo, Y. Zhang, X. Guo, Y. Lu, C. Lee, and F. Wang, Optimization of MEMS vibration energy harvester with perforated electrode, *J. Microelectromech. S.* **30**, 299 (2021).
- [20] J. S. Pulskamp, S. S. Bedair, R. G. Polcawich, G. L. Smith, J. Martin, B. Power, and S. A. Bhave, Electrode-shaping for the excitation and detection of permitted arbitrary modes in arbitrary geometries in piezoelectric resonators, *IEEE transactions on ultrasonics, ferroelectrics, and frequency control* **59**, 1043 (2012).
- [21] COMSOL Multiphysics 5.5 (2019), <http://www.comsol.com>.
- [22] N. R. Skov, J. S. Bach, B. G. Winkelmann, and H. Bruus, 3D modeling of acoustofluidics in a liquid-filled cavity including streaming, viscous boundary layers, surrounding solids, and a piezoelectric transducer, *AIMS Mathematics* **4**, 99 (2019).
- [23] J. S. Bach and H. Bruus, Theory of pressure acoustics with viscous boundary layers and streaming in curved elastic cavities, *J. Acoust. Soc. Am.* **144**, 766 (2018).
- [24] M. A. Hopcroft, W. D. Nix, and T. W. Kenny, What is the Young's modulus of silicon, *J. Microelectromech. Syst* **19**, 229 (2010).
- [25] E. V. Thomsen, K. Reck, G. Skands, C. Bertelsen, and O. Hansen, Silicon as an anisotropic mechanical material: Deflection of thin crystalline plates, *Sensors and Actuators A: Physical* **220**, 347 (2014).
- [26] S. Trolier-McKinstry and P. Mural, Thin film piezoelectrics for MEMS, *Journal of Electroceramics* **12**, 7 (2004).
- [27] M. Settne and H. Bruus, Theoretical analysis of viscous corrections to the acoustic radiation force on cells in microchannel acoustophoresis, in *Proc. 15th MicroTAS, 2 - 6 October 2011, Seattle (WA), USA*, edited by J. Landers, A. Herr, D. Juncker, N. Pamme, and J. Bienvenue (CBMS, 2011) pp. 160–162.
- [28] M. W. H. Ley and H. Bruus, Three-dimensional numerical modeling of acoustic trapping in glass capillaries, *Phys. Rev. Applied* **8**, 024020 (2017).
- [29] P. B. Muller and H. Bruus, Numerical study of thermoviscous effects in ultrasound-induced acoustic streaming in microchannels, *Phys. Rev. E* **90**, 043016 (2014).

- [30] P. Augustsson, J. T. Karlsen, H.-W. Su, H. Bruus, and J. Voldman, Iso-acoustic focusing of cells for size-insensitive acousto-mechanical phenotyping, *Nat. Commun.* **7**, 11556 (2016).
- [31] J. An, J. Lee, S. H. Lee, J. Park, and B. Kim, Separation of malignant human breast cancer epithelial cells from healthy epithelial cells using an advanced dielectrophoresis-activated cell sorter (dacs), *Analytical and bioanalytical chemistry* **394**, 801 (2009).
- [32] K. W. Cushing, F. Garofalo, C. Magnusson, L. Ekblad, H. Bruus, and T. Laurell, Ultrasound characterization of microbead and cell suspensions by speed of sound measurements of neutrally buoyant samples, *Anal. Chem.* **89**, 8917 (2017).
- [33] M. A. Caro, S. Zhang, T. Riekkinen, M. Ylilammi, M. A. Moram, O. Lopez-Acevedo, J. Molarius, and T. Laurila, Piezoelectric coefficients and spontaneous polarization of ScAlN, *J. Phys.-Condens. Mat.* **27**, 245901 (2015).
- [34] R. H. Olsson, Z. Tang, and M. D'Agati, Doping of aluminum nitride and the impact on thin film piezoelectric and ferroelectric device performance, in *2020 IEEE Custom Integrated Circuits Conference (CICC)* (2020) pp. 1–6.
- [35] J. Kim, D.-i. D. Cho, and R. S. Muller, Why is (111) silicon a better mechanical material for MEMS? in *Transducers 01 Eurosensors XV* (Springer, 2001) pp. 662–665.
- [36] P. Hahn and J. Dual, A numerically efficient damping model for acoustic resonances in microfluidic cavities, *Physics of Fluids* **27**, 062005 (2015).
- [37] See Supplemental Material at [http://bruus-lab.dk/files/Steckel\\_membrane\\_Suppl.zip](http://bruus-lab.dk/files/Steckel_membrane_Suppl.zip) for animations of  $p_1$  and  $u_1$  in Fig. 2(a), Fig. 2(c), Fig. 3(a), Fig. 4, and Fig. 5.
- [38] N. R. Skov, P. Sehgal, B. J. Kirby, and H. Bruus, Three-dimensional numerical modeling of surface-acoustic-wave devices: Acoustophoresis of micro- and nanoparticles including streaming, *Phys. Rev. Applied* **12**, 044028 (2019).
- [39] D. Baresch, J.-L. Thomas, and R. Marchiano, Observation of a single-beam gradient force acoustical trap for elastic particles: Acoustical tweezers, *Phys. Rev. Lett.* **116**, 024301 (2016).
- [40] J. T. Karlsen and H. Bruus, Acoustic tweezing and patterning of concentration fields in microfluidics, *Phys. Rev. Applied* **7**, 034017 (2017).
- [41] A. Riaud, M. Baudoin, O. Bou Matar, L. Becerra, and J.-L. Thomas, Selective manipulation of microscopic particles with precursor swirling Rayleigh waves, *Phys. Rev. Applied* **7**, 024007 (2017).
- [42] M. Baudoin, J.-C. Gerbedoen, A. Riaud, O. B. Matar, N. Smagin, and J.-L. Thomas, Folding a focalized acoustical vortex on a flat holographic transducer: miniaturized selective acoustical tweezers, *Science advances* **5**, eaav1967 (2019).
- [43] Z. Gong and M. Baudoin, Particle assembly with synchronized acoustic tweezers, *Phys. Rev. Applied* **12**, 024045 (2019).
- [44] M. Baudoin and J.-L. Thomas, Acoustic tweezers for particle and fluid micromanipulation, *Annual Review of Fluid Mechanics* **52**, 205 (2020).
- [45] B. Hammarström, M. Evander, H. Barbeau, M. Bruzelius, J. Larsson, T. Laurell, and J. Nilsson, Non-contact acoustic cell trapping in disposable glass capillaries, *Lab Chip* **10**, 2251 (2010).
- [46] B. Hammarström, B. Nilson, T. Laurell, J. Nilsson, and S. Ekström, Acoustic trapping for bacteria identification in positive blood cultures with maldi-tof ms, *Anal. Chem.* **86**, 10560 (2014).
- [47] M. Evander, O. Gidlof, B. Olde, D. Erlinge, and T. Laurell, Non-contact acoustic capture of microparticles from small plasma volumes, *Lab Chip* **15**, 2588 (2015).
- [48] B. Hammarström, T. Laurell, and J. Nilsson, Seed particle enabled acoustic trapping of bacteria and nanoparticles in continuous flow systems, *Lab Chip* **12**, 4296 (2012).
- [49] B. Hammarström, M. Evander, J. Wahlström, and J. Nilsson, Frequency tracking in acoustic trapping for improved performance stability and system surveillance, *Lab Chip* **14**, 1005 (2014).
- [50] K. Olofsson, V. Carannante, M. Takai, B. Onfelt, and M. Wiklund, Ultrasound-based scaffold-free core-shell multicellular tumor spheroid formation, *Micromachines* **12**, 329 1 (2021).
- [51] S. M. Hagsäter, A. Lenshof, P. Skaftø-Pedersen, J. P. Kutter, T. Laurell, and H. Bruus, Acoustic resonances in straight micro channels: Beyond the 1D-approximation, *Lab Chip* **8**, 1178 (2008).
- [52] P. Augustsson, R. Barnkob, S. T. Wereley, H. Bruus, and T. Laurell, Automated and temperature-controlled micro-PIV measurements enabling long-term-stable microchannel acoustophoresis characterization, *Lab Chip* **11**, 4152 (2011).
- [53] J. S. Bach and H. Bruus, Suppression of acoustic streaming in shape-optimized channels, *Phys. Rev. Lett.* **124**, 214501 (2020).
- [54] J. Shi, D. Ahmed, X. Mao, S.-C. S. Lin, A. Lawit, and T. J. Huang, Acoustic tweezers: patterning cells and microparticles using standing surface acoustic waves (SSAW), *Lab Chip* **9**, 2890 (2009).
- [55] D. J. Collins, A. Neild, and Y. Ai, Highly focused high-frequency travelling surface acoustic waves (saw) for rapid single-particle sorting, *Lab Chip* **16**, 471 (2016).
- [56] P. Gascoyne, C. Mahidol, M. Ruchirawat, J. Satayavivad, P. Watcharasit, and F. F. Becker, Microsample preparation by dielectrophoresis: isolation of malaria, *Lab Chip* **2**, 70 (2002).
- [57] J. Nilsson, M. Evander, B. Hammarström, and T. Laurell, Review of cell and particle trapping in microfluidic systems, *Analytica Chimica Acta* **649**, 141 (2009).
- [58] K. T. Gustafson, K. T. Huynh, D. Heineck, J. Bueno, A. Modestino, S. Kim, A. Gower, R. Armstrong, C. E. Schutt, and S. D. Ibsen, Automated fluorescence quantification of extracellular vesicles collected from blood plasma using dielectrophoresis dagger, *Lab Chip* **21** (2021), 10.1039/d0lc00940g.
- [59] P. Li, Z. Mao, Z. Peng, L. Zhou, Y. Chen, P.-H. Huang, C. I. Truica, J. J. Drabick, W. S. El-Deiry, M. Dao, S. Suresh, and T. J. Huang, Acoustic separation of circulating tumor cells, *Proc. Natl. Acad. Sci. U.S.A.* **112**, 4970 (2015).
- [60] W. S. Low and W. A. B. W. Abas, Benchtop technologies for circulating tumor cells separation based on biophysical properties, *Biomed. Res. Int.* **2015**, 239362 (2015).
- [61] K. Olofsson, B. Hammarstrom, and M. Wiklund, Acoustic separation of living and dead cells using high density medium, *Lab Chip* **20**, 1981 (2020).
- [62] J. T. Karlsen, P. Augustsson, and H. Bruus, Acoustic force density acting on inhomogeneous fluids in acoustic fields, *Phys. Rev. Lett.* **117**, 114504 (2016).

- [63] J. T. Karlsen, W. Qiu, P. Augustsson, and H. Bruus, Acoustic streaming and its suppression in inhomogeneous fluids, *Phys. Rev. Lett.* **120**, 054501 (2018).
- [64] W. Qiu, J. T. Karlsen, H. Bruus, and P. Augustsson, Experimental characterization of acoustic streaming in gradients of density and compressibility, *Phys. Rev. Appl.* **11**, 024018 (2019).
- [65] P. B. Muller, R. Barnkob, M. J. H. Jensen, and H. Bruus, A numerical study of microparticle acoustophoresis driven by acoustic radiation forces and streaming-induced drag forces, *Lab Chip* **12**, 4617 (2012).
- [66] J. Li, A. Crivoi, X. Peng, L. Shen, Y. Pu, Z. Fan, and S. A. Cummer, Three dimensional acoustic tweezers with vortex streaming, *Communications Physics* **4**, 1 (2021).
- [67] S. B. Q. Tran, P. Marmottant, and P. Thibault, Fast acoustic tweezers for the two-dimensional manipulation of individual particles in microfluidic channels, *Appl. Phys. Lett.* **101**, 114103 (2012).
- [68] T. Hasegawa, Comparison of 2 solutions for acoustic radiation pressure on a sphere, *J. Acoust. Soc. Am.* **61**, 1445 (1977).
- [69] R. Habibi, C. Devendran, and A. Neild, Trapping and patterning of large particles and cells in a 1d ultrasonic standing wave, *Lab Chip* **17**, 33279 (2017).
- [70] W. Qiu, H. Bruus, and P. Augustsson, Particle-size-dependent acoustophoretic motion and depletion of micro- and nano-particles at long timescales, *Phys. Rev. E* **102**, 013108 (2020).
- [71] B. Winckelmann and H. Bruus, Theory and simulation of electroosmotic suppression of acoustic streaming, *J. Acoust. Soc. Am.* **149**, 3917 (2021).

## 5.4 Conference Paper I: Acoustofluidics 2020

*Numerical simulation of acoustic streaming generated by GHz AlN-thin-film transducers on AlN-SiO<sub>2</sub>-Bragg-reflector substrates.*

**Abstract book:** [Acoustofluidics 2020 - Abstract Book](#)

**PDF:** [Conference contribution PDF](#)

**Authors:** [André G. Steckel](#) and Henrik Bruus.

**Conference:** Acoustofluidics 2020 - Abstract Book **115-116** (2020)

[André G. Steckel](#) and Henrik Bruus, *Acoustofluidics 2020 - Abstract Book*, Acoustofluidics conference, 26-27 August 2020, **Oral presentation**. Remark: Contributed talk at virtual conference

# Numerical simulation of acoustic streaming generated by GHz AlN-thin-film transducers on AlN-SiO<sub>2</sub>-Bragg-reflector substrates

André G. Steckel and Henrik Bruus

Department of Physics, Technical University of Denmark, Kongens Lyngby, Denmark  
 E-mail: [angust@fysik.dtu.dk](mailto:angust@fysik.dtu.dk) , URL: <http://www.fysik.dtu.dk/microfluidics>

## Introduction

Gigahertz (GHz) acoustofluidics is an active and exciting field of research with many new challenges and applications, including chemical and biological detection [1], microfluidic mixing [2], on-demand droplet dispensing [3], and nanoparticle trapping [4]. To develop further the initial numerical modeling in the field [5], we apply here our recent 3D fully-coupled acoustofluidic model [6] to a generic GHz AlN-thin-film-transducer device presented in Ref. [2]. The model of the system takes into account the electro-, elasto-, and hydrodynamics as well as the strongly damped acoustics in the transducer, in the substrate below, and in the fluid and glass lid above. Typical acoustic wavelengths at 1.5 GHz are 1  $\mu\text{m}$  (water) and 3  $\mu\text{m}$  (SiO<sub>2</sub>), so a GHz-acoustofluidic system of size 10 to 100  $\mu\text{m}$  typically contains 10 - 100 acoustic wavelengths. The model reveals the complexity that arises from these many wavelengths, and we compute the acoustic streaming that is induced by the acoustic wave, as it is strongly attenuated within a distance of 50  $\mu\text{m}$  from the surface of the AlN-thin-film transducer.

## 3D acoustic simulations of a piezoelectric GHz AlN-thin-film transducer in vacuum

Acoustofluidics for the GHz regime requires specially designed transducers, systems that resonate at those frequencies, and direct contact or close proximity between the transducer and the liquid. This is necessary because of the strong acoustic attenuation at GHz frequencies. At 1.5 GHz the characteristic attenuation length in water is about 12  $\mu\text{m}$ , only 12 times the acoustic wavelength. By having the resonator embedded in the liquid, the energy transfer from the piezoelectric transducer is maximized. In Ref. [2], a pentagon-shaped GHz-AlN-thin-film transducer was placed on top of an AlN-SiO<sub>2</sub> Bragg reflector, resting on a silicon substrate, and used to generate strong acoustic streaming. Here, using our recent 3D acoustofluidic model implemented in COMSOL Multiphysics 5.4 [6] with material parameters for the AlN thin-film from Ref. [7], we model the acoustic modes in this system at first placed in vacuum. We show in Fig. 1 the resulting displacement field in the transducer and substrate when making three different assumptions for the absorption by the substrate.

We note in Fig. 1 the increased complexity of oscillation pattern of the displacement field that arises, when the 50- $\mu\text{m}$ -side-length pentagon in the 100- $\mu\text{m}$ -side-length square system is allowed to oscillate more freely at the high GHz frequencies by changing the absorption assumptions. Whereas some rare modes are found to have a displacement predominately in the vertical  $z$ -direction, the typical mode is a complex pattern exhibiting many small-wavelength structures across the surface.

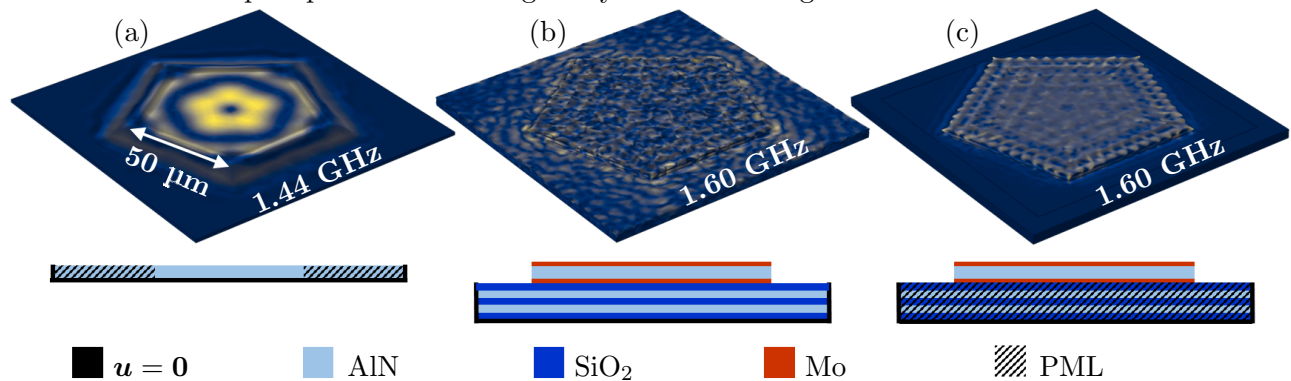


**Figure 1:** 3D simulations of the displacement field from 0 (blue) to 15  $\mu\text{m}$  (yellow) in the GHz AlN-thin-film transducer from Ref. [2] using the different model assumptions that are illustrated by the respective sketches below each result. (a) A 100- $\mu\text{m}$  square, 1.1- $\mu\text{m}$ -thick AlN-thin-film in vacuum with zero displacement on the bottom and sides. The pentagon (50  $\mu\text{m}$  side length) represents the top and bottom electrodes actuated by a  $1\text{-}V_{\text{pp}}$  GHz-ac voltage. The area outside the pentagon is modeled as a perfectly absorbing medium (PML). (b) The same pentagon-shaped transducer protruding from the surface and with the 0.16- $\mu\text{m}$ -thick metal electrodes included. It is placed on a AlN-SiO<sub>2</sub>-Bragg reflector with five 0.64- $\mu\text{m}$ -thick layers and with its bottom and side surfaces clamped. (c) The same as panel (b), but modeling the Bragg reflector as a perfect absorber (PML).

## 2D GHz acoustofluidic simulations of solids, piezoelectrics, and liquids with streaming

As shown in Fig. 2(a), we now insert the transducer of Fig. 1(b) in a larger system: the AlN-SiO<sub>2</sub> Bragg reflector is embedded in a 25- $\mu$ m-thick Si base, and a 40- $\mu$ m-high and 80- $\mu$ m-wide water domain is added above and enclosed in a 10- $\mu$ m-thick Pyrex casing. We simplify the simulation by restricting it to a vertical 2D cross section through the center of the device. Selected results using the method of Ref. [6] for simulating of the coupled Si-base-AlN-transducer-water-Pyrex system are shown in Fig. 2. In Fig. 2(a)-(c) is shown the displacement  $u_1$  (up to 110 pm) of the elastic solids and the highly attenuated acoustic pressure  $p_1$  (up to 890 kPa) in the water emanating from the transducer. The acoustic attenuation acts as a source for acoustic streaming, which we compute numerically using effective boundary layer theory [6]. The resulting streaming is shown in Fig. 2(d)-(f).

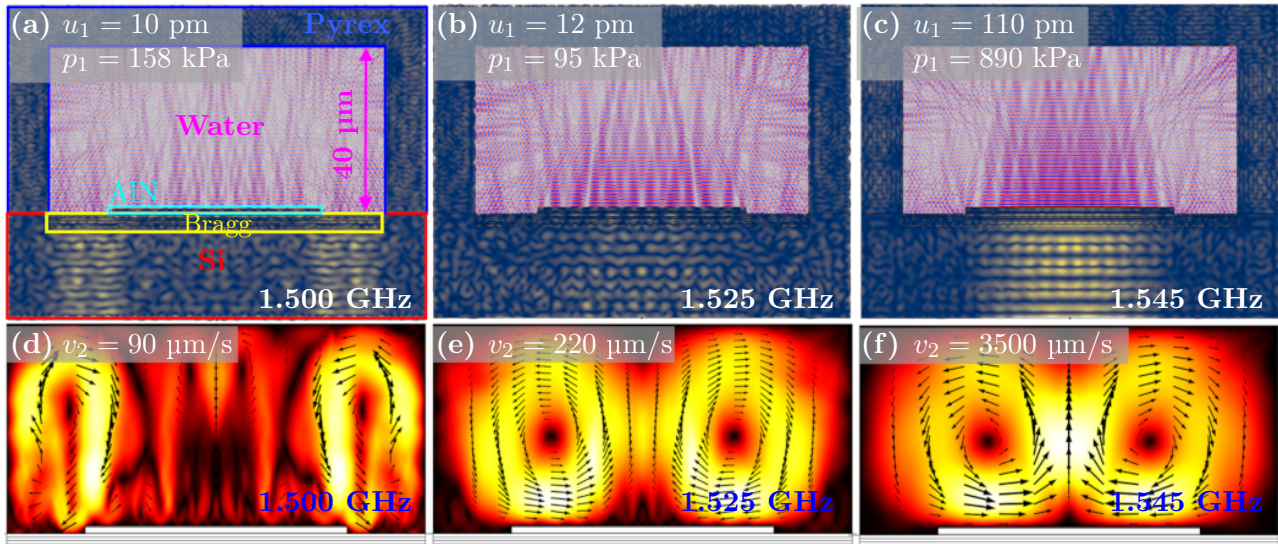


**Figure 2:** (a) Simulation at 1.500 GHz of the acoustic pressure  $p_1$  in the water (magenta) above the AlN-thin-film transducer (cyan), and the displacement  $u_1$  in the Pyrex (blue), the Bragg reflector (yellow), and the Si base (red). (b) The same, but for 1.525 GHz. (c) The same, but for 1.545 GHz. (d) Simulation of the acoustic streaming velocity  $v_2$  corresponding to panel (a). (e)  $v_2$  corresponding to (b). (f)  $v_2$  corresponding to (c).

The three nearly identical actuation frequencies result in qualitatively different acoustic fields, but similar streaming patterns. At 1.500 GHz, a vertical standing wave is set up in the Si-substrate to the sides away from the transducer region. This results in two streaming rolls above the edges of the transducer. At 1.525 GHz, a weak increase in acoustic intensity is seen below the transducer. The result is two weakly overlapping streaming rolls above the transducer and closer to the center. At 1.545 GHz, a strong standing wave is established directly under the transducer. Given the moderate actuation of only 1  $V_{pp}$ , the resulting streaming flow is fast (3.5 mm/s), and the two flow rolls are strongly overlapping with a maximum over the center of the transducer. The two-flow-roll pattern is a fairly robust feature, but the position and magnitude the flow rolls depends on the frequency.

## Conclusion

We have shown that our recent 3D fully coupled acoustofluidic model [6] can be applied to GHz acoustofluidics, in particular to AlN-thin-film-transducer devices. The simulations shown here reveal how complex the acoustic fields are in detail, but they also indicate the overall stability of the streaming rolls, which is ensured by the strong attenuation of the acoustic waves within a 40- $\mu$ m-range from the transducer. Our model is a promising tool for future design studies of GHz acoustofluidic devices.

## Acknowledgments

This work was supported by the BioWings project funded by the European Union's Horizon 2020 Future and Emerging Technologies (FET) programme, grant no. 801267.

## References

- [1] W. Pang, H. Zhao, E.S. Kim, H. Zhang, H. Yuc, and X. Hu. *Lab Chip* **12**, 29 (2012). [doi]
- [2] W. Cui, H. Zhang, Y. Yang, M. He, H. Qu, W. Pang, D. Zhang, and X. Duan. *Appl. Phys. Lett.* **109**, 253503 (2016). [doi]
- [3] M. He, Y. Zhou, W. Cui, Y. Yang, H. Zhang, X. Chen, W. Pang, D. Zhang, and X. Duan. *Lab Chip* **18**, 2540 (2018). [doi]
- [4] W. Cui, L. Mu, X. Duan, W. Pang, and M.A. Reed. *Nanoscale* **11**, 14625 (2019). [doi]
- [5] W. Cui, W. Pang, Y. Yang, T.Li., and X. Duan. *Nanotechnol. Precision Eng.* **2**, 15 (2019). [doi]
- [6] N. R. Skov, J. S. Bach, B. G. Winckelmann, and H Bruus. *AIMS Mathematics*, **4**, 99 (2019). [pdf]
- [7] M.A. Caro, S. Zhang, T. Riekkinen, M. Ylilammi, M.A. Moram, O. Lopez-Acevedo, J. Molarius, and T. Laurila. *J. Phys.-Condens. Mat.* **27**, 245901 (2015). [doi]



## Chapter 6

# Conclusion and outlook

This thesis is a study of some of the opportunities that thin-film electromechanical actuators present in acoustofluidics. The main work presented in this thesis pertains to the articles and each article has their own individual conclusion. In this conclusion, we will try to give a general conclusion that is not limited to discussing each individual result, but rather seeks to connect the results across papers. In the outlook portion, we will discuss how these results might be used in the future, discuss some of the work that would have been interesting to investigate going forward, and finally look at the larger perspective and consider how the results could be used in future acoustofluidic research.

### 6.1 Conclusion

The results presented in this thesis revolve around three separate papers, which are standalone results but which complement each other. The first paper showed that it is possible to actuate bulk acoustic modes in glass through piezoelectric (PZE) thin films that are deposited on it and that our model gives the correct mode spectra. This gives us confidence in our model and helps us in the second paper to predict how PZE thin-film transducers can be used to actuate acoustofluidic devices that can be used for focusing of particles in fluids, or in general, to actuate the system to achieve the same type of acoustofluidic action as with bulk PZE transducers. The thin-film transducers are clean-room and microelectromechanical systems (MEMS)-compatible, and therefore the processes are very reproducible and precise. For instance, as we saw in the first paper, the devices were quite reproducible when comparing the impedance spectra. This reproducibility of the small glass block devices is expected to carry over to the larger devices to an even larger degree, since the small variations in the small device, because of tolerances and small chips on the edge, would be relatively smaller for the large devices. Reproducibility of results, and in this case of devices, is a cornerstone of being able to understand and build upon the results to develop the devices and techniques further in an interdependent development of precision, control and understanding.

The second paper also found that matching the electrode patterning of PZE thin films to the strain pattern in the film, generated by modes in the solid, was important. It

was shown that by patterning the electrodes, it was possible to enhance the acoustofluidic action. By this we mean the first-order pressure field, acoustic streaming field, and acoustic radiation forces in the system of the standing full wave in the device. This was because the in-plane strain pattern was trying to both expand at some places and contract at other at the same time, and through the PZE coupling coefficient  $e_{13}$ , the orthogonal field would try to either compress or expand depending on the polarity of the electric field. A full electrode would therefore work against itself, since it would only try to expand or contract at any given phase. It was understood that this effect would be even more prominent in systems with many wavelengths, since for such systems the area that would effectively actuate the system would be limited to that which did not cancel out, and that area would diminish with a full electrode over more wavelengths. This knowledge was used to predict that it would be possible to access the higher-order modes of a membrane with a thin film deposited on it by patterning the film correspondingly, which turned out to be correct. It was subsequently guessed that, because of the appearance of the Bessel modes in the membrane, these modes might create an interference pattern and a pressure hot spot at a point above the center of the membrane, which might focus particles. This turned out to be the case; however, because of the axisymmetry of the system, the pressure and the central axis must be a node, and therefore only particles with negative acoustic contrast factor would be focused. Therefore, to focus the cancer cells investigated, the submersion fluid had to be changed to Iodixanol concentrations. It was further shown that by tuning the density in the model, the trapping could even be enhanced.

## 6.2 Outlook

This PhD thesis has shown *in situ* experimental determination of parameter values, by using PZE thin films, which could be further developed in the future. It has also shown some simulation of thin-film-PZE-driven bulk whole-system and membrane-driven results that would benefit greatly from experimental validation. How the results can be used in the future will be discussed first. Afterward, some ideas for further exploration in acoustofluidics will be presented. Lastly, we will conclude this thesis with a discussion of the results from a larger perspective.

### Results going forward

The thesis centers around three separate results and the outlook for each is quite different. The first result showed that it is indeed possible to determine the material parameters of a material by matching the impedance spectra of a thin film attached to the device. This worked in part because the thin-film PZE was such a small part of the system that the accuracy of the parameters of the PZE thin-film did not affect the system significantly. The parameters for the isotropic bulk material could therefore be fitted without worrying about the many parameters of the hexagonal aluminum nitride (AlN). One problem with the method is that it is limited to materials that can have AlN thin films deposited onto them and require access to a clean room capable of performing this process. One might imagine that a possible manner of avoiding this could be by using thin film PZE stickers,

that had a sacrificial layer on one side which is stiff but dissolvable, and a thin adhesion layer on the other side of the PZE thin-film, to attach to materials, and then the same procedure could be carried out to fit and match material parameters. This might work, because we do not need high acoustic energy in the system, but only enough to get a response from the material. Whether this could work or not is unknown but it is at least an idea for how this method could be used going forward.

The second result shows that thin-film transducers can actuate bulk devices for uses in acoustofluidics. The results are based on simulations and although the model has previously been validated by other experiments, it would be interesting to compare with experiments to further validate the model, as well as to engage in a feedback loop that could help further understand the mechanism and improve the concept. Early results have shown that the core concept works, in that an acoustofluidic bulk system can indeed be actuated by a thin-film PZE transducer, showing acoustic focusing of particles in a device; however, these are early results, and since they are not this thesis author's results alone, have not been emphasized in this thesis. That said, new experimental results are on the way from some of our experimental collaborators. There are many possibilities for these devices and it is difficult to guess exactly how they may be used in the future.

The third result is the enhancement of the higher order membrane modes by patterning the electrode of the thin film deposited on top of the membrane. These modes are therefore enhanced and the pressure hot spot above the center of the thin film allows for trapping of cells with a change of the submersion fluid. It would be ideal to see this result validated by experiment in the future, as the trapping shows promise. The hope is that in the future this could become a standalone device, used for trapping arrays of cells, when they cannot be allowed to sediment for one reason or other. One example would be studying cells that mimic the conditions of free-floating circulating tumor cells, instead of how cancer cells grow on the surface of a petri dish. One might imagine that the devices would be placed in a petri dish and fluid would be added with the cells containing it, and then turned on, at which point the cells would be suspended in the array above the membranes for the duration of a biological assay. There are of course also many other uses for enhancing membrane modes which the future might show, and we only can speculate on at this point. Some of these speculations will be expanded upon next.

### **Further explorations in acoustofluidics**

One topic that would have been interesting to explore further is expanding the parameter fitting in Paper I to a more advanced and autonomous fitting procedure such that we might not only have achieved a better fit on the Young's modulus and Poisson's ratio of the glass parameters, but might also have achieved a fitting of the dampening in the device. How this dampening would have behaved would have been a nice result to add to the already fitted parameters. The parameters of the thin film would most likely not have been possible to fit to this system, simply because the bulk peaks were so insensitive to the parameters of the film, where changes in the thin-film parameters of  $\pm 25\%$  only changed the resonance peaks by less than one percent. If the thin-film parameters should be fitted as well, then it would properly only be possible if the geometry of such fitting devices put emphasis on the thin film's importance, such as thin membranes where the

PZE thin film would play a large portion of the film thickness. The only parameter in the film that might have been possible to fit with the data from the glass block devices is the PZE coupling coefficient  $e_{31}$  which has a somewhat strong effect, especially on the amplitude; however, this would still only have been possible after the material parameters of the glass were better determined.

For the thin film acoustofluidic devices that were presented in paper II, there were several possible avenues for further exploration. One of most promising is the possibility of using topology optimization on the electrode patterning, to maximize the acoustical energy and minimize losses for optimal acoustofluidic action in the device with minimal heating. The method might be promising because it is possible to control the electrode deposition very precisely with clean-room techniques, and because the electrode patterns that would prove useful in, for example, a flow-through experiment do not necessarily need to have a very clean looking mode along the length of the device in order to perform well. With the technique of looking at the out-of-phase strain pattern of a simulation, this might help the topology optimization algorithm along and serve as a good and efficient starting point.

One small result that would have been interesting to investigate further is small devices that have a membrane resonance and a bulk resonance that lie close to each other, and which showed anti-crossing behavior and amplification of the acoustofluidic modes. These devices lie somewhat between the thin-film bulk acoustofluidic devices results and the thin-film membrane devices results. In the end, they might be difficult to produce and handle as they would require tight tolerances in both the membrane and the device geometries.

The results for the axisymmetric membrane actuation could be extended to include non-axisymmetric membrane actuation. This might allow for strong high-order membrane actuation that also had a phase dependence, such as the Bessel modes with a axial phase mode different from zero, as this would allow for there to be a node in the center of the membrane instead of an anti-node. This might allow for there to be a pressure node in the center, as has been seen in the literature Ref. 35, and therefore it might allow for trapping in the center of the axis of cells and particles with positive acoustic contrast factor.

One of the fields that could be interesting to explore is gigahertz acoustofluidics, since there are many experimental results in the literature, and they are showing very interesting results. However, as their systems are inherently many-wavelength systems, they are often demanding to simulate. The effective boundary layer theory of Bach and Bruus Ref. 78 allows for the possibility of simulating higher-frequency systems than otherwise would be possible because the meshing of the boundary layer that otherwise would be needed would not allow for the large system to be properly be resolved.

One of the more promising concepts that would have been interesting to explore is the possibility of using the acoustic reflections of a cell or particle to determine the type of the particle or cell. Because the acoustic reflections of a cell or particle depend on their acoustical properties then it might be possible to listen to the reflections by a *mechanical ear*, described below, and thereby through electromechanical feedback detect and classify the cell types electronically without the need for any invasive fluid changes, cell harming light, labeling, or time consuming analysis. While the reflections from one cell are not very different from another cell which has close to the same cell diameter with parameter

values that are close to each other in the long wavelength limit, the small differences most likely becomes much more pronounced close to resonances of the cell and even more so at the higher overtones of the cell, because of the complex way acoustic resonances operate in high-wavelength systems. The mechanical ear could be a piezoelectric resonator, such as a thin film, perhaps with a membrane as a resonator at lower frequencies, and just using the bulk resonances in the thin film at high frequencies. As shown by Pulskamp *et al.* Ref. 151, by patterning the electrodes correctly, the sensitivity to different modes can be greatly enhanced. Having a host of different designs to pick up the reflections that would arise from cells at resonance, actuated by a wide frequency sweep, might make it possible to characterize them. Such signals from a host of different mechanical ears would be ideal for training a machine learning algorithm to detect types of cells. Since the overtones likely are very distinct, it might even be possible to pick individual cells out of a tight suspension of other cells. While this is currently speculation, if the PhD had gone on for longer this idea would probably have been high on the list of subjects that would have been interesting to investigate further.

#### **A future of acoustofluidics where these results play a role**

It is difficult to predict the future, and what role these results will have in such a future is more guesswork than anything else. However, to leave the reader with an impression of what the author of this thesis hopes for the future of these results, some guessing will be done. For biomedical diagnostics, it is important to have single use devices, where cross contamination is impossible. It is difficult to imagine a future where such single use devices are made by permanently attached lead-full transducers, partly because lead is environmentally hazardous, and is therefore being phased out, and partly because such devices have been proven to have difficulty in producing consistent results. This is where the thin-film devices come into the picture. Sputtering AlN or AlScN thin-films onto devices in a role-to-role scenario, makes it possible to manufacture mass scale devices in a lead-free manner, which has also been proven to give reproducible results, although the acoustofluidic capabilities remain to be tested. This would probably bring the cost of the devices down to a point where they could be used as single-use devices, which could easily and safely be disposed of. This could open applications that could make acoustofluidic medical devices significant in the market, with applications only being limited by the creativity of the acoustofluidic community. The concept of amplifying specific mechanical thin-film driven modes by looking at the out-of-phase strain, also could see uses in the future. One example of this are membrane-trapping devices, which show promise. If they indeed work as the simulations predict, they could become a staple in research or production environments in the future. There are many situations where such label-free trapping in system that cannot have a lid, could see uses. The example that has been mentioned is an assay study in a petri dish, but many biological studies require that cells be are trapped without being in contact with a surface while other processes are done to them. It may be a farfetched hoped that this or derivations from this could be a mainstay in laboratories in the future. Where exactly the results and ideas presented in this thesis will end up only the future truly will tell.



# Bibliography

- [1] A. G. Steckel and H. Bruus, *Numerical study of bulk acoustofluidic devices driven by thin-film transducers and whole-system resonance modes*. The Journal of the Acoustical Society of America **150**(1), 634–645 (2021).
- [2] A. G. Steckel, H. Bruus, P. Muralt, and R. Matloub, *Fabrication, characterization, and simulation of glass devices with AlN thin-film transducers for excitation of ultrasound resonances*. Physical Review Applied **16**(1), 014014 (2021).
- [3] A. G. Steckel and H. Bruus, *Numerical study of acoustic cell trapping above elastic membrane disks driven in higher-harmonic modes by thin-film transducers with patterned electrodes*. ArXiv **Submitted**, 14 pages (2021).
- [4] O. Cramer, *The variation of the specific heat ratio and the speed of sound in air with temperature, pressure, humidity, and co2 concentration*. The Journal of the Acoustical Society of America **93**(5), 2510–2516 (1993).
- [5] S. Preston, P. Steart, A. Wilkinson, J. Nicoll, and R. Weller, *Capillary and arterial cerebral amyloid angiopathy in alzheimer’s disease: defining the perivascular route for the elimination of amyloid  $\beta$  from the human brain*. Neuropathology and applied neurobiology **29**(2), 106–117 (2003).
- [6] Y. Wang, W.-Y. Lin, K. Liu, R. J. Lin, M. Selke, H. C. Kolb, N. Zhang, X.-Z. Zhao, M. E. Phelps, C. K. Shen, *et al.*, *An integrated microfluidic device for large-scale in situ click chemistry screening*. Lab on a Chip **9**(16), 2281–2285 (2009).
- [7] P. Neuzil, S. Giselbrecht, K. Lange, T. J. Huang, and A. Manz, *Revisiting lab-on-a-chip technology for drug discovery*. Nature reviews Drug discovery **11**(8), 620–632 (2012).
- [8] N. Pamme and C. Wilhelm, *Continuous sorting of magnetic cells via on-chip free-flow magnetophoresis*. Lab on a Chip **6**(8), 974 (2006).
- [9] D. Holmes, D. Pettigrew, C. H. Reccius, J. D. Gwyer, C. van Berkel, J. Holloway, D. E. Davies, and H. Morgan, *Leukocyte analysis and differentiation using high speed microfluidic single cell impedance cytometry*. Lab on a Chip **9**(20), 2881–2889 (2009).
- [10] D. Figeys and D. Pinto, *Lab-on-a-chip: a revolution in biological and medical sciences*. (2000).

- [11] M. Mir, A. Homs, and J. Samitier, *Integrated electrochemical dna biosensors for lab-on-a-chip devices*. *Electrophoresis* **30**(19), 3386–3397 (2009).
- [12] S.-S. Hsieh, C.-Y. Lin, C.-F. Huang, and H.-H. Tsai, *Liquid flow in a micro-channel*. *Journal of Micromechanics and Microengineering* **14**(4), 436 (2004).
- [13] P. J. Kenis, R. F. Ismagilov, and G. M. Whitesides, *Microfabrication inside capillaries using multiphase laminar flow patterning*. *Science* **285**(5424), 83–85 (1999).
- [14] A. J. Mach and D. Di Carlo, *Continuous scalable blood filtration device using inertial microfluidics*. *Biotechnol Bioeng* **107**(2), 302–311 (2010).
- [15] P. Ohlsson, M. Evander, K. Petersson, L. Mellhammar, A. Lehmusvuori, U. Karhunen, M. Soikkeli, T. Seppa, E. Tuunainen, A. Spangar, P. von Lode, K. Rantakokko-Jalava, G. Otto, S. Scheduling, T. Soukka, S. Wittfooth, and T. Laurell, *Integrated acoustic separation, enrichment, and microchip polymerase chain reaction detection of bacteria from blood for rapid sepsis diagnostics*. *Analytical Chemistry* **88**(19), 9403–9411 (2016).
- [16] S. Zheng, H. K. Lin, B. Lu, A. Williams, R. Datar, R. J. Cote, and Y.-C. Tai, *3d microfilter device for viable circulating tumor cell (ctc) enrichment from blood*. *Biomed Microdevices* **13**(1), 203–213 (2011).
- [17] M. Antfolk, C. Magnusson, P. Augustsson, H. Lilja, and T. Laurell, *Acoustofluidic, label-free separation and simultaneous concentration of rare tumor cells from white blood cells*. *Anal. Chem.* **87**(18), 9322–9328 (2015).
- [18] F.-C. Bidard, C. Mathiot, S. Delaloge, E. Brain, S. Giachetti, P. De Cremoux, M. Marty, and J.-Y. Pierga, *Single circulating tumor cell detection and overall survival in nonmetastatic breast cancer*. *Annals of Oncology* **21**(4), 729–733 (2010).
- [19] P. Augustsson, C. Magnusson, M. Nordin, H. Lilja, and T. Laurell, *Microfluidic, label-free enrichment of prostate cancer cells in blood based on acoustophoresis*. *Anal. Chem.* **84**(18), 7954–7962 (2012).
- [20] A. Lenshof, A. Ahmad-Tajudin, K. Jaras, A.-M. Sward-Nilsson, L. Aberg, G. Marko-Varga, J. Malm, H. Lilja, and T. Laurell, *Acoustic whole blood plasmapheresis chip for prostate specific antigen microarray diagnostics*. *Anal. Chem.* **81**(15), 6030–6037 (2009).
- [21] M. Tenje, A. Fornell, M. Ohlin, and J. Nilsson, *Particle manipulation methods in droplet microfluidics* (2018).
- [22] A. Bussonniere, Y. Miron, M. Baudoin, O. Bou Matar, M. Grandbois, P. Charette, and A. Renaudin, *Cell detachment and label-free cell sorting using modulated surface acoustic waves (SAWs) in droplet-based microfluidics*. *Lab Chip* **14**, 3556–3563 (2014).

- [23] A. Fornell, K. Cushing, J. Nilsson, and M. Tenje, *Binary particle separation in droplet microfluidics using acoustophoresis*. *Appl. Phys. Lett.* **112**(6), 063701 (2018).
- [24] D. J. Collins, A. Neild, A. DeMello, A.-Q. Liu, and Y. Ai, *The poisson distribution and beyond: methods for microfluidic droplet production and single cell encapsulation*. *Lab on a Chip* **15**(17), 3439–3459 (2015).
- [25] T. Laurell, F. Petersson, and A. Nilsson, *Chip integrated strategies for acoustic separation and manipulation of cells and particles*. *Chem Soc Rev* **36**(3), 492–506 (2007).
- [26] P. Ohlsson, K. Petersson, P. Augustsson, and T. Laurell, *Acoustic impedance matched buffers enable separation of bacteria from blood cells at high cell concentrations*. *Sci. Rep.* **8**, 2045–2322 (2018).
- [27] D. J. Collins, A. Neild, and Y. Ai, *Highly focused high-frequency travelling surface acoustic waves (saw) for rapid single-particle sorting*. *Lab Chip* **16**, 471–479 (2016).
- [28] P. Augustsson, J. T. Karlsen, H.-W. Su, H. Bruus, and J. Voldman, *Iso-acoustic focusing of cells for size-insensitive acousto-mechanical phenotyping*. *Nat. Commun.* **7**, 11556 (2016).
- [29] K. Olofsson, B. Hammarstrom, and M. Wiklund, *Acoustic separation of living and dead cells using high density medium*. *LAB ON A CHIP* **20**(11), 1981–1990 (2020).
- [30] H.-D. Xi, H. Zheng, W. Guo, A. M. Gañán-Calvo, Y. Ai, C.-W. Tsao, J. Zhou, W. Li, Y. Huang, N.-T. Nguyen, *et al.*, *Active droplet sorting in microfluidics: a review*. *Lab on a Chip* **17**(5), 751–771 (2017).
- [31] C. Zhang, P. Brunet, L. Royon, and X. Guo, *Mixing intensification using sound-driven micromixer with sharp edges*. *Chemical Engineering Journal* **410**, 128252 (2021).
- [32] R. J. Shilton, L. Y. Yeo, and J. R. Friend, *Quantification of surface acoustic wave induced chaotic mixing-flows in microfluidic wells*. *Sensors and Actuators B: Chemical* **160**(1), 1565–1572 (2011).
- [33] J. Nam, W. S. Jang, and C. S. Lim, *Micromixing using a conductive liquid-based focused surface acoustic wave (cl-fsaw)*. *Sensors and Actuators B: Chemical* **258**, 991–997 (2018).
- [34] T. Frommelt, M. Kostur, M. Wenzel-Schaefer, P. Talkner, P. Haenggi, and A. Wixforth, *Microfluidic mixing via acoustically driven chaotic advection*. *Phys. Rev. Lett.* **100**(3), 034502 (2008).
- [35] D. Baresch, J.-L. Thomas, and R. Marchiano, *Observation of a single-beam gradient force acoustical trap for elastic particles: Acoustical tweezers*. *Phys. Rev. Lett.* **116**, 024301 (2016).

- [36] D. Baresch, J.-L. Thomas, and R. Marchiano, *Orbital angular momentum transfer to stably trapped elastic particles in acoustical vortex beams*. Physical review letters **121**(7), 074301 (2018).
- [37] D. Baresch, J.-L. Thomas, and R. Marchiano, *Three-dimensional acoustic radiation force on an arbitrarily located elastic sphere*. J. Acoust. Soc. Am. **133**(1), 25–36 (2013).
- [38] M. Baudoin, J.-C. Gerbedoen, A. Riaud, O. B. Matar, N. Smagin, and J.-L. Thomas, *Folding a focalized acoustical vortex on a flat holographic transducer: miniaturized selective acoustical tweezers*. Science advances **5**(4), eaav1967 (2019).
- [39] D. Foresti, M. Nabavi, and D. Poulikakos, *On the acoustic levitation stability behaviour of spherical and ellipsoidal particles*. J. Fluid Mech. **709**, 581–592 (2012).
- [40] P. Gammel, A. Croonquist, and T. Wang, *A high-powered siren for stable acoustic levitation of dense materials in the earths gravity*. J. Acoust. Soc. Am. **83**(2), 496–501 (1988).
- [41] A. Marzo, S. A. Seah, B. W. Drinkwater, D. R. Sahoo, B. Long, and S. Subramanian, *Holographic acoustic elements for manipulation of levitated objects*. Nat. Commun. **6**, 8661 (2015).
- [42] S. Santesson and S. Nilsson, *Airborne chemistry: acoustic levitation in chemical analysis*. Anal. Bioanal. Chem. **378**(7), 1704–1709 (2004).
- [43] E. Trinh, *Compact acoustic levitation device for studies in fluid dynamics and material science in the laboratory and microgravity*. Rev. Sci. Instrum. **56**(11), 2059–2065 (1985).
- [44] M. A. Andrade, A. Marzo, and J. C. Adamowski, *Acoustic levitation in mid-air: recent advances, challenges, and future perspectives*. Applied Physics Letters **116**(25), 250501 (2020).
- [45] S. Polychronopoulos and G. Memoli, *Acoustic levitation with optimized reflective metamaterials*. Scientific reports **10**(1), 1–10 (2020).
- [46] M. A. Andrade, T. S. Ramos, J. C. Adamowski, and A. Marzo, *Contactless pick-and-place of millimetric objects using inverted near-field acoustic levitation*. Applied Physics Letters **116**(5), 054104 (2020).
- [47] M. A. Andrade, N. Pérez, and J. C. Adamowski, *Review of progress in acoustic levitation*. Brazilian Journal of Physics **48**(2), 190–213 (2018).
- [48] X. Chen, K. H. Lam, R. Chen, Z. Chen, X. Qian, J. Zhang, P. Yu, and Q. Zhou, *Acoustic levitation and manipulation by a high-frequency focused ring ultrasonic transducer*. Applied Physics Letters **114**(5), 054103 (2019).

- [49] V. Vandaele, A. Delchambre, and P. Lambert, *Acoustic wave levitation: Handling of components*. J. Appl. Phys. **109**(12), 124901 (2011).
- [50] V. Vandaele, P. Lambert, and A. Delchambre, *Non-contact handling in microassembly: Acoustical levitation*. Precis. Eng. **29**(4), 491–505 (2005).
- [51] P.-H. Huang, C. Y. Chan, P. Li, N. Nama, Y. Xie, C.-H. Wei, Y. Chen, D. Ahmed, and T. J. Huang, *A spatiotemporally controllable chemical gradient generator via acoustically oscillating sharp-edge structures*. Lab on a Chip **15**(21), 4166–4176 (2015).
- [52] C. Zhang, X. Guo, P. Brunet, M. Costalonga, and L. Royon, *Acoustic streaming near a sharp structure and its mixing performance characterization*. Microfluidics Nanofluidics **23**(9), 104 (2019).
- [53] X. Guo, Z. Ma, R. Goyal, M. Jeong, W. Pang, P. Fischer, X. Duan, and T. Qiu, *Acoustofluidic tweezers for the 3d manipulation of microparticles*. In *2020 IEEE International Conference on Robotics and Automation (ICRA)*, 11392–11397 (IEEE) (2020).
- [54] S. Wang, Z. Wang, Y. Ning, X. Chen, X. Duan, W. Pang, and Q. Yang, *Particle manipulation by a novel lamb wave resonator array with grating reflectors*. In *2020 IEEE International Ultrasonics Symposium (IUS)*, 1–4 (IEEE) (2020).
- [55] W. Cui, L. Mu, X. Duan, W. Pang, and M. A. Reed, *Trapping of sub-100 nm nanoparticles using gigahertz acoustofluidic tweezers for biosensing applications*. Nanoscale **11**(31), 14625–14634 (2019).
- [56] F. Petersson, A. Nilsson, C. Holm, H. Jönsson, and T. Laurell, *Separation of lipids from blood utilizing ultrasonic standing waves in microfluidic channels*. Analyst **129**(10), 938–43 (2004).
- [57] M. Hamilton, Y. Ilinskii, and E. Zabolotskaya, *Acoustic streaming generated by standing waves in two-dimensional channels of arbitrary width*. J. Acoust. Soc. Am. **113**(1), 153–160 (2003).
- [58] B. Hammarström, M. Evander, H. Barbeau, M. Bruzelius, J. Larsson, T. Laurell, and J. Nilsson, *Non-contact acoustic cell trapping in disposable glass capillaries*. Lab Chip **10**(17), 2251–2257 (2010).
- [59] M. Wiklund, C. Günther, R. Lemor, M. Jäger, G. Fuhr, and H. M. Hertz, *Ultrasonic standing wave manipulation technology integrated into a dielectrophoretic chip*. Lab on a Chip **6**(12), 1537–1544 (2006).
- [60] P. Reichert, D. Deshmukh, L. Lebovitz, and J. Dual, *Thin film piezoelectrics for bulk acoustic wave (BAW) acoustophoresis*. Lab Chip **18**(23), 3655–3667 (2018).

- [61] P. Delsing, A. N. Cleland, M. J. Schuetz, J. Knörzer, G. Giedke, J. I. Cirac, K. Srinivasan, M. Wu, K. C. Balram, C. Bäuerle, *et al.*, *The 2019 surface acoustic waves roadmap*. Journal of Physics D: Applied Physics **52**(35), 353001 (2019).
- [62] M. S. Gerlt, N. F. Läubli, M. Manser, B. J. Nelson, and J. Dual, *Reduced etch lag and high aspect ratios by deep reactive ion etching (drie)*. Micromachines **12**(5), 542 (2021).
- [63] M. Gerlt, P. Ruppen, M. Leuthner, S. Panke, and J. Dual, *Acoustofluidic medium exchange for preparation of electrocompetent bacteria using channel wall trapping*. Chem Archive (2021).
- [64] M. Barmatz, *Acoustic radiation potential on a sphere in plane, cylindrical, and spherical standing wave fields*. J. Acoust. Soc. Am. **77**(3), 928 (1985).
- [65] K. Yasuda and T. Kamakura, *Acoustic radiation force on micrometer-size particles*. Appl. Phys. Lett. **71**(13), 1771–1773 (1997).
- [66] P. B. Muller, R. Barnkob, M. J. H. Jensen, and H. Bruus, *A numerical study of microparticle acoustophoresis driven by acoustic radiation forces and streaming-induced drag forces*. Lab Chip **12**, 4617–4627 (2012).
- [67] M. Settnes and H. Bruus, *Theoretical analysis of viscous corrections to the acoustic radiation force on cells in microchannel acoustophoresis*. In J. Landers, A. Herr, D. Juncker, N. Pamme, and J. Bienvenue (eds.), *Proc. 15th MicroTAS, 2 - 6 October 2011, Seattle (WA), USA*, 160–162 (CBMS) (2011).
- [68] G. T. Silva, *Acoustic radiation force and torque on an absorbing compressible particle in an inviscid fluid*. J. Acoust. Soc. Am. **136**(5), 2405–2413 (2014).
- [69] G. T. Silva, *Dynamic radiation force of acoustic waves on absorbing spheres*. Braz. J. Phys. **40**(2), 184–187 (2010).
- [70] G. T. Silva, M. W. Urban, and M. Fatemi, *Multifrequency radiation force of acoustic waves in fluids*. Physica D: Nonlinear Phenomena **232**(1), 48–53 (2007).
- [71] P. Hahn, I. Leibacher, T. Baasch, and J. Dual, *Numerical simulation of acoustofluidic manipulation by radiation forces and acoustic streaming for complex particles*. Lab Chip **15**, 4302–4313 (2015).
- [72] J. T. Karlsen and H. Bruus, *Forces acting on a small particle in an acoustical field in a thermoviscous fluid*. Phys. Rev. E **92**, 043010 (2015).
- [73] P. B. Muller, *Acoustofluidics in microsystems: investigation of acoustic streaming*. Master’s thesis, DTU Nanotech, Department of Micro- and Nanotechnology (2012 ([www.nanotech.dtu.dk/microfluidics](http://www.nanotech.dtu.dk/microfluidics))).
- [74] N. Riley, *Acoustic streaming*. Theoretical and Computational Fluid Dynamics **10**(1), 349–356 (1998).

- [75] J. Lighthill, *Acoustic streaming*. J Sound Vibr **61**(3), 391–418 (1978).
- [76] S. Boluriaan and P. J. Morris, *Acoustic streaming: from rayleigh to today*. International Journal of aeroacoustics **2**(3), 255–292 (2003).
- [77] J. S. Bach and H. Bruus, *Bulk-driven acoustic streaming at resonance in closed microcavities*. Phys. Rev. E **100**, 023104 (2019).
- [78] J. S. Bach and H. Bruus, *Theory of pressure acoustics with viscous boundary layers and streaming in curved elastic cavities*. J. Acoust. Soc. Am. **144**, 766–784 (2018).
- [79] H. G. Lim, Y. Li, M.-Y. Lin, C. Yoon, C. Lee, H. Jung, R. H. Chow, and K. K. Shung, *Calibration of trapping force on cell-size objects from ultrahigh-frequency single-beam acoustic tweezer*. IEEE IEEE T. Ultrason. Ferr. **63**(11), 1988–1995 (2016).
- [80] J. S. Bach and H. Bruus, *Suppression of acoustic streaming in shape-optimized channels*. Phys. Rev. Lett. **124**, 214501 (2020).
- [81] A. Lenshof and T. Laurell, *Continuous separation of cells and particles in microfluidic systems*. Chem Soc Rev **39**(3), 1203–1217 (2010).
- [82] B. Hammarström, B. Nilson, T. Laurell, J. Nilsson, and S. Ekström, *Acoustic trapping for bacteria identification in positive blood cultures with maldi-tof ms*. Anal. Chem. **86**(21), 10560–10567 (2014).
- [83] K. Olofsson, V. Carannante, M. Takai, B. Onfelt, and M. Wiklund, *Ultrasound-based scaffold-free core-shell multicellular tumor spheroid formation*. MICROMACHINES **12**(3) (2021).
- [84] M. Antfolk and T. Laurell, *Continuous flow microfluidic separation and processing of rare cells and bioparticles found in blood - a review*. Anal. Chim. Acta **965**, 9–35 (2017).
- [85] S. Deshmukh, Z. Brzozka, T. Laurell, and P. Augustsson, *Acoustic radiation forces at liquid interfaces impact the performance of acoustophoresis*. Lab Chip **14**, 3394–3400 (2014).
- [86] W. N. Bodé and H. Bruus, *Numerical study of the coupling layer between transducer and chip in acoustofluidic devices*. J. Acoust. Soc. Am. **149**(5), 3096–3105 (2021).
- [87] M. Safaei, H. A. Sodano, and S. R. Anton, *A review of energy harvesting using piezoelectric materials: state-of-the-art a decade later (2008–2018)*. Smart Materials and Structures **28**(11), 113001 (2019).
- [88] T. Takenaka and H. Nagata, *Current status and prospects of lead-free piezoelectric ceramics*. Journal of the European Ceramic Society **25**(12), 2693–2700 (2005).
- [89] K. Uchino, *The development of piezoelectric materials and the new perspective*. In *Advanced Piezoelectric Materials*, 1–92 (Elsevier) (2017).

- [90] S. Priya and S. Nahm, *Lead-free piezoelectrics* (Springer Science & Business Media) (2011).
- [91] E. Ringgaard and T. Wurlitzer, *Lead-free piezoceramics based on alkali niobates*. Journal of the European Ceramic Society **25**(12), 2701–2706 (2005).
- [92] R. Korobko, A. Patlolla, A. Kosoy, E. Wachtel, H. L. Tuller, A. I. Frenkel, and I. Lubomirsky, *Giant electrostriction in gd-doped ceria*. Advanced Materials **24**(43), 5857–5861 (2012).
- [93] N. R. Skov, J. S. Bach, B. G. Winkelmann, and H. Bruus, *3D modeling of acoustofluidics in a liquid-filled cavity including streaming, viscous boundary layers, surrounding solids, and a piezoelectric transducer*. AIMS Mathematics **4**, 99–111 (2019).
- [94] H. Bruus, *Theoretical Microfluidics* (Oxford University Press, Oxford) (2008).
- [95] H. Bruus, *Acoustofluidics 1: Governing equations in microfluidics*. Lab Chip **11**, 3742 – 3751 (2011).
- [96] H. Bruus, *Acoustofluidics 2: Perturbation theory and ultrasound resonance modes*. Lab Chip **12**, 20–28 (2012).
- [97] J. Dual and T. Schwarz, *Acoustofluidics 3: Continuum mechanics for ultrasonic particle manipulation*. Lab Chip **12**, 244–252 (2012).
- [98] J. Dual and D. Möller, *Acoustofluidics 4: Piezoelectricity and application to the excitation of acoustic fields for ultrasonic particle manipulation*. Lab Chip **12**, 506–514 (2012).
- [99] A. Lenshof, M. Evander, T. Laurell, and J. Nilsson, *Acoustofluidics 5: Building microfluidic acoustic resonators*. Lab Chip **12**, 684–695 (2012).
- [100] J. Dual, P. Hahn, I. Leibacher, D. Möller, and T. Schwarz, *Acoustofluidics 6: Experimental characterization of ultrasonic particle manipulation devices*. Lab Chip **12**, 852–862 (2012).
- [101] H. Bruus, *Acoustofluidics 7: The acoustic radiation force on small particles*. Lab Chip **12**, 1014–1021 (2012).
- [102] A. Lenshof, C. Magnusson, and T. Laurell, *Acoustofluidics 8: Applications in acoustophoresis in continuous flow microsystems*. Lab Chip **12**, 1210–1223 (2012).
- [103] P. Glynne-Jones, R. J. Boltryk, and M. Hill, *Acoustofluidics 9: Modelling and applications of planar resonant devices for acoustic particle manipulation*. Lab Chip **12**(8), 1417–1426 (2012).
- [104] H. Bruus, *Acoustofluidics 10: Scaling laws in acoustophoresis*. Lab Chip **12**, 1578–1586 (2012).

- [105] P. Augustsson and T. Laurell, *Acoustofluidics 11: Affinity specific extraction and sample decomplexing using continuous flow acoustophoresis*. Lab Chip **12**, 1742–1752 (2012).
- [106] M. Wiklund, *Acoustofluidics 12: Biocompatibility and cell viability in microfluidic acoustic resonators*. Lab Chip **12**, 2018–28 (2012).
- [107] S. Sadhal, *Acoustofluidics 13: Analysis of acoustic streaming by singular perturbation*. Lab Chip **12**, 2292–2300 (2012).
- [108] M. Wiklund, R. Green, and M. Ohlin, *Acoustofluidics 14: Applications of acoustic streaming in microfluidic devices*. Lab Chip **12**, 2438–2451 (2012).
- [109] S. Sadhal, *Acoustofluidics 15: Streaming with sound waves interacting with solid particles*. Lab Chip **12**, 2600–2611 (2012).
- [110] S. S. Sadhal, *Acoustofluidics 16: acoustics streaming near liquid-gas interfaces: drops and bubbles*. Lab on a chip **12**(16), 2771–2781 (2012).
- [111] M. Gedge and M. Hill, *Acoustofluidics 17: Surface acoustic wave devices for particle manipulation*. Lab Chip **12**, 2998–3007 (2012).
- [112] M. Wiklund, H. Brismar, and B. Önfelt, *Acoustofluidics 18: Microscopy for acoustofluidic micro-devices*. Lab on a Chip **12**(18), 3221–3234 (2012).
- [113] J. Dual, P. Hahn, I. Leibacher, D. Möller, T. Schwarz, and J. Wang, *Acoustofluidics 19: ultrasonic microrobotics in cavities: devices and numerical simulation*. Lab on a chip **12**(20), 4010–4021 (2012).
- [114] M. Evander and J. Nilsson, *Acoustofluidics 20: Applications in acoustic trapping*. Lab Chip **12**, 4667–4676 (2012).
- [115] M. W. H. Ley, C. Johannesson, M. Evander, T. Laurell, and H. Bruus, *Modeling and experiments of acoustic trapping forces in a small glass capillary*. Proc. 20th MicroTAS, 9 - 13 October 2016, Dublin, Ireland 711–712 (2016).
- [116] P. B. Muller and H. Bruus, *Theoretical study of time-dependent, ultrasound-induced acoustic streaming in microchannels*. Phys. Rev. E **92**, 063018 (2015).
- [117] P. B. Muller and H. Bruus, *Numerical study of thermoviscous effects in ultrasound-induced acoustic streaming in microchannels*. Phys. Rev. E **90**(4), 043016 (2014).
- [118] J. H. Joergensen and H. Bruus, *Theory of pressure acoustics with thermoviscous boundary layers and streaming in elastic cavities*. The Journal of the Acoustical Society of America **149**(5), 3599–3610 (2021).
- [119] J. S. Bach and H. Bruus, *Theory of acoustic trapping of microparticles in capillary tubes*. Physical Review E **101**(2), 023107 (2020).

- [120] J. T. Karlsen and H. Bruus, *Acoustic tweezing and patterning of concentration fields in microfluidics*. Phys. Rev. Applied **7**, 034017 (2017).
- [121] B. Lautrup, *Physics of continuous matter: exotic and everyday phenomena in the macroscopic world* (CRC press) (2011).
- [122] M. W. H. Ley and H. Bruus, *Three-dimensional numerical modeling of acoustic trapping in glass capillaries*. Phys. Rev. Applied **8**, 024020 (2017).
- [123] P. Muralt, *Ferroelectric thin films for micro-sensors and actuators: a review*. Journal of micromechanics and microengineering **10**(2), 136 (2000).
- [124] P. Muralt, *Pzt thin films for microsensors and actuators: Where do we stand?* IEEE transactions on ultrasonics, ferroelectrics, and frequency control **47**(4), 903–915 (2000).
- [125] P. Muralt, *Recent progress in materials issues for piezoelectric MEMS*. J. Am. C. Soc. **91**(5), 1385–1396 (2008).
- [126] W. L. Nyborg, *Acoustic streaming near a boundary*. J. Acoust. Soc. Am. **30**(4), 329–339 (1958).
- [127] C. Lee and T. Wang, *Near-boundary streaming around a small sphere due to 2 orthogonal standing waves*. J. Acoust. Soc. Am. **85**(3), 1081–1088 (1989).
- [128] M. R. Spiegel, S. Lipschutz, and J. Liu, *Schaum's Outlines: Mathematical Handbook of Formulas and Tables*, vol. 3 (McGraw-Hill New York) (2009).
- [129] J. S. Bach, *Theory of acoustic fields and streaming with viscous boundary layers in microsystems* (2020).
- [130] M. Settnes and H. Bruus, *Forces acting on a small particle in an acoustical field in a viscous fluid*. Phys. Rev. E **85**, 016327 (2012).
- [131] L. P. Gorkov, *On the forces acting on a small particle in an acoustical field in an ideal fluid*. Sov. Phys.–Dokl. **6**(9), 773–775 (1962), [Doklady Akademii Nauk SSSR **140**, 88 (1961)].
- [132] R. Barnkob, P. Augustsson, T. Laurell, and H. Bruus, *Measuring the local pressure amplitude in microchannel acoustophoresis*. Lab Chip **10**(5), 563–570 (2010).
- [133] M. A. Hopcroft, W. D. Nix, and T. W. Kenny, *What is the Young's modulus of silicon*. J. Microelectromech. Syst **19**, 229–238 (2010).
- [134] E. V. Thomsen, K. Reck, G. Skands, C. Bertelsen, and O. Hansen, *Silicon as an anisotropic mechanical material: Deflection of thin crystalline plates*. Sensors and Actuators A: Physical **220**, 347–364 (2014).
- [135] COMSOL Multiphysics 5.5 (2019), <http://www.comsol.com>.

- [136] Matlab 2019b. <http://www.mathworks.com> (2019).
- [137] P. B. Muller, M. Rossi, A. G. Marin, R. Barnkob, P. Augustsson, T. Laurell, C. J. Kähler, and H. Bruus, *Ultrasound-induced acoustophoretic motion of microparticles in three dimensions*. *Phys. Rev. E* **88**(2), 023006 (2013).
- [138] M. A. Caro, S. Zhang, T. Riekkinen, M. Ylilammi, M. A. Moram, O. Lopez-Acevedo, J. Molarius, and T. Laurila, *Piezoelectric coefficients and spontaneous polarization of ScAlN*. *J. Phys.-Condens. Mat.* **27**(24), 245901 (2015).
- [139] A. Iqbal and F. Mohd-Yasin, *Reactive sputtering of aluminum nitride (002) thin films for piezoelectric applications: A review*. *Sensors* **18**(6), 1797 (2018).
- [140] R. H. Olsson, Z. Tang, and M. D'Agati, *Doping of aluminum nitride and the impact on thin film piezoelectric and ferroelectric device performance*. In *2020 IEEE Custom Integrated Circuits Conference (CICC)*, 1–6 (2020).
- [141] Meggitt A/S, Porthusvej 4, DK-3490 Kvistgaard, Denmark, *Ferroperm matrix data*. <https://www.meggittferroperm.com/materials/>, accessed 2 May 2021.
- [142] SCHOTT, SCHOTT Suisse SA, 2 Rue Galilée, Yverdon, Switzerland, *Borosilicate glass substrates*. [https://www.epfl.ch/research/facilities/cmi/wp-content/uploads/2020/05/D263T\\_d.pdf](https://www.epfl.ch/research/facilities/cmi/wp-content/uploads/2020/05/D263T_d.pdf), accessed 2 May 2021.
- [143] P. Hahn and J. Dual, *A numerically efficient damping model for acoustic resonances in microfluidic cavities*. *Physics of Fluids* **27**, 062005 (2015).
- [144] CORNING, Houghton Park C-8, Corning, NY 14831, USA, *Glass Silicon Constraint Substrates*. <http://www.valleydesign.com/Datasheets/Corning%20Pyrex%207740.pdf>, accessed 2 May 2021.
- [145] R. Barnkob, P. Augustsson, T. Laurell, and H. Bruus, *Acoustic radiation- and streaming-induced microparticle velocities determined by microparticle image velocimetry in an ultrasound symmetry plane*. *Phys. Rev. E* **86**, 056307 (2012).
- [146] P. Augustsson, R. Barnkob, S. T. Wereley, H. Bruus, and T. Laurell, *Automated and temperature-controlled micro-PIV measurements enabling long-term-stable microchannel acoustophoresis characterization*. *Lab Chip* **11**(24), 4152–4164 (2011).
- [147] COMSOL Multiphysics 5.4 (2018), <http://www.comsol.com>.
- [148] T. Manzaneque, J. Hernando, L. Rodríguez-Aragón, A. Ababneh, H. Seidel, U. Schmid, and J. Sánchez-Rojas, *Analysis of the quality factor of aln-actuated micro-resonators in air and liquid*. *Microsystem technologies* **16**(5), 837–845 (2010).
- [149] M. Arita, S. Ishida, S. Kako, S. Iwamoto, and Y. Arakawa, *Aln air-bridge photonic crystal nanocavities demonstrating high quality factor*. *Applied Physics Letters* **91**(5), 051106 (2007).

- [150] J. Qian, R. Yang, H. Begum, and J. E.-Y. Lee, *Reconfigurable acoustofluidic manipulation of particles in ring-like rich patterns enabled on a bulk micromachined silicon chip*. In *2021 21st International Conference on Solid-State Sensors, Actuators and Microsystems (Transducers)*, 365–368 (IEEE) (2021).
- [151] J. S. Pulskamp, S. S. Bedair, R. G. Polcawich, G. L. Smith, J. Martin, B. Power, and S. A. Bhave, *Electrode-shaping for the excitation and detection of permitted arbitrary modes in arbitrary geometries in piezoelectric resonators*. *IEEE transactions on ultrasonics, ferroelectrics, and frequency control* **59**(5), 1043–1060 (2012).